

UNIVERSITY OF HERTFORDSHIRE

School of Life and Medical Sciences

**Department of Clinical, Pharmaceutical and Biological
Science**

**Development of Smart Polymeric Nanocontainers
for The Therapy of Head And Brain Malignancies**

Sara Seriah

**Submitted to the University of Hertfordshire in partial
fulfilment of the requirements of the degree of
PhD**

April 2023

ABSTRACT

Head and brain tumours account for 2% to 4% of all cancers globally. Despite progress made in diagnosis and adjuvant therapies, they remain a global burden with unsatisfactory survival rates, reduced treatment outcome, poor prognosis and high risks of recurrence. First line chemotherapy drugs used in current regimens lack specificity, which ensues long term and unpleasant side effects for the patient. Encapsulating the chemotherapy drugs within nanocontainers (NCs) is one approach to improving their efficacy and therapeutic outcome as well as reducing side effects. Due to their nano-size and suitable modified surface, polymeric NCs can reach critical areas in the head and brain without causing any damage to the healthy tissue. The aim was to synthesize polymeric NCs capable of carrying and delivering chemotherapy drugs in tumour cells to increase their efficacy and reduce their side effects. Hollow P(MAA-co-MBA-co-NIPAM-co-EGDMA) NCs with dual sensitivity were synthesised and characterized structurally and morphologically throughout the synthesis steps. Daunorubicin, cisplatin, and temozolomide loaded NCs, and free NCs were assessed by haemolysis assay, MTT assay, fluorescence microscopy, western blot, and flow cytometry in rhabdomyosarcoma TE671 cell line and glioblastoma U87 MG cell line. The free NCs showed high biocompatibility and non-toxicity trait with good cellular uptake. Also, the loading capacities were between 27% and 63%, and the release studies showed a sustained release profile for up to 72h. Treatment of rhabdomyosarcoma and glioblastoma cells with different drugs loaded in NCs showed high cancer cell cytotoxicity, variation in induced DNA damage levels, induced apoptosis and cell cycles arrest for 24h and 72h. Overall, smart polymeric NCs showed reliability in carrying and delivering chemotherapy drugs in rhabdomyosarcoma and glioblastoma cells with efficiency in tackling the tumour cells. Our polymeric NCs exhibited excellent potential as a novel therapeutic approach for targeted drug delivery in head and

brain tumours. This could be verified in the preclinical models to assess their improved efficacy and reducing side effects of first line cancer therapies. It could further pave the way for clinical trials of head and brain cancers in human patients.

ACKNOWLEDGMENTS

For me, doing PhD was far more than a research degree that includes carrying out experiments in the lab and writing a significant thesis. It was an opportunity for professional and personal growth. A demanding journey that amid the global covid-19 pandemic became more challenging. Yet, I was blessed with enormous amount of support . First and for most, I would like to express my sincere gratitude to Allah the Almighty and thank Him for bestowing upon me his countless blessings, and for providing me with guidance, support, and strength throughout my PhD journey.

I would like also to thank my amazing parents, my pillars, for believing in me and supporting me endlessly both morally and financially throughout this journey. Words can never be enough to describe how grateful I am to have such amazing parents. Surely, my thanks go to my wonderful sister and brother for their encouragement, and immense support with their unique way. I feel extremely lucky to have my great supportive family!

A special thanks go to my supervisors Dr Maria Braoudaki and Dr Eleni Efthimiadou for their great supervision, support, and kindness. I am grateful and honoured to have been part of their research teams, and for all the gained experience, invaluable advice and feedback I got from them throughout my PhD journey. My thanks go also to Prof Jameel Inal whom I had the honour to have as my third supervisor.

I would also like to extend my thanks to my friends and lab mates Maria, Danai, Anastasia, Athina, and Dora for being such great people and supportive friends. Finally, my thanks extend to Dr Shoib Siddiqui for his support, Dr Elias Sakelis for his SEM training, as well as Dr Emmanouilidou, Dr Efthimiopolou and Dr Papazafiri and their teams from the University of Athens for opening the doors of their labs for me.

Table of Contents

	Page No.
Title Page	1
Abstract	2
Acknowledgments	4
Table of contents	5
List of Figures.....	12
List of Tables	20
Abbreviations	22
 CHAPTER 1: INTRODUCTION	
1.1. Head and neck tumours	26
1.2. Brain tumours	31
1.3. Brain anatomy	35
1.4. Blood brain barrier	38
1.5. Nanotechnology and nanoparticles	40
1.5.1. Nanotechnology	40
1.5.2. Nanoparticles	41
1.5.2.1. Dendrimers	41
1.5.2.2. Liposomes	42
1.5.2.3. Polymeric nanoparticles	44
1.5.2.4. Micellar nanoparticles	45
1.5.2.5. Gold nanoparticles	46
1.5.2.6. Iron oxide nanoparticles	48
1.6. Aims and objectives	51

1.6.1. Research questions	51
---------------------------------	----

CHAPTER 2: NANOCONTAINERS AND NANOTECHNOLOGY

2.1. Introduction	53
2.1.1. Nanotechnology	53
2.1.2. Polymeric nanoparticles	55
2.1.3. Targeting Approaches	57
2.1.3.1. Passive targeting	57
2.1.3.2. Active targeting	58
2.1.3.3. Stimuli-responsive targeting	59
2.1.4. Synthesis Methods	66
2.1.4.1. Solvent evaporation	66
2.1.4.2. Emulsification with solvent diffusion.....	67
2.1.4.3. Emulsification with reverse salting-out	67
2.1.4.4. Nanoprecipitation	68
2.1.5. Characterization Methods	68
2.2. Materials and Methods	71
2.2.1. Materials	71
2.2.2. Silica Nanocontainers.....	71
2.2.2.1. Synthesis of silica core spheres.....	71
2.2.2.2. Synthesis of the first thin layer with methacryloxypropyltrimethoxysilane (SiO ₂ @MPS).....	72
2.2.2.3. Multisensitive layer fabrication SiO ₂ @MPS@P(MAA-co-MBA-co-EDGMA) nanocontainers.....	72

2.2.2.4. Hollow silica MPS@P(MAA-co-MBA-co-EGDMA) nanocontainers	73
2.2.3. Polymeric Nanocontainers	73
2.2.3.1. Core PMAA spheres.....	73
2.2.3.2. Multisensitive shell fabrication PMAA@P(MAA-co-MBA-co-EGDMA) and PMAA@P(MAA-co-MBA-co-NIPAM-co-EGDMA) nanocontainers	74
2.2.3.3. Hollow P(MAA-co-MBA-co-EGDMA) and P(MAA-co-MBA-co-NIPAM-co-EGDMA) nanocontainers	75
2.2.4. Fourier Transform Infrared Spectroscopy (FTIR)	76
2.2.5. Dynamic Light Scattering (DLS)	76
2.2.6. Scanning Electron Microscopy (SEM)	77
2.2.7. COOH Back Titration	77
2.2.8. Drug Loading	77
2.2.9. Drug Release	78
2.2.9.1. Stirring method.....	78
2.2.9.2. Dialysis bag method	78
2.2.10. Hemolysis Assay	79
2.2.10.1. Fixation of red blood cells	80
2.3. Results	81
2.3.1. Structural Characterization	81
2.3.1.1. Silica nanoparticles characterization by Fourier transform infrared microscopy (FTIR)	81
2.3.1.2. Silica nanoparticles characterization dynamic light scattering (DLS)	82
2.3.1.3. Polymeric nanocontainers characterization by Fourier transform infrared microscopy (FTIR)	83

2.3.1.4. Polymeric nanocontainers characterization Dynamic light scattering (DLS)	85
2.3.2. Morphological Characterization	86
2.3.2.1. Silica nanocontainers	86
2.3.2.2. Polymeric Nanocontainers	88
2.3.2.3. COOH Concentrations	89
2.3.3. Drug Loading	91
2.3.4. Drug Release	93
2.3.5. Biocompatibility	96
2.4. Discussion	102
2.4.1. Polymeric nanoparticles	104
2.5. Conclusion	110

CHAPTER 3 : RHABDOMYOSARCOMA

3.1. Introduction	112
3.1.1. Epidemiology.....	118
3.1.2. Diagnosis	119
3.1.3. Treatment	124
3.1.3.1. Surgery	124
3.1.3.2. Radiotherapy	125
3.1.3.3. Chemotherapy	126
3.1.3.4. Pioneering Therapy	129
3.1.4. Prognosis	130
3.2. Material and Methods	132
3.2.1. Materials	132

3.2.2. Cell culture	133
3.2.3. MTT assay	133
3.2.4. Fluorescence microscopy	134
3.2.5. Western blot	135
3.2.5.1. Protein extraction and quantification	135
3.2.5.2. Samples and SDS-PAGE gels preparation	135
3.2.5.3. Running the gels	136
3.2.5.4. Developing the films and imaging the membranes	137
3.2.6. Flow cytometry	138
3.3. Results	139
3.3.1. Cytotoxicity	139
3.3.2. Cellular uptake and internalization	155
3.3.3. Western blot	159
3.3.4. Flow cytometry	164
3.4. Discussion	186
3.5. Conclusions	199

CHAPTER 4 : GLIOBLASTOMA

4.1. Introduction	201
4.1.1. Epidemiology	205
4.1.2. Diagnosis	208
4.1.3. Therapy	210
4.1.3.1. Surgery	210

4.1.3.2. Radiotherapy	211
4.1.3.3. Chemotherapy	214
4.1.3.4. Pioneering therapy	215
4.1.4. Prognosis	217
4.2. Materials and Methods	220
4.2.1. Materials	220
4.2.2. Cell culture	221
4.2.3. MTT assay	221
4.2.4. Wound healing	222
4.2.5. Fluorescence microscopy	223
4.2.6. Western blot	223
4.2.6.1. Protein extraction and quantification	223
4.2.6.2. Samples and SDS-PAGE gels preparation	224
4.2.6.3. Running the gels	224
4.2.6.4. Developing the films and imaging the membranes	226
4.2.7. Flow cytometry	226
4.3. Results	228
4.3.1. Cytotoxicity	228
4.3.2. Wound healing	244
4.3.3. Cellular uptake and internalization	248
4.3.4. Western blot	251
4.3.5. Apoptosis	254
4.3.6. Cell cycle	262
4.4. Discussion	269

4.5. Conclusions	282
CHAPTER 5: FINAL DISCUSSIONS	283
5.1. Future prospects	291
REFERENCES	294
APPENDICES	358
List of Publications	361
List of Workshops, Seminars, Talks, Conferences, Awards, and Trainings	371

List of Figures

Page No.

CHAPTER 1

Figure 1 Illustration of the three main parts of the human brain and the four lobes 37

Figure 2 Illustration of different nanoparticles: dendrimers, liposomes, micelles,
polymeric nanoparticles, gold nanoparticles and iron oxide nanoparticles 50

CHAPTER 2

Figure 3 Illustration of polymeric nanoparticles as nanospheres and nanocontainers56

Figure 4 Illustration of the different targeting approaches of nanoparticles: passive,
active and stimuli-response targeting58

Figure 5 FTIR spectra of the 4 synthesis stages of silica polymeric nanoparticles81

Figure 6 DLS spectra of the 4 synthesis stages of silica polymeric nanoparticles82

Figure 7 FTIR spectra of the three synthesis stages of polymeric nanocontainers with
MAA, EGDMA, and MBA83

Figure 8. FTIR spectra of the three synthesis stages of polymeric nanocontainers with MAA,
EGDMA, NIPAM, and MBA84

Figure 9 DLS spectra of the three synthesis stages of polymeric nanoparticles with MAA,
EGDMA and MBA85

Figure 10 DLS spectra of the three synthesis stages of polymeric nanoparticles with MAA,
EGDMA, NIPAM, and MBA86

Figure 11 SEM pictures of polymeric silica nanocontainers at different synthesis steps.....87

Figure 12	SEM pictures of polymeric nanocontainers at different synthesis steps.....	89
Figure 13	Release profile of DNR in pH 4.6 at 37°C and 40°C.	93
Figure 14	Release profile of DNR in pH 7.4 at 37°C and 40°C.	94
Figure 15	Release profile of cisplatin in pH 4.6 at 37°C and 40°C.	95
Figure 16	Release profile of cisplatin in pH 6.8 at 37°C and 40°C	95
Figure 17	Release profile of cisplatin in pH 7.4 at 37°C and 40°C.	96
Figure 18	Haemolysis percentage of the RBCs treated with 25,50,100 µg/ml NCs suspensions for 2h and 24h.	98
Figure 19	Optical microscopy images of the RBCs treated with different concentration of NCs suspensions.	99
Figure 20	Optical microscopy images of RBCs after treatment with different concentration of NCs suspensions.....	100
Figure 21	Scanning electron microscopy images of the RBCs after treatment with different concentration of NCs suspensions.	101
 CHAPTER 3		
Figure 22	Percentages cases of the four types of rhabdomyosarcomas: embryonal, alveolar, pleomorphic, and spindle cell/sclerosing	113
Figure 23	Anatomy of the parameningeal, orbital, non-parameningeal sites in the head	114

Figure 24	Evaluation of the cell viability via MTT assay. Cytotoxicity levels in a). TE671 and b). HEK293 cell line after 24h treatment with free NCs, cisplatin loaded NCs, and free cisplatin	140
Figure 25	Evaluation of the cell viability via MTT assay. Cytotoxicity levels in a). TE671 and b). HEK293 cell lines after 24h treatment with free NCs, DNR-loaded NCs, and free DNR	142
Figure 26	Evaluation of the cell viability via MTT assay. Cytotoxicity levels in a). TE671 and b). HEK293 cell lines after 24h treatment with free NCs, temozolomide-loaded NCs, and free temozolomide	144
Figure 27	Evaluation of the cell viability via MTT assay. Cytotoxicity levels in a).TE671 and b). HEK293 cell lines after 24h treatment with free NCs, DNR/temozolomide combination loaded NCs, and free DNR/temozolomide combination	146
Figure 28	Evaluation of the cell viability via MTT assay. Cytotoxicity levels in a). TE671 and b). HEK293 cell line after 72h treatment with free NCs, cisplatin loaded NCs, and free cisplatin	148
Figure 29	Evaluation of the cell viability via MTT assay. Cytotoxicity levels in a). TE671 and b). HEK293 cell line after 72h treatment with free NCs, DNR loaded NCs, and free DNR	150
Figure 30	Evaluation of the cell viability via MTT assay. Cytotoxicity levels in a). TE671 and b). HEK293 cell lines after 72h treatment with free NCs, temozolomide-loaded NCs, and free temozolomide	152
Figure .31	Evaluation of the cell viability via MTT assay. Cytotoxicity levels in a). TE671 and b). HEK293cell lines after 72h treatment with free NCs, DNR/temozolomide combination loaded NCs, and free DNR/temozolomide combination	154

Figure 32	Immunoblotting results of H2A.X and GAPDH in HEK293 cell line (a and b) and TE671 cell line (c and d) after 24h treatment	160
Figure 33	Western blot analysis results of DNA damage protein expression in TE671 rhabdomyosarcoma cell line. a) and b) after 72h treatment	162
Figure 34	Western blot analysis results of DNA damage protein expression in HEK293 rhabdomyosarcoma cell line. a) and b) after 72h treatment	164
Figure 35	Apoptosis analysis by flow cytometry in rhabdomyosarcoma cells treated by free NCs, loaded and free temozolomide, cisplatin, DNR, and DNR/temozolomide combination for 24h	166
Figure 36	Calculated percentages of cell apoptosis in rhabdomyosarcoma cells treated by free NCs, loaded and free temozolomide, cisplatin, DNR, and DNR/temozolomide combination for 24h	167
Figure 37	Apoptosis analysis by flow cytometry in rhabdomyosarcoma cells treated by free NCs, loaded and free temozolomide, cisplatin, DNR, and DNR/temozolomide combination for 72h	169
Figure 38	Calculated percentages of cell apoptosis in rhabdomyosarcoma cells treated by free NCs, loaded and free temozolomide, cisplatin, DNR, and DNR/temozolomide combination for 72h	171
Figure 39	Apoptosis analysis by flow cytometry in HEK293 cells treated by free NCs, loaded and free temozolomide, cisplatin, DNR, and DNR/temozolomide combination for 24h	173

Figure 40	Calculated percentages of cell apoptosis in HEK293 cells treated by free NCs, loaded and free temozolomide, cisplatin, DNR, and DNR/temozolomide combination for 24h	174
Figure 41	Apoptosis analysis by flow cytometry in HEK293 cells treated by free NCs, loaded and free temozolomide, cisplatin, DNR, and DNR/temozolomide combination for 72h	176
Figure 42	Calculated percentages of cell apoptosis in HEK293 cells treated by free NCs, loaded and free temozolomide, cisplatin, DNR, and DNR/temozolomide combination for 72h	178
Figure 43	Cell cycle analysis of TE671 cells treated by free NCs, loaded and free temozolomide, cisplatin, DNR, and DNR/temozolomide combination for 24h	179
Figure 44	Percentages of the different phases of the cell cycle (G1, S, G2) of TE671 cells treated by free NCs, loaded and free temozolomide, cisplatin, DNR, and DNR/temozolomide combination for 24h	180
Figure 45	Cell cycle analysis of TE671 cells treated by free NCs, loaded and free temozolomide, cisplatin, DNR, and DNR/temozolomide combination for 72h	181
Figure 46	Percentages of the different phases of the cell cycle (G1, S, G2) of TE671 cells treated by free NCs, loaded and free temozolomide, cisplatin, DNR, and DNR/temozolomide combination for 72h	182
Figure 47	Cell cycle analysis of HEK293 cells treated by free NCs, loaded and free temozolomide, cisplatin, DNR, and DNR/temozolomide combination for 24h	183
Figure 48	Percentages of the different phases of the cell cycle (G1, S, G2) of HEK293 cells treated by free NCs, loaded and free temozolomide, cisplatin, DNR, and DNR/temozolomide combination for 24h	184

Figure 49	Cell cycle analysis of HEK293 cells treated by free NCs, loaded and free temozolomide, cisplatin, DNR, and DNR/temozolomide combination for 72h	185
Figure 50	Percentages of the different phases of the cell cycle (G1, S, G2) of HEK293 cells treated by free NCs, loaded and free temozolomide, cisplatin, DNR, and DNR/temozolomide combination for 72h	186
CHAPTER 4		
Figure 51	Illustration of the glioblastoma cell of origin	204
Figure 52	Five-year net survival rates between 2000-2014 and 2010-2014 in Europe, North America, South America, Oceania, Africa and Asia	208
Figure 53	Evaluation of the cell viability via MTT assay. Cytotoxicity levels in a). U87 MG, and b). HEK293 cell lines after 24h treatment with free NCs, cisplatin loaded NCs, and free cisplatin.	230
Figure 54	Evaluation of the cell viability via MTT assay. Cytotoxicity levels in a). U87 MG, and b). HEK293 cell lines after 24h treatment with free NCs, DNR loaded NCs, and free DNR	232
Figure 55	Evaluation of the cell viability via MTT assay. Cytotoxicity levels in a). U87 MG, and b). HEK293 cell lines after 24h treatment with free NCs, temozolomide loaded NCs, and free temozolomide	234
Figure 56	Evaluation of the cell viability via MTT assay. Cytotoxicity levels in a). U87 MG, and b). HEK293 cell lines after 24h treatment with free NCs, DNR/temozolomide loaded NCs, and free DNR/temozolomide	236

Figure 57	Evaluation of the cell viability via MTT assay. Cytotoxicity levels in a). U87 MG, and b). HEK293 cell lines after 72h treatment with free NCs, cisplatin loaded NCs, and free cisplatin	238
Figure 58	Evaluation of the cell viability via MTT assay. Cytotoxicity levels in a). U87 MG, and b). HEK293 cell lines after 72h treatment with free NCs, DNR loaded NCs, and free DNR.	240
Figure 59	Evaluation of the cell viability via MTT assay. Cytotoxicity levels in a). U87 MG, and b). HEK293 cell lines after 72h treatment with free NCs, temozolomide loaded NCs, and free temozolomide	242
Figure 60	Evaluation of the cell viability via MTT assay. Cytotoxicity levels in a). U87 MG, and b). HEK293 cell lines after 72h treatment with free NCs, DNR/temozolomide loaded NCs, and free DNR/temozolomide	244
Figure 61	Wound closure percentage in U87 MG cell line at 19h, 24h, and 40h after NCs, DNR loaded DNR, and free DNR treatment	246
Figure 62	Wound closure percentage in HaCat cell line at 21h, 24h, and 40h after NCs, DNR loaded DNR, and free DNR treatment	248
Figure 63	Fluorescence microscope images of the cellular uptake of DNR loaded NCs and free DNR in U87 MG cell line	250
Figure 64	Fluorescence microscope images of the cellular uptake of DNR loaded NCs and free DNR in HaCat cell line	251
Figure 65	Western blot analysis results of DNA damage protein expression in U87 MG brain cancer cell line.	254

Figure 66	Apoptosis analysis by flow cytometry in U87 MG cells treated by free NCs, loaded and free temozolomide, cisplatin, DNR, and DNR/temozolomide combination for 24h	256
Figure 67	Calculated percentages of cell apoptosis in U87 MG cells treated by free NCs, loaded and free temozolomide, cisplatin, DNR, and DNR/temozolomide combination for 24h ...	257
Figure 68	Apoptosis analysis by flow cytometry in U87 MG cells treated by free NCs, loaded and free temozolomide, cisplatin, DNR, and DNR/temozolomide combination for 72h	260
Figure 69	Calculated percentages of cell apoptosis in U87 MG cells treated by free NCs, loaded and free temozolomide, cisplatin, DNR, and DNR/temozolomide combination for 72h ...	262
Figure 70	Cell cycle analysis of U87 MG cells treated by free NCs, loaded and free temozolomide, cisplatin, DNR, and DNR/temozolomide combination for 24h	263
Figure 71	Percentages of the different phases of the cell cycle (G1, S, G2) of U87 MG cells treated by free NCs, loaded and free temozolomide, cisplatin, DNR, and DNR/temozolomide combination for 24h	265
Figure 72	Cell cycle analysis of U87 MG cells treated by free NCs, loaded and free temozolomide, cisplatin, DNR, and DNR/temozolomide combination for 72h	266
Figure 73	Percentages of the different phases of the cell cycle (G1, S, G2) of U87 MG cells treated by free NCs, loaded and free temozolomide, cisplatin, DNR, and DNR/temozolomide combination for 72h	268

List of Tables

Page No.

CHAPTER 2

Table 1	Examples of pH, temperature, hypoxia, and redox sensitive natural and synthetic polymers	64
Table 2	Different treatment conditions for hollow silica nanocontainers	73
Table 3	Different ratios of multisensitive layer components	75
Table 4	Different treatment periods with water and/or ethanol for hollow PMAA nanocarriers.....	76
Table 5	Components of Eppendorf tubes sets of RBCs treated with different NCs suspension concentrations.	79
Table 6	Back-titrated COOH entities in different hollow NCs samples.....	90
Table 7	Calculated loading capacities and encapsulation efficiencies of different hollow PMAA nanocarriers and the corresponding drugs.....	92
Table 8	Hemolysis assay results after 2 hours and 24 hours incubation.....	97

CHAPTER 3

Table 9	Staging of RMS with TNM criteria.	120
Table 10	Risk groups of RMS based on TNM staging, clinical groups, and <i>PAX/FOX01</i> fusion gene status.	122

Table 11	Cellular uptake evaluation of rhodamine loaded-nanocontainers and free rhodamine by fluorescence microscopy TE671 rhabdomyosarcoma cell line	155
Table 12	Cellular uptake evaluation of rhodamine loaded-nanocontainers and free rhodamine by fluorescence microscopy in HEK293 control cell line	156
Table 13	Evaluation of the cellular uptake of rhodamine loaded-nanocontainers and free rhodamine by fluorescence microscopy in HEK293 control cell line	157
Table 14	Evaluation of the cellular uptake of rhodamine loaded-nanocontainers and free rhodamine by fluorescence microscopy in TE671 rhabdomyosarcoma cell line.....	158

CHAPTER 4

Table 15	Wound closure monitoring in U87-MG cell line by optic microscope at different time points.	245
Table 16	Wound closure monitoring in HaCat cell line by optic microscope at different time points.....	247

ABBREVIATIONS

3D-CRT	Three-dimensional conformal radiation therapy
ACN	Acetonitrile
AIBN	Azobisisobutyronitrile
APC	Astrocyte precursor cells
ARMS	Alveolar rhabdomyosarcoma
ASCO	The American Society of Cancer Oncology
ASL MR	Arterial spin labelling magnetic resonance
BAF	BRG1-associated factor
BBB	Blood brain barrier
CBTRUS	The Central Brain Tumour Registry of the United States
CNS	Central nervous system
COG	Children’s Oncology Group
COL4A1	Collagen, type IV, alpha 1
CT	Computed tomography
DCE MR	Dynamic contrast enhanced magnetic resonance
DLS	Dynamic light scattering
DNR	Daunorubicin
DOX	Doxorubicin
DSC MR	Dynamic susceptibility contrast magnetic resonance
EANO	European Association of Neuro-Oncology
EBV	Epstein-Barr virus
EGDMA	Ethylene glycol dimethylacrylate
EGFR	Epidermal growth factor receptor
ERMS	Embryonal rhabdomyosarcoma
EtOH	Ethanol
FBN2	fibrillin Glycoprotein
FBN2	Fibrillin glycoprotein

FDA	Food and drug administration
FTIR	Fourier transform infrared spectroscopy
Gy	Gray
HA	Hyaluronic acid
HCl	Hydrochloric acid
HF	Hydrofluoric acid
HFRT	Hypofractionated radiotherapy
HH-GLI	Hedgehog- glioma-associated oncogene pathway
HPV	Human papilloma virus
IDH	Isocitrate dehydrogenase
IMRT	Intensity-modulated radiation therapy
IVA	Ifosfamide, Vincristine, actinomycin-D
JNK	c-Jun N-terminal kinase
KPS	Karnofsky performance scale
MAA	Methacrylic acid
MBA	N,N'-Methylenebisacrylamide
MGMT	O⁶-methylguanine-DNA methyltransferase
MPS	3-methacryloxypropyltrimethoxysilane
Mrfs	Myogenic regulatory factors
MRI	Magnetic resonance imaging
mSWI/SNF	Mammalian mSWI/SNF
NaOH	Sodium hydroxide
NCs	Nanocontainers
NIPAM	N-Isopropylacrylamide
NIPAM	N-isopropylacrylamide
NPC	Neural progenitor cells
NPs	Nanoparticles
NSCs	Neural stem cells
OPC	Oligodendrocyte precursor cells

PBAF	Poly-bromo BRG1-associated factor
PCL	poly (ϵ-caprolactone)
PD-1	Programmed death receptor-1
PD-L1	Programmed death-ligand 1
PEG	Polyethylene glycol
PEG-PLA	Polyethylene glycol-poly(lactide)
PI3K	Phosphatidylinositide 3-kinase
PLA	poly(lactide)
PLGA	Poly L-glutamic acid
PLOD1	Procollagen-lysine,2-oxoglutarate 5-dioxygenase 1
PLOD2	Procollagen-lysine,2-oxoglutarate 5-dioxygenase 2
PTEN	Phosphatase and tensin homolog
PVPA	Poly vinylphosphonic acid
Rb	Retinoblastoma signalling pathway
RMS	Rhabdomyosarcoma
RTK	Receptor tyrosine kinase
SEM	Scanning electron microscopy
SHH	Sonic hedgehog
SiO₂	Silicon dioxide
SVZ	Subventricular zone
TEM	Transmission electron microscopy
TEOS	Tetraethyl orthosilicate
TERTp	Telomerase reverse transcriptase promoter
TNM	Tumour, Node, Metastasis
TP53	Tumour protein P53
VAC	Vincristine, actinomycin-D, cyclophosphamide
WHO	World health organization

CHAPTER 1

1. INTRODUCTION

1.1. Head and Neck Tumours

Head and neck neoplasm is a term that encompasses an array of tumours developing in the skin and cavities of the head and neck area, including the nasal cavity, the oral cavity, the pharynx, and the larynx (Yan et al., 2020). The most common type of head and neck tumours, with 90% of cases, is head and neck squamous cell carcinomas. Squamous cell carcinoma arises in the surface tissue of the mucosal epithelium of the nasal cavity, oral cavity, pharynx and larynx (Groeger & Meyle, 2019; Johnson et al., 2020). With nearly 900,000 cases diagnosed and 450,000 deaths in 2018 only, head and neck squamous carcinoma represents the sixth most prevalent cancer worldwide. (Bose, Brockton, & Dort, 2013; Johnson et al., 2020). Also, about a 30% increase is anticipated in the number of head and neck squamous carcinoma by 2030, reaching 1.08 million new cases (Johnson et al., 2020). Based on the neoplasm's anatomical site, there are four types of head and neck squamous carcinoma (Johnson et al., 2020).

Oral and oropharyngeal is the most common type of head and neck cancers, and this site includes the mouth, tongue, salivary glands, and middle of the throat (Moro, Maroneze, Ardenghi, Barin, & Danesi, 2018). The oral and oropharyngeal squamous carcinoma can either be human papilloma virus (HPV) positive with a more favourable prognosis or HPV-negative with a less favourable prognosis. (Oren, Vaysberg, & Ginat, 2019). HPV-positive oral and oropharyngeal squamous carcinoma are more sensitive to chemotherapy and radiotherapy, contrary to the HPV-negative type. Yet, the precise explanation of this behaviour remains to be well defined by research (Perri et al., 2020).

Laryngeal and hypopharyngeal squamous cell carcinoma of this site comprise the larynx, also known as the voice box, which interfaces the upper respiratory tract to the lower respiratory tract (Hernández-Morato, Yu, & Pitman, 2023). This site also comprises the hypopharynx, which is the lower part of the throat i.e. under the nasopharynx and oropharynx, and it connects the pharynx and larynx to the oesophagus (Kwon & Miles, 2018). Late presentation of tumours in this site i.e. at advanced stages of diagnosis, ensues the worst prognosis among all other subsites of head and neck (Kwon & Miles, 2018). Every year, laryngeal and hypopharyngeal squamous cell carcinoma types affect about 170,000 and 42,000 worldwide, respectively (Abdeyrim et al., 2020). At an early stage, cervical lymph node metastasis is promoted by an abundant submucosal lymphatic network in this site (Zhang, Li, Wen, Wu, & Ma, 2022). Therefore, the “lymph node ratio” was reported to be a prognostic factor for squamous cell carcinomas of the laryngeal and hypopharyngeal areas (Abdeyrim et al., 2020). The nasal cavity and paranasal sinus site comprise the nose and surrounding areas where the air passes through. This anatomical site is characterised by its complexity since it comprises interconnected spaces filled with air allowing for significant tumour growth before the onset of symptoms. Thus, patients are diagnosed at late stages with extensive spread to neighbouring sites. (König, Osnes, Bratland, & Meling, 2019; Lucidi et al., 2023). Therefore, the poor prognosis is related to the anatomical complexity of this site, diagnosis at late stages, and the high risks of involving neighbouring sites (König, Osnes, Bratland, & Meling, 2019; Sanghvi et al., 2013). Tumour management in the nasal cavity and paranasal sinus sites is complicated due to their proximity to critical areas (e.g. skull base, orbit, and the central nervous system) (König, Osnes, Bratland, & Meling, 2019).

The nasopharyngeal site includes the area connecting the nasopharynx (upper part of the throat) with the back of the nose and nasal cavity. Similarly, with most nasopharyngeal

cancers, nasopharyngeal squamous cell carcinoma is associated with Epstein-Barr virus (EBV) exposure (Shen et al., 2022). Cancers developing in this site have a poor prognosis, and it is related to the neoplasm's high tendency to metastasize to distant areas, including lungs, liver and bone (Al-Anazi et al., 2023). Nasopharyngeal carcinoma is known as endemic in South China, Southeast Asia, Malaysia, and Indonesia (Jicman Stan et al., 2021).

With more than 800,000 cases of head and neck cancers diagnosed yearly, incidence rates of head and neck tumours vary depending on the anatomical site (de Bakker et al., 2022). The most prevalent diagnosed sites of head and neck squamous cell carcinoma are the oral and laryngeal, with about 354,864 and 177,422 cases (Bray et al., 2018). Geographically, it was reported by Bray et al. (2018) based on the GLOBOCAN 2018 estimates that lip and oral cavity cancers are highly frequent in the Pacific Islands and southern Asia (Bray et al., 2018). In Europe, head and neck mortality rates were higher than in the USA. Throughout the anatomical sites, head and neck squamous carcinomas are more common in men than women with a 2:1 ratio, with an average age of 50 to 70 years at diagnosis for both gender (Sabatini & Chiocca, 2019). In the past decade, a worldwide 36% increase was noted in the incidence rates of head and neck squamous carcinomas (McDermott & Bowles, 2019). The risk factors most related to head and neck squamous cell carcinomas are consumption of tobacco and alcohol, HPV infection and EBV exposure (Sabatini & Chiocca, 2019). Overall, *TP53* mutations and epidermal growth factor receptor (EGFR) overexpression were reported to be the most frequent genetic alterations in head and neck squamous carcinoma (Ju et al., 2021; Sabatini & Chiocca, 2019).

Rhabdomyosarcoma is a soft tissue cancer that arises in the head and neck in 40% of cases in children, and it is the most common soft tissue neoplasm in the pediatric population. Pediatric

rhabdomyosarcoma accounts for 3.5% of all childhood malignancies (Chen, Ricciotti, Futran, & Oda, 2016). In adults, rhabdomyosarcoma of the head and neck is very rare, with 4% - 9%, and it accounts for 1% of all head and neck neoplasms in adults (Hahn et al., 2022). Rhabdomyosarcoma is a neoplasm of the skeletal muscles with four main types, which include embryonal, alveolar, pleomorphic, and spindle cell/sclerosing rhabdomyosarcoma. Embryonal type and alveolar types are the most frequent, with 70% and 20% of cases, respectively (Chen, Ricciotti, Futran, & Oda, 2016; Rhee et al., 2020). The embryonal type mainly appears in the head and neck area and genital organs; however, it is also likely to appear anywhere in the body (Martin-Giacalone, Weinstein, Plon, & Lupo, 2021). Similarly, with squamous cell carcinomas, embryonal rhabdomyosarcoma comprises three primary anatomic sites in the head and neck area. Those comprise parameningeal (nasopharynx, the nasal cavity, infratemporal and pterygopalatine fossa, and surrounding areas), orbital (in-between nasal cavity and paranasal sinuses, and the area surrounding the eyes), and non-parameningeal (rest of the areas in the head excluding the parameningeal and orbital areas) (Casey & Wolden, 2018).

Age, tumour size, histological type, and site of the tumour in the head and neck area are factors that define the prognosis of rhabdomyosarcoma (Wang et al., 2020). Embryonal rhabdomyosarcoma has the most favourable prognosis compared to the alveolar type (Simon, Paulino, Smith, & Buatti, 2002, Wang et al., 2020). Genetic alterations related to embryonal rhabdomyosarcoma include aberrant activation of the sonic hedgehog (SHH) and RAS pathways (Sun et al., 2015; Azatyan et al., 2019).

The latest World Health Organization (WHO) classification update dedicated a chapter to soft tissue cancers of the head and neck and included all four subtypes of rhabdomyosarcomas in the skeletal muscle tumours of the head and neck (Jo & Demicco, 2022). Interestingly,

rhabdomyosarcoma was also listed in the WHO's latest central nervous system (CNS) tumours classification. It was listed under the mesenchymal, non-meningothelial tumours and skeletal muscle tumour subtypes (Louis et al., 2021).

The treatment regimen for head and neck tumours mainly consists of surgery and adjuvant radiotherapy and/or chemotherapy (Anderson et al., 2021). Platin-based drugs (e.g. cisplatin), docetaxel, cetuximab (EGFR targeted therapy), and 5- fluorouracil drugs are generally used for the treatment of head and neck neoplasms (Anderson et al., 2021; Sindhu & Bauman, 2019). Of note, cetuximab has been the only EGFR targeted therapy for head and neck squamous carcinomas by the Food and Drug Administration (FDA) since 2006 (Li, Tie, Alu, Ma, & Shi, 2023).

In 2016, pembrolizumab was conferred accelerated approval by FDA for metastatic or recurrent head and neck squamous carcinoma (Larkins et al., 2017). Pembrolizumab is a humanized monoclonal antibody that binds to the programmed death receptor-1 (PD-1). It works by restoring anti-tumour immune response via halting the interaction between PD-1 on the surface of T-cells and programmed death-ligand 1 (PD-L1) expressed on tumour cells (Fasano et al., 2022; Larkins et al., 2017).

1.2. Brain Tumours

Brain and central nervous system tumours are among the top ten deadliest tumours in several countries around the globe (Fan et al., 2022). The development of the CNS neoplasm arises in any part of the brain or spinal cord (Ostrom et al., 2022). The origination is triggered by a single or a series of DNA mutations in essential genes, including *EGFR*, *TP53*, and telomerase reverse transcriptase (*TERT*) promoter (Brat et al., 2018; Lassman et al., 2022; Lee et al., 2020; Louis et al., 2021). These encode crucial proteins and regulate key cellular processes (e.g. DNA repair, cell cycle, and apoptosis) and pathways (e.g. RAS/MAPK pathway), and their mutation results in aberrant cellular growth, hence tumour formation (Lee et al., 2020; Oprita et al., 2021; Trybek, Kowalik, Gózdź, & Kowalska, 2020).

According to the Global Cancer Observatory (GCO), there are around 5,500 brain and CNS cancer-related deaths in the UK, 53,600 in Europe, 18,000 in the USA, 15,150 in Africa and a total of approximately 251,300 CNS cancer-related deaths worldwide in 2020 (Cancer Tomorrow, 2022; Fan et al., 2022). Based on the statistical studies and estimations of the WHO and the GCO, in several parts of the world, these numbers are subject to double due to several factors, including access to advanced diagnostic tools, economic and financial conditions, and unhealthy lifestyles (Cancer Tomorrow, 2022). Several types of CNS tumours are listed in the WHO's fifth edition of CNS tumours classification report, including glioblastoma, neuroblastoma, astrocytomas, medulloblastomas, low and high-grade diffuse gliomas, and various other types. This latest issue, published in 2021, also referred to as the "WHO CNS 5", features several remarkable changes in the classification of CNS tumours by routing towards more molecular-based classification and diagnostic methods without disregarding the

importance of the classical approaches, including histology and immunohistochemistry for the diagnosis and characterization of the CNS tumours (Louis et al., 2021).

The report also implemented the use of Arabic numerals instead of classic Roman numerals for grading CNS tumours. This substitution was introduced to follow the same favoured grading numerals as other organ systems and to avoid threatening consequences that could result from mistaking the Roman numerals (II, III, IV) for one another (Louis et al., 2021).

The most common brain malignancies are adult type gliomas representing about 80% of all malignant brain neoplasms. Gliomas include astrocytoma - Isocitrate dehydrogenase (IDH)-mutant, oligodendroglioma - IDH-mutant and 1p/19q-co-deleted, and glioblastoma - IDH-wildtype as referred to in the latest 5th edition of WHO CNS classification (Louis et al., 2021). Low grade gliomas have 5-year survival rates of 80%, while high grade gliomas have low 5 year-survival rates of 5% to 17% (Gilard et al., 2021; Girardi et al., 2022, Whitfield & Huse, 2022). Gliomas are generally highly infiltrative regardless of their grade and prognosis, with a remarkable resistance to treatment which results in low survival rates (Whitfield & Huse, 2022).

Astrocytomas have WHO grades 2, 3 and 4 and are associated with *IDH1*, *IDH2*, *ATRX*, *TP53*, and *CDKN2A/B* mutations (Louis et al., 2021). Oligodendroglioma have grades 2 and 3 and are associated with a mutation in *IDH1*, *IDH2*, co-deletion of the short arm in chromosome 1 and long arm in chromosome 19 (1p/19q), *TERT promoter*, *CIC*, *FUBP1*, and *NOTCH1* (Louis et al., 2021). Overall, the IDH-mutated gliomas exhibit a better prognosis compared to the IDH wild type. However, a combination of IDH-mutation with *ATRX* and *TP53* mutations (astrocytoma) was associated with a less favourable prognosis compared to a better prognosis associated with IDH and *TERTp* mutations and whole arm co-deletion 1p/19q (oligodendrogliomas) (Reuss, 2023). Glioblastoma IDH-wildtype are associated with *TERT promoter* and *EGFR*

mutations as well as +7/−10 chromosome copy number changes (Kim, Park, & Lee, 2021; Louis et al., 2021). As a grade 4, this type of glioma is the most aggressive with a poor prognosis (Chen et al., 2021; Reuss, 2023).

To diagnose almost all types of CNS tumours, clinicians typically run neuroimaging tests. For instance, computed tomography scan (CT) and Magnetic Resonance Imaging (MRI) of the brain and the spinal cord to look for any abnormal growth of cells appearing as a solid neoplasm. These tools are used for tumour diagnosis, neoplasm resection surgery planning, and verifying therapy response (Mabray, Barajas & Cha, 2015). Molecular and genetic tests can also be performed since there is a series of gene abnormalities related to CNS tumours (e.g. IDH, *ATRX*, *TP53*, *EGFR*, among others) as mentioned in the 2021 issue of WHO CNS classification report (Louis, 2021).

The therapeutic strategy for brain tumours consists of surgical operations, radiotherapy, and chemotherapy. In most cases, the patient receives at least two treatments, surgical resection of the tumour followed by either chemotherapy or radiotherapy (Rasheed, Rehman, & Akash, 2021). In brain tumour types with achieved resection of all the neoplasm surgery is usually enough (Pollack, Agnihotri & Broniscer, 2019). The first line chemotherapy drugs included in standard protocol for gliomas therapy consists of temozolomide, a combination of procarbazine, CCNU (lomustine), and vincristine (PCV) (Taal, Bromberg, & van den Bent, 2015). Trials have been extensively investigating the use of bevacizumab (monoclonal antibody against circulating VEGF), mainly in recurrent glioblastoma (Taal, Bromberg, & van den Bent, 2015). The chemotherapeutic drugs that are currently used to treat brain tumours affect the cell cycle at one or multiple stages. They attain anti-tumour affect by either damaging or altering the cell's DNA and RNA. They also affect the tumour cells by inhibiting the production

of proteins required for cell reproduction during the cell cycle and eventually preventing the cells from any renewal or further growth (Cancer Research UK, 2019; Taal, Bromberg, & van den Bent, 2015).

Age, performance status (based on Karnofsky performance scale (KPS)), the extent of resection, the O⁶-methylguanine-DNA methyltransferase (MGMT) methylation status, and mutational status of genes such as *TERTp*, *CDKN2A* among others are generally considered prognostic factors in gliomas (Pellerino, Caccese, Padovan, Cerretti, & Lombardi, 2022).

1.3. Brain Anatomy

The brain is one of the most complex organs in the human body, and together with the spinal cord, they are often referred to as CNS. The three main parts of the brain are the cerebrum, the cerebellum, and the brainstem (Wang, Pan & Li, 2020).

The cerebrum is the upper part of the brain and comprises four different lobes controlling an array of functions. The frontal lobe, which is also the largest lobe of the brain, is located in the front part of the brain, and it is associated with decision-making, personality characteristics, movement and speech ability (Collins & Koechlin, 2012; John Hopkins Medicine, 2022; OpenStax and Lumen Learning, 2019).

Located in the middle part of the brain, the parietal lobe is involved in a person's ability to recognise a spatial relationship with the surroundings and to identify objects. Additionally, this lobe engages in speech understanding and interpreting body pain and touch. Also, white matter areas related to sensory, motor language, visual and visuospatial functions intersect in

this lobe (Dziedzic, Bala, & Marchel, 2021; John Hopkins Medicine, 2022; OpenStax and Lumen Learning, 2019).

The temporal lobe occupies the sides of the brain, and it is involved in hearing, speech, short-term memory, emotions, and musical rhythm. An important auditory processing area known as the “auditory cortex” is located within the temporal lobe (John Hopkins Medicine, 2022; Kiernan, 2012; OpenStax and Lumen Learning, 2019). Another crucial area for speech production and comprehension, named Wernicke’s area, is also located within this lobe (Binder, 2015; OpenStax and Lumen Learning, 2019).

The occipital lobe is located at the back of the brain, and it comprises the primary visual cortex that is involved with the interpretation of incoming vision-related information (Flores, 2002; John Hopkins Medicine, 2022; OpenStax and Lumen Learning, 2019).

The second main part of the brain is the cerebellum, also known as “the little brain” in Latin. It is located at the back part of the brain, under both the temporal and occipital lobes but above the brainstem, and it represents about 5% and 11% of the human brain weight in adults and neonates, respectively. Around 80% of the overall brain neurons are part of this “little brain”. The cerebellum plays crucial roles in the heterogeneity of functions, including sensorimotor, cognitive functions, balance, and coordination (Amore et al., 2021). The third part of the brain is the brainstem, which is the connecting point of the cerebrum and spinal cord, and it is composed of three main structures known as the midbrain, the pons, and the medulla (Benaghanem et al., 2020; John Hopkins Medicine, 2022; OpenStax and Lumen Learning, 2019).

The midbrain, a complex structure also known as mesencephalon, comprises a variety of neuron clusters (nuclei and colliculi), neural pathways, and substantia nigra, which is an area

with abundant dopamine neurons that are usually affected in Parkinson's disease. The midbrain is then involved in the sleep-wake cycle, movement and coordination control, as well as enabling functions like hearing and calculating responses (Benghanem et al., 2020; John Hopkins Medicine, 2022; OpenStax and Lumen Learning, 2019). Pons or "the bridge" as known in the Latin language, connects the midbrain and the medulla, and it is the origination point of four of the twelve cranial nerves that are involved in an array of functions, including facial expression, chewing, blinking and tear production among others (John Hopkins Medicine, 2022; OpenStax and Lumen Learning, 2019; Tate et al., 2014). At the bottom of the brainstem, the medulla is where the brain meets the spinal cord. Functions of the medulla include regulating heart rhythm, breathing, blood pressure, and oxygen and carbon dioxide levels. The medulla also regulates reflexes such as coughing, sneezing, vomiting, and swallowing. (Diek, Smidt, & Mesman, 2022; John Hopkins Medicine, 2022; OpenStax and Lumen Learning, 2019).

Of note, the spinal cord starts from the bottom part of the medulla, precisely in the "medulla oblongata" area. The spinal cord is the connection wire that carries neural messages between the brain and the rest of the human body. The structure of the brain, including all four lobes, is illustrated in Figure 1.

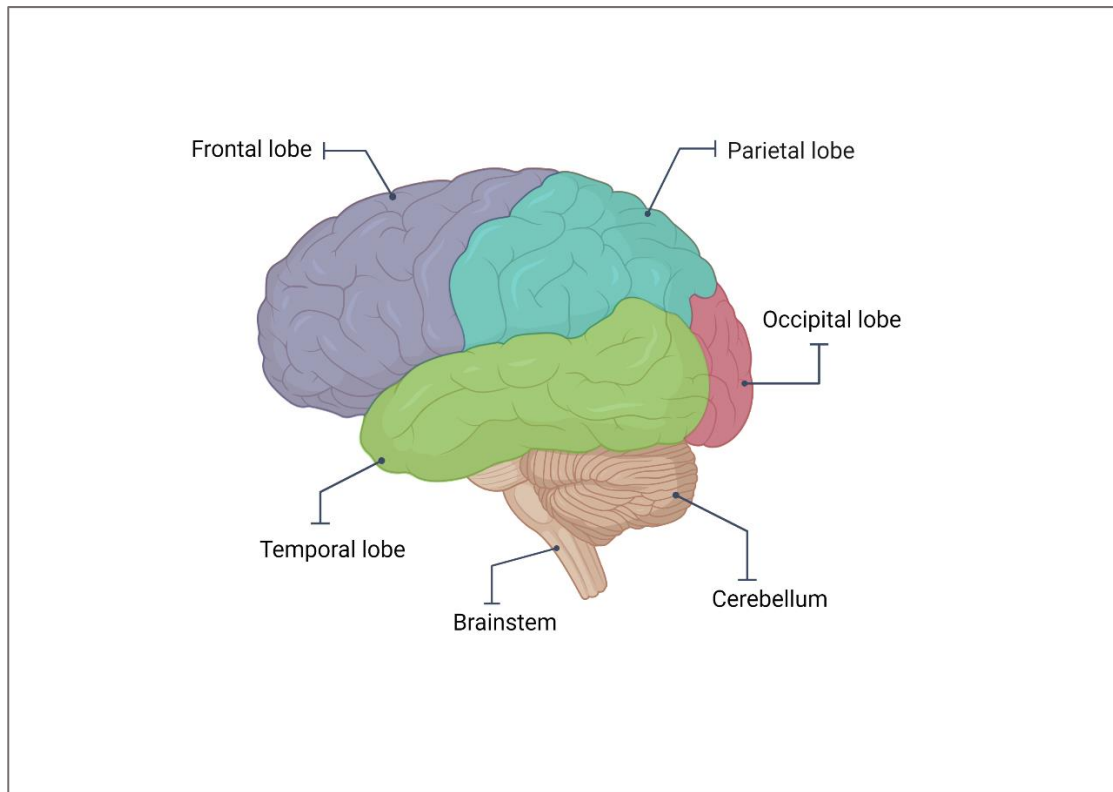


Figure 1. Illustration of the three main parts of the human brain and the four lobes.

(Illustration created using BioRender.com)

1.4. Blood Brain Barrier

As an anatomical and functional unit, the neurovascular unit (NVU) notably regulates cerebral blood flow as a response to neuronal energy demands. The NVU comprises six main elements: brain endothelial cells, astrocytes, mural cells including vascular smooth muscle cells and pericytes, microglia, neurons, and extracellular matrix components. The blood brain barrier is the main component of the microvascular endothelial cells of the NVU. Characterised by its high selectivity that is ensured by the tight junctions sealing the endothelial cell wall, the blood brain barrier (BBB) is the term used to indicate the exceptional vessels in the CNS that selectively allow the paracellular passage of molecules to the brain (Lochhead, Yang, Ronaldson & Davis, 2020)

The BBB is highly selective and controls the movement of particles and molecules, including cells, ions, and proteins, from the blood to the CNS. More precisely, molecules that can passively diffuse to the BBB are mainly lipophilic molecules and molecularly weigh less than 500 Da in addition to a small number of hydrogen donors and acceptors. Therefore, this physical and metabolic barrier maintains and ensures proper neural functions and protection of the brain from any potentially harmful particles. As a “strong protection wall,” the BBB notably controls the stability and equilibrium of the internal environment of the brain by the homeostasis process (Abbott, Rönnbäck & Hansson, 2006; Lochhead, Yang, Ronaldson & Davis, 2020), which is crucial for the preservation of normal neural functions. Hence, any alteration or dysfunction in this protective wall leads to disequilibrium in the brain homeostasis, i.e., penetration of toxins and bacteria into the brain, which then leads to severe damage such as neurodegenerative diseases, stroke, traumatic brain injuries, epilepsy, among others (Małkiewicz et al., 2019). The advantageous strict permeability of the BBB exemplifies

a challenging obstacle for accurate diagnostics and effective drug delivery for therapeutics, especially in brain and CNS-associated cancers. Therefore, abundant efforts have been made to prevail over this physical and metabolic barrier without causing pathologically significant damage, using novel targeted drug delivery systems, such as polymeric nanoparticles (Dong, 2018; Zorkina et al., 2020).

The random and untargeted delivery of the chemotherapy drugs results in unpleasant and long-term side effects, including neural disturbances, neural toxicity, oxidative stress, neurogenesis disruption, apoptosis, and cardiotoxicity, which are commonly observed in epilepsy, brain injuries and trauma, as well as in neurodegenerative diseases (Cheng et al., 2015; Ikonomidou, 2018; Stone, Kanneganti, Abbasi, & Akhtari, 2021). For this reason, scientists are exerting efforts to surpass the burden of “efficient yet targeted” head and CNS tumour treatment. They are aiming to surpass this burden by developing alternative, novel, and more effective therapeutic strategies, such as targeted drug delivery systems by nanocarriers (Mukhtar et al., 2020; Viegas, Pereira, & Fonte, 2022).

In fact, an escalating urge to opt for novel and targeted therapy systems is anticipated. For instance, drug delivery systems are innovated to deliver the drug in a targeted manner that will ensure the *in situ* delivery of the drug to the tumour cells while avoiding damage to healthy cells. Subsequently, this approach will lead to less painful and destructive side effects as well as improved treatment for the patient and better quality of life after cancer survival.

1.5. Nanotechnology and Nanoparticles

1.5.1. Nanotechnology

Nanotechnology is referred to the ensemble of disciplines and sciences (biology, physics, chemistry, engineering, medicine) operating at a nanoscale, which is 1 billionth of a meter (10^{-9} m). It was first described by the physicist Richard Feynman in 1959 at the annual American Physical Society Meeting, where he said, “there is plenty of room at the bottom” referring to the world of nanoscale (Feynman, 1992). At an engineering conference in Tokyo in 1974, Norio Taniguchi, a science professor at the University of Tokyo, was the first to introduce the term nanotechnology (Ahire et al., 2022).

At the nanometre scale, the properties of components can be altered and engineered to obtain materials with better or optimal physical and chemical properties compared to properties of the same component at a larger scale (bulk material) (Jeevanandam, Barhoum, Chan, Dufresne & Danquah, 2018). The current research era is highly influenced by nanoscience and nanotechnology through exploiting the advantages granted by the unique rearrangement of the atoms at the nanoscale and the novel application of nanomaterials in several research fields (Ahire et al., 2022). The advantageous properties offered by nanoscale and nanomaterials include a larger surface area to volume ratio, optimal physical and chemical properties, better stability and longevity, and optimal electric and magnetic properties (Ahire et al., 2022; Kolahalam et al., 2019). Owing to these outstanding characteristics, nanomaterials afford versatile applications in several fields, including medicine, engineering, electronics, industry, construction, and forensics (Abid et al., 2022; Ahire et al., 2022; Huseien, Shah, & Sam, 2019; Shukla, 2016).

For instance, in drug fabrication by nanotechnology, characteristics such as solubility, stability, and drug release can be controlled and enhanced to attain improved treatment results and fewer side effects (Mitchell et al., 2020). Also, nanomaterial self-healing concretes fabricated by means of nanoparticles, nanofibers, and carbon nanotubes provide unique concretes (e.g. cementitious composites or bendable concrete) with better endurance, more sustainability, lower carbon footprint, and reduced environmental pollution (Huseien, Shah, & Sam, 2019).

As a breakthrough field, nanotechnology has gained worldwide attention, which resulted in a significant increase of 46,915 in the *“the number of Science Citation Index (SCI) papers”* between 2000 and 2008 only. The SCI reflects discoveries in the nanotechnology area based on title-abstract keyword searches (Roco, 2011). In addition, the US government launched the National Nanotechnology Initiative (NNI) in 2000 with a vision of *“a future in which the ability to understand and control matter at the nanoscale leads to ongoing revolutions in technology and industry that benefit society”*. As a research and development governmental initiative, the NNI aims to improve coordination between organizations in nanotechnology research and development to translate the understating of matter at the nanoscale into technological innovations (Ahire et al., 2022; National Nanotechnology Initiative, 2023; Roco, 2011).

1.5.2. Nanoparticles

1.5.2.1. Dendrimers

Dendrimers are nanosized colloidal molecules that are radially symmetric with a uniform star-like structure. They consist of a central core from which multiple polymeric arms or branches are grown outward and end with functional groups (Najafi, Salami-Kalajahi, & Roghani-Mamaqani, 2020). Dendrimers are multifunctional as they afford several unique properties, including water solubility, predictable molecular weight, high conjugation surface, strong encapsulation of entrapped moiety (e.g. drugs, genes), controlled release, and high deforming and flexing ability (Janaszewska, Lazniewska, Trzepiński, Marcinkowska, & Klajnert-Maculewicz, 2019; Najafi, Salami-Kalajahi, & Roghani-Mamaqani, 2020). These characteristics enable their application in several areas, including agriculture (Kaphle, Navya, Umapathi, & Daima, 2017), veterinary (Ahire et al., 2022), cosmetics (Patel, Patel, Patel, & Patel, 2022), and biomedical fields (Chis et al., 2020; Mignani, Shi, Rodrigues, Tomás, & Majoral, 2022).

Targeted administration of doxorubicin loaded pH-triggered PAMAM–DMA (2,3-dimethylmaleic anhydride) dendrimers showed significant therapeutic efficacy by inhibiting the tumour growth in mice bearing breast cancer cells (Cao et al., 2018). Multi-drug-resistant *Pseudomonas aeruginosa* is the most common Gram-negative bacteria that affects patients with deep burns and induces infection of the wound. It also initiates nosocomial infection outbreaks in hospital burn units, which result in costly care and increased morbidity and mortality rates. The G3KL and G3RL are polycationic dendrimers and are known as antimicrobial peptide dendrimers against *P. aeruginosa*. In combination with biological bandages, these potent antimicrobial dendrimers have been assessed for wound healing. *In vitro* results of this combination showed improvement in wound healing and enhancement of

angiogenesis conferred by the effectiveness of the antimicrobial dendrimers and biological bandages in killing *P. aeruginosa* (Abdel-Sayed et al., 2016).

1.5.2.2. Liposomes

Liposomes are small and spherical vesicles with a hydrophilic aqueous core enclosed by a hydrophobic lipid bilayer (Patra et al., 2018). With a size ranging from 50µm to 500µm, liposomes afford several applications in the biomedical field, including drug delivery systems (Nsairat et al., 2022). Owing to the lipid bilayer that is described as “analogous” to the cellular phospholipid membrane and their ability to entrap both hydrophilic and hydrophobic drugs, liposomes are considered one of the most suitable carriers for drug delivery (Patra et al., 2018). Despite the hydrophobicity or hydrophilicity of the encapsulated drugs, liposomes improve their biodistribution and provide better stability (Patra et al., 2018; Sercombe et al., 2015). To bypass the biological obstacles encountered upon drug delivery such as immunogenicity and opsonisation, there are four distinct types of liposomes. Those include conventional liposomes, sterically stabilised surface PEGylated liposomes, ligand-targeted liposomes, and theranostic liposomes (Patra et al., 2018; Sercombe et al., 2015).

Liposomes were first discovered in 1960 by Alec Bangham, and currently, they are used in clinical applications. Doxil was the first FDA approved liposome nano-based drug carrier in 1995 (Patra et al., 2018). Liposomal Doxil is loaded with doxorubicin, and it is used in the treatment of ovarian cancer, HIV-related Kaposi sarcoma, and multiple myeloma (Bulbake, Doppalapudi, Kommineni, & Khan, 2017). This liposomal formulation of doxorubicin was reported to minimize both the uptake and clearance by the reticuloendothelial system, resulting in extended plasma half-life and targeted accumulation of doxorubicin in the tumour

tissue (Sercombe et al., 2015). DaunoXome® (liposome-based Daunorubicin), Myocet® (liposome-based doxorubicin), and Marqibo® (liposome-based vincristine) are liposome-based formulation approved by the FDA in 1996, 2000, and 2012 respectively, for clinical application including cancer chemotherapy (Bulbake, Doppalapudi, Kommineni, & Khan, 2017).

1.5.2.3. Polymeric nanoparticles

Polymeric nanoparticles or nanocarriers (NPs or NCs) are nanosized, spherical shaped, and solid particles called colloidal, inside which a drug, gene, or vaccine can be entrapped for the targeted and specific delivery. As nanosized spheres, polymeric nanoparticles have a size ranging from 10 to 1000 nm. Polymeric NPs are made of natural polymers like alginate, chitosan, and albumin or synthetic polymers such as polylactide, polycaprolactones polylactide–polyglycolide copolymers, and polyacrylates (Zazo, Colino & Lanao, 2016). In 1979, the adsorption of anticancer drugs to polyalkylcyanoacrylate nanoparticles was studied, and that was one of the first reports about the use of polymeric NPs in cancer therapy (Bolhassani et al., 2013). With the possession of a plethora of advantages, nanoparticles have attracted considerable attention over the past recent years. Thus, polymeric NPs afford promising therapeutic tools for brain tumours. These include being biocompatible, biodegradable, non-immunogenic, non-toxic, non-invasive, water-soluble, easy to synthesize, and inexpensive (Mitchell et al., 2020). Additionally, encapsulation of drugs in nanoparticles reduces the required dose as the nanoparticles have enhanced cellular uptake. Therefore, the drug will be fully administrated to the tumour in each treatment cycle, thus lowering the required dose and less off-target delivery and release, which will subsequently lead to less

side effects (Niculescu & Grumezescu, 2022). Characterised by their nano-size, modifiable surface, and several aforementioned characteristics, polymeric NPs can cross the BBB without causing any damage to this critical barrier (Mitchell et al., 2020; Saucier-Sawyer et al., 2015). Passive and active targeting are two modes of administration of the NPs. Administration of the nanoparticles by passive targeting takes place through the accumulation of the NPs around the neoplasm and diffuse into its vessels as a result of the leaky and abnormal permeability of the vessels' membrane in a phenomenon known as enhanced permeability and retention effect (EPR) (Clemons et al., 2018). Active targeting of the NPs enhances the passive targeting by binding the nanoparticles covered with targeting moieties (e.g. peptide, antibody, ligand) to a corresponding receptor which is overexpressed in the tumour cells compared to healthy cells such as the EGFR which is overexpressed in several malignancies including lung cancer, breast cancer, brain cancer, head and neck cancers, and soft tissue sarcoma (Braun et al., 2018; Byeon, Ku, & Yang, 2019; Clemons et al., 2018; Janani et al., 2022; Wang et al., 2018; Xu et al., 2017).

1.5.2.4. Micellar nanoparticles

Micelles or micellar nanoparticles are nanostructured blocks of spontaneously self-assembled amphiphilic copolymers forming micelles of about 100 nm in size (Patra et al., 2018). Micelles are characterised by their hydrophobic core that can encapsulate hydrophobic drugs, concurrently the hydrophilic layer stabilizes the core and renders the entirety of the system soluble in water. With their small size, micelles generally exhibit narrow distribution, which allows them to avoid fast renal excretion (Patra et al., 2018). Paclitaxel is a hydrophobic chemotherapy drug used for the treatment of various cancers, including lung cancer.

Paxceed® is a paclitaxel loaded polymeric micelles fabricated by PLA-b-mPEG diblock copolymers. Intraperitoneal injection of Paxceed® in MV-522 lung tumour-bearing mouse model showed enhanced treatment efficacy indicating the increase of paclitaxel hydrophilicity when encapsulated in micelles (Ma, 2013).

Paclitaxel and lapatinib drugs were loaded in dual targeted micelles that were developed for the treatment of brain cancer metastases from breast cancer. *In vitro* results showed a significant accumulation of the drug loaded micelles in the brain cells by bypassing the *in vitro* blood brain barrier model. Additionally, *in vivo* results showed a remarkable accumulation of the paclitaxel and lapatinib-loaded micelles in the brain metastasis when injected intravenously, with a prolonged survival period of the mouse model (Lu et al., 2022).

1.5.2.5. Gold nanoparticles

Gold (Au) nanoparticles are nanostructures of different shapes (e.g. rods, spheres, cubes, triangles, star-like) with sizes up to 100nm (Hammami, Alabdallah, jomaa, & kamoun, 2021; Hu, Zhang, Ding, Liu, & Zhao, 2020). Spherical gold nanoparticles have several advantageous characteristics, including a high surface-to-volume ratio, low toxicity, high biocompatibility, and optical and electric properties (Hammami, Alabdallah, jomaa, & kamoun, 2021). These remarkable properties of gold nanoparticles render them suitable for drug delivery, bioimaging and biosensing applications (Si et al., 2021; Yang et al., 2022). Noble metal nanoparticles such as gold and silver have a distinct ability to interact with light through surface plasmon resonance (SPR) (Hu, Zhang, Ding, Liu, & Zhao, 2020). This phenomenon initiates a shift in the UV-visible region of the maximum absorption peak wavelength of the

gold nanoparticles, resulting in color change. This change is dependent on the size, shape, and distance between particles (Liu, Lu, Huang, Li, & Xu, 2018). For instance, the color of spherical gold nanoparticles in aqueous solutions ranges from brown color in particles with 30nm size to purple color in particles near 100nm in size (Hammami, Alabdallah, jomaa, & kamoun, 2021). This colorimetric sensing property of gold nanoparticles allows for their utilization as promising analytical colorimetric sensors that are capable of distinguishing analytes and detecting several molecules, including proteins, peptides, amino acids, nucleic acids, heavy metals, and biotoxins. The main mechanism of that is the covalent or non-covalent bond formation between the targeted substance and gold nanoparticles, causing their aggregation or de-aggregation, which then causes agglomeration of gold nanoparticles and shifts the solution color from dark red to blue (Liu, Lu, Huang, Li, & Xu, 2018).

Pregnancy test, a well-known colorimetric assay that is cost effective and rapid in detecting pregnancy by means of gold nanoparticles. The color change in the colloidal solution results from the aggregation of the gold nanoparticles. This aggregation is triggered by the interaction of the human chorionic gonadotropin (hCG) hormone (released by pregnant women) with anti-hCG antibody conjugated on the surface of gold nanoparticles (Amendola, Pilot, Frasconi, Maragò, & Iati, 2017)._Following the same concept, diagnosis of SARS-CoV-2 (Covid-19) was reported via rapid colorimetric assay based on gold nanoparticles covered with thiol-modified antisense oligonucleotides that are specific for nucleocapsid phosphoprotein of SARS-CoV-2 (Moitra, Alafeef, Dighe, Frieman, & Pan, 2020).

Gold nanoparticles can be employed as radiation sensors to monitor the dose of ionizing radiation in radiotherapy (Hammami, Alabdallah, jomaa, & kamoun, 2021; Wang et al., 2020). Highly Gamma sensitive nano-sensor was developed with gold nanoparticles as “signal

reporter” and single-stranded DNA as “radiation sensitive material” (Wang et al., 2020). When the nano-sensor was Gamma irradiated, DNA strands were broken into small fragments, followed by salt-induced aggregation of AuNPs. The change was detected and quantified with visible spectra and SPR, then associated with Gamma radiation dose. This simple and rapid approach provides a new potential application in gamma-radiation dosimeter to assess the biological effect of radiation (Hammami, Alabdallah, jomaa, & kamoun, 2021; Wang et al., 2020).

1.5.2.6. Iron-oxide nanoparticles

Iron oxide-nanoparticles are made of magnetite (Fe_3O_4), maghemite ($\gamma\text{-Fe}_2\text{O}_3$) which are forms of iron oxide found in nature (Ali et al., 2016). In addition to their small size and simplified separation method, iron oxide nanoparticles have superparamagnetic properties (Ali et al., 2016). Under a magnetic field, iron oxide nanoparticles produce thermal energy by the magnetothermal effect resulting from Néel relaxation or Brownian relaxation (Fan et al., 2018). Néel relaxation and Brownian relaxation are based on inner “magnetization relaxation” within the magnetic nanoparticle, and “rotational diffusion” of the entire magnetic nanoparticle in fluids/liquids, respectively (Ilg & Kröger, 2020; Kötitz, Weitschies, Trahms, & Semmler, 1999). They are the two mechanisms through which the relaxation of magnetisation of iron oxide nanoparticles -or ferrofluids- can occur (Ilg & Kröger, 2020). The contribution of these two mechanisms is important for the optimum use of magnetic nanoparticles, including biological applications (Ilg & Kröger, 2020; Kötitz, Weitschies, Trahms, & Semmler, 1999). Iron oxide nanoparticles afford a versatility of application in different fields, including biomedical,

agriculture and food, energy, and electronics fields (Ali et al., 2016; Dulińska-Litewka et al., 2019).

For instance, Ferumoxytol is an iron oxide nanoparticles-based treatment for anaemia (iron deficiency) in chronic kidney disease (Huang, Hsu, Koo, & Cormode, 2022). It was approved by the FDA in 2009 (Lu, Cohen, Rieves, & Pazdur, 2010). Iron oxide nanoparticles-based hyperthermia is a type of adjuvant cancer treatment by application of increased temperature, mainly 40 °C to 43°C locally on cancer tissue. It works by destroying the cancer cells by altering cellular processes such as DNA repair pathways and factors that are crucial for tumour survival, such as oxygen supply and vasculature (Crezee, Franken, & Oei, 2021). Hyperthermia is attained mainly through photothermal therapy and magnetic fluid hyperthermia (Palzer et al., 2021a). Hyperthermia in photothermal therapy is generated by light absorption and the conversion of electromagnetic waves into thermal energy (Palzer et al., 2021a; Palzer et al., 2021b). In magnetic fluid hyperthermia, the iron oxide nanoparticles generate heat Brownian and Néel relaxation when passed through an alternating magnetic (Palzer et al., 2021a).

Iron oxide nanoparticles also afford theragnostic properties (Janko et al., 2019). For instance, cross linked iron oxide nanoparticles conjugated to an effective vascular disrupting agent azademethylcolchicine (ICT) were used for the treatment of glioblastoma. Results showed significant disruption of the MMP-14 expressing glioblastoma tumour vasculature and reduced tumour growth significantly (Mohanty et al., 2017). The iron core of the ICT- cross linked iron oxide nanoparticle provided *in vivo* tracking of the drug via MRI imaging. Additionally, the treatment combination of temozolomide and theragnostic ICT-cross linked

iron oxide nanoparticles exhibited tumour remission, and the survival of the human glioblastoma bearing mice was enhanced by more than two-fold compared to the administration of temozolomide alone (Mohanty et al., 2017).

Figure 2 below illustrates the different nanoparticles discussed above, showing their diverse shapes and composition with the potential multimodal application.

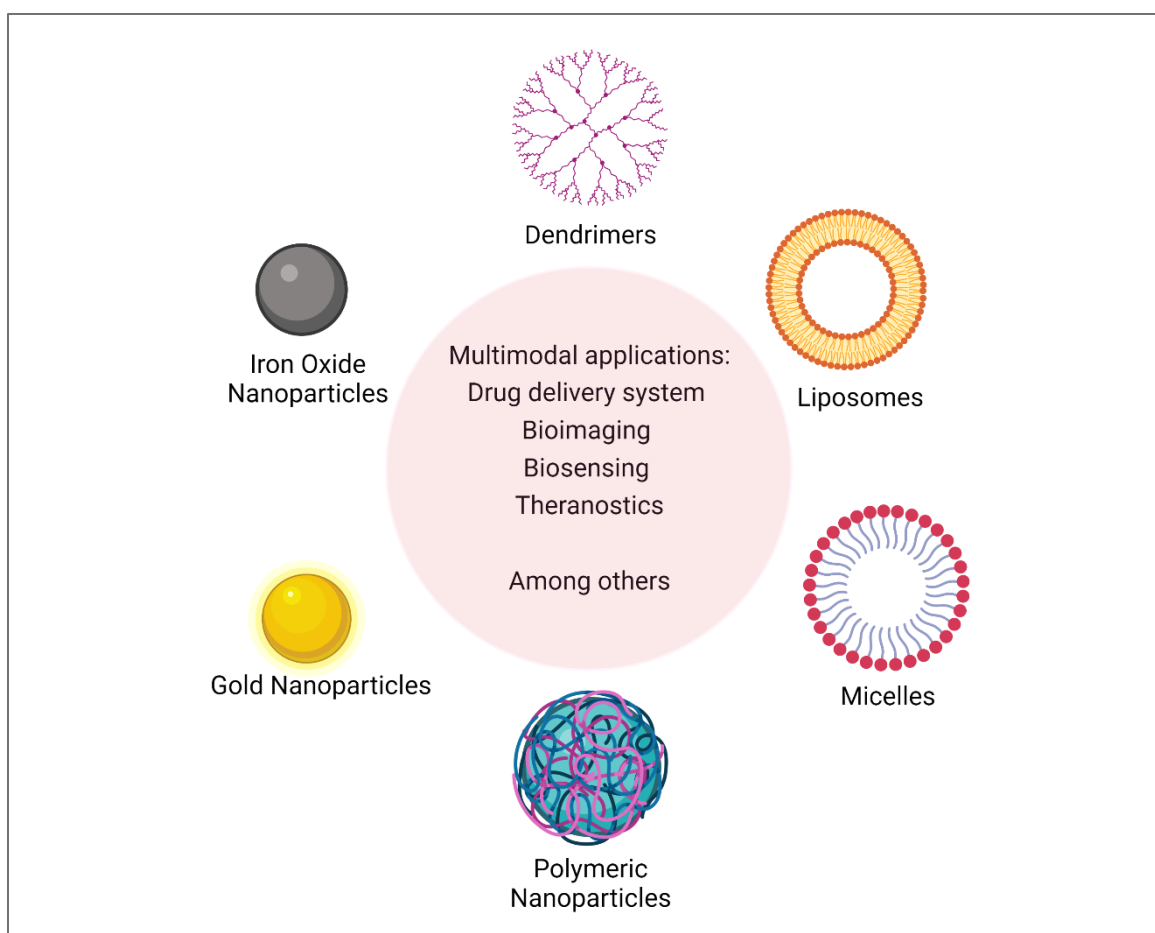


Figure 2. Illustration of different nanoparticles: dendrimers, liposomes, micelles, polymeric nanoparticles, gold nanoparticles and iron oxide nanoparticles

(Illustration created using BioRender.com)

1.6. Aims and Objectives

Hypothesis: Polymeric nanocontainers can treat aggressive brain and head tumours, including glioblastoma and rhabdomyosarcoma, by delivering the drug *in-situ* to the neoplasm. Therefore, resulting in more accurate and efficient treatments as well as less side effects and damage to the healthy cells during chemotherapy.

Aim: The aim of the project was to synthesize polymeric nanocontainers capable of delivering currently used chemotherapies at the site of the tumour to increase their efficacy and reduce the ensuing side effects.

Objectives: Synthesizing biocompatible and non-toxic polymeric nanocontainers to load them with anti-cancer drugs (daunorubicin, cisplatin, temozolomide and vincristine). The drug loaded polymeric NCs were evaluated *in vitro* on glioblastoma and rhabdomyosarcoma cell lines to test the NCs' efficacy as a therapeutic approach to cure the neoplasms.

1.6.1. Research questions

- 1) Will the developed polymeric nanocontainers carrying the therapeutic drug be able to treat the tumour effectively?
- 2) With the use of targeted drug delivery systems, will one type of drug be enough for the treatment of the tumour, or a drug combination will be required?

CHAPTER 2

2. NANOCONTAINERS AND NANOTECHNOLOGY

2.1. Introduction

2.1.1. Nanotechnology

Nanotechnology, a multidisciplinary field that is based on the application of atoms and molecules at the nanoscale. It involves the engineering, creation, and development of structures and systems with optimized physical, chemical, and biological properties. At the nanoscale which is 10^{-9} of a meter, atoms are arranged differently than higher scales, creating unique phenomena and enabling novel applications (Bayda, Adeel, Tuccinardi, Cordani, & Rizzolio, 2019; Hulla, Sahu, & Hayes, 2015; Mulvaney, 2015).

Of note, the thickness of a DNA double helix is of 1nm, a eukaryotic cell is around 30 μ m in size, and a hair strand thickness is about 60 μ m (Bayda, Adeel, Tuccinardi, Cordani, & Rizzolio, 2019; Gnach, Lipinski, Bednarkiewicz, Rybka, & Capobianco, 2015).

For instance, at the nanoscale, material and particles have different colors due to the distinct light scattering which results from the atoms rearrangement. For instance, materials like gold can appear in dark red to purple color and silver can appear in yellow to brown color. This phenomenon is attributed to the interaction of particles of different sizes with light and causing a shift in the absorption wavelength of the surface plasmon to longer wavelengths (Jafari, Karimi, Mirjalili, & Derakhshan, 2016; Liu et al., 2018; Mashwani, & Nadhman, 2019; Theodosiou, Boukos, Sakellis, Zachariadis, & Efthimiadou, 2019).

Fabrication of materials at the nanoscale increases the surface area to volume ratio -compared to the bulk material- allowing more interaction between the atoms and materials. The smaller the nano-fabricated material, the larger the surface area to volume ratio, which signifies a large surface area and smaller volume. This characteristic renders the nano-material stronger

and enables significant reactivity between the particles and their surrounding environment physically, chemically, and biologically (Khan et al., 2022; Joudeh & Linke, 2022).

The first scientist to have depicted the concept of nanotechnology and is considered the father of modern nanotechnology was the theoretical physicist Richard Feynman. The Nobel Prize laureate presented a lecture entitled “There's Plenty of Room at the Bottom” during the annual meeting of the American Physical Society at the California Institute of Technology in Caltech in 1959 (Bayda, Adeel, Tuccinardi, Cordani, & Rizzolio, 2019; Feynman, 1959). Fifteen years later, a Japanese scientist Norio Taniguchi marked history as the first to apply and define the term “nanotechnology” in 1974. Taniguchi’s definition of nanotechnology was: “nanotechnology mainly consists of the processing of separation, consolidation, and deformation of materials by one atom or one molecule” (Bayda, Adeel, Tuccinardi, Cordani, & Rizzolio, 2019).

In 1981, a new type of the microscope for nano-materials imaging called Scanning Tunneling Microscope (STM) was invented by physicists Gerd Binnig and Heinrich Rohrer at the IBM Zurich Research Laboratory (Binnig, Rohrer, Gerber, & Weibel, 1982). Five years later, the first book on nanotechnology, entitled “Engines of Creation: The Coming Era of Nanotechnology” was published by K. Eric Drexler in 1986. In his book, Drexler described the top-down and bottom-up approaches employed in manufacturing nanostructures (Bayda, Adeel, Tuccinardi, Cordani, & Rizzolio, 2019).

Nowadays, nanotechnology has become multidisciplinary since it has marked a significant role in several fields, including chemistry, biology, physics, material science, engineering, and medicine, among others. Using nanotechnology, different nano-sized structures have been developed to be exploited in different fields, and those include nanowires, nanofibers,

nanotubes, nanorods, quantum dots, nanoparticles, and hollow spheres (Bayda, Adeel, Tuccinardi, Cordani, & Rizzolio, 2019; Kargozar & Mozafari, 2018).

2.1.2. Polymeric Nanocontainers

Polymeric nanocontainers, are miniature carriers of 1 to 1000nm in size and are synthesized in different shapes including spheres, capsule micelles, dendrimers, fibres, and core-shells.

Micelles were the first polymeric nanoparticles to be made in 1960 - 1970 for therapeutic application. Commonly, polymeric nanocontainers consist of an inner core, a matrix and or a core-shell, also known as a polymeric shell (Figure 3). Drugs and several other therapeutic and bioactive molecules can be entrapped within the nanoparticles and/or absorbed on the core-shell surface (Zielińska et al., 2020). For instance, multi-layered hollow polymeric nanoparticles were successfully loaded with Daunorubicin Hydrochloride (DNR) with a 63% loading capacity that induced toxicity levels as high as 80% in breast cancer cells. Yet, plain nanoparticles have significantly low or no toxicity levels (0% to 20%) (Toniolo, Efthimiadou, Kordas, & Chatgialiloglu, 2018).

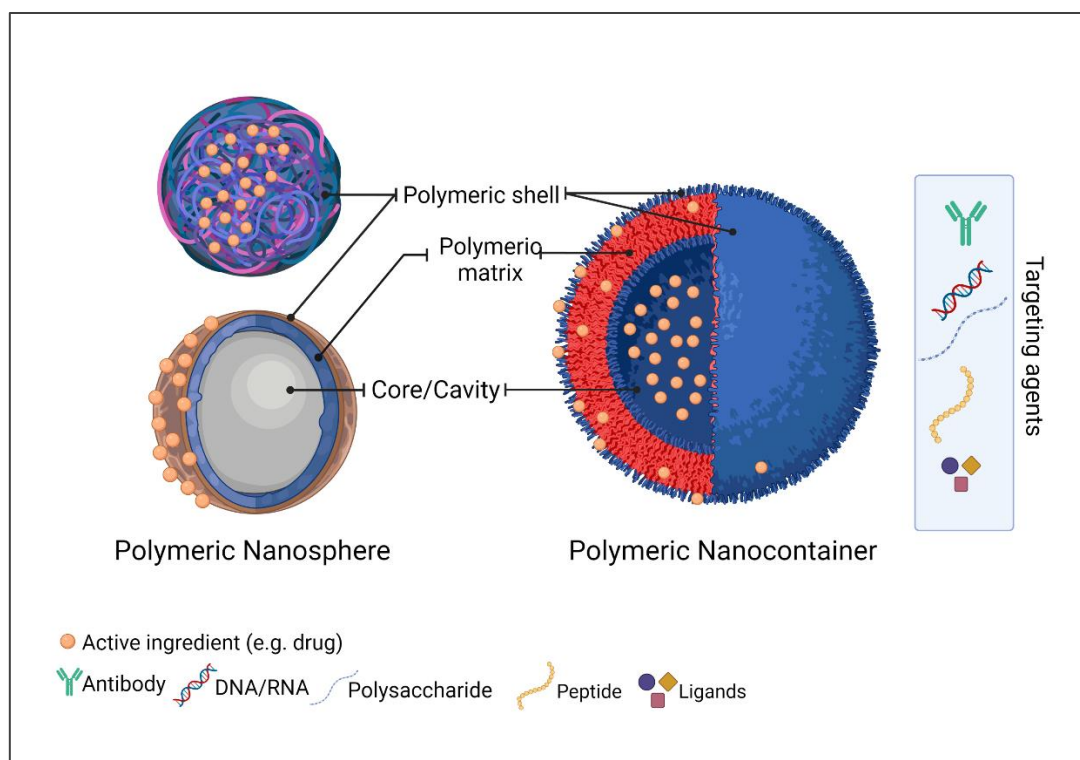


Figure 3. Illustration of polymeric nanoparticles as nanospheres and nanocontainers

Created with BioRender.com

Polymeric nanoparticles also afford synergistic treatment and controlled delivery of chemotherapy and gene therapy's active molecules. For instance, photoactivatable prodrug-backboned polymeric nanoparticles showed good light controlled codelivery of platinum (IV)-azide prodrug and RNA interference (RNAi) in platinum-resistant ovarian cancer. Both *in vitro* and *in vivo* results showed the effectiveness of photoactivatable polymeric nanoparticles and their synergetic therapeutic effect in targeting the tumour cells and reversing the drug resistance in platinum-resistant ovarian cancer (Zhang et al., 2020).

Among several types of nanoparticles, polymeric nanocontainers have attracted considerable attention from scientists due to their versatility in biomedical application field. Polymeric nanocontainers afford several advantageous properties due to their small size including

controlled and targeted drug release, improving the drug's bioavailability and therapeutic outcome, and bypass critical physiological/anatomical barriers including the blood brain barrier (Gagliardi et al., 2021). Polymeric nanoparticles are considered targeting systems for the delivery of active ingredients including drugs and biomolecules. There are three main targeting approaches through which polymeric nanocontainers target cancer cells to deliver their cargo molecules for diagnostic and/or therapeutic purposes.

2.1.3. Targeting Approaches

2.1.3.1. Passive targeting

This targeting approach relies on the aberrant anatomical and pathological vasculature of the tumour that is characterised by large pores of 100 to 800nm. The nanoparticles preferentially accumulate on the surrounding perivascular space of the tumour's vasculature by passive diffusion (Figure 4). This phenomenon is known as the enhanced permeability and retention effect (EPR). In the majority of solid tumours, drug delivery via the polymeric nanoparticle occurs through this phenomenon (Gagliardi et al., 2021). However, the overall accumulation of nanoparticles by the EPR effect on the tumour site is affected by their size. Polymeric nanoparticles with 80 to 200nm exhibit better retention in the tumour than smaller nanoparticles that diffuse deeper to other compartments due to their small size. Several Food and Drug Administration (FDA) and European Medicines Agency (EMA) approved nanomedicines including Doxil and Abraxane, have their antitumour efficacy partially based on the passive targeting and EPR effect (Gagliardi et al., 2021). Yet, the relevance of applying this description to all nanoparticles remains vague. Passive targeting of nanoparticles can be dramatically affected *in vivo* by physico-chemical properties of the nanoparticles, tumour type, and animal model or patient's pathological state (Gagliardi et al., 2021).

It was reported that the average percentage of the administered dose of nanoparticles that reaches the solid tumours was only 0.7% (Wilhelm et al., 2016). Therefore, the enhancement of nanomedicine systems and the targeting process are taking place in order to maximise the average of nanoparticles that reach the tumour site (Gagliardi et al., 2021; Wicki, Witzigmann, Balasubramanian, & Huwyler, 2015).

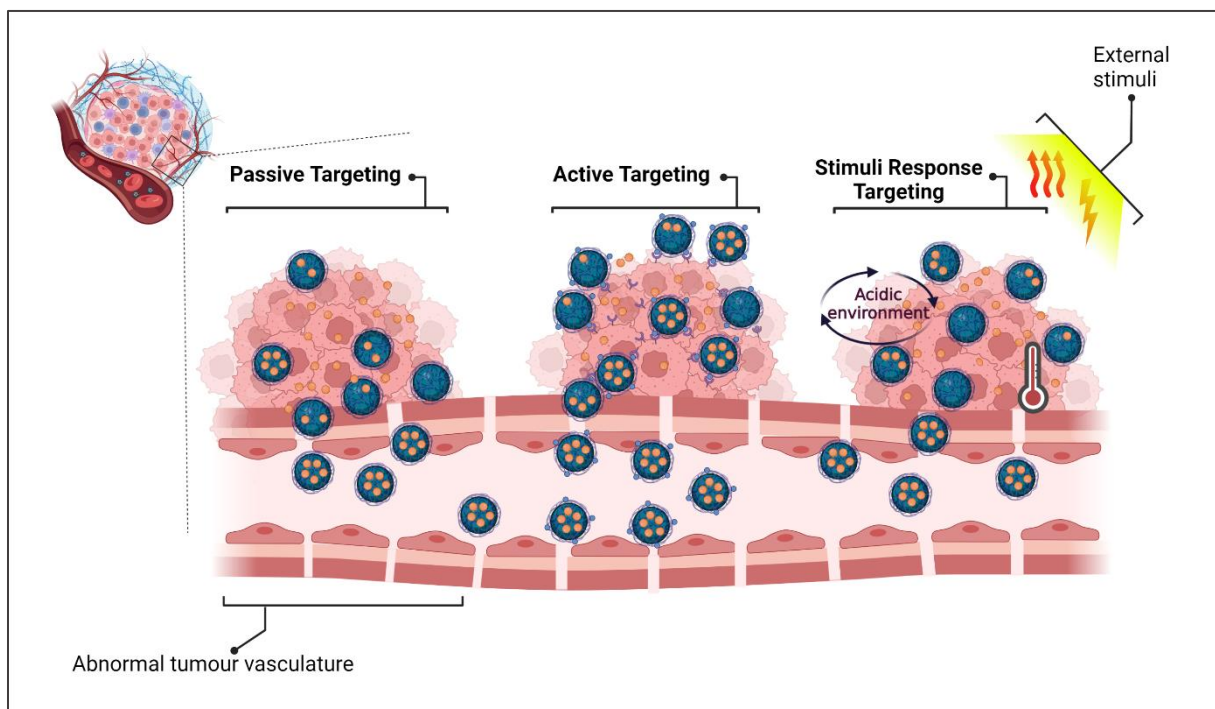


Figure 4. Illustration of the different targeting approaches of nanoparticles: passive, active and stimuli-response targeting.

Created with BioRender.com

2.1.3.2. Active targeting

This approach is based on the ligands conjugated on the surface of the nanoparticles and their interaction enhancement with the specific overexpressed receptor on the cancer cell surface (Figure 4). This ensures minimum interactions with healthy cells, hence, inducing less

cytotoxicity and side effects, and increasing the treatment efficacy. Polymeric nanoparticles can have their surfaces conjugated with one or more ligands including carbohydrates, folic acid, antibodies, oligonucleotides, aptamers, peptides, and proteins (Yoo, Park, Yi, Lee, & Koo, 2019).

Functionalisation of polymeric nanoparticles with links can be achieved by chemical conjugation, physical adsorption, and linkage to the polymers forming the nanoparticles pre-synthesis (Yoo, Park, Yi, Lee, & Koo, 2019).

Several anti-cancer drugs that are classified as ligand-targeted therapeutics can be conjugated to delivery systems to improve selectivity and accumulation on the tumour. These ligand-targeted therapeutics include trastuzumab, an anti-ERBB2, cetuximab an anti-EGFR, bevacizumab an anti-VEGF, etaracizumab an anti- $\alpha v \beta 3$ antibody (Gagliardi et al., 2021). For instance, cetuximab was conjugated to polymeric nanoparticles loaded with combretastatin A4 and 2-methoxyestradiol drugs for the treatment of hepatocellular carcinoma (HCC) (Poojari et al., 2022). Results showed potent accumulation of the HCC tumour with a prolonged circulation of up to 48h. The combinational loaded treatment in nanoparticles showed significant inhibition of the tumour growth compared to the free version of the combinational treatment (Poojari et al., 2022).

2.1.3.3. Stimuli-responsive targeting

Response to internal and/or external stimuli promoting drug release is another approach to nanoparticles targeting. Internal triggers include alteration in pH, ionic strength, redox, and shear stress, among others, all known as pathophysiological and pathochemical conditions

(Figure 4). External or physical triggers, on the other hand include temperature, light, electric fields, ultrasound, and magnetic force (Gagliardi et al., 2021).

The microenvironment of neoplastic tissue is different from the healthy tissue one. Among these differences is the acidic pH induced by the higher lactate concentration. Thus, drug release from polymeric nanoparticles made with pH-sensitive polymers is facilitated by the acidic pH of the tumour's microenvironment (Gagliardi et al., 2021). For instance, pH-sensitive polymeric poly(ethylene glycol)-block-poly(D,L-lactide acid) (PEG-PDLLA) micelles with a hydrophobic core loaded with insoluble paclitaxel is one of the approaches undergoing clinical trials to enhance the solubility of paclitaxel and the effectiveness of its delivery (Cho, Gao, & Kwon, 2016; Palanikumar et al., 2020). Also, pH-sensitive and cleavable pegylated nano-assemblies (PEG-s-PEI) that were loaded with docetaxel showed enhanced anti-tumour activity compared to free docetaxel both *in vivo* and *in vitro*. Results also showed good accumulation in the tumour due to the pH-sensitivity, and prolonged circulation in the blood due to the PEGylation. Additionally, results revealed an enhanced efficacy of the cellular internalization of the pH-sensitive nano-assemblies and rapid intracellular drug release reaching 80% pH 5 (Zhao et al., 2017).

The microenvironment of tumours is also depicted as hypoxic. The aberrant and uncontrolled growth of tumour cells results in outgrowing its blood supply, thus, several areas of the tumour become oxygen deprived compared to healthy tissue (Petrova, Annicchiarico-Petruzzelli, Melino, & Amelio, 2018). Hypoxia-responsive polymeric nanoparticles (polymersomes) conjugated to estradiol were loaded with doxorubicin for targeted stimuli-responsive delivery in the hypoxic regions of the estrogen positive breast cancer Mamnoon et al., 2020).

For instance, *in vitro* doxorubicin release from hypoxic-sensitive nanoparticles was up to 90%

in a hypoxic environment (2% oxygen) compared to ~30% normoxic one (21% oxygen) (Mamnoon et al., 2020). Also, the cytotoxicity induced by these hypoxic sensitive nanoparticles in breast cancer spheroids under hypoxic conditions was significantly higher than the cytotoxicity in a normoxic environment. Similar results were reported by Feng and colleagues (2020) in breast cancer cells, where hypoxic sensitive micelles loaded with doxorubicin induced higher toxicity levels in a hypoxic environment compared to a normoxic environment (Feng et al., 2020).

The increased vasculature and metabolic activity of tumours generate heat. This induces a temperature increase overall in the cancerous tissue compared to healthy surrounding tissue. This rationale/characteristic can be exploited for treatment and diagnosis (Knapp, Kakish, Bridle, & Speicher, 2022).

Polymers that are thermosensitive respond to temperature stimuli that trigger the release of the loaded drug and/or track the internalisation process. Polymers that are thermosensitive respond to temperature changes based on a phenomenon called low critical solution temperature (LCST), during which the polymer undergoes a phase transition from water soluble to insoluble hydrophobic state (Ghaeini-Hesaroeiye, Razmi Bagtash, Boddohi, Vasheghani-Farahani, & Jabbari, 2020).

For instance, a multifunctional thermos-responsive nano drug delivery system was developed based on cationic conjugated polymer poly(fluorene-co-vinylene) (PFV) and temperature-responsive polymer PNIPAM loaded with doxorubicin model drug. *In vitro* release profile showed an increased drug release rate as the temperature increased. Cytotoxicity assessment results in breast cancer cells showed an ~85% decrease in cell viability after 72h of treatment

with doxorubicin loaded thermos-responsive polymeric nanoparticles (Lu, Zhang, & Tang, 2019).

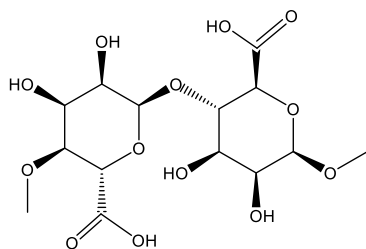
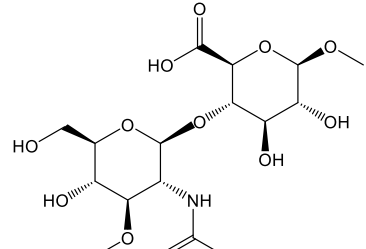
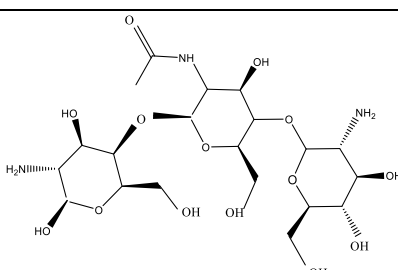
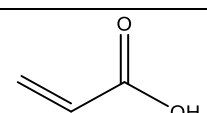
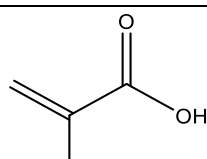
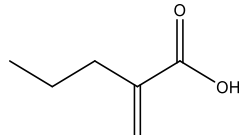
Redox homeostasis, also known as balance in reactive oxygen species (ROS), is crucial for the normal functioning of physiological processes in healthy cells. The ROS are eliminated and balanced by the antioxidant enzymes produced by the reduction system of the cells. Yet, cancer cells also need redox homeostasis, but the ROS generation during tumourigenesis is high, and amplified antioxidant activity is involved in maintaining tumour development (Zhang et al., 2017).

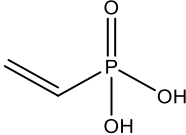
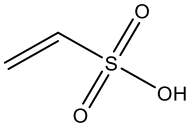
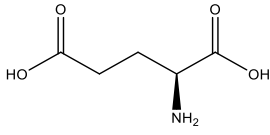
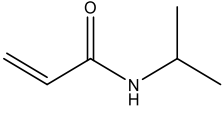
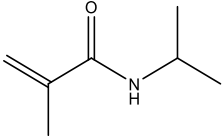
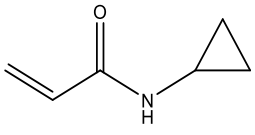
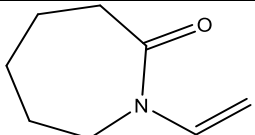
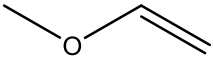
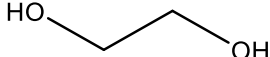
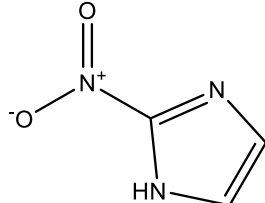
For instance, redox-responsive polymeric nanoparticles with disulfide-containing poly(β -amino ester) were loaded with doxorubicin and were used to treat brain glioma. Results showed significant redox responsiveness and release *in vitro*, as well as successfully bypassing the blood brain barrier (BBB) model. The doxorubicin redox-responsive nanoparticles also showed good internalization and significant inhibition of the tumour cell growth (Feng, Chen, Zhou, Wang, & Yan, 2018).

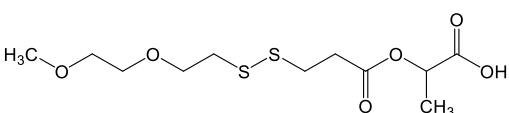
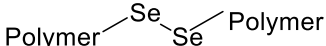
Heat, light, magnetic field, ultrasound and several other physical stimuli can be applied together with the pathophysiological and petrochemical stimuli to enhance the selectivity and accumulation of the stimuli responsive nano drug delivery system in tumours. These stimuli can also be used for theragnostic polymeric nanoparticles for therapeutic, tracking and diagnostic purposes. For instance, a pH-thermosensitive hybrid nanocontainers system with a ternary sulfide (CuCo_2S_4) core showed controlled doxorubicin release in breast cancer MCF7 cells. The release was controlled and promoted by the thermal energy converted after the

exposure of the nanocarriers to near-infrared (NIR) irradiation. With NIR laser irradiation, the hybrid nanosystem also served as a photoacoustic (PA) imaging contrast agent in the MCF-7-carrying mice model *in vivo* and as an effective chemotherapy delivery system (Fan et al., 2020). There are several polymers that are responsive and sensitive to internal and external stimuli. The table below (Table 1) lists a number of natural and synthetic polymers that are sensitive to pH, temperature, hypoxia and redox (Ofridam et al., 2021; Singh, Kim, & Park, 2021; Weng & Xie, 2015).

Table 1. Examples of pH, temperature, hypoxia, and redox sensitive natural and synthetic polymers (Ofridam et al., 2021; Singh, Kim, & Park, 2021; Weng & Xie, 2015)

	Polymer name	Abbreviation	Structure	Sensitivity
Natural Polymers	Alginate	-		pH
	Hyaluronic acid	HA		
	Chitosan	-		
Synthetic Polymers	Poly acrylic acid	PAAc		
	Poly methacrylic acid	PMAAc		
	Poly propylacrylic acid	PPAAc		

Poly vinylphosphonic acid	PVPA			
Poly vinylsulfonic acid	PVSA			
Poly L-glutamic acid	PLGA			
Poly(N-isopropylacrylamide)	PNIPAAM		Temperature	
Poly(N-isopropylmethacrylamide)	PNIPMAM			
Poly(N-cyclopropylacrylamide)	PNCPAL			
Poly(N-vinylcaprolactam)	PVCL			
Poly(methyl vinyl ether)	PMVE			
polyethylene glycol	PEG			
nitro-aromatic (Azo-derivatives derivatives)	AzP1 2- nitroimidazole			Hypoxia

	<p>Disulfide-linked/containing polymers</p>	<p>e.g. MPEG-SS-PLA</p>		Redox
	<p>Diselenide linked/containing polymer</p>	<p>e.g. Bi(mPEG-SeSe)-PCL Bi(mPEG-PLGA)-Se2</p>		

2.1.4. Synthesis Methods

There are several methods to synthesise polymeric nanoparticles including solvent evaporation, emulsification/solvent diffusion, emulsification/reverse salting-out, and nanoprecipitation. All methods involve the use of preformed polymers or polymers resulting from the polymerisation of monomers (Zielińska et al., 2020). Additionally, polymers used in the fabrication process are either synthetic or natural. Synthetic polymers include poly(lactide) (PLA), poly(lactide-co-glycolide) (PLGA) copolymers, and poly (ϵ -caprolactone) (PCL), and natural polymers include poly(amino acids), alginate, chitosan, gelatine, and albumin. All these polymers are known for their biocompatibility and biodegradability (Zielińska et al., 2020).

2.1.4.1. Solvent evaporation

This method uses preformed polymers, and it consists of two primary phases called the organic and aqueous phases. The polymer and the active ingredient, including the therapeutic drug, are dissolved and dispersed in an organic solvent in the organic phase. The organic phase

is then emulsified in a surfactant containing an aqueous phase. The whole mixture is processed by ultrasonication or high speed-homogenization. The yielded dispersion is then brought to a solvent-evaporation state, and nanoparticles are formed. The formed nanoparticles are harvested by washing and centrifugation and then freeze-dried for storage (Hoa, Chi, Nguyen, & Chien, 2011; Jana, Shyam, Singh, Jayaprakash, & Dev, 2021; Zielińska et al., 2020).

2.1.4.2. Emulsification with solvent diffusion

This method consists of emulsifying two solutions, an organic one that contains the preformed polymer, the drug or the active ingredient and oil in a partial water solution solvent, and an aqueous one that contains water and surfactant. The emulsified mixture is then diluted with large amount of water to induce solvent diffusion from the nanodroplets to the external phase. This results in the formation of colloidal particles. The last step to obtain polymeric nanoparticles consists of solvent evaporation or filtration (Pineda-Reyes et al., 2021; Zielińska et al., 2020)

2.1.4.3. Emulsification with reverse salting-out

This method is similar to the emulsification/solvent diffusion method with a slight modification. In the latter method, the organic solution contains polymer and active ingredients in oil, whereas the organic solution in the reverse salting-out method consists of polymer and active ingredients in water miscible solvent. The aqueous solution in this method consists of a surfactant and salting-out agent instead of plain water. The remaining steps are identical to the steps in emulsification/solvent diffusion (Hyde et al., 2017; Jana, Shyam, Singh, Jayaprakash, & Dev, 2021; Zielińska et al., 2020).

2.1.4.4. Nanoprecipitation

This method is marginally similar to the solvent evaporation method. It consists of dissolving the polymer in an organic solvent and is added drop wise to the aqueous solution containing the aqueous solution under continuous stirring. The nanoparticles precipitate as the solvent evaporates and diffuses out of the nanodroplets (Lammari, Louaer, Meniai, & Elaissari, 2020). The nanoparticles produced by this method are distinguished by the well-defined size and narrow size distribution compared to nanoparticles produced by the previously mentioned methods (Lammari, Louaer, Meniai, & Elaissari, 2020; Yadav & Sawant, 2010; Zielińska et al., 2020).

2.1.5. Characterization Methods

Characterization of polymeric nanoparticles comprises several techniques, including scanning and transmission electron microscopy (SEM and TEM), dynamic light scattering (DLS) fourier transform infrared spectroscopy (FTIR) and others. Each technique assesses different properties of nanoparticles, including morphology, size distribution, surface zeta potential, structure, and chemical composition.

Morphological characterization of nanoparticles is achieved by both SEM and TEM. These two techniques have become conventional since they have been broadly used in assessing the size and shape of polymeric NCs. Both techniques are electron based and produce clear pictures of nanoparticles (Brodusch et al., 2021). However, TEM reveals more detailed information regarding the different layers of the nanoparticles. The reason behind this difference between SEM and TEM is that SEM produces images by the detection of backscattered electrons that penetrate the sample to a certain depth and secondary electrons that originate from the sample's surface (Brodusch et al., 2021). Yet in TEM, transmitted electrons that have passed

through the sample before collection result in further information regarding the inner structure of the sample (Brodusch et al., 2021; Thermo Fisher Scientific, 2022).

Another technique that assesses the surface of nanoparticles revealing the presence or absence of pores and cavities, is atomic force microscopy (AFM). This imaging technique produces highly detailed 3D images thanks to the AFM tips (Main et al., 2021). The atoms on the surface of the sample are sensed by the atoms on the apex of the tips, which have their frequency vibration altered (Main et al., 2021). The altered frequency vibrations are then collected and mapped, resulting in highly detailed and high-resolution images. The AFM technique can analyse even biomolecules without any required pre-treatments (Main et al., 2021).

The unimodality of size distribution, hydrodynamic size, polydispersity, and zeta potential are all assessed by several techniques, including dynamic (DLS) light scattering, which is the most common (Zielińska et al., 2020). The intensity of the scattered light by the particles in the solution sample allows the determination of the translational diffusion coefficients, also known as Brownian motion, i.e., particle size (Stetefeld, McKenna, & Patel, 2016). Zeta potential, which refers to the net charge of the particle, also known as electrokinetic potential, is also measured by DLS (Bhattacharjee, 2016). The particles in the suspension are put under an electric field, and the potential difference between their electric double layer and the layer of surrounding dispersant at the slipping plane is translated into a negative or positive zeta potential value (electrophoretic mobility) (Bhattacharjee, 2016; Zielińska et al., 2020). Also, the zeta potential measurements provide more information regarding the stability of the particles. High zeta potential values of around ± 30 mV are crucial for the stability of the colloidal suspension because of the high repulsive force between particles that prevents nanoparticle aggregation (Bhattacharjee, 2016; Crucho & Barros, 2017).

Analysis of the nanoparticles' surface composition and functional groups is commonly attained by fourier transform infrared spectroscopy (FTIR). This technique assesses the composition of nanoparticles by detecting the change in the functional groups induced by infrared radiation (Taha, Hassan, Essa, & Tartor, 2013). In more detail, the covalent bonds in the molecules absorb the radiation that excites them at a specific wavelength. These changes in the vibrational energy in the bonds -either by bending or stretching - depend on the atoms of the functional groups (Taha, Hassan, Essa, & Tartor, 2013; Zielińska et al., 2020). The results are expressed in the form of transmittance spectra, where different bonds in different functional groups absorb distinct frequencies and produce distinct transmittance patterns (Taha, Hassan, Essa, & Tartor, 2013, Zielińska et al., 2020).

The aim of the current study was to synthesise hollow and smart polymeric nanocontainers with dual sensitivity to pH and temperature. The study's aim was also to assess their biocompatibility and ability to encapsulate and release first line chemotherapy drugs sustainably *in vitro*.

2.2. Materials and Methods

2.2.1. Materials

Tetraethyl orthosilicate (TEOS) (Fluka, Buchs, Switzerland), 2,2-azobis(2-methylpropionitrile) (AIBN) (Sigma, Munich, Germany), 3-methacryloxypropyltrimethoxysilane (MPS) (Acros Organics, Geel, Belgium). Ethyleneglycol dimethacrylate (EGDMA) (Sigma-Aldrich, Missouri, USA) N,N'-Methylenebis(acrylamide) (MBA 99%) (Sigma-Aldrich, Missouri, USA), Methacrylic acid (MAA 99%) (Sigma-Aldrich, Missouri, USA), N-Isopropylacrylamide (NIPAM, >99%) (Acros Organics, Geel, Belgium) Acetonitrile (ACN) (Sigma Aldrich Sigma-Aldrich, Missouri, USA), Hydrofluoric acid (HF 48%) (Merck, Darmstadt, Germany), Daunorubicin Hydrochloride (DNR) (Pharmacia & Upjohn, Michigan, United States), Vincristine (Sigma-Aldrich, Missouri, USA). Cisplatin (Sigma Aldrich, Missouri, USA), Vincristine (Sigma Aldrich, Missouri, USA), colchicine (Sigma Aldrich, Missouri, USA). FTIR instrument Perkin Elmer Spectrum 100 spectrometer (Perkin Elmer, Massachusetts, United States); Malvern Instrument Zetasizer Nano Series (Malvern Analytics, Worcestershire, United Kingdom); SEM images were obtained on an FEI Inspect microscope with W Tungsten filament operating at 12.5 kV to 25 kV.

2.2.2. Silica Nanocontainers

2.2.2.1. Synthesis of silica core spheres

Silica core spheres were synthesised by the Stöber method (Stöber, Fink & Bohn, 1968). TEOS was added to a mixture of ethanol (EtOH) and distilled water while under magnetic motor stirring. Three ml of NH₃ was added to the stirring mixture, and all was left to stir overnight. After the overnight reaction, the suspension was centrifuged in 3 cycles, 5 min each (5 min, 3x 8000rpm), with washing/resuspending in water and then in ethanol. Then, precipitated particles were left to dry at 37°C in the oven overnight.

2.2.2.2. Synthesis of the first thin layer with methacryloxypropyltrimethoxysilane (SiO₂@MPS)

Fifty milligrams of silica nanocarriers (SiO₂ NCs) were suspended in 2 ml distilled water and 30ml ethanol; in order to assure well suspension of the nanoparticles in the aqueous alcoholic solution, NCs were sonicated for about 30 min before proceeding to the next step of the reaction. Then, while the suspension was stirred, 1.5 ml of MPS was added to it. After 10 min stirring, 3 ml of NH₃ was added to the suspension and left for stirring overnight. After that, the mixture was centrifuged (5 min, 3x8000rpm), washed and resuspended in water once and twice in ethanol.

2.2.2.3. Multisensitive layer fabrication SiO₂@MPS@P(MAA-co-MBA-co-EDGMA) nanocontainers

In a spherical vial attached to a distillation system, 200 mg of SiO₂@MPS NPs were suspended in 80ml acetonitrile (ACN). When the temperature of the oil bath reached ~55°C, the suspension was then treated with nitrogen to remove the oxygen and avoid the inhibition of radical polymerization. After 30 min, 75.6mg of MBA, 205 µl of MAA, and 280µl of EDGMA were added to the mixture, then the temperature was increased to 80°C and the AIBN was introduced for the polymerization initiation. When 50% of the ACN solvent was distilled, the reaction was stopped, and the mixture was left to cool down at room temperature before centrifugation. Harvesting of particles coated with a multi-sensitive layer took place following three cycles of centrifugation/resuspension using ACN once and ethanol twice (5 min, 3X8000rpm).

2.2.2.4. Hollow silica MPS@P(MAA-co-MBA-co-EGDMA) nanocontainers

The SiO₂@MPS@P(MAA-co-MBA-co-EDGMA) NCs were well suspended in ammonium fluoride (NH₄F/HF) buffer solution or pure HF (48%) then put under continuous stirring for different periods of time (Table 2). The material was harvested by centrifugation (5 min, x 8000 rpm) using EtOH.

Table 1. Different treatment conditions for hollow silica nanocontainers.

Sample	HF buffer	Pure HF	Temperature (°C)	Stirring time
SS2010	X		Room temperature	20 min
SS2010.A	X		Room temperature	1h
SS2016.A		X	Room temperature	10 min
SS2020.A	X		60	15 min
SS2020.B	X		60	30 min
SS2020.C	X		60	1h
SS2021.A		X	Room temperature	15 min
SS2021.B		X	Room temperature	30 min
SS2021.C		X	Room temperature	45 min

2.2.3. Polymeric Nanocontainers

The synthesis of hollow PMAA nanocarriers went through three steps:

2.2.3.1. Core PMAA spheres

The core spheres were made by polymerization/distillation reaction using acetonitrile as a solvent, MAA polymer, and AIBN as an initiator. After 4 hours of polymerization/distillation,

50 % of ACN solvent was collected, and the reaction was stopped and left to cool down at room temperature. After that, the reaction was centrifuged and washed (3 x 8000rpm, 5 min each) using ACN only to harvest the core PMAA spheres.

2.2.3.2. Multisensitive shell fabrication PMAA@P(MAA-co-MBA-co-EGDMA) and PMAA@P(MAA-co-MBA-co-NIPAM-co-EGDMA) nanocontainers

The core spheres were coated with a layer of MAA and EGDMA using MBA as a crosslinker, AIBN as an initiator and ACN as a solvent (Table 3). PMAA core spheres were first well sonicated in ACN until fully dispersed, and then the two-neck spherical vial containing the suspension of NCs was introduced into an oil bath of 60°C under continuous stirring. The system was treated with N₂ to remove the oxygen to avoid the inhibition of radical polymerization. After that, MAA, MBA, and EGDMA were added with 5 min intervals between them. When the temperature reached 75-80°C, the initiator AIBN was added, and the reaction was left to polymerize for 45 min. Then, the temperature was increased to 90-100°C to start the distillation. After 50% of the ACN was distilled, the reaction was stopped and left to cool down at room temperature. The material harvesting was carried out by three cycles of centrifugation/resuspension using ACN only (5 min, 3X8000 rpm).

For PMAA@(MAA-co-MBA-co-NIPAM-co-EGDMA) NCs, NIPAM was added together with the MAA and the EGDMA following the SS2062 ratios of MAA: PMAA NCs: MBA: NIPAM: EGDMA (3:3:2:1:2). Then the same aforementioned procedure of polymerization/distillation was followed to synthesize and harvest the multisensitive layer coated nanocontainers. Of note,

all samples synthesised after the SS2062 had NIPAM introduced in the multisensitive polymeric layer.

Table 3. Different ratios of multisensitive layer components

Sample	MAA (μ l)	PMAA (mg)	MBA (μ l)	EGDMA (μ l)	ACN (ml)
SS2025	500	180	90	150	55
SS2032	128	100	85	40	100
SS2035	1000	180	75	100	75
SS2037	40	40	30	20	80
SS2041	40	50	38	25	100
SS2044	55	75	42	32	120
SS2056	65	85	40	30	120
SS2062	157	145	85	66	250

2.2.3.3. Hollow P(MAA-co-MBA-co-EGDMA) and P(MAA-co-MBA-co-NIPAM-co-EGDMA) nanocontainers

Nanocontainers harvested from the previous synthesis step were sonicated in an ethanol/dH₂O solution and left under continuous stirring at room temperature for different timings (Table 4). The material was harvested by three cycles of centrifugation/resuspension using ethanol only (10 min, 3x9000rpm). Of note, all samples synthesised after the SS2033.A had their core removed following the 1:1 ratio and 48h stirring.

Table 4. Different treatment periods with water and/or ethanol for hollow PMAA nanocarriers

Sample	Ethanol/dH ₂ O	Stirring Time (h)
SS2026.A	1:1	2
SS2026.B	1:1	24
SS2026.C	1:0	2
SS2026.D	1:1	48
SS2036	1:1	48
SS2033.A	1:1	48

2.2.4. Fourier Transform Infrared Spectroscopy (FTIR)

Dried samples at different synthesis steps were assessed by the FTIR. A small amount of the sample in powder form was introduced on the stage of the FTIR instrument Perkin ElmerSpectrum 100 spectrometer (Perkin Elmer, Massachusetts, United States) and the measurements were run. The spectra obtained by the instrument were scanned over the range of 4000–400 cm⁻¹.

2.2.5. Dynamic Light Scattering (DLS)

Samples were well suspended in distiller water (0.5mg/ml) with a 10 min sonication to insure a complete dispersion. The suspensions were then measured by Malvern Instrument Zetasizer Nano Series (Malvern Analytics, Worcestershire, United Kingdom); each measurement was the average value of three measurements, with 11–15 runs for each measurement.

2.2.6. Scanning Electron Microscopy (SEM)

On a stand covered with conductive carbon adhesive tape, a very small amount of the NCs sample was spread and gold-plated for scanning electron microscopy analysis. The SEM images were obtained on an FEI Inspect microscope with W (Tungsten) filament operating at 12.5 kV to 25 kV.

2.2.7. COOH Back Titration

Back titration was used to determine the carboxylic group acid entities. An amount of 3 mg of hollow nanocontainers was well suspended in 3ml sodium hydroxide (NaOH) (C= 0.1M). then, phenolphthalein was added as an indicator, and small volumes of hydrochloric acid (HCl) solution (C= 0.1M) was added to back titrate the excess of the NaOH. The procedure was done in triplicates and the average volumes of HCl solution added were used to determine the amount of COOH groups based on the following equation:

$$n_{\text{COOH}} = n_{\text{NaOH}} - n_{\text{HCl}}$$

2.2.8. Drug Loading

Daunorubicin (DNR), vincristine and cisplatin were loaded in hollow NCs by either shaking or stirring method. Either method used, the loading was mostly carried-out in PBS (pH = 7.4, T=37°C), for three to five days in different NCs/drug ratios (1:1, 1:2, and 1:4).

The loaded material was harvested by centrifugation and washing with PBS (8,000 to 10,000 rpm) until the supernatant was clear, and the loaded material was dried under vacuum. The supernatant absorbances were measured using UV-vis spectroscopy at drugs' characteristic wavelengths (DNR at 468nm, cisplatin at 301nm, vincristine at 256nm, temozolomide at

328nm, and colchicine at 352nm) and the concentrations were calculated based on standard curve equation. The loading capacity (LC%) and encapsulation efficiency (EE%) were calculated as follows:

$$LC\% = \left(\frac{\text{Weight of the drug in nanocarriers}}{\text{The total weight of the nanocarriers}} \right) \times 100$$

$$EE\% = \left(\frac{\text{Weight of the drug in nanocarriers}}{\text{Weight of the feeding drug}} \right) \times 100$$

The UV-vis absorption spectra (UV-vis) in the wavelength range of 200–900 nm were obtained on a Jasco V-650 spectrometer (Jasco, Easton, United States).

2.2.9. Drug Release

2.2.9.1. Stirring method

In an Eppendorf, the loaded material was suspended in a buffer solution (pH 4.6 and 7.4) and put under continuous stirring at different temperatures (37°C and 40°C). At different time points, 50 µl of the suspension was taken and the corresponding buffer was added to obtain a 500 µl final volume. Absorbance measurements were carried out by UV-Vis spectrometry spectra (UV-vis Jasco V-650 spectrometer (Jasco, Easton, United States)) in the wavelength range of 200–900 nm and values obtained had their concentrations determined by standard curve equation.

2.2.9.2. Dialysis bag method

The loaded material was suspended in dH₂O and introduced in a dialysis bag. The “candy like” formed bag containing the suspended loaded material was introduced in a tube containing buffer solution and put under continuous stirring. The release was examined under different

pH (4.6 and 7.4) and temperature (37°C and 40°C) conditions. At different time points, 0.5ml of the buffer was taken for absorbance measurement by UV-Vis spectrometry and the values obtained had their concentration determined by a standard curve equation.

2.2.10. Hemolysis Assay

The blood sample collected from a healthy donor was washed and centrifuged with isotonic PBS without Ca²⁺ and Mg²⁺. The precipitated red blood cells (RBCs) were introduced into two sets of three different Eppendorf tubes, each one containing 150µL of one of the different concentrations of hollow NCs suspension (Table 5). This is in addition to a positive control tube (Tube 1) and one negative control (Tube 2) (Table 5).

Table 5. Components of Eppendorf tubes sets of RBCs treated with different NCs suspension concentrations.

Tube 1 Positive control	Tube 2* Negative control	Tube 3	Tube 4	Tube 5
150µL of water + 10µL of RBCs	150µL of PBS (without Mg ²⁺ and Ca ²⁺) + 10µL of RBCs	150µL of 25µg/ml NCs suspension + 10µL of RBCs	150µL of 50µg/ml NCs suspension + 10µL of RBCs	150µL of 100µg/ml NCs suspension + 10µL of RBCs

The first set of tubes was left for 2h in the incubator at 37°C while the second set was left for 24h under the same conditions. After the incubation time was over, samples were centrifuged once at 8000 rpm for 5min. Supernatant from each sample tube was introduced in a 96well plate and had their absorbance measured by an ELISA microplate reader at 540nm.

2.2.10.1. Fixation of red blood cells

1st Method: The RBCs were washed twice with PBS without Ca^{2+} and Mg^{2+} , then they were fixed with glutaraldehyde (GA) for 30min. After that, fixed RBCs were washed 3 times with PBS and cells were then dehydrated with increasing concentrations of ethanol for 10min for each concentration (50%, 60%, 70%, 80%, 90%, 95%, and 100%).

2nd Method: The RBCs and the different NCs suspensions were introduced in a 24 well plate instead of Eppendorf tubes and treated the same way as described in the haemolysis assay procedure in (2.2.9). After the incubation time was over, the RBCs in the wells were fixed following the same procedure in the first method above.

2.3. Results

2.3.1. Structural Characterization

2.3.1.1. Silica nanoparticles characterization by Fourier transform infrared microscopy (FTIR)

Figure 5 shows the FTIR characterization results of the silica nanocarriers at all syntheses. Spectrum (5a) which corresponds to core silica, showed one characteristic peak at 1058cm^{-1} . In Figure 5b, the FTIR spectrum corresponds to the nanocarriers coated with the MPS layer, which showed characteristic peaks at 1035cm^{-1} and 3062cm^{-1} . The spectrum corresponding to $\text{SiO}_2@\text{MPS}@P(\text{MAA-co-MBA-co-EGDMA})$ NCs (Figure 5c) showed characteristic peaks at 1719cm^{-1} and 1082cm^{-1} . The $\text{MPS}@P(\text{MAA-co-MBA-co-EGDMA})$ hollow NCs' corresponding spectrum (Figure 5d) showed characteristic peaks at 1700cm^{-1} and 1160cm^{-1} .

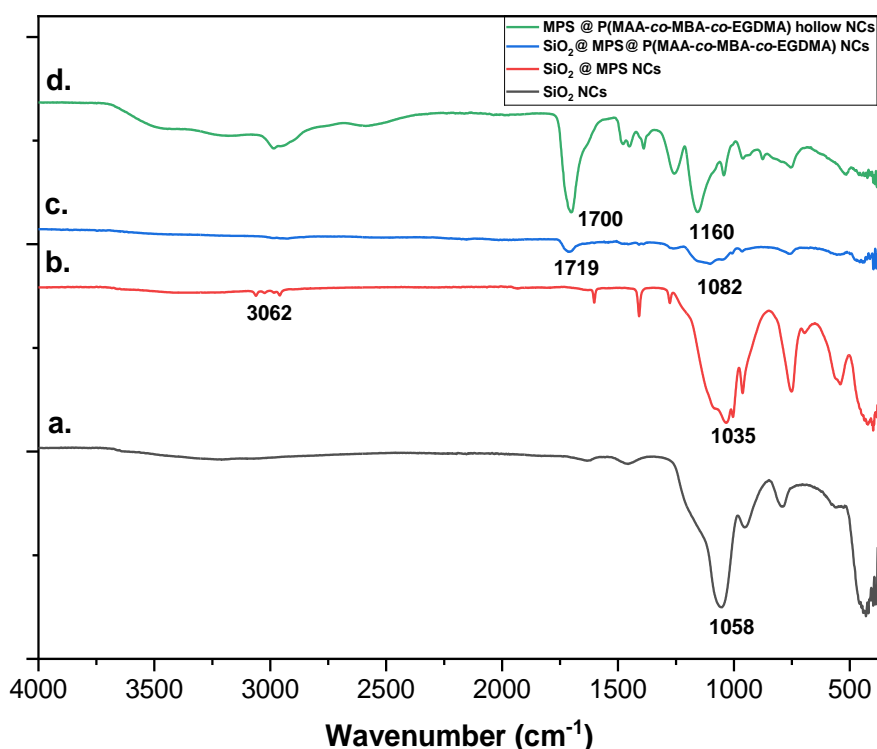


Figure 5. FTIR spectra of the 4 synthesis stages of silica polymeric nanoparticles.

(a). SiO_2 NCs, **(b).** $\text{SiO}_2 @ \text{MPS}$ NCs, **(c).** $\text{SiO}_2 @ \text{MPS}@P(\text{MAA-co-MBA-co-EGDMA})$ NCs, **(d).** $\text{MPS}@P(\text{MAA-co-MBA-co-EGDMA})$ NCs

2.3.1.2. Silica nanoparticles characterization dynamic light scattering (DLS)

The DLS measurement of the different synthesised silica cores (Figure 6) showed hydrodynamic diameter sizes (H_d) of 416nm (± 10). The core spheres coated with MPS ($\text{SiO}_2@MPS$) showed a hydrodynamic diameter of 500nm (± 30), and the multisensitive-layer coated NCs ($\text{SiO}_2@MPS@P(\text{MAA-co-MBA-co-EGDMA})$) showed a hydrodynamic diameter of 270nm ($20\pm$). All NCs from the three synthesis steps had a zeta potential (ζ) between -16mV (± 4) and -32mV (± 6). DLS measurements of hollow silica nanocontainers were not possible due to its sticky and peculiar texture.

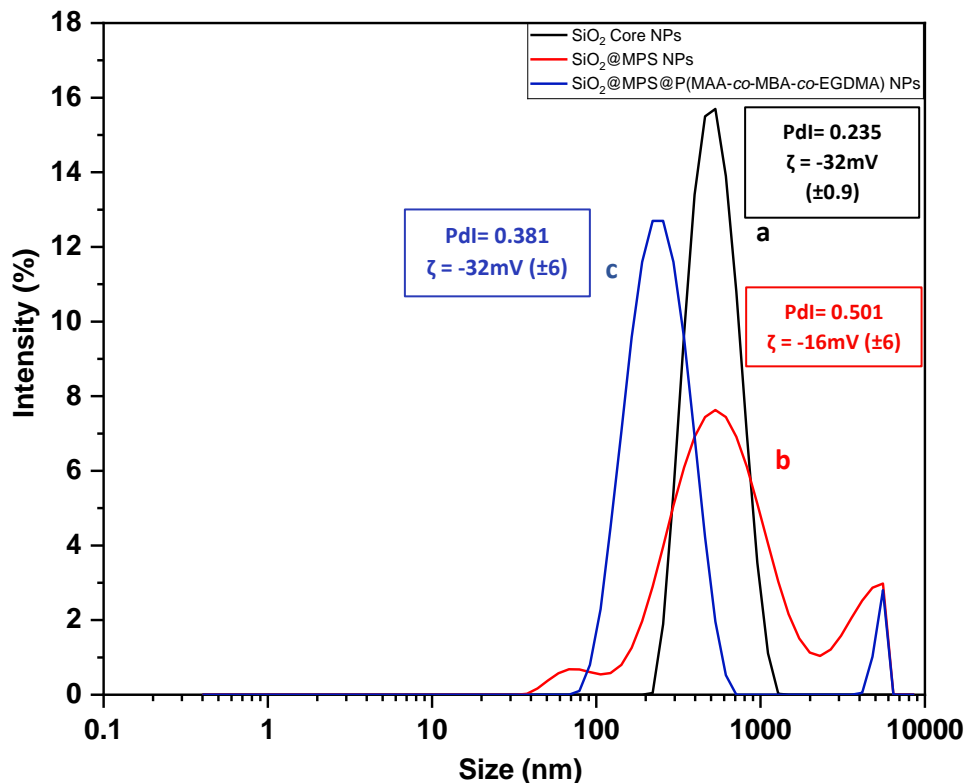


Figure 6. DLS spectra of the 4 synthesis stages of silica polymeric nanoparticles.

(a). SiO₂ core NPs, **(b).** SiO₂@MPS NPs, **(c).** SiO₂@P(MAA-co-MBA-co-EGDMA) NPs

2.3.1.3. Polymeric nanocontainers characterization by Fourier transform infrared microscopy (FTIR)

The FTIR spectrum corresponding to the PMAA@P(MAA-co-MBA-co-EGDMA) NCs (Figure 7a) showed characteristic peaks at 1697 cm^{-1} and 1172 cm^{-1} . The spectrum corresponding to the multisensitive-layer coated PMAA@P(MAA-co-MBA-co-EGDMA) NCs (Figure 7b) showed the appearance of new characteristics at 1386, 1532 cm^{-1} . The spectrum of the hollow P(MAA-co-MBA-co-EGDMA) NCs (Figure 7c) showed the same characteristic peaks as the previous step, with a decrease in the intensity of the MAA carboxylic group's characteristic peak.

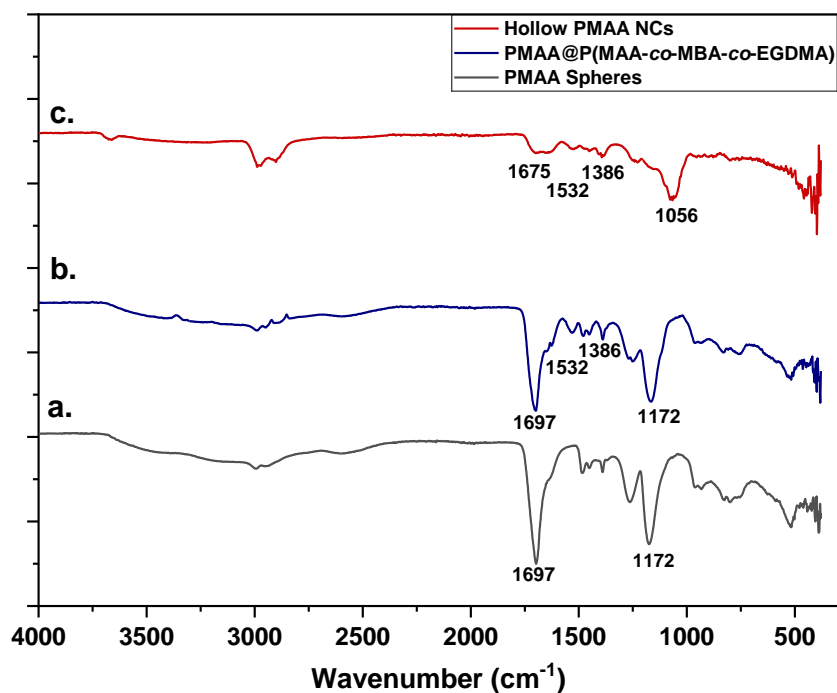


Figure 7. FTIR spectra of the three synthesis stages of polymeric nanocontainers with MAA, EGDMA, and MBA.

(a). MAA NCs, **(b).** PMAA@P(MAA-co-MBA-co-EGDMA) NCs, **(c).** P(MAA-co-MBA-co-EGDMA) hollow NCs.

The peak at 1702 cm^{-1} corresponds to the amide band from the PNIPAM. Since the C=O stretching of the COOH from the PMAA and the amide band of the NIPAM overlap, there was an increase in the 1702 cm^{-1} peak intensity in the presence of NIPAM compared to its absence.

After the PMAA core removal, there was a decrease in the characteristic peak of the COOH from the PMAA and the appearance of the 1633 cm^{-1} peak that corresponds to the NIPAM's amide and falls in the range of $1600\text{ to }1800\text{ cm}^{-1}$.

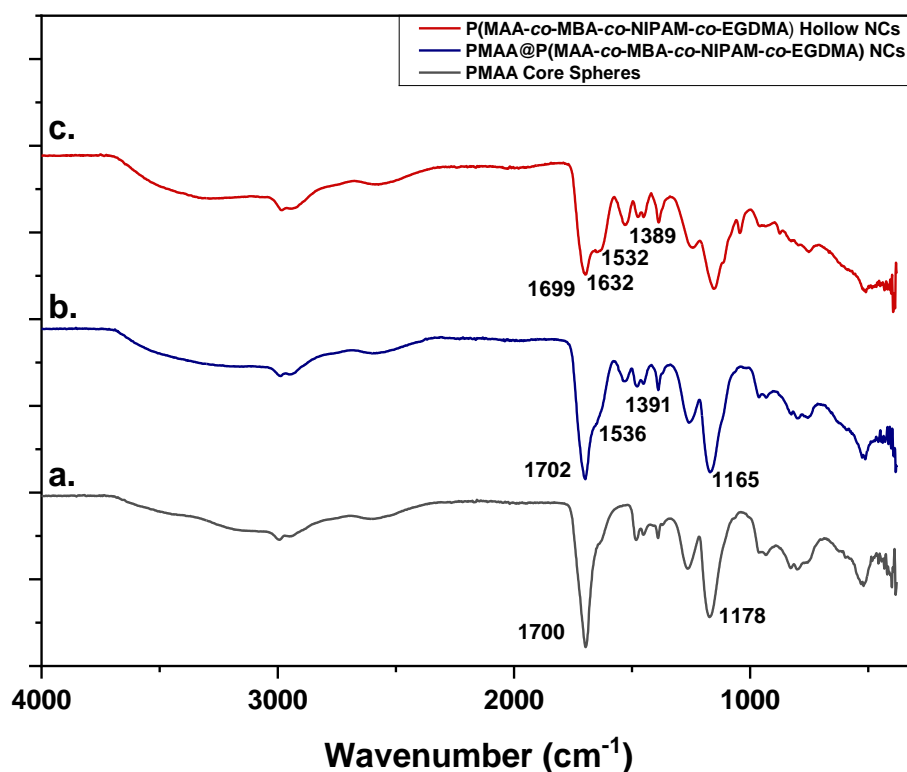


Figure 8. FTIR spectra of the three synthesis stages of polymeric nanocontainers with MAA, EGDMA, NIPAM, and MBA.
(a). MAA NCs, **(b).** PMAA@P(MAA-co-MBA-co-NIPAM-co-EGDMA) NCs, **(c).** P(MAA-co-MBA-co-NIPAM-co-EGDMA) hollow NCs.

2.3.1.4. Polymeric nanocontainers characterization Dynamic light scattering (DLS)

The DLS measurement of the different synthesised PMAA core spheres (Figure 9) showed hydrodynamic diameter sizes (H_d) ranging from 442nm (± 61). The PMAA@P(MAA-co-MBA-co-EGDMA) NCs had a hydrodynamic diameter ranging from 526nm (± 1.7). The hollow P(MAA-co-MBA-co-EGDMA) NCs' DLS measurement showed hydrodynamic diameter sizes within the range of 574 (± 8). The zeta potential (ζ) throughout the three synthesis steps was negative and ranged between -32mV to -18mV (± 2).

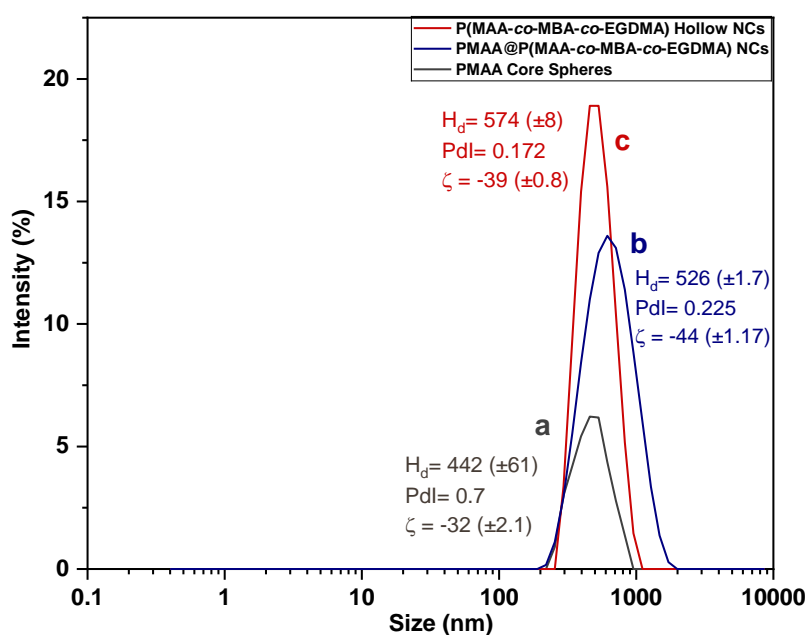


Figure 9. DLS spectra of the three synthesis stages of polymeric nanoparticles with MAA, EGDMA and MBA.

(a). PMAA@P(MAA-co-MBA-co-EGDMA) NCs, **(b).** Shell coated PMAA@P(MAA-co-MBA-co-

The DLS measurement of the PMAA core spheres showed hydrodynamic diameter sizes (H_d) of about 270nm (± 32). The PMAA@P(MAA-co-MBA-co-NIPAM-co-EGDMA) NCs had a hydrodynamic diameter ranging from 640nm (± 30). The H_d measurements of the hollow

P(MAA-co-MBA-co-NIPAM-co-EGDMA) NCs' were about 733nm (± 24). The zeta potential (ζ) throughout the three synthesis steps was negative and ranged between -40mV to -20mV (± 3).

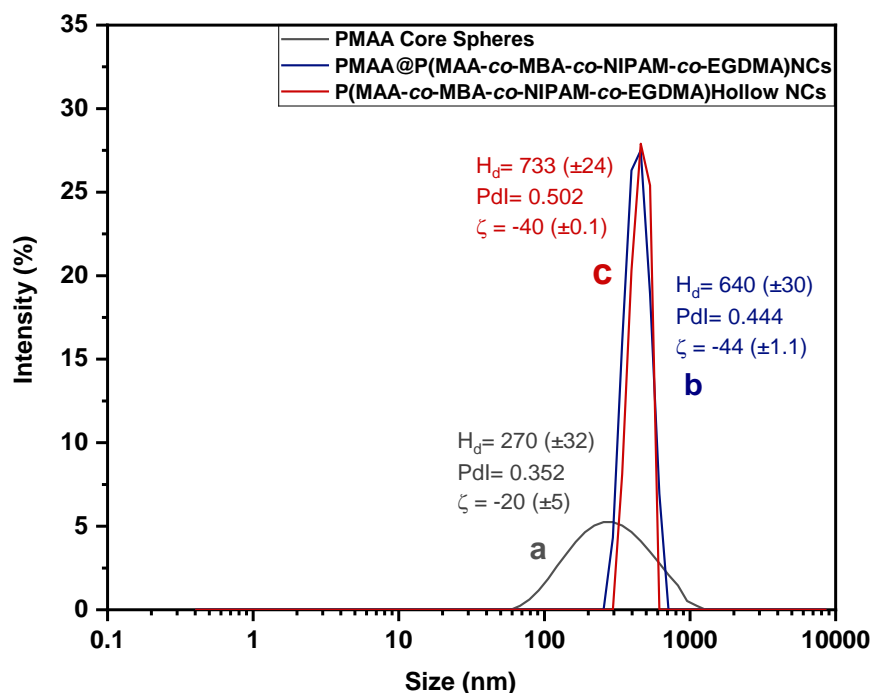


Figure 10. DLS spectra of the three synthesis stages of polymeric nanoparticles with MAA, EGDMA, NIPAM, and MBA.

(a). PMAA core spheres, (b). Sell coated PMAA@P(MAA-co-MBA-co-NIPAM-co-EGDMA) NCs, (c). Hollow P(MAA-co-MBA-co-NIPAM-co-EGDMA) NCs.

2.3.2. Morphological Characterization

2.3.2.1. Silica nanocontainers

The morphological characterisation of silica nanocarriers at the different synthesis steps by SEM (Figure 11), showed spherical and homogenous silica core spheres with sizes of 480nm (± 45) and 100 (± 11) (Figures 11a to 11c). The analysis of MPS coated NCs (Figures 11d to 11f) showed spherical shaped NCs with a size of 450nm (± 11). The analysis of multisensitive-layer

coated NCs (Figures 11g to 11i) showed spherical nanocontainers with a size of 500nm (± 20).

The analysis of nanocarriers that underwent core removal showed spherical but non-hollow NCs (Figures 11j to 11l).

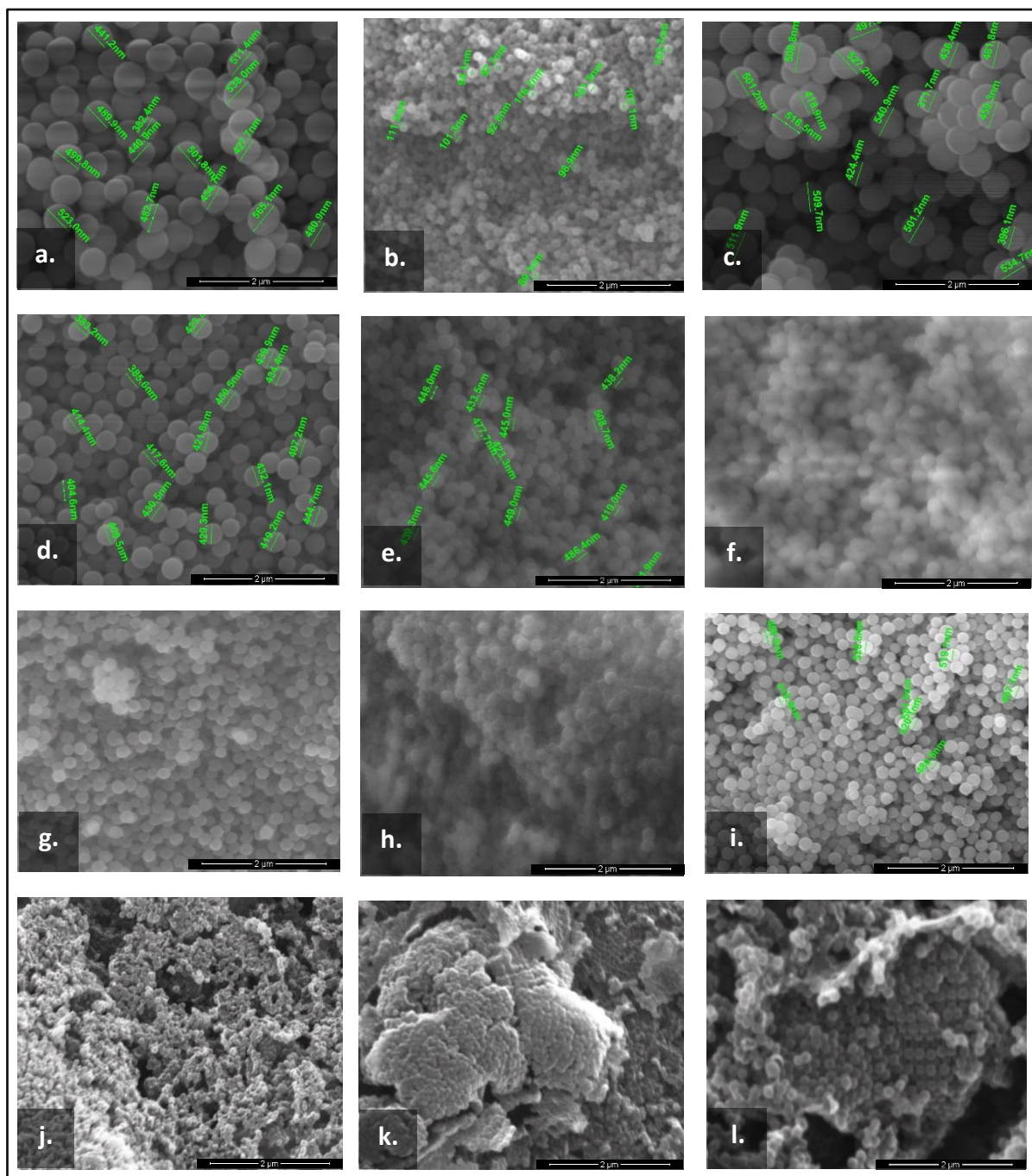


Figure 11. SEM pictures of polymeric silica nanocontainers at different synthesis steps.

a-c). Silica core spheres, **(d-f).** MPS coated NCs ($\text{SiO}_2\text{@MPS}$), **(g-i).** Multisensitive layer coated NCs ($\text{SiO}_2\text{@MPS@P(MAA-co-MBA-co-EGDMA)}$), **(j-l).** Hollow NCs ($\text{MPS@P(MAA-co-MBA-co-EGDMA)}$)

2.3.2.2. Polymeric Nanocontainers

The morphological characterisation of PMAA nanocarriers at the three synthesis steps by SEM (Figure 12) revealed spherical and homogenous core PMAA spheres (Figures 12a to 12f) with 170nm to 240nm (± 20). The SEM analysis of the multisensitive layer coated NCs PMAA@P(MAA-co-MBA-co-EGDMA) and PMAA@P(MAA-co-MBA-co-NIPAM-co-EGDMA) (Figures 12g to 12i) showed spherical nanoparticles with sizes ranging between 280nm and 383nm (± 35), indicating a size increase of about 150nm. The hollow NCs P(MAA-co-MBA-co-EGDMA) and P(MAA-co-MBA-co-NIPAM-co-EGDMA) (Figures 12m to 12r) showed concave-like shaped nanocarriers with cavity and average sizes of 383nm (± 35).

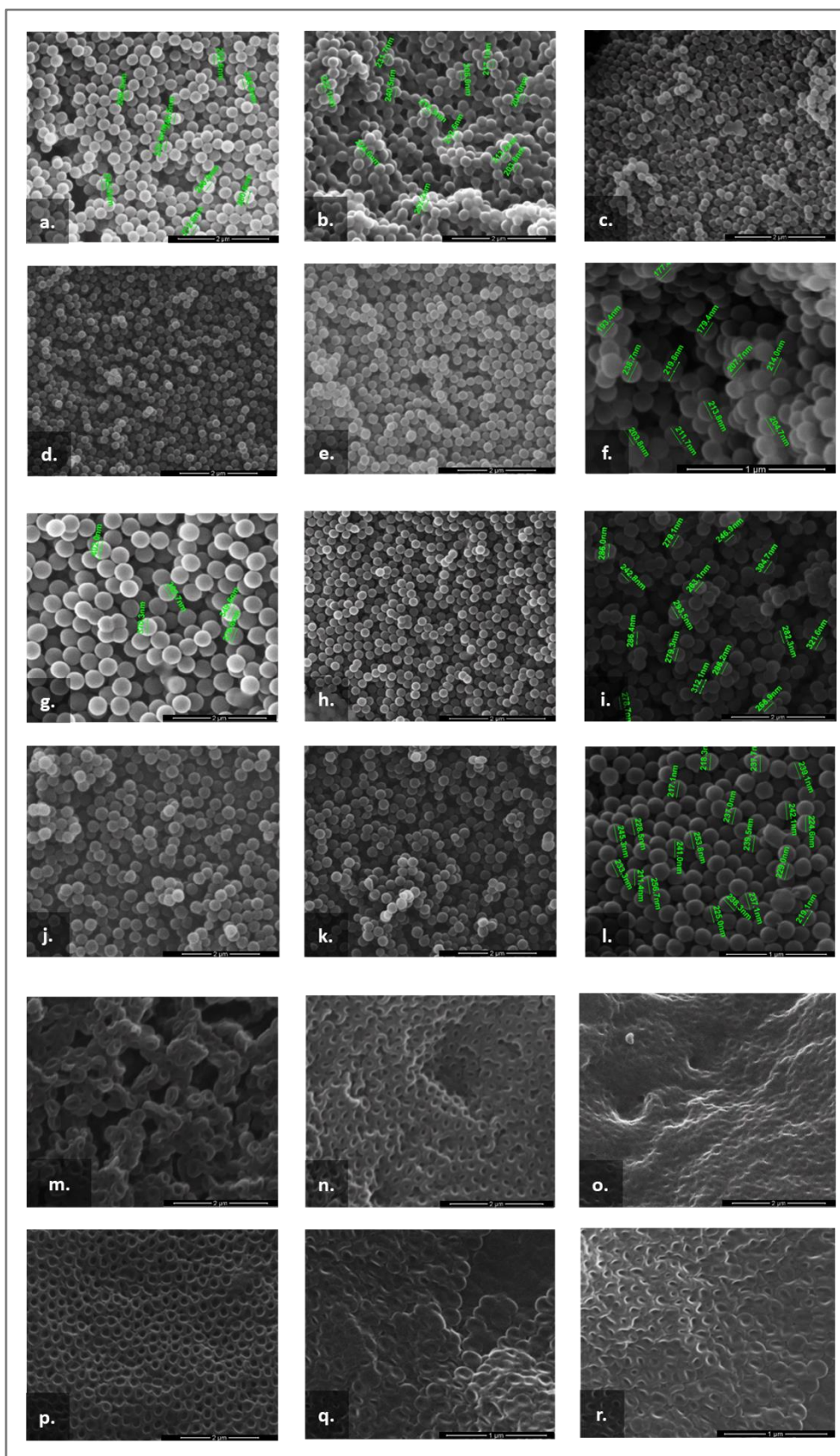


Figure 12. SEM pictures of polymeric nanocontainers at different synthesis steps. **(a-f)**. PMAA core spheres, **(g-i)**, Multisensitive Shell coated NCs (PMAA@P(MAA-co-MBA-co-EGDMA)) and (PMAA@P(MAA-co-MBA-co-NIPAM-co-EGDMA)), **(m-r)**. Hollow NCs P(MAA-co-MBA-co-EGDMA)) and (PMAA@P(MAA-co-MBA-co-NIPAM-co-EGDMA))

2.3.2.3. COOH Concentrations

Following SEM analysis, back-titration was performed on hollow NCs. Different COOH concentrations depending on the amount of polymerized MAA in the multisensitive layer are shown (Table 6).

Table 6. Back-titrated COOH entities in different hollow NCs samples

Hollow NCs	Amount of COOH entity
SS2026.D	28.85 (\pm 1.5) μ Mol/mg of NCs
SS2033.A	
SS2039	
SS2045	47.7 (\pm 2) μ Mol/mg of NCs
SS2058	
SS2061	
SS2063	
SS2065	

All samples synthesised with a ratio 1:1 PMAA NCs: MAA had higher COOH amount on the coating layer (47.7 (\pm 2) μ Mol/mg of NCs). Therefore, all layers synthesised afterwards followed the same PMAA NCs:MAA ratio in their composition.

2.3.3. Drug Loading

The calculated loading capacities (LC) and encapsulation efficiencies (EE) of the different loaded hollow PMAA nanocontainers (Table 7) showed loading capacities of less than 54% for all samples loaded with ratios 1:1, 1:2 and a COOH amount of $28.85 (\pm 1.5)$ μMol of COOH/mg of NCs. However, the samples with a higher COOH amount ($47.7 (\pm 2)$ μMol of COOH/mg of NCs) that were loaded in 1:2 and 1:4 ratios showed higher loading capacities reaching 63% and 69%, for DNR and cisplatin, respectively (Table 7).

Vincristine loading trials showed only one successful run -among the five runs- with only 29%, whereas all the results of the other 4 attempts had no positive results regardless of the loading method applied. On the other hand, loading attempts of colchicine in nanocontainers were ineffective and no positive loading capacities were recorded. Temozolomide loading trial with shaking and a 1:2 ratio was successful and showed a loading capacity and encapsulation efficiency of 27.3% and 96.5%.

Overall, the combination of the stirring method and 1:2 NCs/drug ration showed 6% to 30% higher drug loading capacity percentages than the combination of the shaking method and 1:1 or 1:2 NCs/drug ration in these hollow PMAA@P(MAA-co-MBA-co-NIPAM-co-EGDMA) NCs.

Table 7. Calculated loading capacities and encapsulation efficiencies of different hollow PMAA nanocarriers and the corresponding drugs.

Sample	NCs/Drug Ratio	Loading Method	Drug	LC (%)	EE (%)
SS2026D	1:1	Shaking	DNR	23.9	47.7
	1:1	Shaking	DNR	13.7	27.5
	1:1	Shaking	vincristine	29.5	58.9
SS2033A	1:1	Shaking	DNR	31.2	60.4
SS2042	1:2	Shaking	DNR	29	70
	1:2	Shaking	DNR	53.8	80.8
SS2058	1:2	Shaking	Cisplatin	34.9	50.6
SS2063	1:2	Shaking	DNR	19.5	29.3
		Stirring		43.4	66.1
	1:2	Shaking	Cisplatin	47.8	71.8
SS2061	1:4	Stirring	DNR	61.7	74.8
			Cisplatin	45	55.3
SS2065	1:4	Stirring	DNR	69.5	90.3
SS2078	1:2	Stirring	Cisplatin	60.2	89.5
SS2080	1:2	Stirring		63.06	93.8
SS2083	1:2	shaking	Vincristine	-	
SS2085	1:1			-	
SS2085	1:2	stirring	Vincristine	-	
SS2085		Stirring In H ₂ O	Vincristine	-	
SS2085		Stirring in acidic pH	Vincristine	-	
SS2085	1:2	Stirring in H ₂ O Stirring in PBS	Colchicine	-	
SS2085	1:2	shaking	Temozolomide	27.3	96.5

2.3.4. Drug Release

The DNR release experiments that were carried out under stirring had a maximum release of almost 3% after 72 hours at the different pH (4.6 and 7.4) and temperature (37°C and 40°C) conditions.

For this, the DNR release studies by dialysis bag and the results in pH 4.6 (Figure 13) showed a moderate release of 33.7% for the first 6 hours at 37°C. Then, the release kept increasing steadily, reaching a plateau of ~69% after 72 hours. On the contrary, at 40°C, there was a burst release of ~48% for the first 6 hours, i.e. 14% more than the release at 37°C at the same time point. After 48h, the release amount reached its highest value of 78.5% and remained steady with almost the same release percentage after 72h.

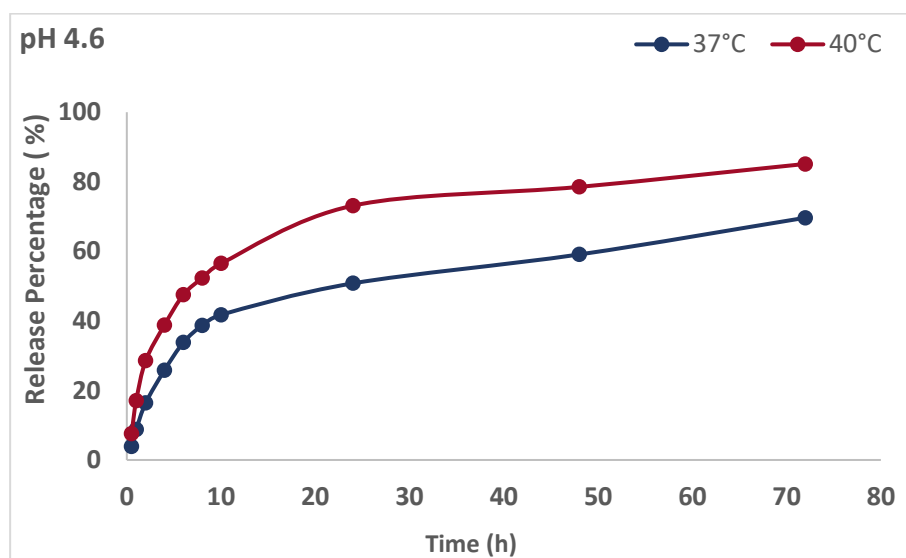


Figure 13. Release profile of DNR in pH 4.6 at 37°C and 40°C. duplicate experiments.

Results of the release in pH 7.4 (Figure 14) showed a moderate release for the first 6 hours at 37°C, reaching 27% then, the release amount reached ~52% at 72h. On the contrary, at 40°C ~38% of the drug was released at 6h, which was 11% more than the release amount in 37°C

after 6h and ~9% less than the release at 40°C in pH 4.6. After 24h, the release reached its highest value of 52% and 70% for 37°C and 40°C, respectively, and remained steady with the same release percentage after 72h.

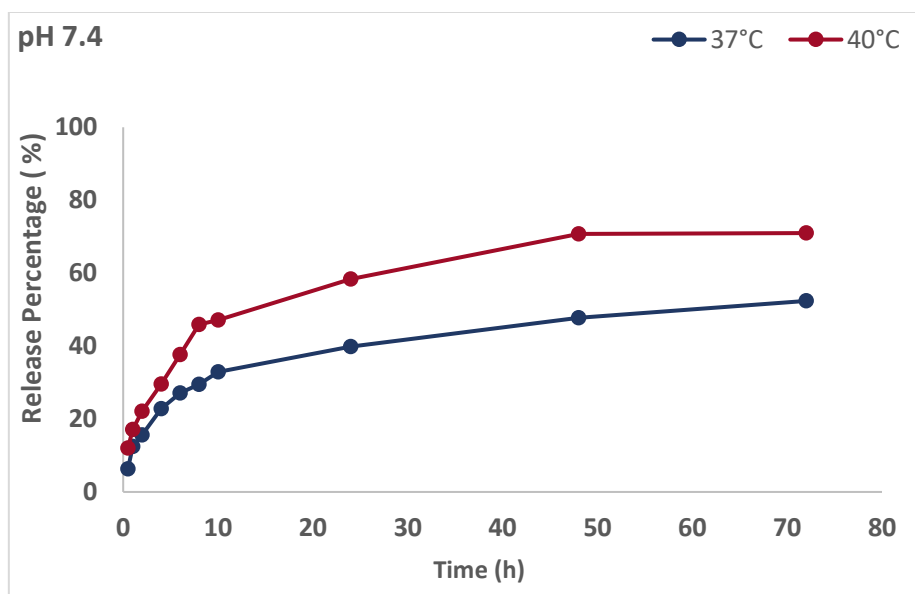


Figure 14. Release profile of DNR in pH 7.4 at 37°C and 40°C. duplicate experiments

The cisplatin release studies by stirring were in pH 4.6 (Figure 15) and showed fast release for the first 6 hours at 37°C, ranging from 26% to 21%. Then, the release kept increasing steadily, reaching a plateau of ~30% to 38% between 10h and 72h. On the contrary, at 40°C there was a burst release of ~41% for the first 6 hours, i.e., ~19% more than the release at 37°C at the same time point. The release kept increasing, forming a pattern of a steady plateau and reaching its highest value of 64% after 72h. Throughout the time points, the release of cisplatin at pH 4.6 at 40°C was 24% higher on average compared to the release at 37°C.

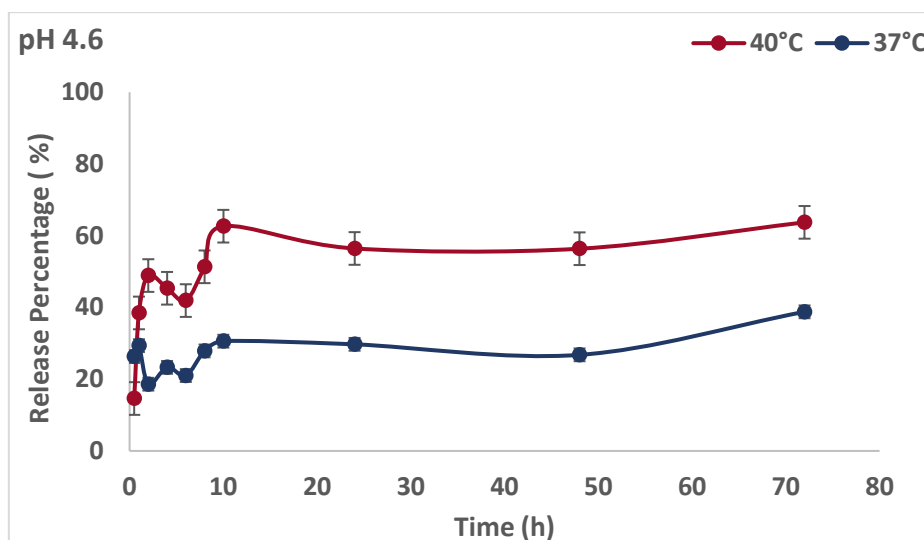


Figure 15. Release profile of cisplatin in pH 4.6 at 37°C and 40°C. Error bars based on \pm SEM of triplicate experiments.

In an environment with pH 6.8, the release of cisplatin at 37°C and 40°C (Figure 16) for the first 24h showed an increasing release from 8% to 37% for both temperatures. After 24h and up to 72h, the release at 40°C was ~12% higher than the release at 37°C. At 72h, the release reached 72% and 54% at 40°C and 37°C, respectively.

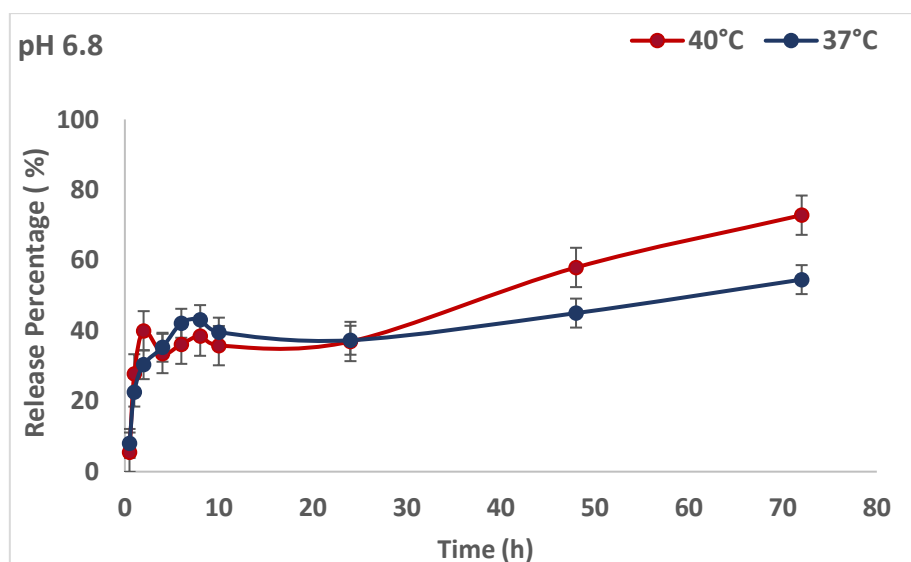


Figure 16. Release profile of cisplatin in pH 6.8 at 37°C and 40°C. Error bars based on \pm SEM of triplicate experiments.

Results of the cisplatin release in pH 7.4 (Figure 17) showed burst release for the first 6 hours at 37°C and 40°C, reaching 49%. Then, the release amount at 37°C decreased to ~31% at a 10h time point and retained the steady release plateau reaching 35% after 72h. On the contrary, at 40°C, the drug release increased and reached its highest value of ~57% at 6h. Then, the release decreased by 15% and remained steady up until 72h.

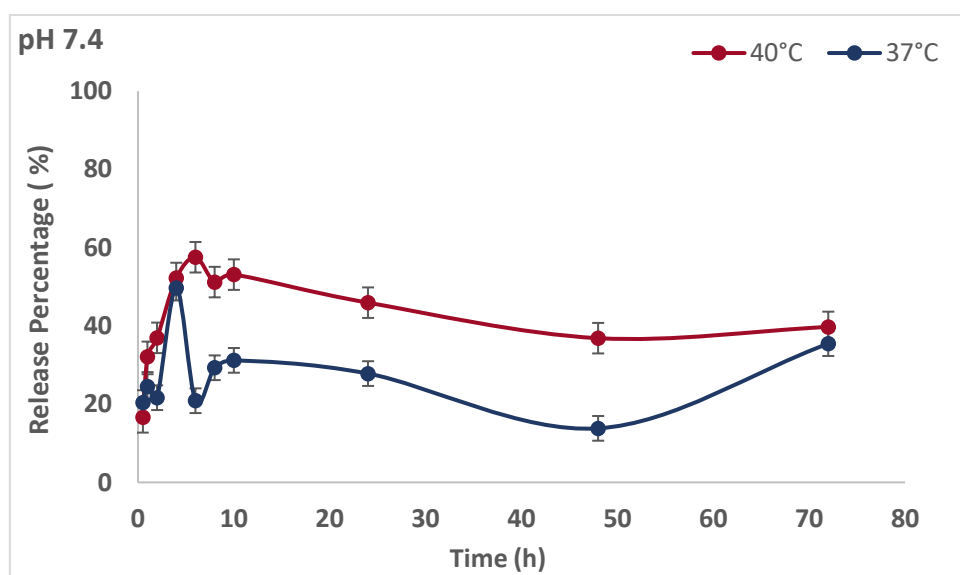









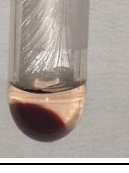


Figure 17. Release profile of cisplatin in pH 7.4 at 37°C and 40°C. Error bars based on \pm SEM of triplicate experiments.

2.3.5. Biocompatibility

The haemolysis assay results (Table 8) showed no visible haemolysis for all concentrations of NCs suspensions 100 μ g/ml, 50 μ g/ml, and 25 μ g/ml in tubes 3, 4, and 5, respectively, for both 2 hours and 24 hours incubation. The supernatant, which represents the NCs suspension where the RBCs were incubated in tubes 3, 4 and 5 for 2h was visibly clear and similar to the negative control results and contrary to the positive control. The supernatant in the tubes with

the RBCs incubated for 24h with the different NCs suspensions appeared slightly pinkish compared to the fully red positive control tube.

Table 8. Hemolysis assay results after 2 hours and 24 hours incubation.

Incubation time (h)	Tube 1 Positive control In H ₂ O	Tube 2 Negative control in PBS	Tube 3 100 µg/ml	Tube 4 50 µg/ml	Tube 5 25 µg/ml
2					
24					

Calculated haemolysis percentages of RBCs treated with 25, 50 and 100µg/ml for 2h and 24h incubation (Figure 18), showed low haemolysis percentages for 2h incubation all <4%, while the 24h incubation results showed slightly higher haemolysis percentage than the 2h incubation, but all <8%.

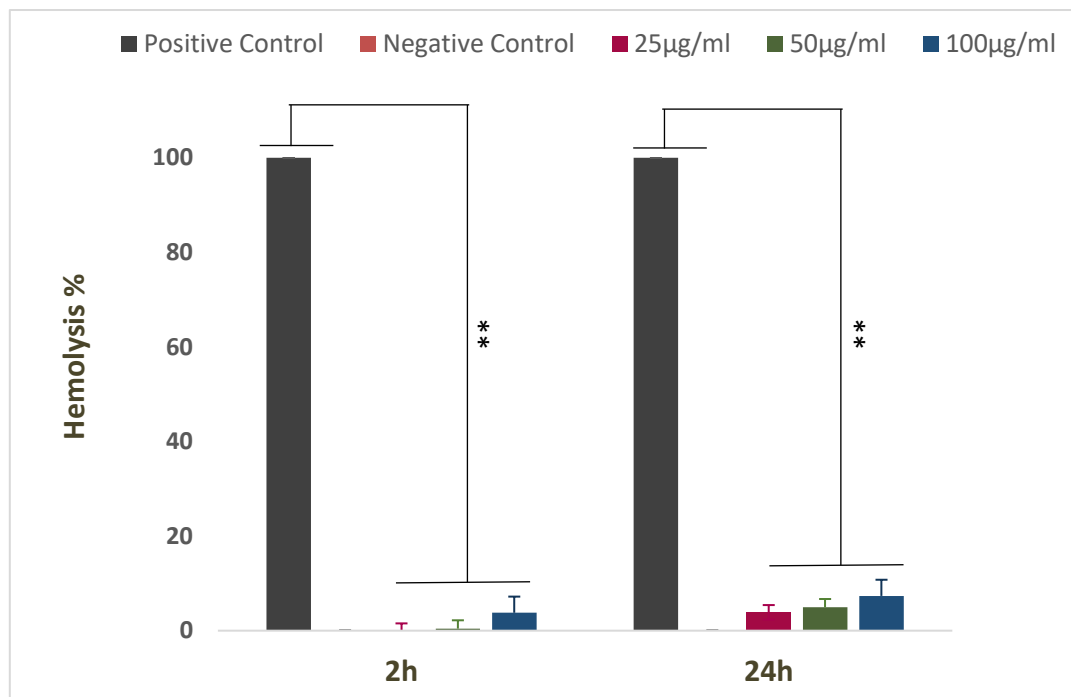


Figure 18. Haemolysis percentage of the RBCs treated with 25, 50, 100 µg/ml NCS suspensions for 2h and 24h. Error bars based on \pm SEM of triplicate experiments. **Two-way Anova test ($p \leq 0.01$)

Microscope pictures of the RBCs (Figure 19) that were fixed as described in first method in section (2.2.10.1) were not suitable for proper analysis due to the fixed sample's poor quality.

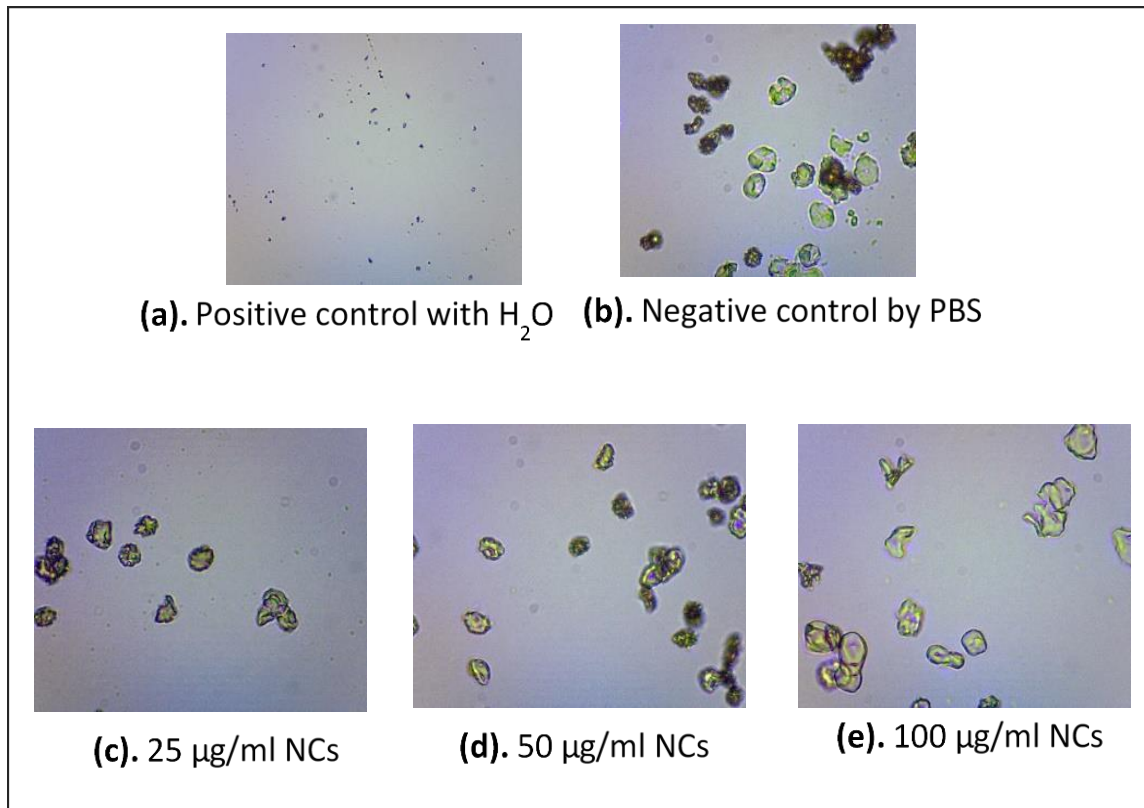


Figure 19. Optical microscopy images of the RBCs treated with different concentrations of NCs suspensions.

(a). Positive control, **(b).** Negative control, **(c).** RBCs treated with 25 µg/ml, **(d).** RBCs treated with 50 µg/ml, **(e).** RBCs treated with 100 µg/ml.

Microscope images of the incubated RBCs with the increasing concentration of NCs suspensions (Figure 20) and fixed by the second method described in section 2.2.10.1 showed non-haemolysed and normal RBCs (Figures 20c to 20e) similar to the RBCs in the negative control (Figure 20b) and in contrast to the positive control (Figure 20a) where RBCs appear haemolysed with shape alteration.

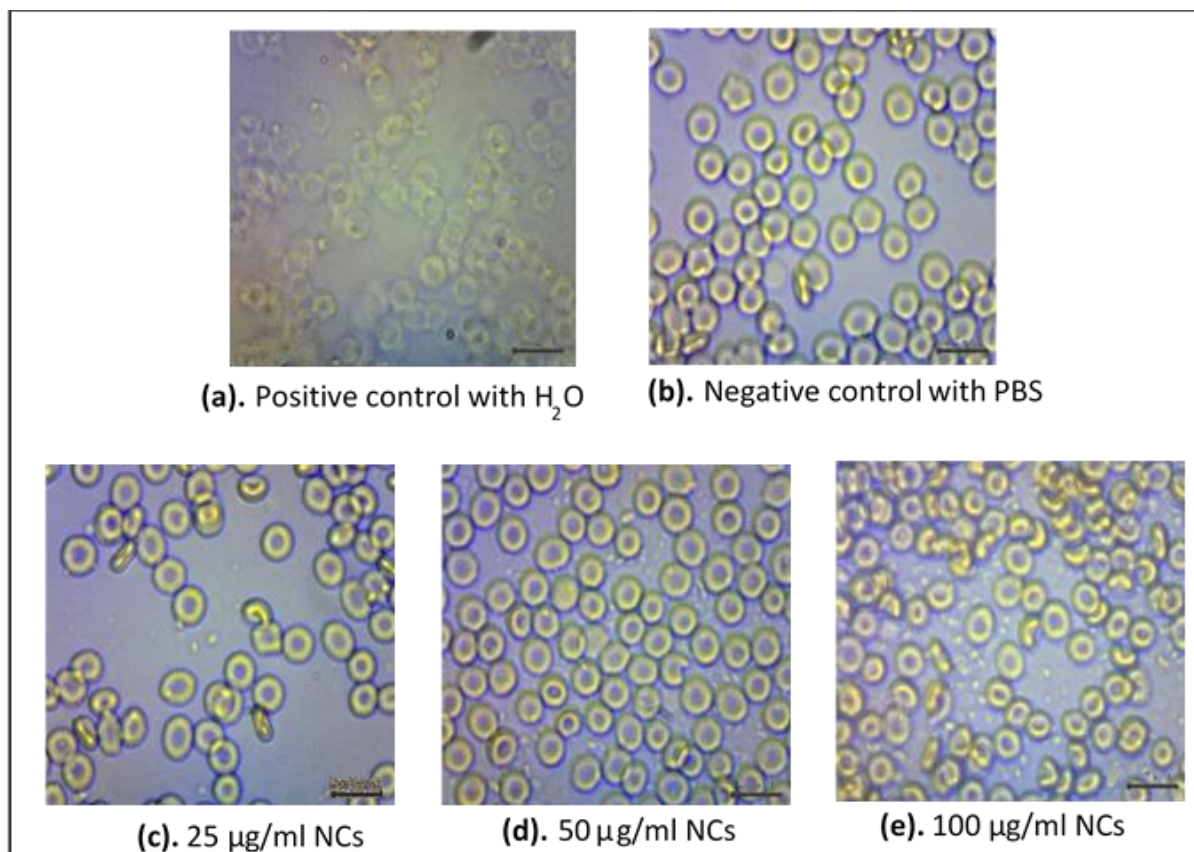


Figure 20. Optical microscopy images of RBCs after treatment with different concentration of NCs suspensions.

(a). Positive control, **(b).** Negative control, **(c).** RBCs treated with 25 µg/ml, **(d).** RBCs treated with 50 µg/ml, **(e).** RBCs treated with 100 µg/ml.

Scanning electron microscopy images of the RBCs incubated with the increasing concentration of NCs suspensions (Figure 21) showed non-haemolysed and normal RBCs (Figures 21c to 21e) similar to the RBCs in the negative control (Figure 21b). The RBCs appeared healthy, with a concave shape and absence of any overall shape alteration. In contrast, RBCs in the positive control (Figure 21a) appeared flattened and haemolysed with major shape alterations.

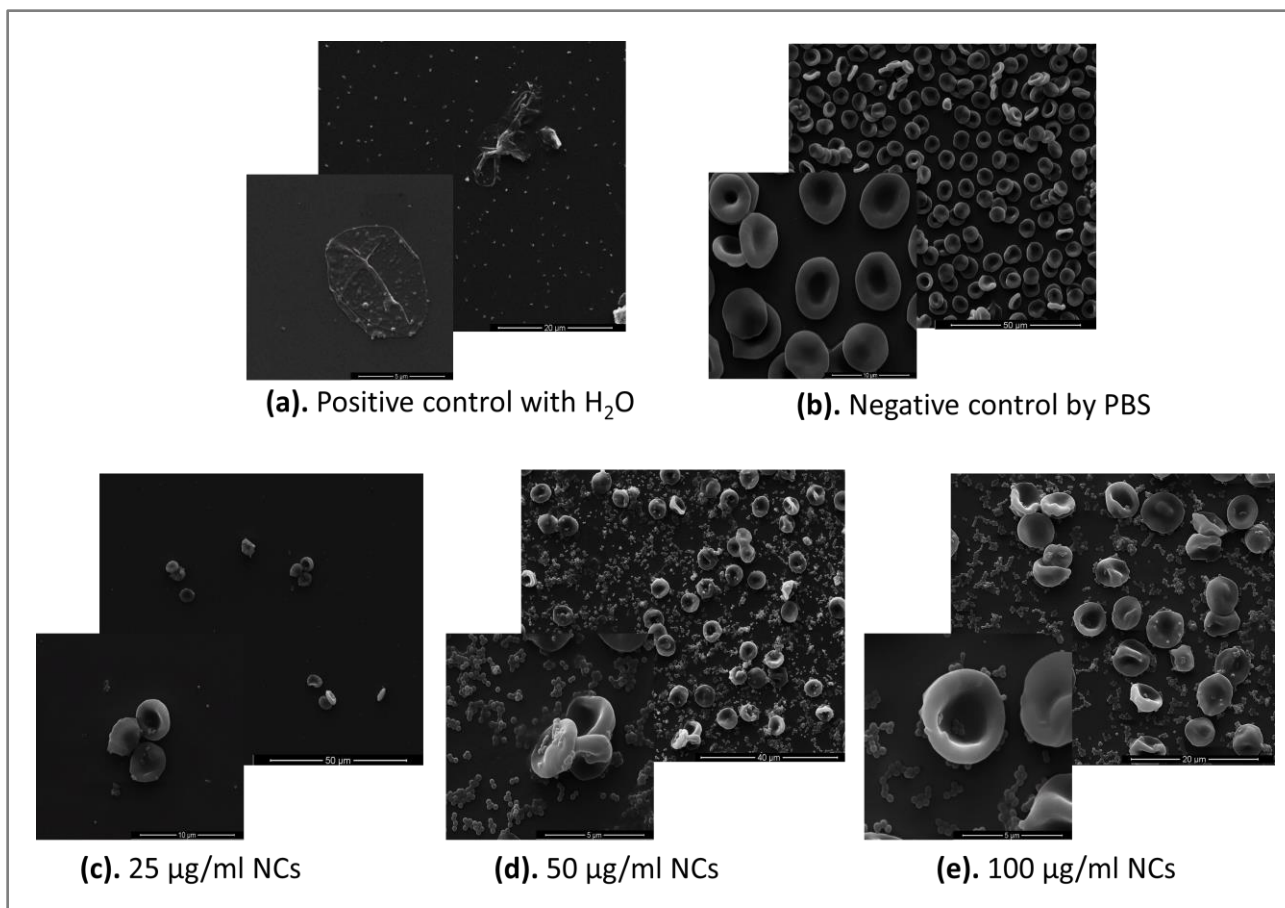


Figure 21. Scanning electron microscopy images of the RBCs after treatment with different concentration of NCs suspensions.

(a). Positive control, **(b).** Negative control, **(c).** RBCs treated with 25 µg/ml, **(d).** RBCs treated with 50 µg/ml, **(e).** RBCs treated with 100 µg/ml.

2.4. Discussion

Structural characterization of the silica nanospheres (template core) by FTIR, showed characteristic peaks attributed to Si-O-Si vibration. The spectra of silica nanospheres coated with the MPS layer showed a new characteristic peak at 3062cm^{-1} which was attributed to the free vinyl groups (carbon-carbon double bonds) of MPS, confirming the successful coating of nanocarriers with the MPS layer. The multisensitive layer coating P(MAA-co-MBA-co-EGDMA) was confirmed by the appearance of the characteristic peaks 1719cm^{-1} and 1082cm^{-1} corresponding to the carboxylic group of MAA and to C-O-C bond vibration of EGDMA, respectively. The disappearance of the silica (Si-O-Si) bond vibration indicated the removal of the silica core. In relatively comparable polymeric nanoparticles with a silica core, the peak of Si-o-Si bond vibration disappeared after silica core removal and obtention of hollow nanoparticles (Metaxa, Efthimiadou, Boukos, & Kordas, 2012). The decrease rather than the disappearance of the same peak in our results could explain the incomplete and unachieved silica-core removal in our results.

The DLS measurement throughout the synthesis steps of the silica nanocontainers showed increasing hydrodynamic sizes by around 100nm (± 40) after every coating, indicating the successful layering by MPS and then by MAA and EGDMA. The negative zeta potential of the nanocontainers at all synthesis steps was attributed to the deprotonated carboxylic groups (COO^-) at the surface of the NCs. Structural characterisation results of nanoparticles with a similar silica core and polymeric layer -by DLS and FTIR- were reported by Metaxa and colleagues (2012) to have comparable structural characteristics, including the distinctive peaks of the functional groups and the overall negative charge (Metaxa, Efthimiadou, Boukos, & Kordas, 2012).

The SEM analysis of silica core spheres showed spherical nanocarriers MPS coating and multisensitive layer coating were confirmed by the increase in the size by 100nm (± 20). Analysis of the hollow silica nanocontainers after several treatments with HF at different conditions resulted in spherical and non-hollow NCs, which signified that the total silica core-removal was not achieved. The results contradict the claims of several studies regarding the effective silica core removal by HF etching (Metaxa, Efthimiadou, Boukos, & Kordas, 2012); Kosari, Borgna, & Zeng, 2020; Zhang et al., 2015).

We managed to synthesize silica core spheres and coat them with MPS and multisensitive layers. Despite all attempts to remove the silica core at different conditions, hollow shaped nanocarriers were not obtained. This could be due to the condensation level of the silica core upon synthesis and the inability of the $\text{NH}_4\text{F}/\text{HF}$ buffer to etch the core of silica. Upon exposure to an etching solution, highly condensed silica is harder to etch compared to a less condensed silica core (Grau-Carbonell et al., 2021). Also, silica is more soluble in an environment with a pH higher than water (7.4) (Grau-Carbonell et al., 2021). These suggested that less condensation of the silica core and adjustment of the pH of the etching solution to become more basic could be a potential solution for a successful etching. For this reason, we switched the core material from silica to MAA, and MAA based hollow nanocarriers were synthesised instead. The reason behind this swap is that MAA is soluble in water, which could result in easier and simple core removal. MAA is a monomer known universally for its water solubility and ethanol miscibility and hydrolysis of the PMAA polymer in ethanol and water (Nishchaya, Rai, & Bansode, 2023).

2.4.1. Polymeric nanoparticles

The FTIR analysis of the PMAA NCs showed characteristic peaks at 1697 cm^{-1} and 1172 cm^{-1} corresponding to the MAA's C=O carboxylic group and C–O bending, respectively. The appearance of the new peaks at 1386 and 1532 cm^{-1} corresponded to the C–O–C of PEGDMA and the N–H amide bending of the MBA crosslinker, respectively (Toniolo et al., 2018; Socrates, 2001). Nanocontainers with NIPAM included in their coating layer had a characteristic peak at 1702 cm^{-1} corresponding to the amide band from the PNIPAM. Since the C=O stretching of the COOH from the PMAA and the amide band of the NIPAM overlap, there was an increase in the 1702 cm^{-1} peak intensity in the presence of NIPAM compared to its absence (Toniolo et al., 2018). After the PMAA core removal, there was a decrease in the intensity of the characteristic peak of the carboxylic group of the PMAA, resulting in hollow P(MAA-co-MBA-co-EGDMA) and hollow P(MAA-co-MBA-co-NIPAM-co-EGDMA) NCs. Yet, in the hollow NCs that included NIPAM in their multigeniture layer, there was also the appearance of the 1633 cm^{-1} peak, which corresponded to the NIPAM's amide and fell in the range of 1600 to 1800 cm^{-1} (Socrates, 2001).

The increase in the hydrodynamic size measured by DLS between the PMAA core spheres and the multisensitive layer coated nanocontainers by around 140 nm to $200 (\pm 25)$ indicated the successful coating by MAA, EGDMA and NIPAM. The increase of the hydrodynamic size after the core removal-despite absence of additional coating- was attributed to the swelling of the hollow nanocarriers due to the repulsive inter- and intra-molecular interactions between the spheres and the water molecules where they were dispersed. The negative zeta potential of the nanocontainers at all synthesis steps was attributed to the negatively charged deprotonated carboxylic groups (COO^-) at the surface of the NCs. Water is known to have a

pH of 7.4, and the carboxylic groups in the methacrylic acid have a pKa of 4.6 to 4.7. Therefore, in an environment with a pH higher than the pKa of methacrylic acid, the COOH get deprotonated (COO⁻) (Farooqi, Khan, Shah, & Siddiq, 2017). Also, high zeta potential values of around ± 30 mV are crucial for the aggregation prevention and stability of the nanoparticles (Bhattacharjee, 2016; Crucho & Barros, 2017). Our nanocontainers had a high negative zeta potential of around -40mV. This value line in the range of high zeta potential values that ensure the stability of the NCs' colloidal suspension and prevention of their aggregation as a result of electrostatic repulsive forces (Bhattacharjee, 2016; Crucho & Barros, 2017).

Morphological characterisation of PMAA nanocontainers at the three synthesis steps confirmed the multisensitive-layer coating by the noticeable increase in size by 150nm (± 20) compared to the core PMAA spheres. The PMAA core removal was confirmed by SEM analysis which showed hollow NCs with a cavity for all samples that were treated for 48h in 1:1 water/Ethanol. This indicated that the 1:1 water/ethanol solution with 48h stirring time were the most suitable combination for the total hydrolysis and dissociation of the MAA polymer core used in these nanoparticles. After the core removal, the nanocontainers were left with a large cavity where the drug could be encapsulated. Therefore, the cavity is crucial in the hollow morphology of the NCs as it is where the drug is carried, and it contributes to the increased loading capacity (Zhao et al., 2021).

The loading of DNR, cisplatin, vincristine, colchicine, and temozolomide revealed varying loading capacities and encapsulation efficiencies. The loading capacity of the NCs depends on their ability to form electrostatic and hydrogen-bonding interactions with the drug, i.e., binding of the negative carboxylic group of the MAA co-polymer either inside or outside of the nanocarrier with the amine group and OH groups of the drug. Daunorubicin and cisplatin

showed higher loading capacities compared to the lower loading capacity of temozolomide and low or no loading of vincristine and colchicine. This was attributable to the higher number of free and reactive NH_2 and OH groups in DNR and cisplatin compared to temozolomide, vincristine, and colchicine and their interaction with the COOH groups in the cavity and on the surface of the hollow nanocarriers. These results built up on reported moderate to high loading capacities (30% to 90%) of DNR, cisplatin and temozolomide in polymeric nanoparticles (Chen et al., 2015; Sultan et al., 2022; Fu et al., 2019; Zahariev, Draganova, Zagorchev, & Pilicheva, 2023). Yet, the negative loading capacity of vincristine and colchicine did not align with the reported average 10% to 40% loading capacity in folic acid-chitosan polymeric nanocontainers (Kumar, Salar, Prasad, & Ranjan, 2018; Salar & Kumar, 2016).

Therefore, the combination of higher COOH entities in the hollow nanocontainer and higher drug to NCs ratios used for loading resulted in higher interaction between the drug and the nanocarriers, hence, a more loaded amount of the drug. This statement lined with the results of the work done by She et al., 2015, where nanoparticles functionalised with COOH and NH_2 resulted in higher drug loading capacities compared to other functionalization. The COOH and NH_2 had an improved electrostatic interaction with the hydrophobic (5-FU) drug used (She et al., 2015).

The nanocarriers evaluated in this project showed the ability and efficiency to encapsulate several drugs separately, including gold standard DNR, cisplatin, and temozolomide. Thus far, recently published research has not reported similar various drug encapsulations for the same nanosystem; rather, testing and adapting their nanosystem with merely one or co-loaded first line chemotherapy drug (Ulbrich et al., 2016; Xu et al., 2015)

The DNR and cisplatin release studies were carried out in different pH and temperature conditions to test the sensitivities of the nanocarriers. The *in vitro* drug release studies were carried out by stirring for cisplatin loaded in hollow P(MAA-co-MBA-co-NIPAM-co-EGDMA) NCs. DNR drug release studies were carried out alternatively by dialysis bag to overcome the insignificance of the first release results obtained by stirring, and hollow P(MAA-co-MBA-co-EGDMA) NCs were used. The rapid release of DNR and cisplatin after the first 4 to 6h, or so-called burst release, under acidic pH 4.6 and 40°C temperature was attributed to the repulsive interactions between protonated COOH of the NCs and the encapsulated drug. In pH 4.6, the carboxylic group of the PMAA co-polymers are fully protonated and unable to interact with the amine group of the DNR and cisplatin (Sims, He, Koo, & Benoit, 2020, Toniolo et al., 2018).

The EGDMA and NIPAM co-polymer exhibit thermosensitive behaviour and have a lower critical solution temperature (LCST) (Luzon et al., 2010; Koda, Lutz, 2008, Takahashi, Sasaki & Akiyoshi, 2019). Above this temperature, the molecular interactions and hydrogen bonding of the EGDMA and NIPAM co-polymers get altered when in contact with the outside environment (drug and buffer) (Ghaeini-Hesaroeiye et al., 2020; Toniolo et al., 2018). This phenomenon explained the higher release percentage at 40°C compared to release at 37°C throughout the time points. After 72h, the release of DNR and cisplatin in pH 4.6 at 40°C remained higher than the release at 37°C by around 20% and 25%, respectively.

At pH 7.4, the release percentage at 40°C was higher than the release at 37°C by around 10 to 20% throughout the 72h for both DNR and cisplatin. Yet, it was also lower than the release percentage at acidic pH and higher temperatures. This was attributed to the fully deprotonated carboxylic group of the PMAA co-polymer at pH 7.4, which preserved the ability of the NCs to retain the drug and form high electrostatic interactions with the amine group of

the DNR and the cisplatin, resulting in lower release profile. Cisplatin loaded nanocontainers showed an intermediate percentage release at pH 6.8 compared to the acidic pH 4.6 and basic pH 7.4 environments for both 37°C and 40°C. This was attributable to the partial deprotonation of the carboxylic group of the PMAA co-polymer; hence, intermediate drug release. Drug release from a comparable nanosystem with a pH sensitive shell made with MAA showed a relatively similar intermediate release profile of encapsulated DNR at pH 6 compared to pH 4 and pH 7.4 (Toniolo et al., 2018). Another instance comparable to our nanoparticles was PLGA (pH sensitive core) hybrid polymeric nanoparticles decorated with acidity-triggered rational membrane (ATRAM) peptide and loaded with doxorubicin. In accordance with our results, doxorubicin release was higher in acidic pH 5 environment (79%) compared to the release at pH 5.8 (45%) and 6.5 (<20%) (Palanikumar et al., 2020).

The drug release from the hollow P(MAA-co-MBA-co-NIPAM-co-EGDMA) NCs showed a 25% higher release in acidic pH and high temperature compared to the 20% difference in drug release from hollow P(MAA-co-MBA-co-EGDMA) NCs at the same condition. Moreover, the highest release percentage reached by hollow P(MAA-co-MBA-co-NIPAM-co-EGDMA) NCs is lower than the hollow P(MAA-co-MBA-co-EGDMA) NCs at different conditions. Both aforementioned results were attributed to the fact that EGDMA has an LCST of 25°C while the LCST of NIPAM is about 32°C. In other words, Thermo-responsiveness was higher in nanocarriers with both EGDMA and NIPAM in their pH-thermosensitive layer compared to the nanocarriers with only EGDMA. This supports the fact that NIPAM has a higher LCST (32°C) which above it, the phase separation takes place resulting in the co-polymer dissociation together with its intramolecular hydrogen bonding.

Overall, the drug release in pH 4.6 and 6.8 at 40°C was higher than the release at pH 7.4 at the same temperature. The data contributed to the understanding of the ability of pH-thermoresponsive nanocarriers to release and deliver the drug sustainably under an acidic environment and high temperature stimuli, which are analogous to the characteristics of the microenvironment of tumours (Bobde, Biswas, & Ghosh, 2020; Qi et al., 2016; Xu et al., 2015). This data is also built on the ability of this nanosystem to enhance the systemic delivery and efficacy of the first line chemotherapy drugs to the tumour (Qi et al., 2016; Maritim et al., 2017; Zou et al., 2018).

Biocompatibility of the synthesised hollow polymeric nanocontainers was confirmed by the haemolysis assay in which all different concentrations of NCs used showed haemolysis percentages lower than 8%. The optical and scanning electron microscopy analysis of the RBCs treated by plain nanocontainers showed no significant structural alterations of the RBCs in comparison to control samples for the different increasing concentrations of the used NCs. The different concentrations of plain hollow nanocontainers showed no negative effect on the morphology of the RBCs. The RBCs appeared in a healthy concave shape similar to the negative control and in contrast to the haemolysed and morphologically altered positive control. These data findings provide clear evidence of the hemocompatibility of the synthesised polymeric nanocontainers. These results build on existing findings regarding the biocompatibility of polymeric based nanocontainers which have gained growing interest over the years (Calzoni et al., 2019). Even though the polymeric nanocontainers in this project were synthesised with synthetic polymers (PMAA, PNIPAM, and PEGDMA), the biocompatibility characteristic of the nanocontainers was preserved, analogous to reported nanosystems made with other biocompatible synthetic polymers including lactide, poly-glutamic acid, and polyethylene glycol (Calzoni et al., 2019; Ghaeini-Hesaroeiye et al., 2020; Ulbrich et al., 2016)

2.5. Conclusion

In conclusion, the developed pH-thermosensitive hollow nanocontainers in this project showed small sizes of 383nm (± 35) and negative zeta potentials of -40mV (± 1). The hollow polymeric nanoparticles had a well-defined spherical shape with a clear cavity that successfully encapsulated three different first line chemotherapy drugs. The nanosystem exhibited responsiveness to pH and temperature in acidic and high temperature environments, with a sustained drug release profile for up to 72h. The hollow NCs were proven to be highly biocompatible when incubated with red blood cell samples. The developed hollow polymeric P(MAA-co-MBA-co-NIPAM-co-EGDMA) nanocontainers represent a good and promising platform for the encapsulation and release of several chemotherapy drugs for cancer treatment by stimuli-responsiveness targeting, passive targeting or further decoration with targeting agents for active targeting.

CHAPTER 3

3. RHABDOMYOSARCOMA

3.1. Introduction

Rhabdomyosarcoma (RMS) is one of the rarest types of pediatric tumours, yet it is the most common soft tissue cancer in children, and it accounts for 4.5% of all pediatric malignancies (Martin-Giacalone, Weinstein, Plon, & Lupo, 2021). Rather rare in adults, head and neck rhabdomyosarcoma accounts for about 30% to 40% of RMS cases in children (Dasgupta, Fuchs, & Rodeberg, 2016; Chen, Ricciotti, Futran, & Oda, 2016). Survival rates are mostly associated with tumour location and histological type. Histologically, there are four main types of rhabdomyosarcomas including embryonal (ERMS), alveolar (ARMS), spindle cell/sclerosing, and pleomorphic (Chen, Ricciotti, Futran, & Oda, 2016). The embryonal type appears mainly in the head and neck area and genital organs, but it can also appear anywhere in the body. The alveolar type appears mostly on the limbs, thorax, abdomen, or genital area. The spindle cell/sclerosing type, which arises mostly in the paratesticular area, can also arise in the trunk area. Pleomorphic type of RMS arises in the large muscles and lower parts of the limbs and trunk areas, and it is the least common type of pediatric RMS (Martin-Giacalone, Weinstein, Plon, & Lupo, 2021; Rudzinski et al., 2015). Among all four histological subtypes (Figure 22), the most frequently diagnosed subtypes in children are the embryonal type, with 70% of RMS cases and alveolar types, with 20% of RMS cases, and ERMS being the subtype with the more favourable prognosis (Chen, Ricciotti, Futran, & Oda, 2016; Rhee et al., 2020).

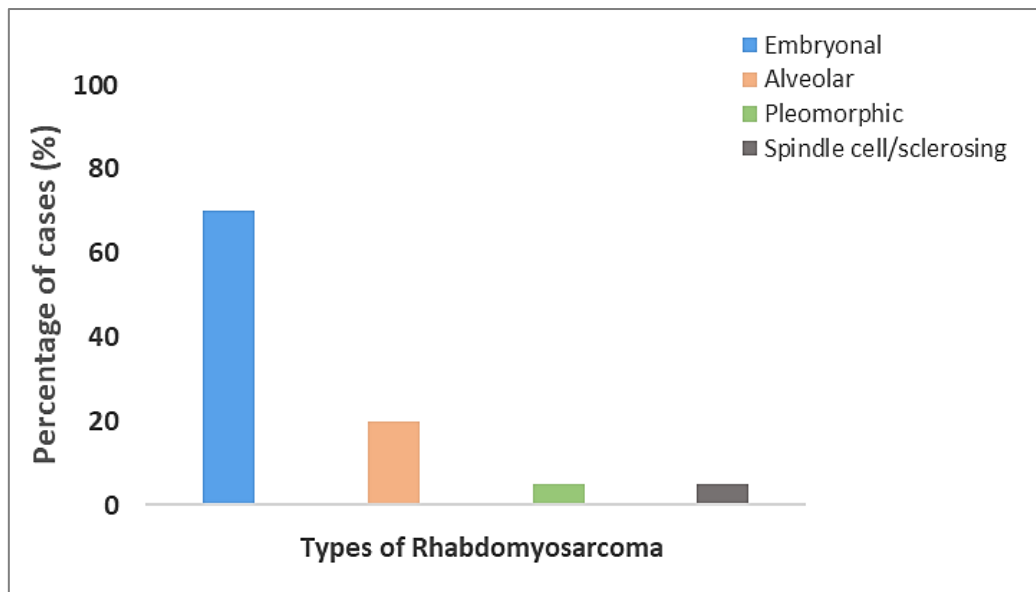


Figure 22. Percentages cases of the four types of rhabdomyosarcomas: embryonal, alveolar, pleomorphic, and spindle cell/sclerosing (Chen, Ricciotti, Futran, & Oda, 2016; Martin-Giacalone, Weinstein, Plon, & Lupo, 2021; Rhee et al., 2020; Rudzinski et al., 2015).

As a sarcoma of the skeletal muscles, RMS originates from a primitive mesenchymal cell, and it develops in muscle progenitor cells which are also known as myogenic progenitors. In the head and neck RMS, muscles have a different embryonic origin than trunk and limb muscles and are derived from cranial mesoderm and brachial arches (Drummond et al., 2018). The primary anatomic sites of the head and neck rhabdomyosarcoma comprise parameningeal, orbital, and non-parameningeal (Figure 23). The parameningeal site includes the nasopharynx, the nasal cavity, the paranasal sinuses, the middle ear, and the area behind the eye also known as the infratemporal and pterygopalatine fossa. The orbital region mainly includes the eyes and the area separated by the nasal cavity and paranasal sinuses. The non-parameningeal includes the rest of the areas in the head except for the parameningeal, and the orbital areas (Casey & Wolden, 2018).

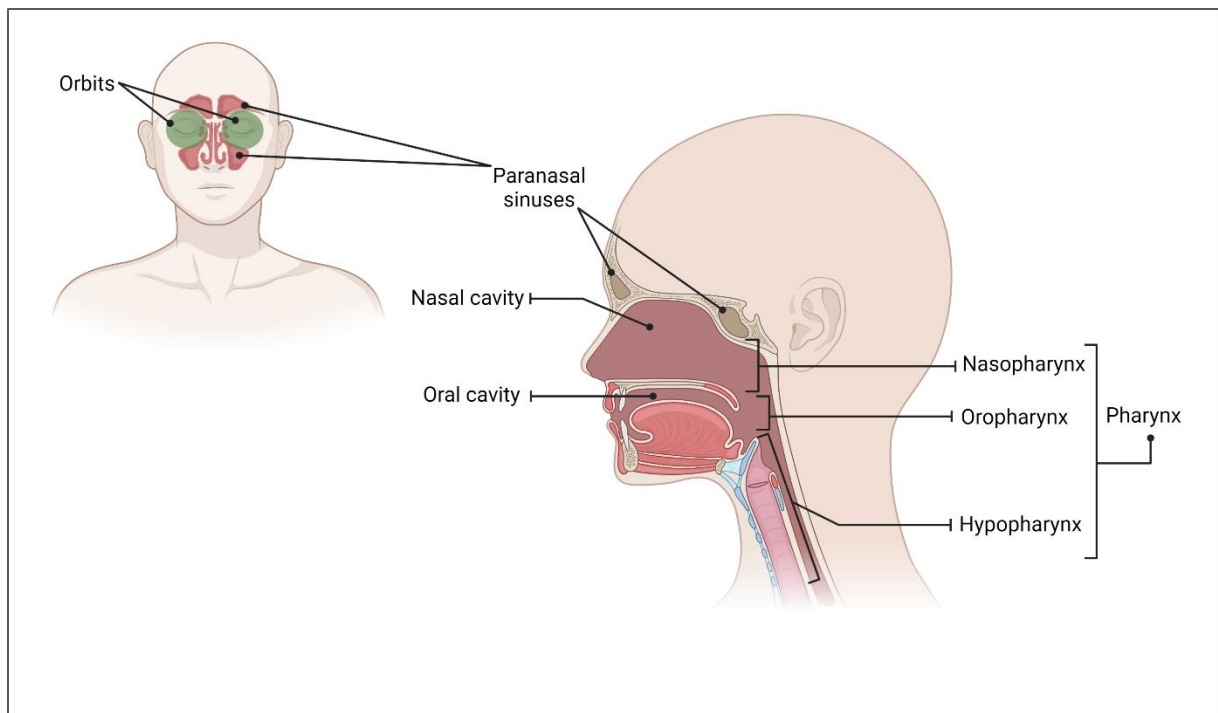


Figure 23. Anatomy of the parameningeal, orbital, non-parameningeal sites in the head.

Created in BioRender.com

On the molecular level, myogenic regulatory factors (Mrfs) that play a crucial role in myogenesis in head and neck RMS are directed by a combination of transcription factors including LHX2, TBX1 and PITX2, unlike the limbs and trunk muscles, where the Mrfs are regulated by *PAX3*. Yet, the precise and defined contribution of these different transcription and regulatory factors to RMS tumourigenesis remains unclear (Drummond et al., 2018). Several genetic alterations can be associated with embryonal and alveolar types of RMS and the presence and absence of what is known as oncogenic fusion proteins outperform the histological classification in reflecting the biological and clinical differences between these two types.

On the one hand, a loss of heterozygosity on the short arm of chromosome 11(11p15.5), encoding for IGF II can be correlated with embryonal RMS (Casey & Wolden, 2018; Drummond et al., 2018). Further crucial regions with high gain frequency include the long arm of

chromosome 12 (12q13.3–q14.1) and the short arm of chromosome 8 (8p11.2–11.2) (Liu et al., 2014). The aforementioned regions comprise several genes, including *SARNP*, *GLI1*, *OS9*, *CDK4*, *GEFT*, *PIP5K2C*, and *CYP27B1*. These genes are part of the regulatory network, and they engage in crucial regulatory and signalling pathways -including the sonic hedgehog (SHH) pathway- by the transcriptional or translational modulation of cell growth and metabolism (Gallego Melcón & Sánchez, 2007; Sun et al., 2015).

On the other hand, the alveolar RMS can be associated with *PAX/FKHR* translocation between chromosome 2;13 more commonly than between chromosomes 1;13. There are fusion positive (FP-RMS) and fusion negative (FN-RMS) types of RMS. While FN-RMS does not reflect any genes and chromosomal fusions, the most common translocation in fusion positive RMS mainly arises from interactions between the *PAX3* gene on chromosome 2 and the *FOXO1* gene on chromosome 13 (Laubscher et al., 2021; Rudzinski et al., 2015).

Mammalian SWI/SNF (mSWI/SNF) complexes are multiprotein complexes known as ATP-dependent enzymes that remodulate chromatin conformation and alter the location of the nucleosome along the DNA. The mSWI/SNF facilitate a range of biomolecular processes including transcription, splicing, DNA recombination, and DNA repair. These multiprotein complexes are mutated in 20% of adult cancers; hence, they also afford tumour suppressor function. However, pediatric cancers often depend on the activity of the mSWI/SNF complexes, which direct their oncogenic gene expression programs and maintain their proliferative state, particularly in fusion driven RMS (Laubscher et al., 2021). The BRG1-associated factor (BAF) and the poly-bromo BRG1-associated factor (PBAF) are two major complexes in the mSWI/SNF multiprotein, and all complexes contain either of the catalytic ATPase subunits, BRG1 (encoded by *SMARCA4*) or BRM (encoded by *SMARCA2*). It was found

that the ARID1A subunit of BAF was overexpressed in both fusion negative and fusion positive RMS tissue in contrast to its lower expression muscle tissue (Laubscher et al., 2021). Conversely, AIRID1B showed low expression in RMS tissue and higher expression in healthy muscle tissue. Also, BRG1 catalytic subunit was found to be overexpressed in RMS in contrast to the other catalytic subunit BRM that showed lower expression in RMS cells. This signifies that rhabdomyosarcoma is among the cancers that are highly BRG1 dependent, as the BRG1 plays a key role in the activation of muscle gene expression in the myoblast differentiation at preliminary stages (Albini et al., 2015). Accordingly, the BRM subunit plays a role at later myogenic differentiation stages by targeting mainly Cyclin-D1 and regulates cell cycle arrest to assure proper muscle proliferation (Albini et al., 2015). Impairment in the BRG1 and BRM functions balance results in altered muscle cell differentiation and, therefore, proliferation of RMS cancer cells (Laubscher et al., 2021).

Soft tissue sarcomas usually metastasise to the lungs, liver, and bone. However, in rare cases reported around the globe -around 16 cases-, pediatric rhabdomyosarcoma of the head can metastasise to the brain and lead to death within one month to a year post diagnosis, regardless of all attempted therapies (Gusho, Blank, & Batus, 2021). Data about these cases are rare, yet in a single institution experience, it has previously been reported that the involvement of CNS in pediatric rhabdomyosarcoma was recorded in 7 out of 59 patients (11.9%). The progression of the malignancy was extremely rapid in these cases, and the median survival rates were as low as 14 days (Moreira, Macy, Cost, Greffe, & Garrington, 2019).

Pediatric rhabdomyosarcomas, particularly ERMS, share several similarities with medulloblastoma - the most common aggressive pediatric brain tumour and one of the most

studied childhood cancers- including the altered SHH (Azatyan et al., 2019; Ngum et al., 2022). One of the major pediatric rhabdomyosarcoma cell lines was even originally used as a medulloblastoma, and it was until later on shown through cytogenetics and molecular biology analyses that it is actually a rhabdomyosarcoma (Hinson et al., 2013; Ngum et al., 2022).

The SHH pathway, a crucial pathway in vertebrates' embryonic development, is hyperactivated in several cancers, including basal cell nevus syndrome, also known as Gorlin syndrome, sporadic basal cell carcinoma, meningiomas, and medulloblastomas. Its aberrant activation is also implicated in rhabdomyosarcoma. A small molecule also known as Rita activates *p53*, subsequently downregulating SHH signalling in human medulloblastoma and rhabdomyosarcoma effectively through a reactive oxygen species (ROS) independent activation of the MAP kinase c-Jun N-terminal kinase (JNK) and regardless of *p53*. Another major signalling pathway in both tumour and normal development is the hedgehog- glioma-associated oncogene (HH-GLI) pathway in which the *GLI1* acts as an activator of the HH pathway by amplifying its signal (Azatyan et al., 2019).

Another pathway that is mutated in ERMS is the RAS pathway. Signals from the extracellular environment are transduced by the RAS pathway to the cell nucleus, where certain genes are activated. For this, RAS pathway and its corresponding proteins play a crucial role in modulating cell growth, proliferation, and migration. The most mutated genes in ERMS from the RAS family are *NRAS*, *KRAS*, and *HRAS*, which are highly related to ERMS development (Sun et al., 2015). It was reported that the majority of ERMS expressed RAS pathway activation either by point mutations in one of the aforementioned RAS members or by homozygous deletion of *NF1* (Sun et al., 2015). Regardless of notable genetic and molecular heterogeneity, 93% of RMS tumours exhibit alterations in the receptor tyrosine kinase/RAS/ PIK3CA axis. It could occur via two alternative mechanisms: rearrangement of a *PAX* gene and accumulation

of mutations that were downstream targets of the PAX fusion protein (Sun et al., 2015). Due to the involvement of the *PAX* gene in almost all altered aforementioned pathways, the presence or absence of a *PAX* gene fusion provides more sub-categorization accuracy since it captures the actual genomic landscape and biology of RMS than the classic ARMS/ERMS histological categorization (Shern et al., 2014).

3.1.1. Epidemiology

As part of the pediatric tumours, rhabdomyosarcoma represents 3.5% of all pediatric malignancies, and head and neck RMS accounts for about 30% to 40% of all childhood RMS cases. There are about 4.6 cases of rhabdomyosarcoma per 1 million diagnosed every year (Chen, Ricciotti, Futran, & Oda, 2016). The number of epidemiological studies investigating head and neck pediatric malignancies, including childhood RMS is relatively scarce compared to overall pediatric tumours. According to a systemic review by Arboleda et al. (2020), out of 2688 publications, only 19 studies met the inclusion criteria and were therefore included in the systemic review (Arboleda et al., 2020). The studies were registered between 1987 and 2019 in different geographic regions, with just seven of these studies achieving the majority of the critical methodological criteria that assesses the risk of bias in prevalence studies (Albright, Topham, & Reilly, 2002; Arboleda, Hoffmann, Cardinalli, Santos-Silva, & de Mendonça, 2018; Gosepath, Spix, Talebloo, Blettner, & Mann, 2007 ; Levi, Zini, Fischman, & Czerninski, 2017). The demographic profile of pediatric head and neck malignancies, including rhabdomyosarcoma shows higher incidence rates in Europe and Africa compared to the rest of the world. The incidence rates range from 2.6 to 8 cases of pediatric RMS per million. The highest rates were recorded in Africa and Europe, with up to 8 and 6.1 cases per million,

respectively. The lower rates of 4.5 and 3.5 cases per million were recorded in the USA and Asia, respectively (Lychou, Gustafsson, & Ljungman, 2015; Martin-Giacalone, Weinstein, Plon, & Lupo, 2021).

The most diagnosed RMS histological subtypes worldwide are embryonal and alveolar rhabdomyosarcomas. Pediatric rhabdomyosarcoma affects children aged ≤ 19 years old, with incidence peaks recorded between the ages of one and five (Darwish et al., 2020; Martin-Giacalone et al., 2021). Similarly, with other pediatric cancers, pediatric RMS affects relatively more males than females, with a ratio of 1.4:1 (Darwish et al., 2020).

3.1.2. Diagnosis

The diagnostic procedure of rhabdomyosarcoma of the head and neck comprises different criteria than the ones followed in most cancers. Usually, any symptoms of the head and neck rhabdomyosarcoma exhibited by the child are followed by a primary diagnosis that consists of scans such as computed tomography (CT), or magnetic resonance imaging (MRI) and tissue biopsy (ZHU et al., 2014). Further diagnosis is proceeded to confirm the type of the RMS, its degree of severity, its stage, and its metastatic state (ZHU et al., 2014).

As already stated above, rhabdomyosarcoma staging upon diagnosis is different from the rest of other cancers. The first three key criteria that doctors assess and determine are the TNM stage, the clinical group, and the presence or absence of the *PAX/FOXO1* fusion gene. Based on these criteria, the treatment plan and strength of the treatment can be set (America Cancer Society, 2020; Meza, Anderson, Pappo, & Meyer, 2006).

Based on Meza, Anderson, Pappo and Meyer (2006), the TNM staging is identified as follows:

- T stands for tumour, and this criterion checks for characteristics of the main tumour, i.e., size and location at the primary anatomic site. The size of the tumour is assessed as ≤ 5 cm or >5 cm in diameter size, and the location is assessed as the size of the tumour extension to surrounding tissue either ≤ 5 cm or >5 cm diameter. The orbit, the head and neck, excluding the parameningeal areas, the genital or the urinary site, excluding the bladder or the prostate gland, and the bile ducts are considered favourable sites. On the contrary, the arms and/or legs, the bladder/prostate, and the parameningeal areas are considered unfavourable areas.
- N stands for node, and this criterion checks for the possible spread of the tumour to adjacent or regional lymph nodes. The clinical involvement of the regional node is classified into three degrees: no clinical involvement of local nodes, confirmed involvement of local nodes by the tumour, and unknown clinical status of the local nodes corresponding to N0, N1, and Nx, respectively.
- M stands for metastasis, and this criterion assesses tumour metastasis to further body parts. The absence and presence of metastasis are referred to as M0 and M1, respectively.

Based on the TNM criteria, there are four stages of RMS as shown in Table 9.

Table 9. Staging of RMS with TNM criteria.

	Stage 1	Stage2	Stage3		Stage4
Tumour size	Any size	≤ 5 cm	≤ 5 cm	>5 cm	Any size
Tumour site	Favourable	unfavourable	unfavourable	unfavourable	Any part
Spread to regional nodes	N0 or N1	N0 or Nx	N1	N0 or N1 or Nx	N0 or N1
Metastasis	M0	M0	M0	M0	M1

The clinical grouping of RMS for surgical classification is based on the tumour's extent and its complete resection amid primary surgery (Meza, Anderson, Pappo, & Meyer, 2006).

- Group I comprises a localized RMS tumour that has not spread to the regional lymph node or other areas of the body and has been completely resected surgically.
- Group II includes three subgroups: a) Total tumour resection with regional spread and evidence of tumour remnants during surgery. b) total tumour resection with lymph node involvement and no evidence of tumour remnants. c) the disease has spread to regional areas with node involvement and tumour remnant after resection.
- Group III includes incomplete tumour resection i.e., major tumour residues with lymph node involvement.
- Group IV is characterised by metastasis of the primary tumour at the onset.

The last criterion is the *PAX/FOXO1* gene fusion status in RMS cells. The presence of *PAX/FOXO1* gene fusion is related to the tumour's severity i.e., the gene fusion signifies more aggressive and more RMS. Associating all the criteria together reveals different risk groups by which clinicians can determine the strength or aggressiveness of the treatment (Meza, Anderson, Pappo, & Meyer, 2006).

According to the American Cancer Society, there are three risk groups; low, intermediate, and high-risk groups, as shown in Table 10 (American Cancer Society, 2020).

Table 10. Risk groups of RMS based on TNM staging, clinical groups, and PAX/FOX01 fusion gene status.

Risk group	Characteristics		
	TNM stage	Clinical group	PAX/FOX01 fusion gene status
Low risk	1	I, II, or III	Absent
	2 or 3	I or II	Absent
Intermediate risk	2 or 3	III	Absent
	1, 2, or 3	any	Present
High-risk	4	III, IV	Absent
	4	III, IV	Present

One of the major criteria that affect the level of riskiness in these groups is age. As aforementioned, RMS in children older than 10 is more aggressive and harder to control. Therefore, these risk groups characteristics are not definite and can be affected by age, especially the intermediate and high-risk groups (Meza, Anderson, Pappo, & Meyer, 2006).

Since several inherited genetic mutations and syndromes are associated with pediatric RMS and based on the latest World Health Organization (WHO) classification report and classification, clinicians are advised to recommend the performance of molecular and genetic testing (Pfister et al., 2021; Wachtel et al., 2006). The tests are in purpose of increasing the diagnostic accuracy to distinguish RMS from pathologically similar sarcomas and lymphomas including Ewing’s sarcoma and lymphoblastic lymphoma and to ensure the setting of an appropriate and most effective treatment plan. Molecular tests include assessing the presence of characteristic markers and genes by immunohistochemistry and Reverse

Transcription Polymerase Chain Reaction (RT-PCR). These include testing for epidermal Growth Factor Receptor (EGFR) and fibrillin Glycoprotein (FBN2) combination, and AP2b and P-cadherin combination as markers for ERMS and translocation positive ARMS, respectively (Grass et al., 2009). These combinations of biomarkers were suggested for implementation in the RMS diagnosis since they were able to detect their respective type of RMS by immunohistochemistry with 90% sensitivity and 76% - 97% specificity (Grass et al., 2009; Pfister et al., 2021).

RNA expression of collagen, type IV, alpha 1 (COL4A1), fibrillin glycoprotein (FBN2), and procollagen-lysine,2-oxoglutarate 5-dioxygenase 1 and 2 (PLOD1 & PLOD2) in pediatric RMS was relatively increased in RMS compared to healthy skeletal muscles (Lian et al., 2021). These three genes are collectively major components of the basement membranes of most body tissues and their aberrant expression in RMS facilitates the tumour invading regionally as well as metastasis (Lian et al., 2021). They are also involved in myogenesis, cell differentiation, proliferation, and survival. This suggests that these genes can be implemented as diagnostic biomarkers for an accurate RMS diagnosis and, ultimately, more effective treatment (Lian et al., 2021). Although the *PAX/FOXO* gene fusion is major genetic evidence of RMS, especially for the alveolar type, this gene fusion is considered a prognostic marker (Lian et al., 2021).

3.1.3. Treatment

The treatment of pediatric rhabdomyosarcoma is depicted as multimodal because it combines surgery, chemotherapy and/or radiotherapy, depending on the staging and the appointed clinical group after diagnosis (as described in Tables 9 and 10). The multimodal treatment is recommended according to risk groups, but in high-risk group patients, the treatment is ensued by follow-up chemotherapy, also known as “maintenance” chemotherapy. The 5-year survival rates of ~75 % in children with localised and metastatic tumours are commonly recorded when treatment is group-adapted (Chen, Ricciotti, Futran, & Oda, 2016). This approach of treatment adaptation is based on all the aforementioned staging and categorization criteria, including histological types, age, tumour size, tumour site, involvement of regional node, *PAX/FOXO1* status, and clinical groups.

3.1.3.1. Surgery

The first and most important treatment option that clinicians opt for the head and neck rhabdomyosarcoma is surgery. In the early years of the 20th century, surgery was the only available therapy option for RMS and survival rates were as low as 7 to 25% in 1970. Yet, following the advances in oncology research, surgical techniques and combination therapy have led to a leap in survival rates by up to 75 % (Dombrowski et al., 2020). Tumour resection surgeries comprise of thoroughgoing resection of the growing mass of the tumour in conjunction with negative surgical margins at the end of the surgery i.e., attaining clean margins and absence of tumour cells on the edges of the resected tissue (Dombrowski et al., 2020).

Total resection of the tumour with macro and microscopic surgeries has contributed to

increasing survival rates (Dombrowski et al., 2020). In a study of 97 pediatric patients with head and neck rhabdomyosarcoma from the database of the internal pathology and otolaryngology databases between 1970 and 2015 of Boston Children's Hospital depicted about 21 % higher 5-year survival rates (82.1%) in children who underwent surgery compared to the ones who did not (60.7%) (Dombrowski et al., 2020; Radzikowska et al., 2016). Yet, challenges remain high with the treatment of patients with recurrent RMS in spite of undergoing resection surgery (Radzikowska et al., 2016).

3.1.3.2. Radiotherapy

After the resection procedure, children with head and neck RMS undergo radiotherapy as part of the multimodal therapy paradigm (Frankart, Breneman, & Pater, 2021). It is designated for all head and neck RMS patients, excluding those with fusion-negative and fully resected tumours. Children with the fusion-positive type of RMS undergo radiotherapy regardless of the resection status (Frankart, Breneman, & Pater, 2021). The radiotherapy protocol applied currently consists of delivering 1.8 Gray (Gy)/ fraction typically after 12 to 13 weeks of chemotherapy. In patients with intracranial extension of the tumour or symptomatic tumour, radiation can start earlier (Frankart, Breneman, & Pater, 2021). Patients with microscopic residuals after resection or with tumours with an unfavourable histology type receive a dose of 36 Gy, whereas patients with a gross tumour receive a higher dose of 50.4 Gy (Frankart, Breneman, & Pater, 2021). Tumours with a size ≥ 5 can receive up to 59.4 Gy based on the D9803 phase 2 trial conducted by the Children's Oncology Group (COG) (Wolden et al., 2015). In cases where the tumour nodes are involved, the child receives 41.4 Gy if the tumour was resected and 50.4 Gy if the tumour remains unresected. For tumours with susceptibility to volume change in locations adjacent to soft tissue, the use of image guidance during

treatment is critical. Site-directed radiotherapy is recommended in metastatic tumours, although the foundation treatment of this type is chemotherapy (Frankart, Breneman, & Pater, 2021). Techniques used in radiotherapy include three-dimensional conformal radiation therapy (3D-CRT), intensity-modulated radiation therapy (IMRT) and proton therapy. Multiple fields of pre-determined shape and intensity are used in the 3D-CRT technique to deliver the radiation dose to the targeted tumour volume, which was defined by CT imaging upon diagnosis (Frankart, Breneman, & Pater, 2021). The IMRT provides active shaping of the photon and proton beams of radiation in order to increase the conformality to the tumour shape and ultimately reduce toxicity by reducing the exposure of adjacent structures to radiation dose (Frankart, Breneman, & Pater, 2021).

Proton therapy is commonly used in pediatric cancers since it affords the ability to reduce the dose to adjacent healthy tissue. Also, this technique minimizes the overall radiation dose to the patient compared to IMRT. Proton therapy employs relatively heavy and positively charged particles to deliver the dose to a precise depth, offering a substantial advantage over conventional photon-based therapy (Frankart, Breneman, & Pater, 2021; Mohan & Grosshans, 2017).

3.1.3.3. Chemotherapy

Chemotherapy is usually planned after surgery and before radiotherapy. Yet, clinicians decide the order of the multimodal treatment -chemotherapy and/or radiotherapy- based on the primary diagnosis and surgery outcome. Current chemotherapy protocols applied for RMS are set according to the most recent COG protocols. Vincristine, actinomycin-D, and cyclophosphamide (VAC), are three first line chemotherapy drugs that are considered the

backbone of the head and neck RMS treatment (National Cancer Institute, 2022). In low-risk patients, only vincristine and actinomycin-D (VA) are included in the 22 to 24 weeks treatment plan in order to reduce the child's exposure to alkylating agents that induce bone marrow depression and infertility (National Cancer Institute, 2022). The 5-year survival rates were not significantly affected with VA only chemotherapy (90%) compared to VAC chemotherapy (93%). Therefore, treatment with VA only resulted in good chemotherapy outcomes with reduced toxicity exposure (Bisogno et al., 2022). Vincristine belongs to the vinca alkaloids class of chemotherapy drugs. They are also known as antimicrotubule agents as they affect the cells during the several phases of mitosis. Vinca alkaloids act on DNA level by tubulin-binding mechanism and ultimately inhibition of its polymerization into microtubules (Dhyani et al., 2022; National Cancer Institute, 2022). Actinomycin-D is an antitumour antibiotic and falls under the chromomycin type. It acts during distinct phases of the cell cycle and is considered cell cycle specific (Skolnik et al., 2021). These types of antibiotics mainly interfere with DNA/RNA synthesis by binding to the DNA and intercalating its strands to obstruct DNA replication. They act typically on the inhibition of topoisomerase II (Skolnik et al., 2021). Cyclophosphamide belongs to the large family of alkylating agents and falls under the mustard gas derivatives group. The alkylating agents are typically active during the rest phase of the cell cycle, and are considered non-specific cell cycle drugs (Chen, Dorado Garcia, Scheer, & Henssen, 2019; Sun, Liu, Ma, & Hu, 2021). The alkylating agents act directly on DNA and induce DNA strand breaks by the crosslinking phenomenon, which leads to aberrant base pairing and, eventually inhibition of cell division and cell death (Sun, Liu, Ma, & Hu, 2021). For intermediate-risk RMS, the VAC protocol is also followed for 40 weeks. The multiagent VAC chemotherapy is followed in the US, whereas in Europe, ifosfamide is used instead of cyclophosphamide (Lucas & Pappo, 2019). Aiming at reducing the cytotoxicity caused by the

chemotherapy, a Children's Oncology Group (COG) trial (ARST0531) showed that reduction of cyclophosphamide doses per cycle to 1.2 g/m² was related to poor outcome and reduced local control of the tumour (Lucas & Pappo, 2019). Yet, it remains unclear whether the dose or delivery pattern of cyclophosphamide is what applies a higher impact on the treatment outcome. Therefore, the optimal aim is to attain an ideal balance between cyclophosphamide's therapeutic benefit and toxicity (Lucas & Pappo, 2019). High-risk group patients have metastatic tumours, and the VAC-three-agents chemotherapy remains the standard systemic therapy. This standard chemotherapy regimen is followed by the COG in North America, whereas the European Pediatric soft tissue sarcoma Study Group (EpSSG) replaces cyclophosphamide with ifosfamide (IVA) (Makimoto, 2022). However, patients with advanced stages of ERMS who received primary therapy with vincristine, dactinomycin, and cyclophosphamide (VAC) have encountered tumour relapse with 5-year post relapse survival rate of nearly 10 % (Mascarenhas et al., 2019). As survival remains inadequate, new trials are ongoing, including the recently opened (November 2022) International Frontline and Relapsed Rhabdomyosarcoma (FaR-RMS) study (NCT04625907). The primary aim of this phase II clinical trial is to investigate the impact of implementing new therapeutic regimens for both newly diagnosed and relapsed RMS. The therapeutic agents included in the clinical trial are irinotecan, actinomycin D, doxorubicin, ifosfamide, vincristine, vinorelbine, cyclophosphamide, temozolomide, and regorafenib, in combination with radiation (van Ewijk et al., 2021).

3.1.3.4. Pioneering Therapy

Aiming at enhancing the treatment outcomes in paediatric neoplasms, several innovative therapy methods have been developed and investigated by research teams around the globe. Yet, the pace of these enhancements has slowed in recent years as survival rates might have been intensely improved in several widespread paediatric tumours, including leukaemia, with a 5-year survival rate of up to ~90% (Butler et al., 2021). Despite collaborative efforts to clinically study rhabdomyosarcoma, no substantial improvement has been noted in the past 30 years in the survival rates of metastatic and recurrent rhabdomyosarcoma that remained below 30% (Chen, Dorado Garcia, Scheer, & Henssen, 2019; Yohe et al., 2019). Therefore, there is an unmet need for innovative therapies to improve the survival rates in metastatic rhabdomyosarcoma and high-risk groups and further optimise the survival rates in low-risk groups (Chen, Dorado Garcia, Scheer, & Henssen, 2019). As aforementioned, GLI1 is a nuclear mediator of the Hh signalling pathway. Therefore, GLI could afford an effective target for the therapy of embryonal rhabdomyosarcoma (Liu et al., 2014). Among the strategies being evaluated for clinical trials and pre-clinal models, different vaccines have developed against small fragments of peptide covering the *PAX3-FOXO1* fusion, *EGFR* tyrosine kinase inhibitors, and rapamycin analogues (Gallego Melcón & Sánchez, 2007).

The use of nanoparticles as drug carriers is another approach for the targeted treatment of several paediatric tumours, including rhabdomyosarcoma. Hydrolysed galactomannan (hGM)-based amphiphilic nanoparticles were shown to be selectively 100% accumulated intratumourally in paediatric sarcomas including rhabdomyosarcoma (Zaritski et al., 2019). Despite their promising results, the number of similar recent studies in paediatric

rhabdomyosarcoma remains inadequate compared to other prevalent cancer types (De Lima et al., 2020).

3.1.4. Prognosis

The prognosis of pediatric rhabdomyosarcoma is depicted differently according to several factors that affect the treatment outcome including mainly histological type, age, and site of the tumour in the body, head, and neck (Wang et al., 2020). The histological type related to prognosis is notably better in the embryonic type compared to the alveolar type (Simon, Paulino, Smith, & Buatti, 2002, Wang et al., 2020).

Age related prognosis is more favourable between ages 0 to 14 with a 5-year survival rate close to 70%, however, children older than 14 years of age have a 20% lower 5-year survival rate than the younger age group. The mere explanation for this could be the fact that younger children tolerate treatment better than older ones, and the alveolar type of RMS was found to be more prevalent in older children compared to younger children (Simon, Paulino, Smith, & Buatti, 2002, Wang et al., 2020).

The tumour size is also considered a prognostic factor, as it affects the resection level and the surgery outcome; bigger size tumours can affect and metastasize to several other regions in the head and neck or to other organs. In more detail, patients with RMS tumours ≤ 5 cm in size have a 5-year survival rate close to 75% while children with an RMS tumour > 5 cm have a lower 5-year survival rate with just 38% (Zhang et al., 2020).

Collectively, the age and the tumour size can afford predictive/prognostic survival factors and children with a median age of ≤ 12.5 years and an RMS tumour size of ≤ 5 cm have an average 5-year survival rate of 84% ($\pm 8\%$), while lower 5-year survival rates of 25% ($\pm 4\%$)

are more correlative with a median age of > 14 years and a tumour size of > 5 cm (Simon, Paulino, Smith, & Buatti, 2002, Wang et al., 2020; Zhang et al., 2020).

The aim of the current study was to assess the ability of dual sensitive polymeric nanocontainers to deliver first line chemotherapy drugs sustainably and effectively in pediatric rhabdomyosarcoma. Hence, aiming at improving the efficacy of the chemotherapy drugs and reducing their side effects through targeted delivery.

3.2. Material and Methods

3.2.1. Materials

DMEM High Glucose w/L-Glutamine w/Sodium Pyruvate culture media (Biosera, NUAILLE, France), Dulbecco's phosphate buffered saline (DPBS) (Biosera, NUAILLE, France), Foetal Bovine Serum (Biosera, NUAILLE, France), Trypsin-EDTA (Biosera, NUAILLE, France), Poly-L-Lysine (Innoprot, Derio, Pais Vasco, Spain), MTT Reagent in powder (Cayman, Michigan, USA), RIPA Lysis Buffer System (Santa Cruz Biotechnology, Inc, Texas, USA), Mini Trans-Blot System (Bio-Rad, California, USA), p-Coumaric acid (Sigma-Aldrich Darmstadt, Germany), Luminol (Sigma-Aldrich Darmstadt, Germany), BCA Protein Assay Kit (Cell Signalling, Massachusetts, USA.), Glycine for molecular biology (PanReac AppliChem, ITW Reagents Division, Chicago, USA), Tris (PanReac AppliChem, ITW Reagents Division, Chicago, USA), Tween 20 (PanReac AppliChem, ITW Reagents Division, Chicago, USA), GAPDH antibody, rabbit anti-mouse IgG-HRP, m-igG fc BP -HRP anti-mouse antibody (Santa Cruz Biotechnology, Inc, Texas, USA), Phospho-Histone H2A.X (Ser139) Antibody (Affinity Biosciences, China), Opti-Protein marker (ladder) (Applied Bioscience Material, Richmond, Canada), Sodium dodecyl sulfate or SDS (Bio-Basic, Toronto, Canada), Amersham Protran nitrocellulose blotting membranes 0.2µm (Cytiva, Germany), Thick Blot Filter Paper (Bio-Rad, California, USA), Buffered formalin 10% (Atom Scientific, Manchester, UK), Anatomix RP Fixer and Anatomix RP Developer Replenisher (FUJIFILM, Tokyo, Japan), Medical X-ray Film (FUJIFILM, Tokyo, Japan), Amersham hypercsette autoradiography cassettes (Fisher scientific, Massachusetts, USA), Propidium iodide (Sigma-Aldrich Darmstadt, Germany), Annexin-V, 7AAD, and binding buffer (BD Bioscience, New Jersey, USA). Incubator thermos HEPA class 100 (Thermofisher Scientific. Massachusetts, USA), OMAX Fluorescent microscope 40X-1600X EPI (OMAX, USA). Rocking and waving shaker (OHAUS, New Jersey,

USA), Becton Dickinson FACSCalibur flow cytometer (BD Bioscience, New Jersey, USA), Elisa microplate reader (Biobase Biodustry, Shandong, China). Band intensity quantification in western blot membranes was quantified by GelQuantNet 1.6.6 (BiochemLab Solutions.com, University of California, San Francisco) software. Statistical analysis was carried out using Prism GraphPad 9 and Microsoft Excel Spreadsheet software.

3.2.2. Cell culture

Pediatric head rhabdomyosarcoma cell line TE671 (Dr George Lambrou, Choremeio Research Laboratory, National and Kapodistrian University of Athens, Greece) and HEK293 (ATCC, Maryland, USA) healthy cell lines were thawed and introduced into a T 75mm² culture flask with 20ml of 10% FBS high glucose DMEM culture media. The cells were then left inside the incubator for growth and attachment at 37°C and 5% CO₂. After the cells' attachment the following day, the media was changed, and the cells were examined under the microscope in order to verify their growth and morphology. After ~85% confluency, cells were subcultured in a 1 to 10 ratio. The rest of the collected cells were either cryopreserved and kept in liquid nitrogen or seeded for further experiments in the appropriate plate, accordingly.

3.2.3. MTT assay

The TE671 and HEK293 cell lines were seeded in 96 well plates with a concentration of 6×10^3 to 8×10^3 cells/well. Cells were left in the incubator to grow one night prior to the experiment and until reaching ~75% confluency. Then, 100µl of the seven different increasing concentrations of free NCs, loaded and free DNR, cisplatin, temozolomide, and DNR/temozolomide combination, were introduced in the wells in triplicates. The control

wells contained only culture medium. Plates were then introduced in the incubator and after 24h and 72h, suspensions were removed from the wells and replaced with 100µl of MTT solution and introduced back in the incubator. After 2-4h, after observing the formation of the formazan crystals, MTT solution was removed from each well and replaced with 100µl of DMSO. After the full dissolution of crystals, the absorbance of each plate was measured using an ELISA microplate reader (Biobase Biodustry, Shandong, China) at 560nm wavelength. Cell viability percentage calculations were carried out as follows:

$$\text{Cell Viability \%} = \left(\frac{\text{Mean } OD_{560}(\text{Sample})}{\text{Mean } OD_{560}(\text{Control})} \right) \times 100$$

3.2.4. Fluorescence microscopy

In a 24 well plate, round coverslips (12mm) were placed in each well and then soaked in polylysine for 30min. After removing the polylysine and drying the wells, cells were seeded with 7×10^4 cells/well about 12h prior to the experiment. After ensuring the cells' attachment on the surface of the coverslips with an 80% confluency, the culture medium was then replaced with 500µl of loaded NCs and free rhodamine-B suspensions in 5µM and 50µM concentrations. After each set time point, the suspensions were removed from the corresponding wells and fixed with 250µl 4% PFA or 10% buffered formalin solution. After 30min, the fixation solution was removed, and the wells were washed twice with PBS. After that, the coverslips were gently picked using tweezers and flipped on a pre-mounted microscope slide. The microscope slides were viewed and evaluated using fluorescent microscope 40X-1600X EPI (OMAX, USA).

3.2.5. Western blot

3.2.5.1. Protein extraction and quantification

Both TE671 and HEK293 were seeded in 6 well plates and treated with 30 μ M of different suspensions of free NCs, loaded and free DNR, cisplatin, temozolomide, and DNR/temozolomide combination. After 24h and 72h incubation, suspensions were removed and 100 μ l of RIPA lysis buffer was introduced in each well while the plates were placed on ice. The lysis buffer was prepared according to the manufacturer's instructions and every 1ml of the lysis buffer contained 10 μ l of protease inhibitors cocktail, PMSFA, and sodium orthovanadate. About 5min later, cells were scratched, collected, and introduced in Eppendorf tubes and preserved on ice until all other cells were collected from the rest of the wells. Then, Eppendorf tubes containing lysed cells were sonicated for 10 sec and introduced back to the ice for another 10 sec. This action was repeated about 10 times before centrifuging the cells at 4°C, 16128 RCF for 20 min. After centrifugation, the supernatant was collected, and the palette was discarded. The protein quantification was determined using BCA protein assay kit (Cell Signalling, Massachusetts, USA) and BSA standard curve.

3.2.5.2. Samples and SDS-PAGE gels preparation

Next, the required amount of protein for loading - 30 μ g/40ul in these experiments- was calculated and samples were prepared with $\frac{1}{4}$ of the final sample volume as Laemmli buffer (see appendix 1 for Laemmli buffer preparation).

Running gels were prepared based on the size of the protein of interest i.e., the smaller the protein, the higher the SDS gel concentration. The following proteins were the target of the western blot H2A.X, BCL-2, Caspase-8 with 15kDa, 26kDa, and 55kDa molecular weight,

respectively. Therefore, the gels prepared were 15% SDS. Afterwards the solidification of the gels, loading samples were boiled for 5min at 95°C.

3.2.5.3. Running the gels

After assembling the gels in the chamber and introducing them in the buffer tank, combs were removed and the chamber between the two gels was filled with running buffer. Samples were then loaded in the corresponding wells with the ladder in the first well. A running buffer was added to the appropriate level and the tank was closed. The gels were run for 15 to 20 min at 80V until the sample surpassed the staining gel before increasing the voltages in the power supply to 110V. After 2h and after the protein separation reached the bottom of the gel, the power supply was turned off and the running step was stopped. The sandwiches for protein transfer from the gels to the membranes were prepared with sponges or foam pads, membranes and filter paper, all pre-soaked in transfer buffer. The components ordered in the gel holder cassette were as follows: black side of the gel holder cassette, sponge, filter paper, gel, membrane, filter paper, sponge, and white side of the cassette. The sandwiches were then closed and introduced inside the electrode assembly with its black side facing one of the cassettes to insure the appropriate transfer of the protein from the gel to the membrane. The electrode assembly containing both sandwich cassettes was introduced in the transfer tank, then filled with cold transfer buffer, and the whole tank was introduced inside an ice container, with ice surrounding the transfer tank. The transfer step was run at 400mA for 2.5 hours using a current power supply connected by power cables to the transfer tank. After the transfer was over, membranes were retrieved from the sandwiches and stained with red ponceau in order to have a primary evaluation of the protein separation and bands quality.

After that, the membranes were well washed with dH₂O until most of the red stain was removed before they were blocked with 5% non-fat milk for 1h. Primary antibodies of the protein of interest were prepared in 5% non-fat milk in 1:1000 final concentration. In order to avoid using large volumes of antibodies, a 3ml final volume with 1:1000 antibody concentration solution was introduced in a 50ml falcon in which the membrane was introduced and left to shake on a rocking shaker overnight at 4°C. The next morning, the membranes were removed from the falcons and washed with TBS-T buffer 3 times, 10min each. Secondary antibodies were prepared with the way as the primary antibody (1:2000 to 1:10000), and membranes were left to probe on a rocking shaker (OHAUS, New Jersey, USA) for an hour, after which washing was carried out 3 times, 10min each, with TBS-T buffer.

3.2.5.4. Developing the films and imaging the membranes

After the washing was over membranes were incubated for 3min with ECL solutions (prepared from scratch in the lab, see appendix 2), then wrapped in a transparent film and fixed on an autoradiography cassette. In a dark room with only safe red light, x-ray film was exposed to the membranes in the cassettes for 3 to 5min. Immediately after the exposure time was over, films were dipped in developing solutions in the following order: developer solution for 5 sec, water, fixer solution for 5 secs then water again. Based on the intensity of the bands, exposure might be repeated for a shorter or longer time until bands with appropriate intensity and suitable for quantification were obtained. Membrane images were obtained by Fluorchem 8800 imager (Alpha Innotech, San Leandro, USA), where the membranes were covered with ECL immediately before imaging and the exposure time was set between 3 to 8 min.

An initial trial/run of western blot experiments was carried out to assess the whole process step by step, determine the suitable amount of protein to load, and to verify the sensitivity of antibodies in detecting the targeted protein. The trials were initially carried out with both TE671 and HEK293 cell lines with untreated cells, free NCs, loaded and free temozolomide, cisplatin, and DNR treated cells for 24h. Then, further experiments were conducted with same aforementioned treatments for 72h in addition to samples treated with loaded and free DNR/temozolomide combination.

3.2.6. Flow cytometry

Both TE671 and HEK293 were seeded in 6 well plates or 25mm² culture flask at least 12h prior to their treatment with 30µM of different suspensions of free NCs, loaded and free DNR, cisplatin, temozolomide, and DNR/temozolomide combination. After 24h and 72h of treatment, cells were harvested by trypsin and then centrifuged at 800rpm for 3 min. For the Annexin-7AAD protocol, about 1x10⁵ cells were well resuspended in 100µl of binding buffer, then stained 5µl of annexin-V and 5µl of 7AAD and left to incubate for 20min in the dark. After the incubation time was over, 400µl of binding buffer was added and the sample was measured with a Becton Dickinson FACSCalibur flow cytometer (BD Bioscience, New Jersey, USA).

For Propidium Iodide (PI) protocol, 1x10⁶ cells were fixed with cold 70% ethanol. The fixation was done with a thorough vortex of the cells (pipetting cells up and down) in order to avoid clumping. After 1h, cells were washed with PBS and resuspended in 500ml PI solution and left to incubate for 40min before Fluorescence-Activated Cell Sorting (FACS) measurement.

3.3. Results

3.3.1. Cytotoxicity

The MTT assay results after 24h incubation with free NCs, cisplatin-loaded NCs and free cisplatin (Figure 24) showed high cell viability of more than 75% throughout the increasing concentrations of the free NCs in both TE671 (Figure 24a) and HEK293 (Figure 24b) cell lines. Conversely, increasing concentrations of cisplatin loaded NCs and free cisplatin in both cell lines showed decreasing cell viability i.e., increasing cytotoxicity. The lowest cell viability percentages in both cell lines were recorded at 30 μ M with ~55% and ~50% for loaded NCs and free cisplatin, respectively.

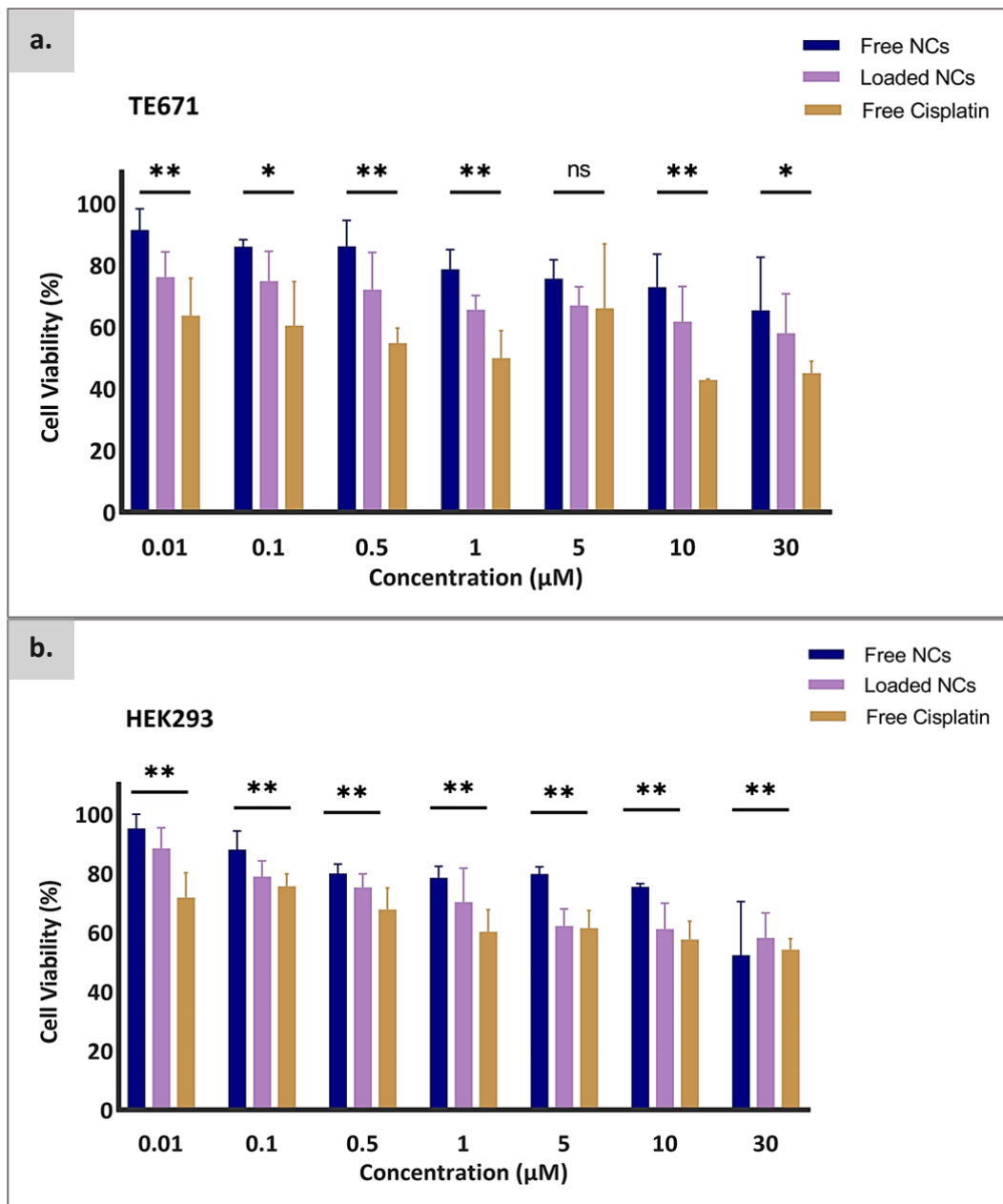


Figure 24. Evaluation of the cell viability via MTT assay. Cytotoxicity levels in **a).** TE671 and **b).** HEK293 cell line after 24h treatment with free NCs, cisplatin loaded NCs, and free cisplatin. Two-way ANOVA test (TE671) and 2 tailed paired student t test (HEK293) (* $P \leq 0.05$, ** $P \leq 0.01$, ns $P > 0.05$); error bars are based on mean \pm SD of three independent experiments.

In TE671 and HEK293 cells that were treated with free NCs, DNR-loaded NCs, and free DNR (Figure 25a and 25b, respectively), cell viability percentages were all higher than 70% across the increasing concentration of free NCs. Yet, a pattern of decreasing viability percentages was recorded in both cell lines treated with increasing concentrations of loaded and free DNR, reaching 60% and 50%, respectively, at 30 μ M.

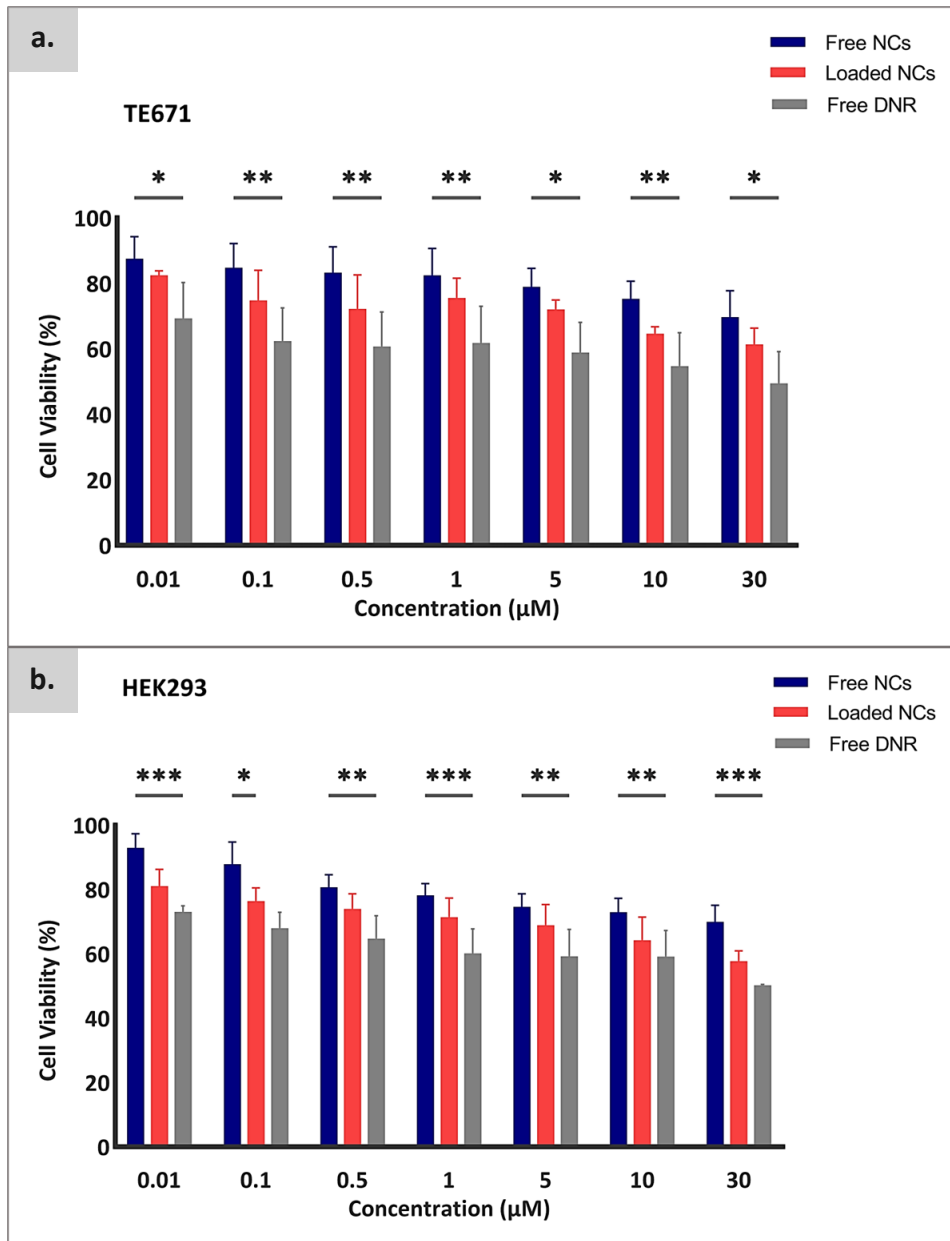


Figure 25. Evaluation of the cell viability via MTT assay. Cytotoxicity levels in **a).** TE671 and **b).** HEK293 cell lines after 24h treatment with free NCs, DNR-loaded NCs, and free DNR. Two-way ANOVA test (* $P \leq 0.05$, ** $P \leq 0.01$, *** $P \leq 0.001$); error bars are based on mean \pm SD of three independent experiments.

Similarly, with the aforementioned treatments, both TE671 and HEK293 cells were also treated with free NCs, temozolomide-loaded NCs, and free temozolomide (Figure 26a and 26b, respectively). Results showed high percentages of cell viability (>70%) in cells treated with free NCs regardless of the increasing concentration. Cellular viability percentages of temozolomide-loaded NCs and free temozolomide treated cells reached ~60% to 67% at 30 μ M, which is 20% less than the cell viability recorder at lower treatment concentrations 0.01 μ M.

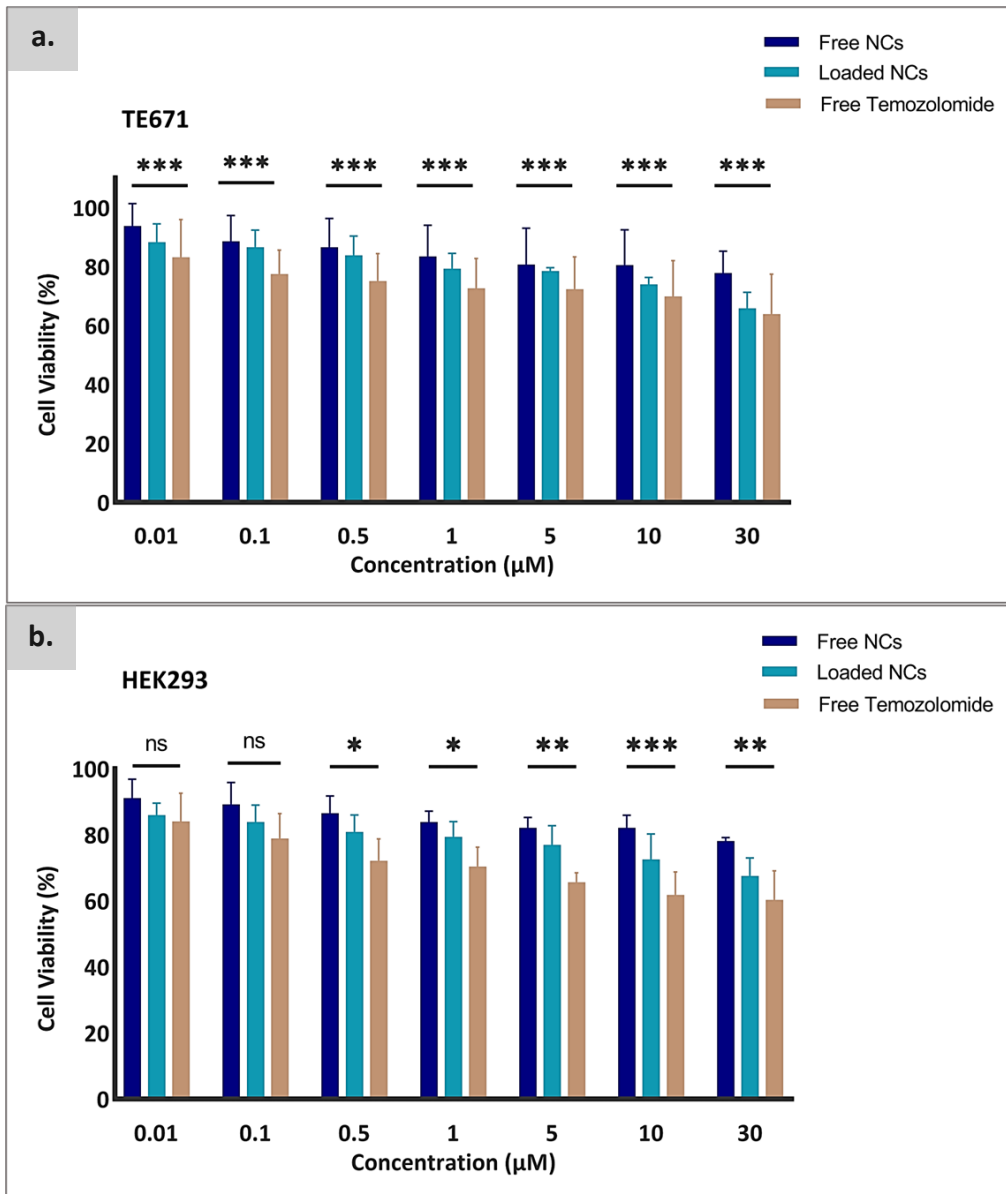


Figure 26. Evaluation of the cell viability via MTT assay. Cytotoxicity levels in **a).** TE671 and **b).** HEK293 cell lines after 24h treatment with free NCs, temozolomide-loaded NCs, and free temozolomide. Two-tailed paired student t-test (TE671) and two-way ANOVA test (HEK293) (ns $P > 0.05$, * $P \leq 0.05$, ** $P \leq 0.01$, *** $P \leq 0.001$); error bars are based on mean \pm SD of three independent experiments.

The cell viability percentages of both TE671 and HEK293 cells treated with the free and loaded combination of temozolomide and DNR (Figure 27a and 27b, respectively) were ~5 to 10% lower than the cells treated with the same drugs separately across the different concentrations. For the NCs treated cells, results showed high percentages of cell viability (>70%) regardless of the increasing concentration, similarly with the aforementioned MTT experiments. Cellular viability percentages of temozolomide/DNR-loaded NCs and free temozolomide/DNR treated cells reached 58% and 43% at 30 μ M, respectively. These viability percentages were ~50% lower than the cell viability levels recorded at lower treatment concentrations of 0.01 μ M.

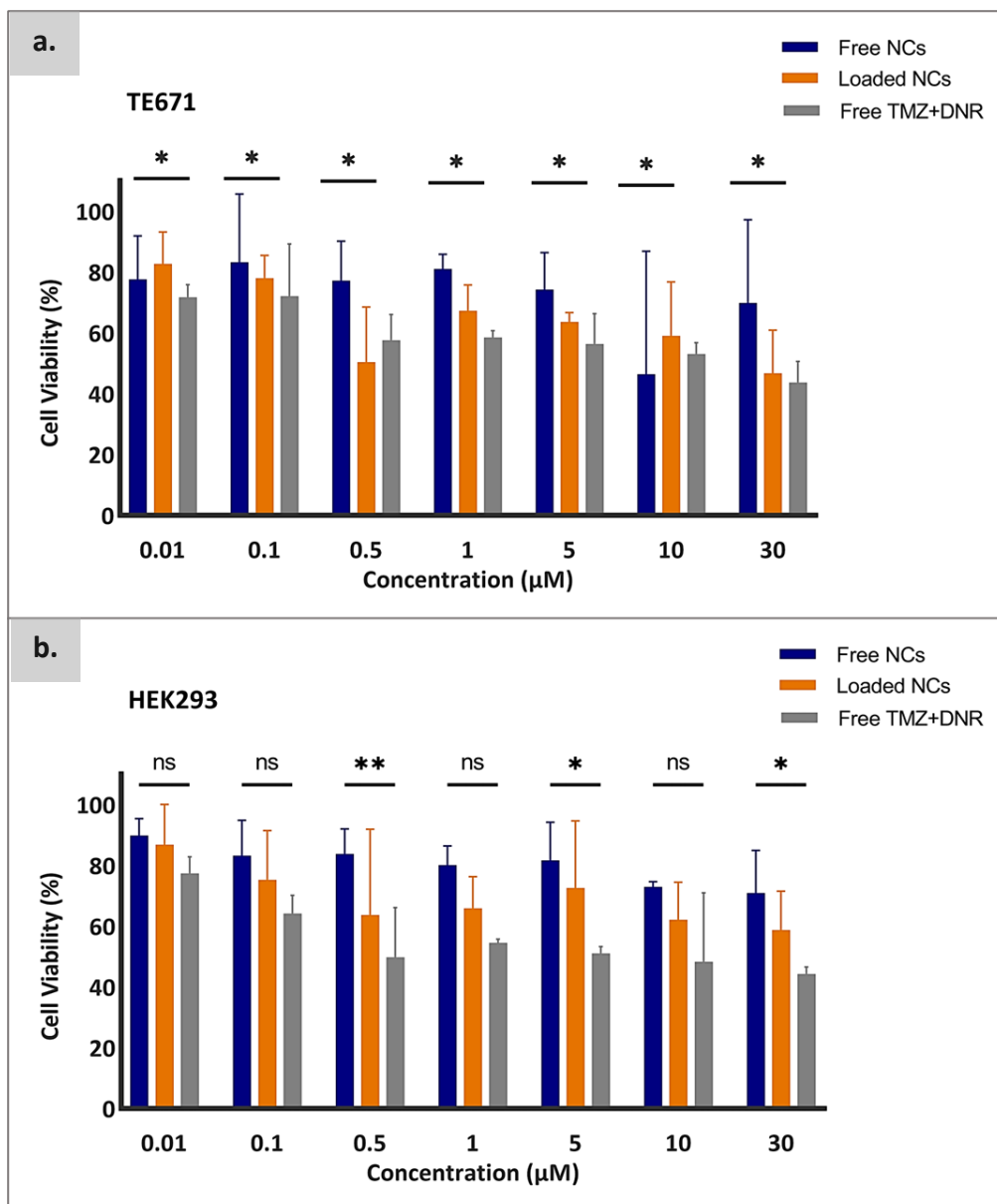


Figure 27. Evaluation of the cell viability via MTT assay. Cytotoxicity levels in **a).**TE671 and **b).** HEK293 cell lines after 24h treatment with free NCs, DNR/temozolomide combination loaded NCs, and free DNR/temozolomide combination. Two-tailed paired student t test (TE671) and two-way ANOVA test (HEK293) (ns $P>0.05$, $*P\leq 0.05$, $**P\leq 0.01$); error bars are based on mean \pm SD of three independent experiments.

In the set of all the 24h MTT experiments results with the different loaded and free drugs treatments, lower cell viability levels by ~5% were observed in TE671 cell lines compared to the HEK293 cell line.

The MTT assay results after 72h incubation with free NCs, cisplatin loaded NCs and free cisplatin (Figure 28) showed high cell viability of more than 70% throughout the increasing concentrations of the free NCs in both TE671 (Figure 28a) and HEK293 (Figure 28b) cell lines. On the contrary, increasing concentrations of cisplatin loaded NCs and free cisplatin in both cell lines, showed decreasing cell viability percentages. The lowest cell viability percentages in both cell lines were recorded at 30 μ M of loaded and free cisplatin. The cisplatin loaded NCs showed ~50% viability in both cell lines. However, free cisplatin showed about 20% lower cell viability in the HEK293 cell line compared to the TE671 cell line at the same 30 μ M concentration.

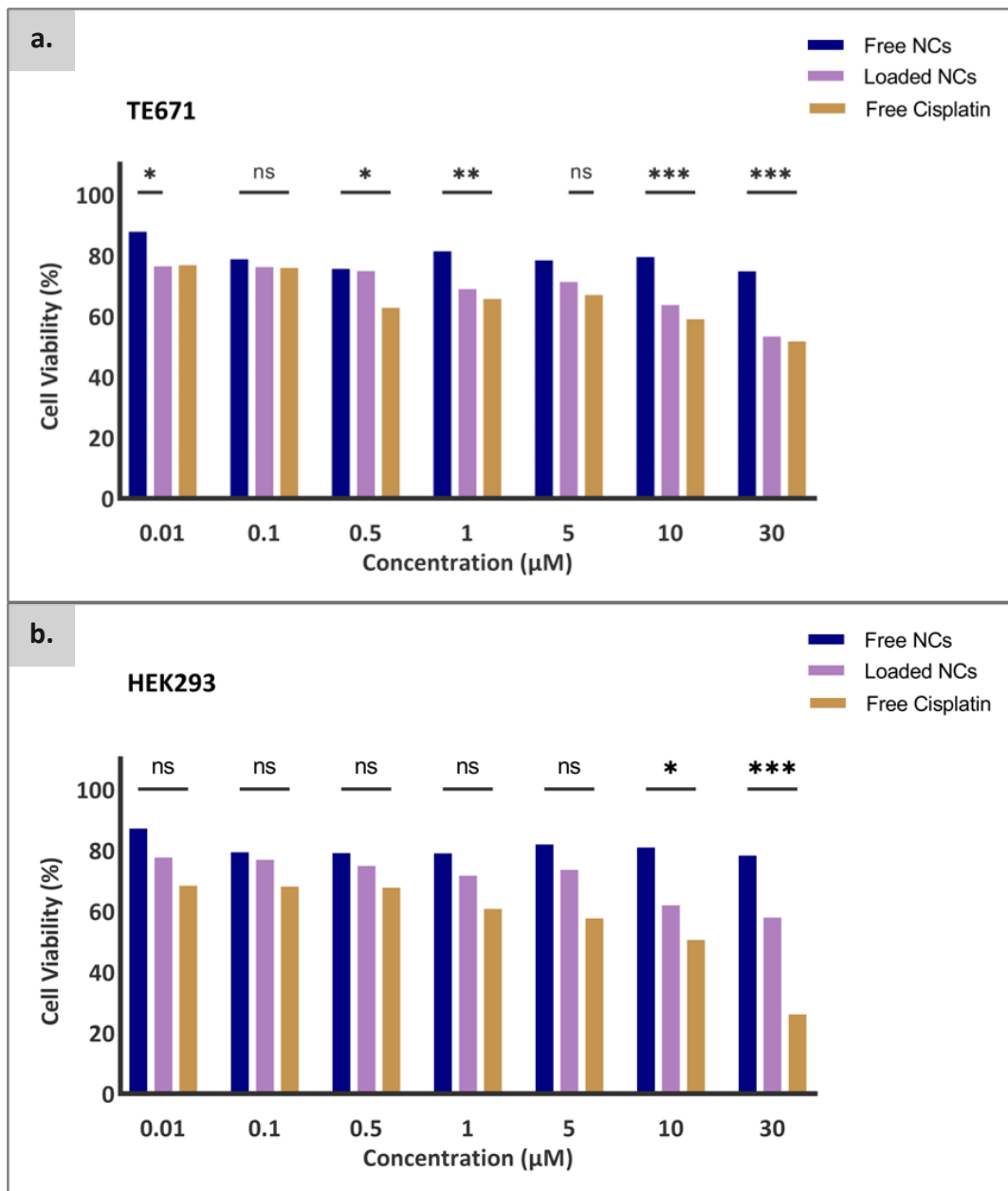


Figure 28. Evaluation of the cell viability via MTT assay. Cytotoxicity levels in **a).** TE671 and **b).** HEK293 cell line after 72h treatment with free NCs, cisplatin loaded NCs, and free cisplatin. Two-way ANOVA test (ns $P > 0.05$, $*P \leq 0.05$, $**P \leq 0.01$, $***P \leq 0.001$), two independent experiments.

The cell viability in both TE671 and HEK293 cell lines treated with free NCs for 72h were above 72% regardless of the concentration (Figure 29a and 29b, respectively). Conversely, treatment of both cell lines for 72h with increasing concentrations of DNR-loaded NCs and free DNR showed a remarkable decrease in cell viability percentages reaching 50% and 20%, respectively, at 30 μ M (Figure 29). Free NCs retained high viability percentages for both 24h and 72h. However, DNR-loaded NCs and free DNR showed 10% and 25% decrease, respectively, in cell viability percentages compared to the 24h treatment.

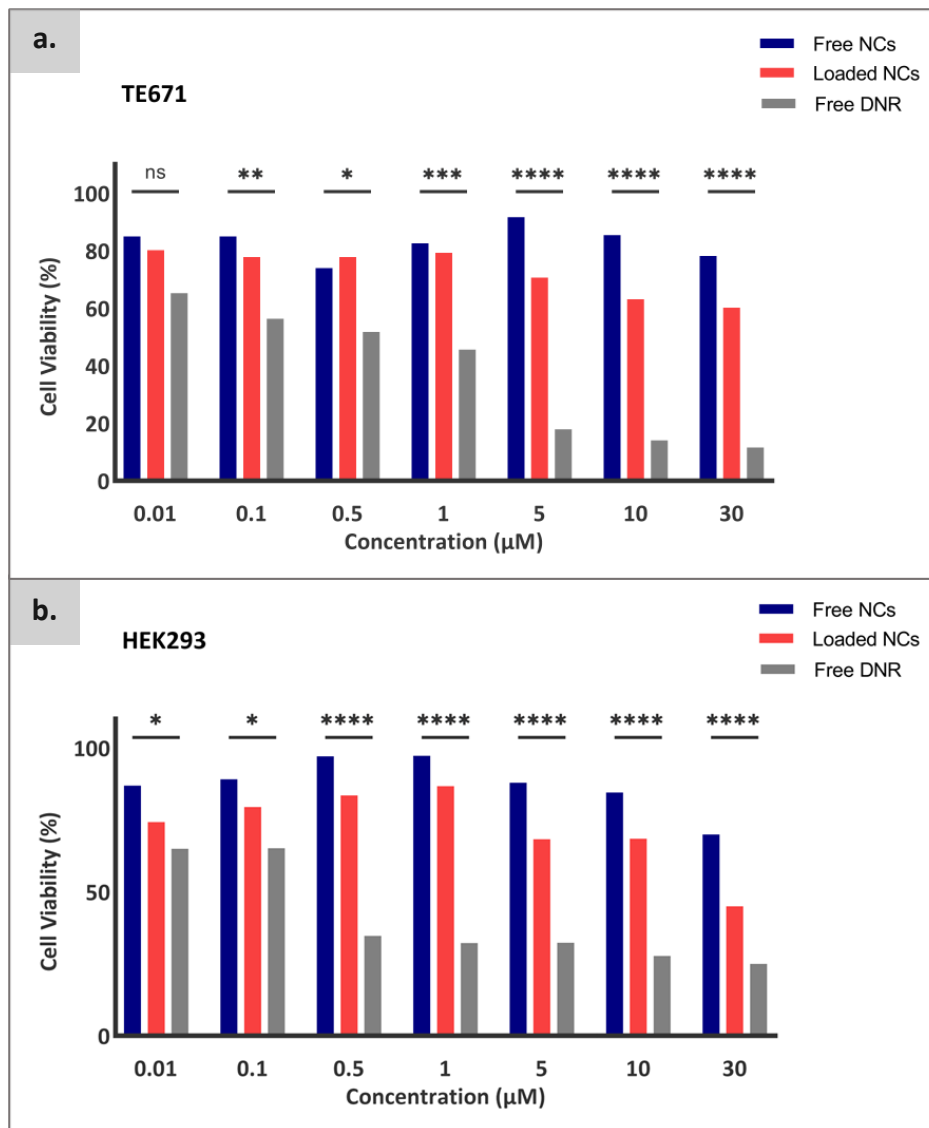


Figure 29. Evaluation of the cell viability via MTT assay. Cytotoxicity levels in **a).** TE671 and **b).** HEK293 cell line after 72h treatment with free NCs, DNR loaded NCs, and free DNR. Two-way ANOVA test (ns $P > 0.05$, $*P \leq 0.05$, $**P \leq 0.01$, $***P \leq 0.001$, $****P \leq 0.0001$); two independent experiments.

Treatment with loaded and free temozolomide for 72h in both TE671 (Figure 30a) and HEK293 (Figure 30b) cell lines showed a decreasing pattern of cell viability percentages reaching the lowest levels of 50% and 40% respectively at 30 μ M (Figure 30). These levels were about 10% to 20% lower than the treatment with loaded and free temozolomide at 24h. The 72h treatment with free NCs retained the cell viability percentages between 90% and 78% throughout the increasing concentrations for both cell lines.

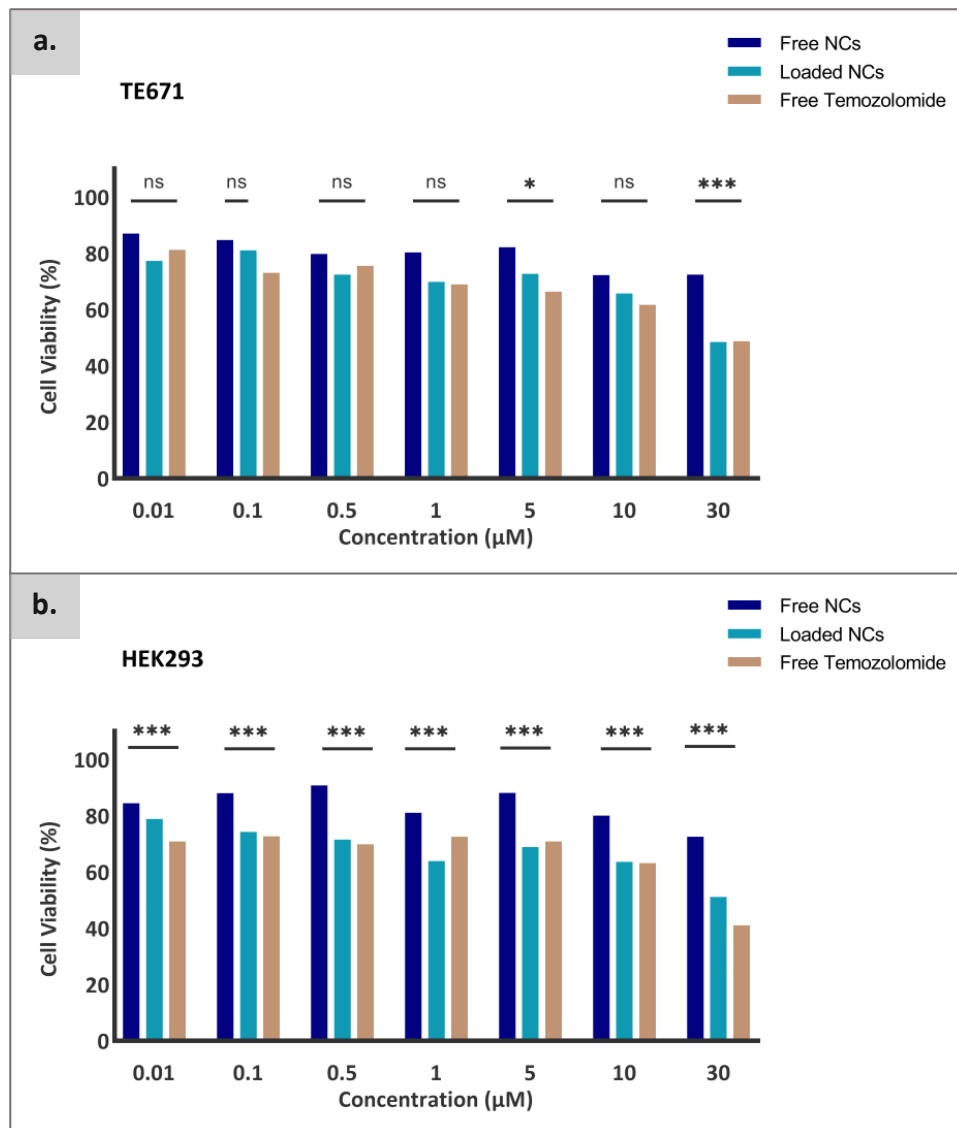


Figure 30. Evaluation of the cell viability via MTT assay. Cytotoxicity levels in **a).** TE671 and **b).** HEK293 cell lines after 72h treatment with free NCs, temozolomide-loaded NCs, and free temozolomide. Two-way ANOVA test (TE671) and 2 tailed paired student t test (ns $P > 0.05$, * $P \leq 0.05$, *** $P \leq 0.001$), two independent experiments.

The 72h treatment with a free and loaded combination of DNR and temozolomide showed decreasing cell viability percentages throughout the increasing concentrations in both TE671 (Figure 31a) and HEK293 (Figure 31b) cell lines. At 30 μ M, the lowest cell viability levels of 40% and 20% were recorded for loaded and free DNR and temozolomide, respectively. Free NCs maintained cell viability levels above 75% throughout the increasing concentrations. The cell viability levels at 72h treatment with the loaded and free DNR and temozolomide combination was ~15% to 20% lower compared to the 24h with the same combination.

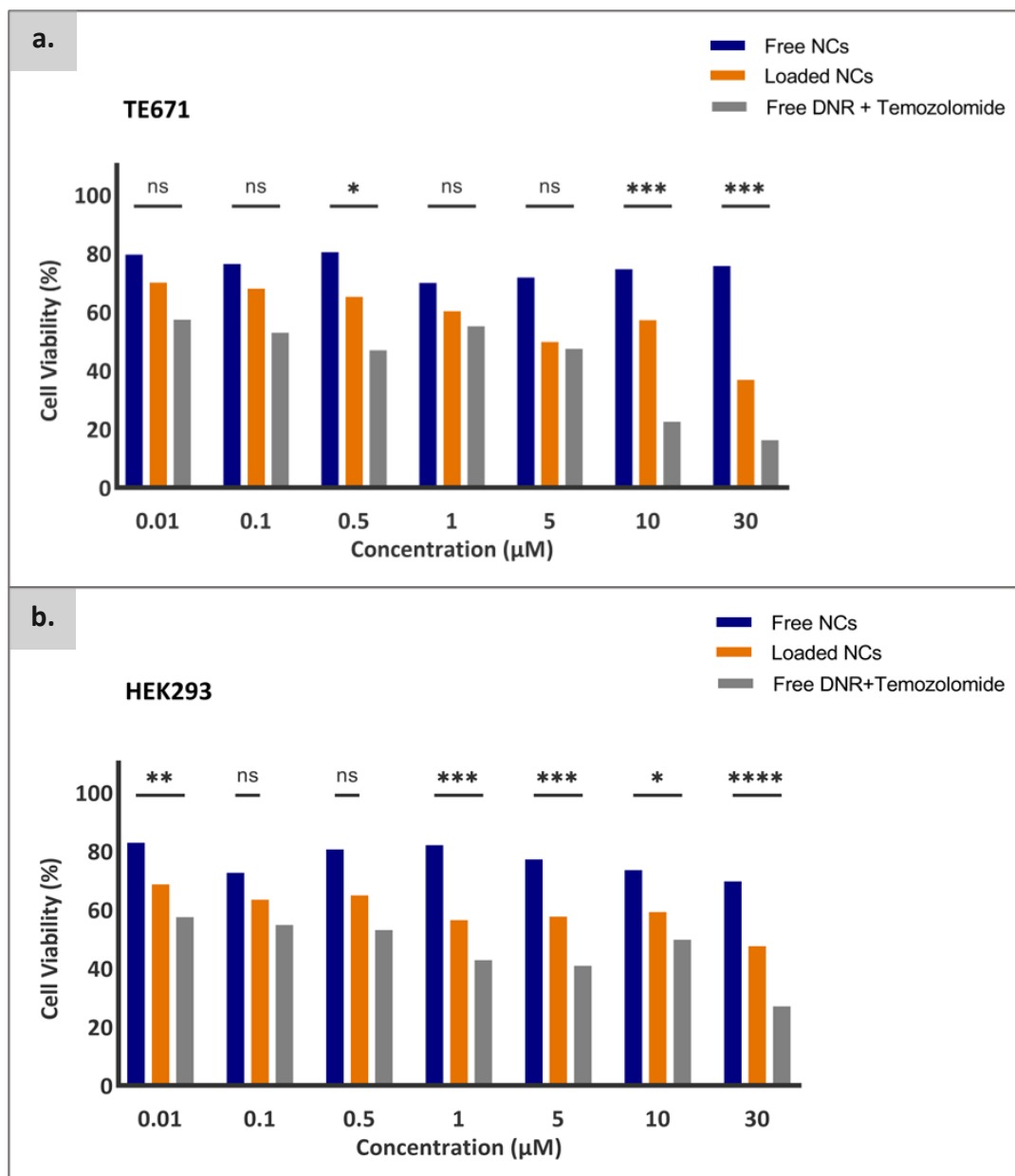


Figure 31. Evaluation of the cell viability via MTT assay. Cytotoxicity levels in **a).** TE671 and **b).** HEK293 cell lines after 72h treatment with free NCs, DNR/temozolomide combination loaded NCs, and free DNR/temozolomide combination. Two-way ANOVA test (ns $P > 0.05$, * $P \leq 0.05$, ** $P \leq 0.01$, *** $P \leq 0.001$, **** $P \leq 0.0001$), two independent experiments.

3.3.2. Cellular uptake and internalization

The cellular uptake of 5 μM rhodamine-loaded NCs (Table 11 & 12) by the two cell lines showed increasing red fluorescence as the incubation time increased (1h to 5h). This pattern was similar in the cells incubated with free rhodamine where fluorescence intensity increased as the incubation time increased. Free rhodamine showed slightly higher overall red fluorescence intensity compared to the loaded rhodamine. In both free and loaded rhodamine, the morphology of the cells appeared altered after the treatment exposure.

Table 11. Cellular uptake evaluation of rhodamine loaded-nanocontainers and free rhodamine by fluorescence microscopy TE671 rhabdomyosarcoma cell line.

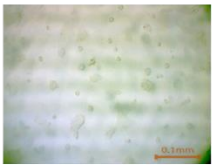
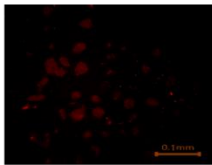
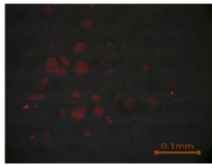
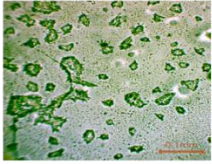
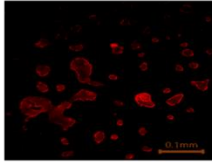
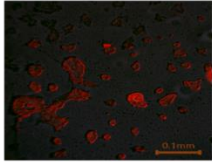
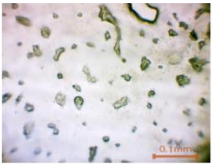
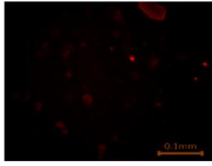
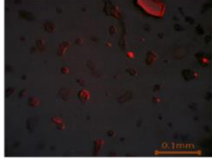
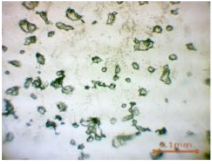
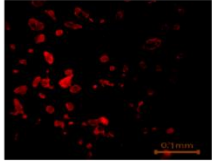
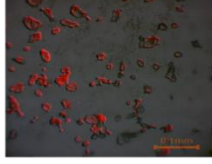
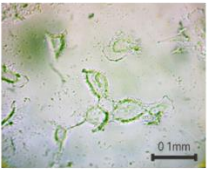
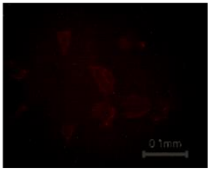
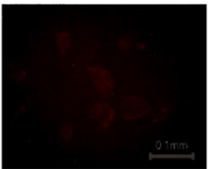
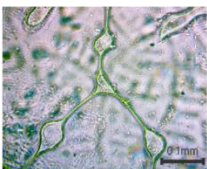
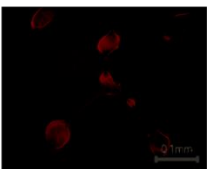
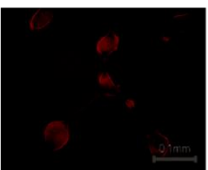
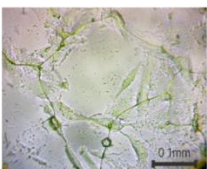
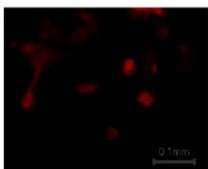
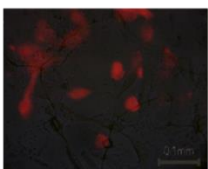
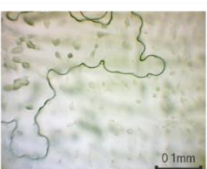
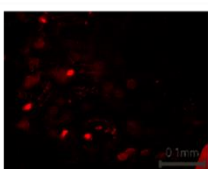
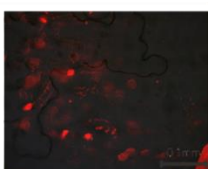
Time point (h)		Standard Light	Green Light	Overlay
1	Loaded RhB			
	Free RhB			
5	Loaded RhB			
	Free RhB			

Table 12. Cellular uptake evaluation of rhodamine loaded-nanocontainers and free rhodamine by fluorescence microscopy in HEK293 control cell line.

Time point (h)		Standard Light	Green Light	Overlay
1	Loaded RhB			
	Free RhB			
5	Loaded RhB			
	Free RhB			

The cellular uptake analysis in HEK293 (Table 13) and TE671 cell lines (Table 14) of the free and rhodamine loaded NCs was repeated since the previous experiments showed altered morphology of the cells. In addition to the free and loaded rhodamine, the cells were also stained with 200nM MitoView. The fluorescence of 50 μ M free and rhodamine loaded NCs loaded, showed increasing red fluorescence at increasing time points of incubation (30 min, 4h, and 24h) in the HEK293 cell line (Table13) as well as in the TE671 cell line (Table 14). The fluorescence of the rhodamine loaded NCs (50 μ M) in both cell lines was similar to the fluorescence exhibited in the cells incubated with free rhodamine (50 μ M) at the same time

points and had a matching fluorescence pattern as the green fluorescence exhibited by the MitoView. Yet, the overall exhibited fluorescence of free rhodamine was marginally higher than the loaded version.

Table 13. Evaluation of the cellular uptake of rhodamine loaded-nanocontainers and free rhodamine by fluorescence microscopy in HEK293 control cell line.

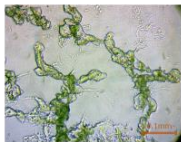
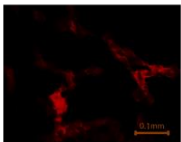
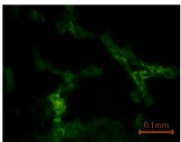
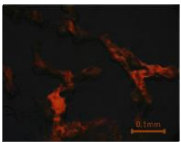
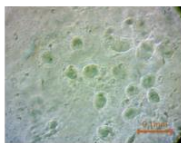
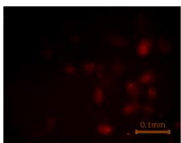

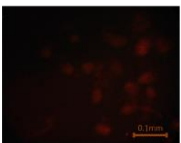
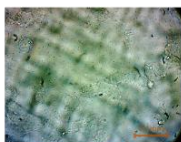
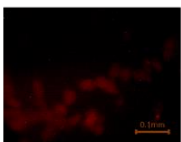


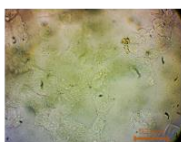
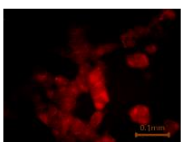
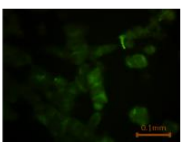

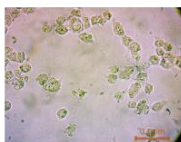
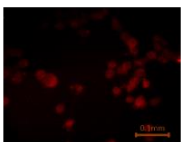
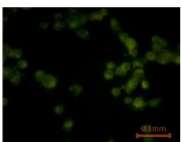
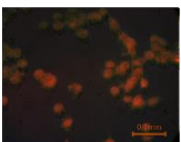
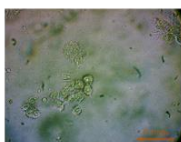
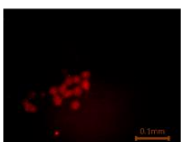
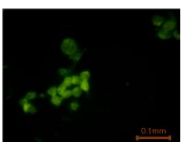

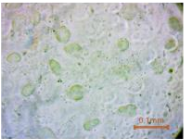
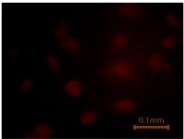
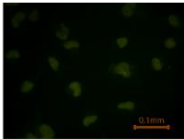
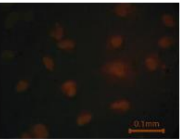
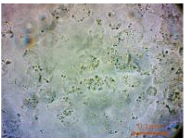
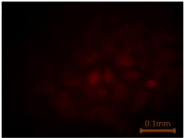
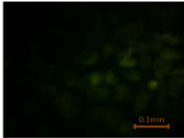
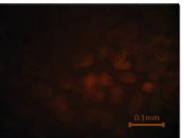
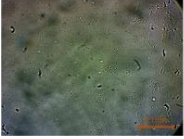
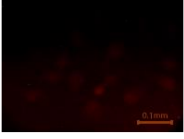


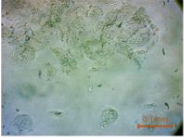
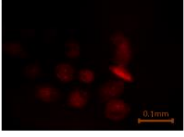
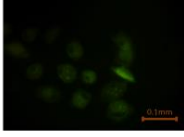
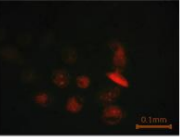
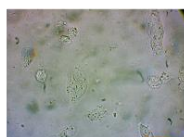
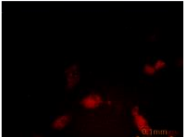
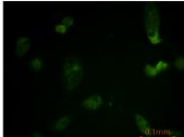
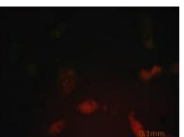

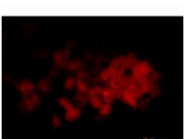

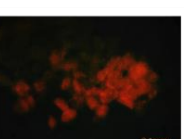
Time point (h)		Standard Light	Green Light	Blue Light	Overlay
0.5	Loaded RhB				
	Free RhB				
4	Loaded RhB				
	Free RhB				
24	Loaded RhB				
	Free RhB				

Table 14. Evaluation of the cellular uptake of rhodamine loaded-nanocontainers and free rhodamine by fluorescence microscopy in TE671 rhabdomyosarcoma cell line.

Time point (h)		Standard Light	Green Light	Blue Light	Overlay
0.5	Loaded RhB				
	Free RhB				
4	Loaded RhB				
	Free RhB				
24	Loaded RhB				
	Free RhB				

3.3.3. Western blot

Western blot results from 24h treated cells showed variance in H2A.X bands across the samples (Figure 32). All the lanes representing treated TE671 samples with different loaded and free drugs (loaded and free temozolomide, cisplatin, and DNR) in Figure 32d, bands appeared fainter compared to the control, untreated, and NCs samples (Figure 32d). The GAPDH bands appeared equally intense for all the samples (Figure 32c). The band intensities of H2A.X in all samples of HEK293 appeared equally intense, whereas the GAPDH bands appeared relatively intense, as shown in Figures 32a&b.

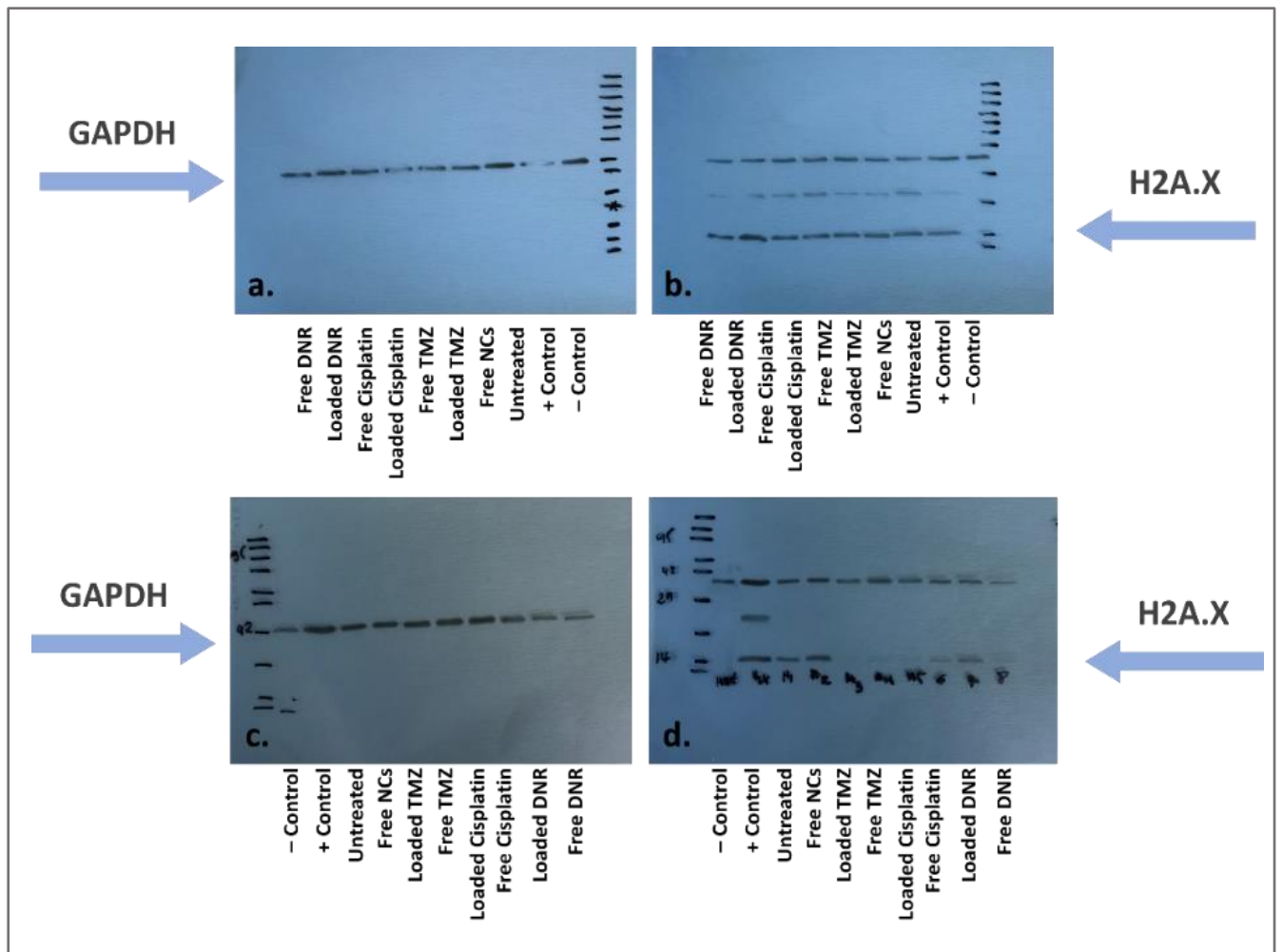


Figure 32. Immunoblotting results of H2A.X and GAPDH in HEK293 cell line (a and b) and TE671 cell line (c and d) after 24h treatment. Both cell lines were treated with free NCs, loaded and free temozolomide, cisplatin, and DNR. The H2A.X represents the protein of interest and the GAPDH represents the house keeping gene.

Assessment of DNA damage protein expression by western blot in rhabdomyosarcoma cell line treated with different loaded and free chemotherapy drugs (temozolomide, cisplatin, DNR, DNR/temozolomide combination) for 72h showed the good quality of bands (Figure 33a and b) and various levels of proportional H2A.X/GAPDH intensities (Figure 33c). Therefore, only the experiments with the 72h treated samples have proceeded for further analysis and calculations. Results of the visualised membranes by Fluorchem 8800 imager (Figure 33b)

showed protein bands at 15kDa in the TE671 samples treated with free NCs, loaded temozolomide, free temozolomide, and loaded cisplatin. In samples treated with free cisplatin, loaded DNR, free DNR, loaded DNR/temozolomide, and free DNR/temozolomide, negative bands were recorded in their corresponding lanes at 15kDa. Figure 32a showed equal housekeeping gene GAPDH bands for all samples at 37kDa. The results of the calculated proportional intensity of phosphorylated H2A.X and GAPDH (Figure 33c) corresponded to the band intensity results in Figures 32a and b. The highest H2A.X intensity levels were recorded in the positive control with a 1.5 ratio followed by ~1.4 less intensity in the untreated and the free NCs treated samples, respectively. Samples treated with loaded temozolomide, free temozolomide, and loaded cisplatin showed intensity ratios between 0.08 and 0.1. Accordingly, with the membranes' images, no H2A.X/GAPDH ratios were recorded in samples treated with free cisplatin, loaded DNR, free DNR, loaded temozolomide/DNR combination, and free temozolomide/DNR combination.

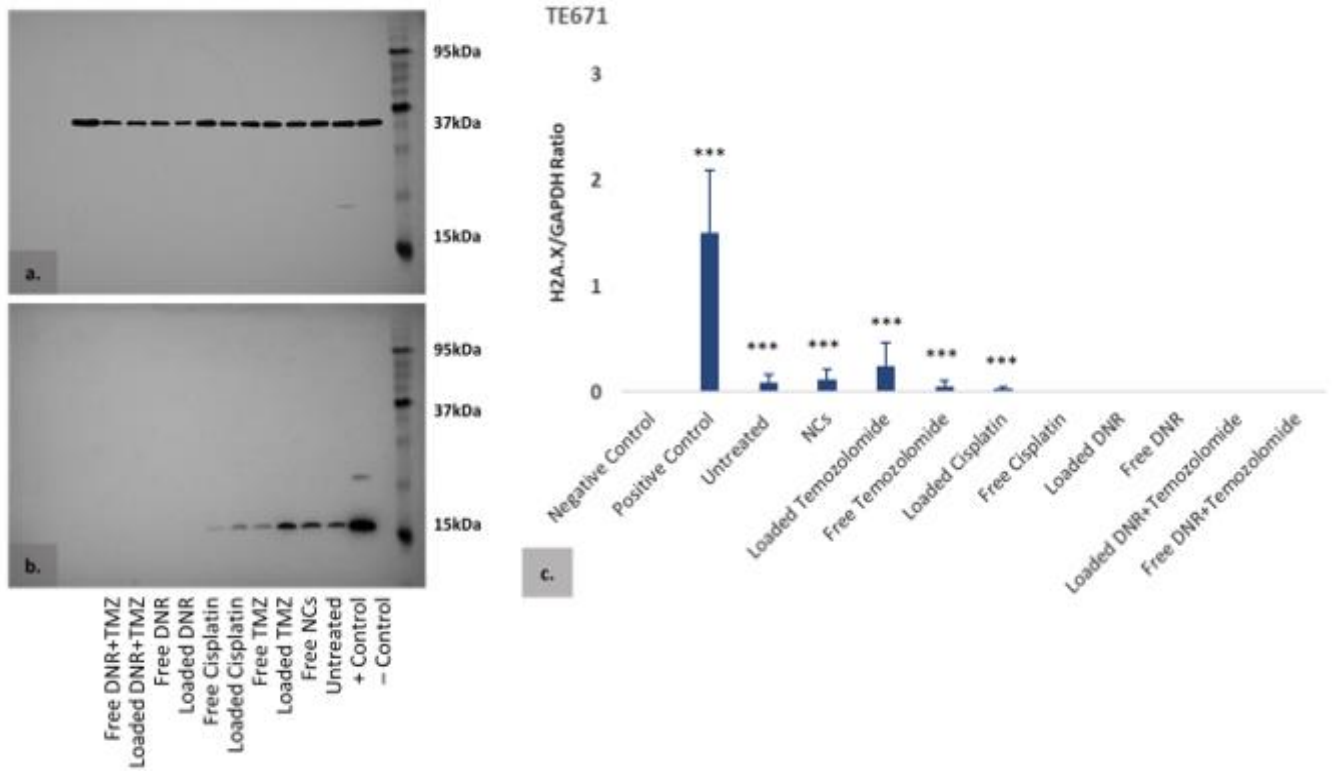


Figure 33. Western blot analysis results of DNA damage protein expression in TE671 rhabdomyosarcoma cell line. a) and b) after 72h treatment. GAPDH and γ -H2A.X protein expression in TE671 cell line; Samples of TE671 cell line were treated with free nanocontainers, free and loaded temozolomide, cisplatin, DNR, and DNR/temozolomide combination. HaCat and HEK293 cell lines were used as negative and positive control, respectively; c). Protein bands quantification results expressed as ratio of H2A.X/GAPDH. Error bars represent \pm SD of three experiments. *** $P \leq 0.001$; P-values were calculated with one-way ANOVA.

Western blot results of HEK293 showed variation in phosphorylated H2A.X bands intensities for the different samples (Figure 34). Samples treated with free NCs, loaded temozolomide, free temozolomide, and loaded cisplatin showed the highest bands intensity compared to the fainter bands in samples treated with free cisplatin, loaded DNR, free DNR, loaded DNR/temozolomide, and free DNR/temozolomide (Figure 34b). The GAPDH bands at 37kDa appeared equally intense for all analysed samples (Figure 34a). The results of the calculated proportional intensity of H2A.X and GAPDH (Figure 34c) corresponded to the bands intensity results in Figures 33a and 33b. The highest H2A.X intensity levels were recorded in the untreated samples and loaded cisplatin treated samples with 1.2 and ~1.5, respectively. Samples treated with loaded temozolomide, free temozolomide, and free cisplatin showed intensity ratios between 0.9 and 0.4. The lowest H2A.X/GAPDH ratio of 0.1 to 0.3 was recorded in samples treated with loaded DNR, free DNR, loaded temozolomide/DNR combination, and free temozolomide/DNR combination.

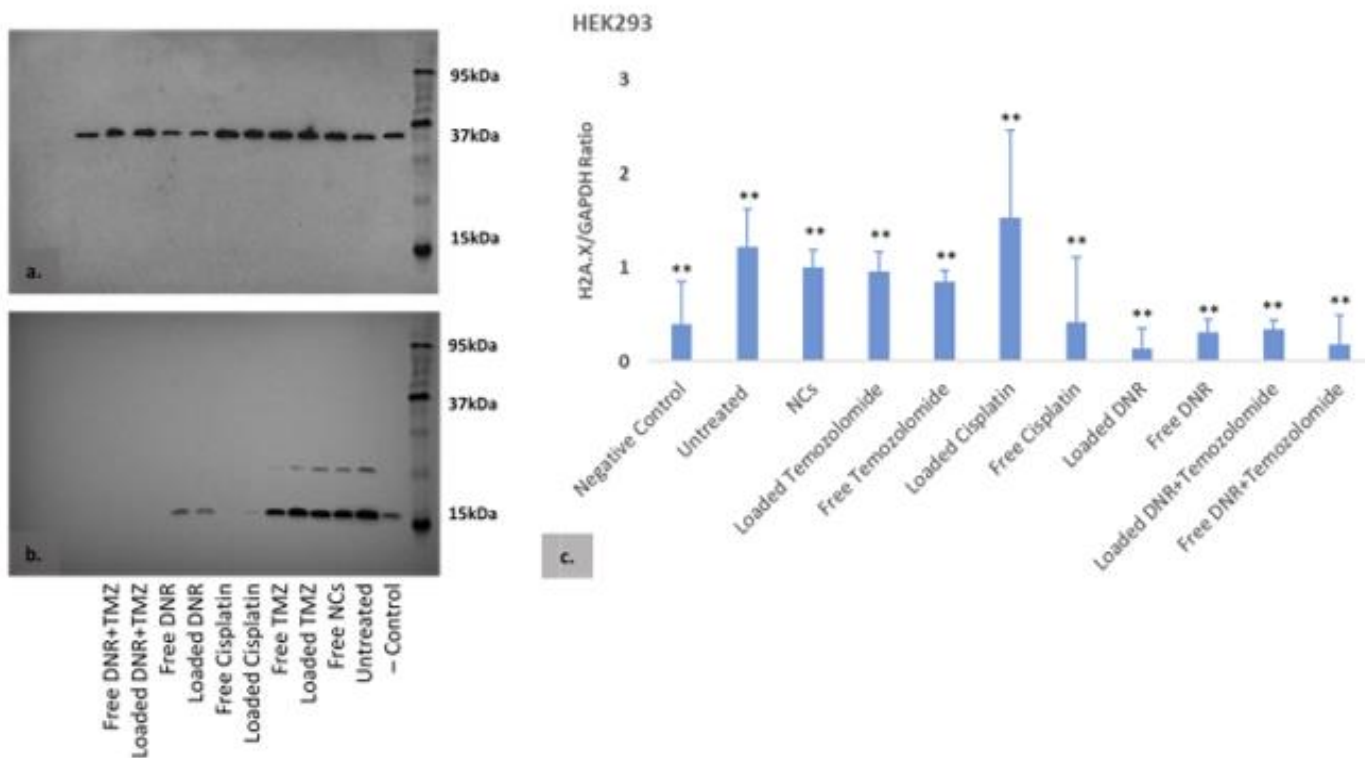


Figure 34. Western blot analysis results of DNA damage protein expression in HEK293 rhabdomyosarcoma cell line. a) and b) after 72h treatment. GAPDH and γ -H2A.X protein expression in HEK293 cell line; Samples of HEK293 cell line were treated with free nanocontainers, free and loaded temozolomide, cisplatin, DNR, and DNR/temozolomide combination. HaCat cell line was used as negative control; c). Protein bands quantification results expressed as ratio of H2A.X/GAPDH. Error bars represent \pm SD of three experiments. ****P \leq 0.01**; P-values were calculated with one-way Anova.

Of note, the BCL-s and caspase-8 antibodies were not effective even at the lowest dilution (1:50). There was no signal detected in the last lane (position 13 and 11 on the left of the ladder in TE671 and HEK293 membranes, respectively) that was used as a positive control for caspase 8. There was no available positive control for BCL-2 in the lab.

3.3.4. Flow cytometry

Apoptosis analysis by flow cytometry for 24h in the TE671 cell line showed different apoptosis levels for the different treatments applied (Figure 35). The four different quadrants Q4, Q3, Q2, and Q1 in the dot plots corresponded to the viable cells, early apoptotic cells, late apoptotic cells, and necrotic cells, respectively. Higher percentages of early apoptotic, late apoptotic, and necrotic cells were observed in samples treated with loaded and free temozolomide, cisplatin, DNR, and DNR/temozolomide combination compared to the untreated and NCs treated samples.

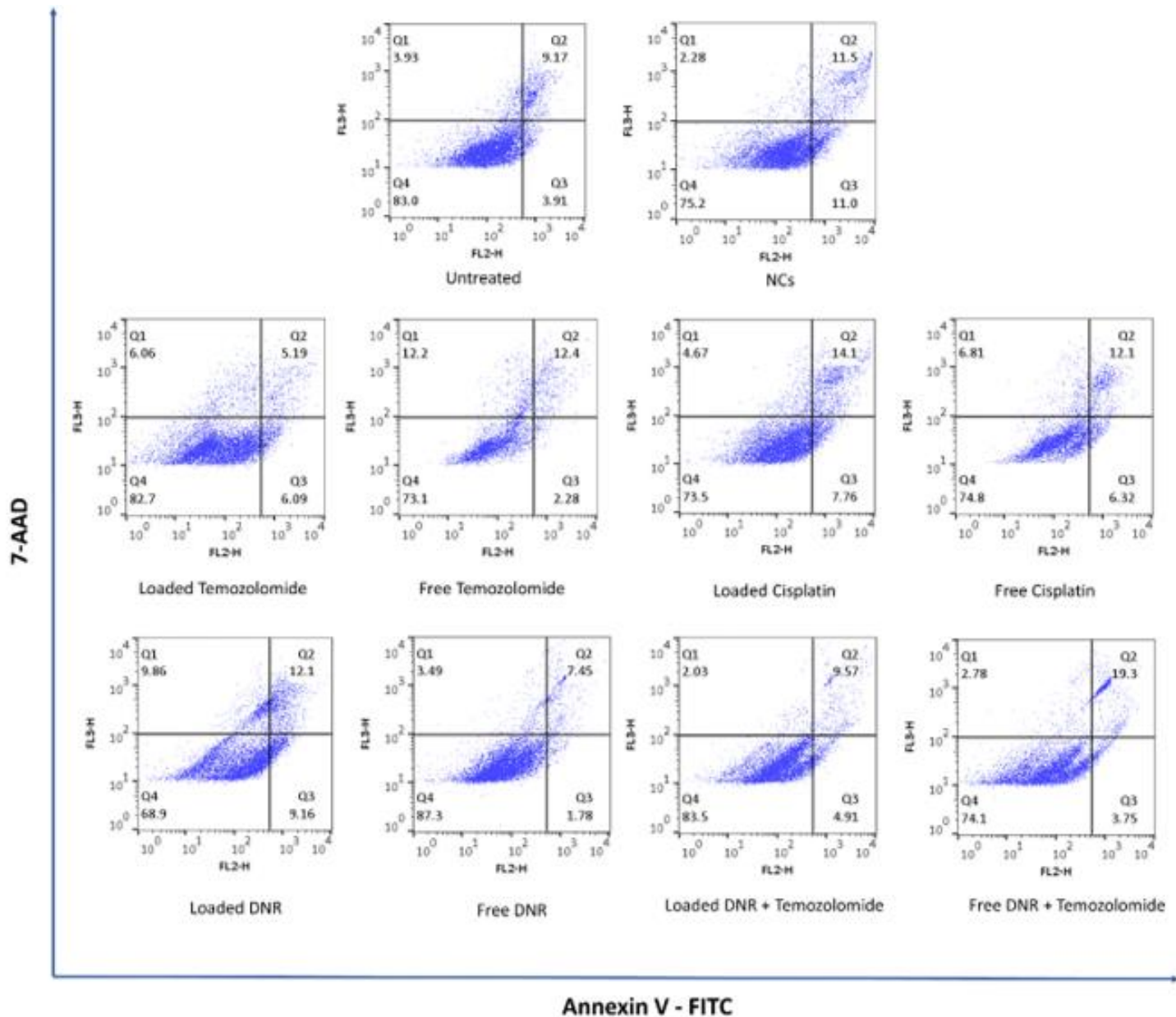


Figure 35. Apoptosis analysis by flow cytometry in rhabdomyosarcoma cells treated by free NCs, loaded and free temozolomide, cisplatin, DNR, and DNR/temozolomide combination for 24h. Based on Annexin V/7AAD staining, Q4 (Annexin V⁻/7AAD⁻) represents viable cells, Q3 (Annexin V⁺/7AAD⁻) represents early apoptotic cells, Q2 (Annexin V⁺/7AAD⁺) represents late apoptotic cells, Q1 (Annexin V⁻/7AAD⁺) represent necrotic/dead cells.

Calculated percentages of total apoptotic, necrotic, and viable cells for the different treatments applied are shown in Figure 36. Higher total apoptotic percentages of 18% to 30% were recorded in all samples treated with the loaded and free temozolomide, cisplatin, DNR, and DNR/temozolomide combination compared to the untreated and NCs treated samples. Highest necrotic percentages of 10% to 18% were recorded in samples treated with loaded temozolomide, free temozolomide, loaded cisplatin, free cisplatin, and loaded DNR. Viable cells percentages were all above 70%, excluding loaded cisplatin and loaded DNR samples which had a 10% lower cell viability than the rest of the samples.

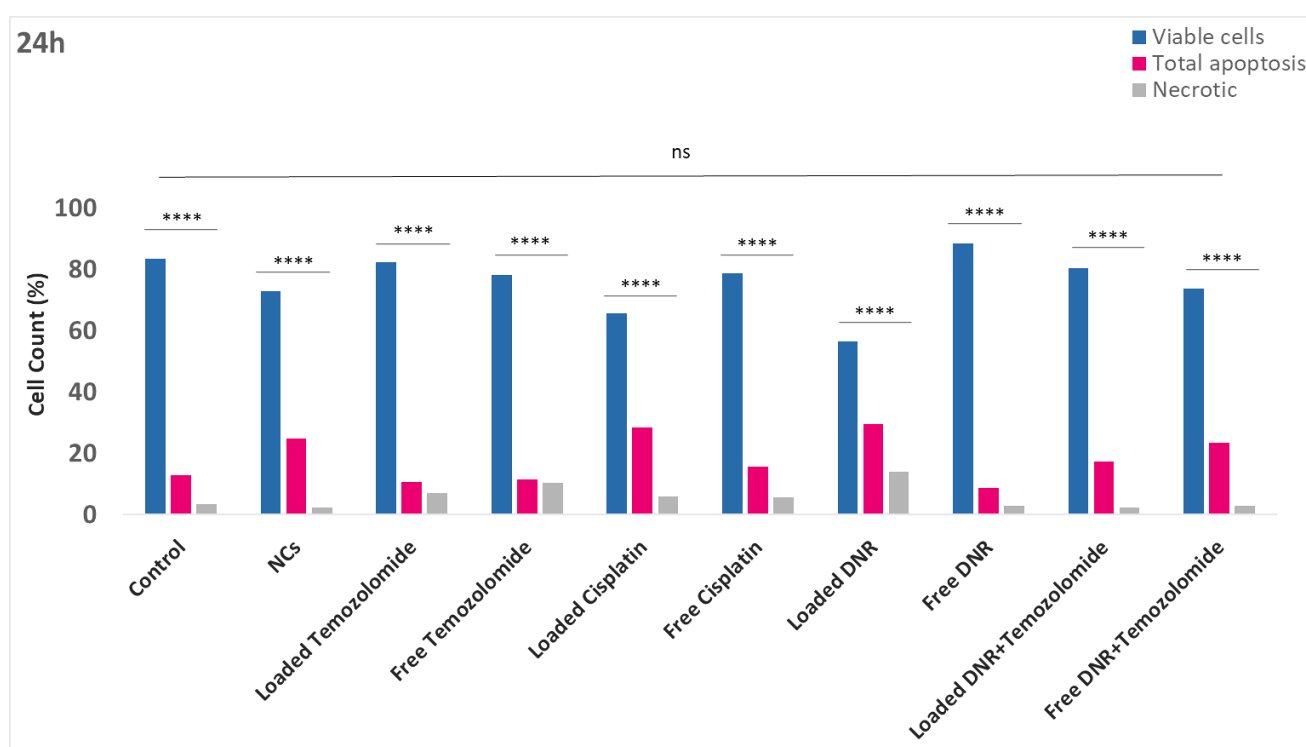


Figure 36. Calculated percentages of cell apoptosis in rhabdomyosarcoma cells treated by free NCs, loaded and free temozolomide, cisplatin, DNR, and DNR/temozolomide combination for 24h. Total apoptosis percentage represents the late and early apoptosis percentages together. **** $P \leq 0.0001$, ns $P > 0.05$ and it was a comparison between all treatments; p-values were calculated for duplicates with two-way ANOVA.

Apoptosis analysis of the TE671 cell line after 72h treatment (Figure 37) showed higher apoptosis levels for the different treatments applied compared to the 24h. Higher percentages of early apoptotic, late apoptotic, and necrotic cells were observed in corresponding quadrants for the samples treated with loaded and free temozolomide, cisplatin, DNR, and DNR/temozolomide combination compared to the untreated and NCs treated samples.

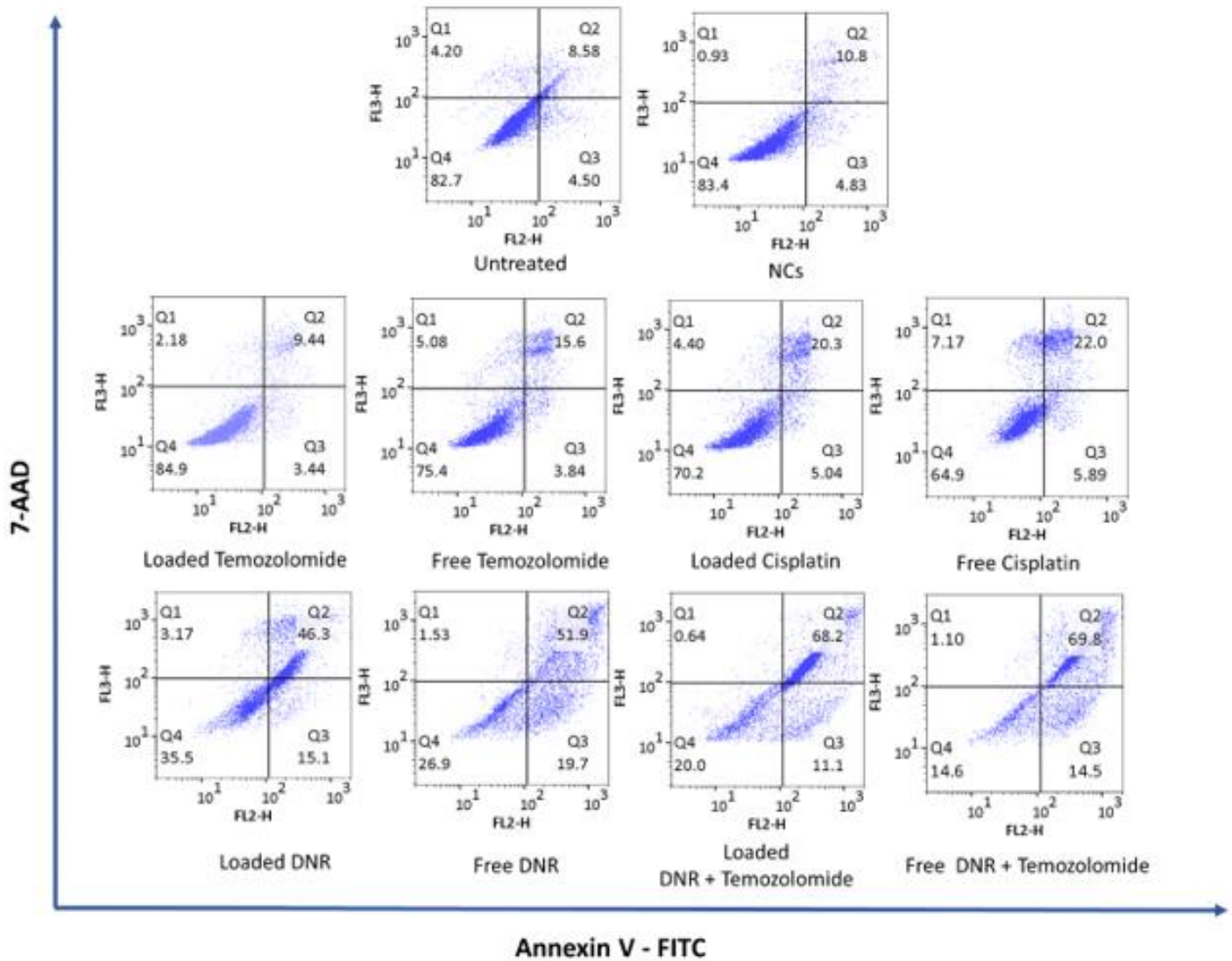


Figure 37. Apoptosis analysis by flow cytometry in rhabdomyosarcoma cells treated by free NCs, loaded and free temozolomide, cisplatin, DNR, and DNR/temozolomide combination for 72h. Based on Annexin V/7AAD staining, Q4 (Annexin V⁻/7AAD⁻) represents viable cells, Q3 (Annexin V⁺/7AAD⁻) represents early apoptotic cells, Q2 (Annexin V⁺/7AAD⁺) represents late apoptotic cells, Q1 (Annexin V⁻/7AAD⁺) represent necrotic/dead cells.

Calculated percentages of total apoptotic, necrotic, and viable cells for the different treatments applied to TE671 cells are shown in Figure 38. Higher total apoptotic percentages of 78% to 82% were recorded in samples treated with loaded DNR, free DNR, loaded DNR/temozolomide, and free DNR/temozolomide. These percentages were ~ 40% to 50% higher than the total apoptosis percentages after 24h with the same treatments. Samples treated with loaded and free temozolomide and cisplatin showed a 5% to 10% increase in total apoptotic cell percentages compared to the 24h treatment, with > 60% cell viability. Untreated cells and NCs treated cells showed relatively similar total apoptotic percentages of 10% to 14% and > 70% viable cells for both 24h and 72h. Necrotic cells retained a $\leq 6\%$ in all samples.

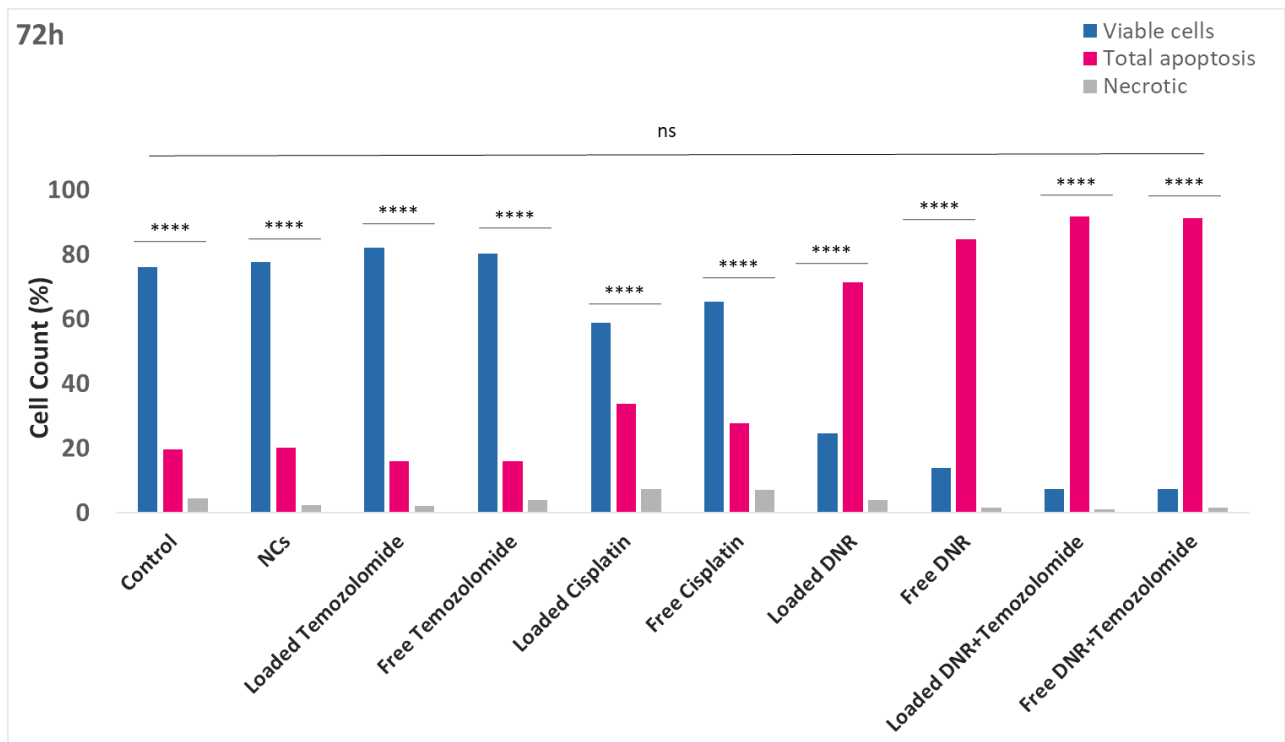


Figure 38. Calculated percentages of cell apoptosis in rhabdomyosarcoma cells treated by free NCs, loaded and free temozolomide, cisplatin, DNR, and DNR/temozolomide combination for 72h. Total apoptosis percentage represents the late and early apoptosis percentages together. **** $P \leq 0.0001$, ns $P > 0.05$ and it was a comparison between all treatments; p-values were calculated for duplicates with two-way ANOVA.

Apoptosis levels were assessed by flow cytometry in the HEK293 cell line and showed different apoptosis levels for the different treatments applied for 24h (Figure 39). The four different quadrants Q4, Q3, Q2, and Q1 in the dot plots corresponded to the viable cells, early apoptotic cells, late apoptotic cells, and necrotic cells, respectively. Higher percentages of early apoptotic, late apoptotic, and necrotic cells were observed in samples treated with NCs, loaded and free temozolomide, cisplatin, DNR, and DNR/temozolomide combination compared to the untreated samples.

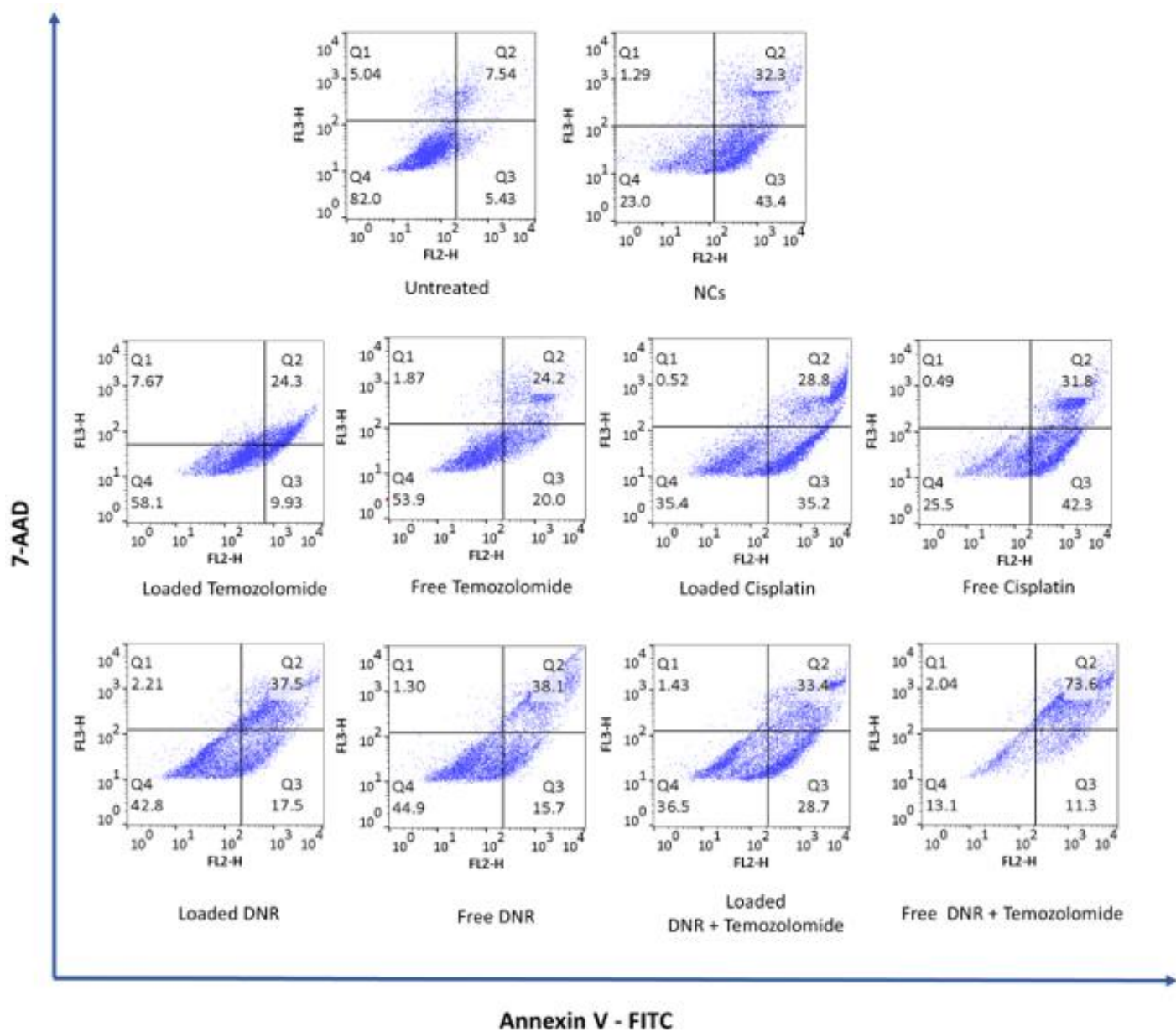


Figure 39. Apoptosis analysis by flow cytometry in HEK293 cells treated by free NCs, loaded and free temozolomide, cisplatin, DNR, and DNR/temozolomide combination for 24h. Based on Annexin V/7AAD staining, Q4 (Annexin V-/7AAD-) represents viable cells, Q3 (Annexin V+/7AAD-) represents early apoptotic cells, Q2 (Annexin V+/7AAD+) represents late apoptotic cells, Q1 (Annexin V-/7AAD+) represent necrotic/dead cells.

Calculated percentages of total apoptotic, necrotic, and viable cells for the different treatments applied in HEK293 for 24h were shown in Figure 40. All treatments applied for 24h showed 20% to 70% higher apoptotic levels than the 10% apoptosis in the untreated samples. The highest apoptosis percentage of ~85% was recorded in the samples treated with a free DNR/temozolomide combination. The necrotic percentages remained under 7% in all samples. Viable cell percentages showed an inversely proportional trend with the total apoptosis percentages in all samples.

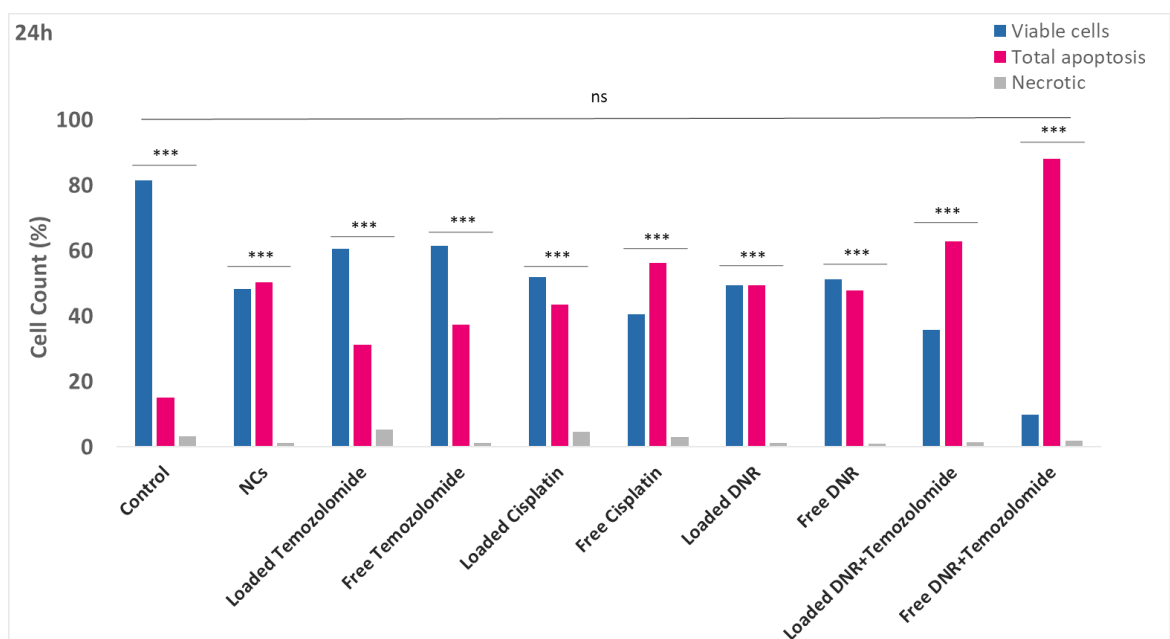


Figure 40. Calculated percentages of cell apoptosis in HEK293 cells treated by free NCs, loaded and free temozolomide, cisplatin, DNR, and DNR/temozolomide combination for 24h. Total apoptosis percentage represents the late and early apoptosis percentages together. *** $P \leq 0.001$, ns $P > 0.05$ and it was a comparison between all treatments; p-values were calculated for duplicates with two-way ANOVA.

Apoptosis analysis of the HEK293 cell line after 72h treatment (Figure 41) showed relatively similar apoptosis levels for the different treatments applied compared to the 24h. Yet, higher necrotic levels were observed in the Q1 quadrants compared to the levels observed in 24h treatment.

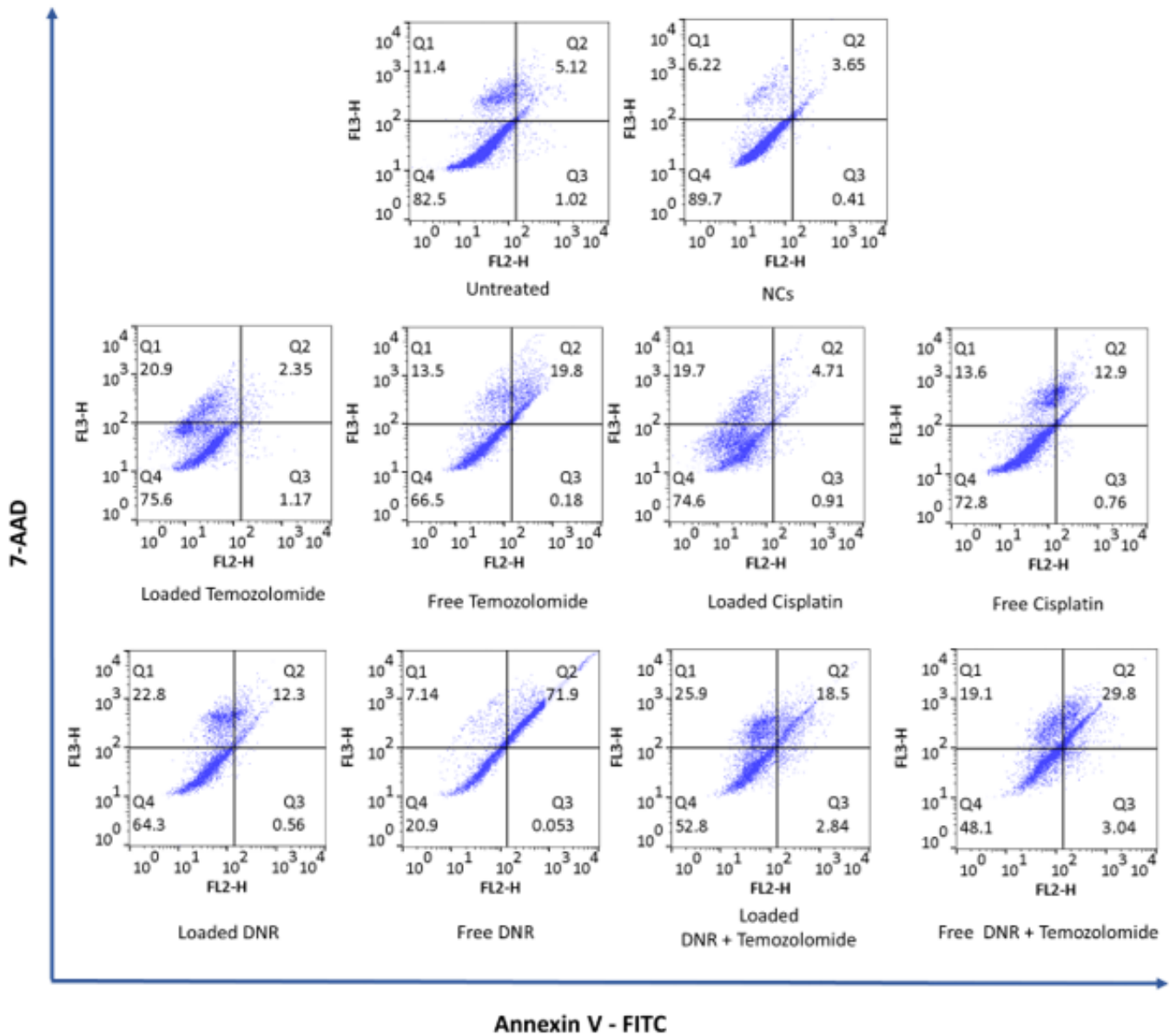


Figure 41. Apoptosis analysis by flow cytometry in HEK293 cells treated by free NCs, loaded and free temozolomide, cisplatin, DNR, and DNR/temozolomide combination for 72h. Based on Annexin V/7AAD staining, Q4 (Annexin V-/7AAD-) represents viable cells, Q3 (Annexin V+/7AAD-) represents early apoptotic cells, Q2 (Annexin V+/7AAD+) represents late apoptotic cells, Q1 (Annexin V-/7AAD+) represent necrotic/dead cells.

Calculated percentages of total apoptotic, necrotic, and viable cells for the different treatments applied on the HEK293 cell line for 72h were shown in Figure 42. All treatments applied for 72h showed an average of ~30% higher apoptotic levels than apoptosis in the untreated samples. Also, the total apoptotic percentages were ~20% lower than the 24h across treatments applied. Yet, necrotic percentages were on average ~15% higher than the levels recorded in the 24h treatment. The highest apoptotic percentage of ~30% and ~60% were recorded in the free DNR, and free DNR/temozolomide, respectively. In all samples analysed after 72h treatment, viable cells retained > 50% levels, excluding the sample treated with free DNR that showed 20% viable cells.

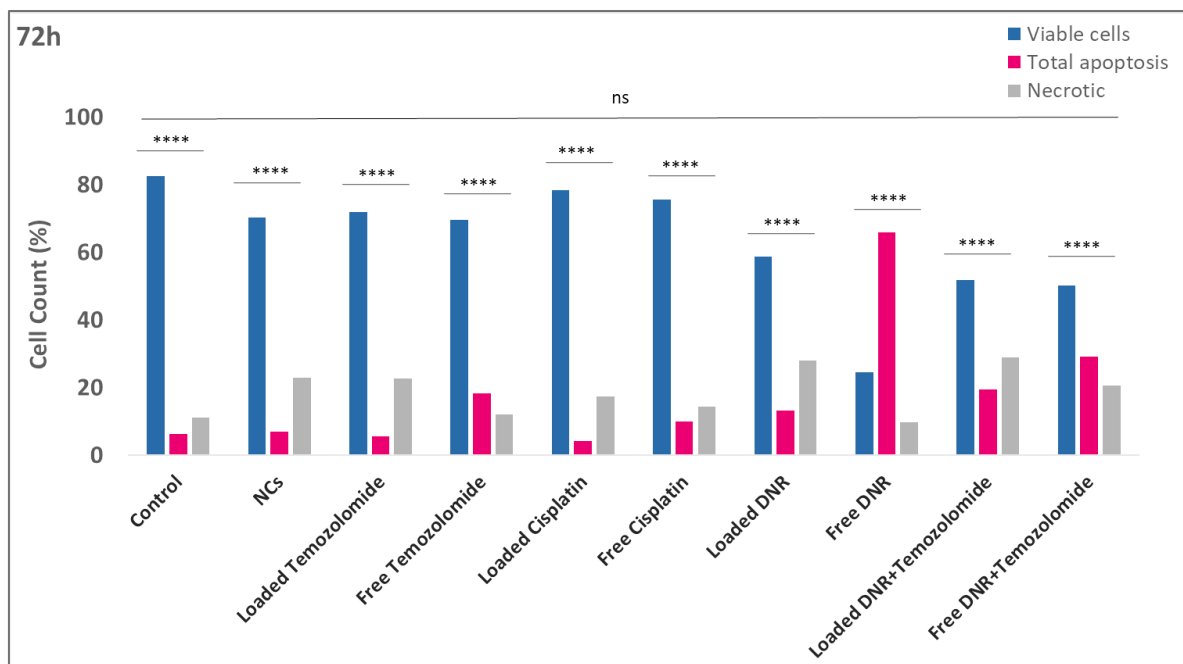


Figure 42. Calculated percentages of cell apoptosis in HEK293 cells treated by free NCs, loaded and free temozolomide, cisplatin, DNR, and DNR/temozolomide combination for 72h. Total apoptosis percentage represents the late and early apoptosis percentages together. **** $P \leq 0.001$, ns $P > 0.05$ and it was a comparison between all treatments; P-values were calculated for duplicates with two-way ANOVA.

Results of the cell cycle analysis by flow cytometry of TE671 after 24h treatment with NCs, loaded and free temozolomide, cisplatin, DNR, and DNR/temozolomide combination showed variations in the levels of cell cycle phases G1, S and G2 (Figure 43).

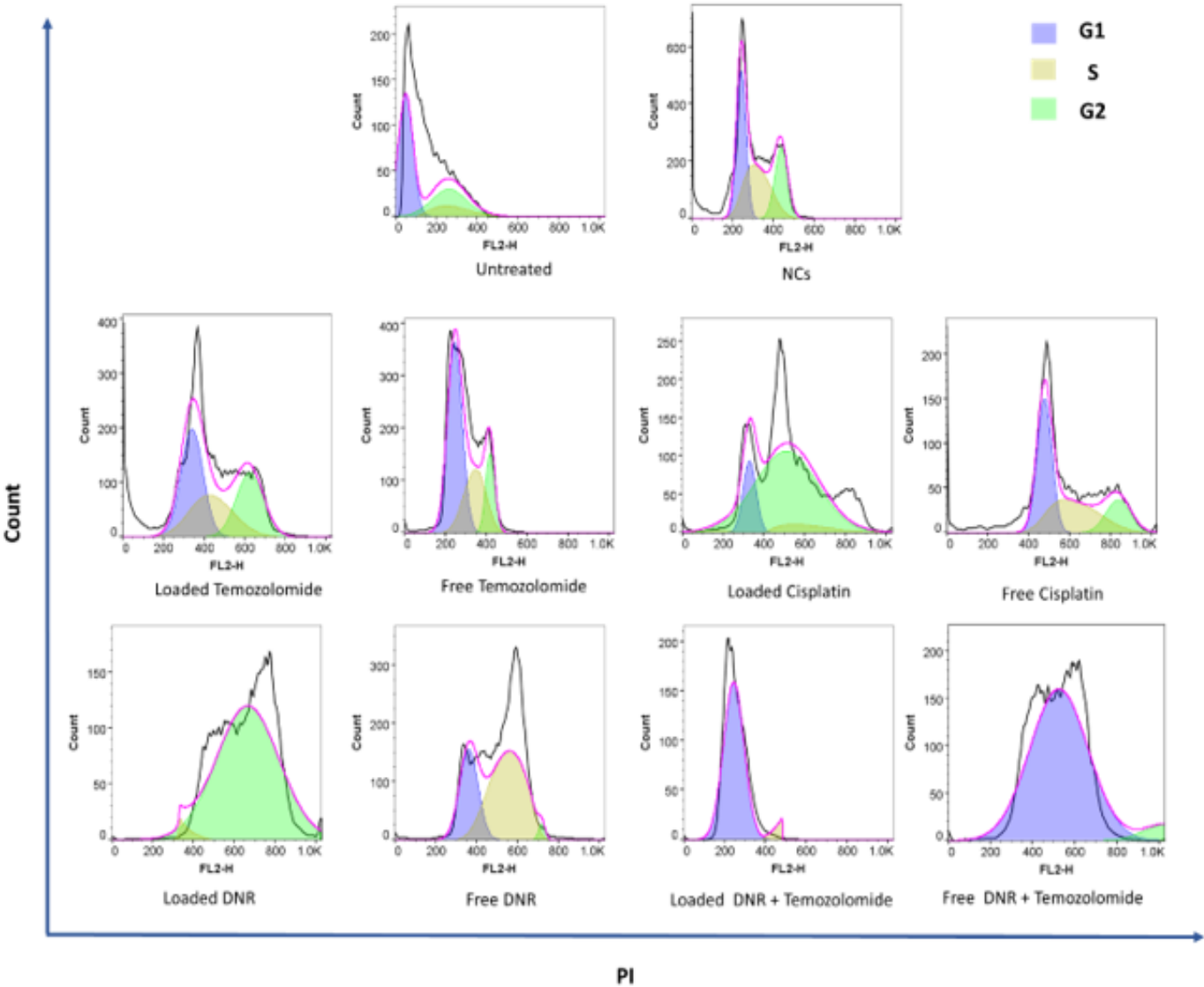


Figure 43. Cell cycle analysis of TE671 cells treated by free NCs, loaded and free temozolomide, cisplatin, DNR, and DNR/temozolomide combination for 24h. Propidium iodide (PI) stain distinguishes between the G1, S, and G2 phases based on DNA content.

Percentages of the G1, S and G2 phases of the cell cycle were variant across the applied treatments on TE671 cells for 24h (Figure 44). Similarly, with the control (untreated) cells, treatment with NCs, loaded temozolomide, free cisplatin, and free DNR showed 8% to 38% S phase cells. The rest of the treatments showed S phase percentages between 2% and 6%. Also, the highest G1 levels of > 50% were recorded in samples treated with free temozolomide, loaded DNR/temozolomide, and free DNR/temozolomide. The highest G2 levels of > 50% were recorded in samples treated with loaded cisplatin, free cisplatin and loaded DNR.

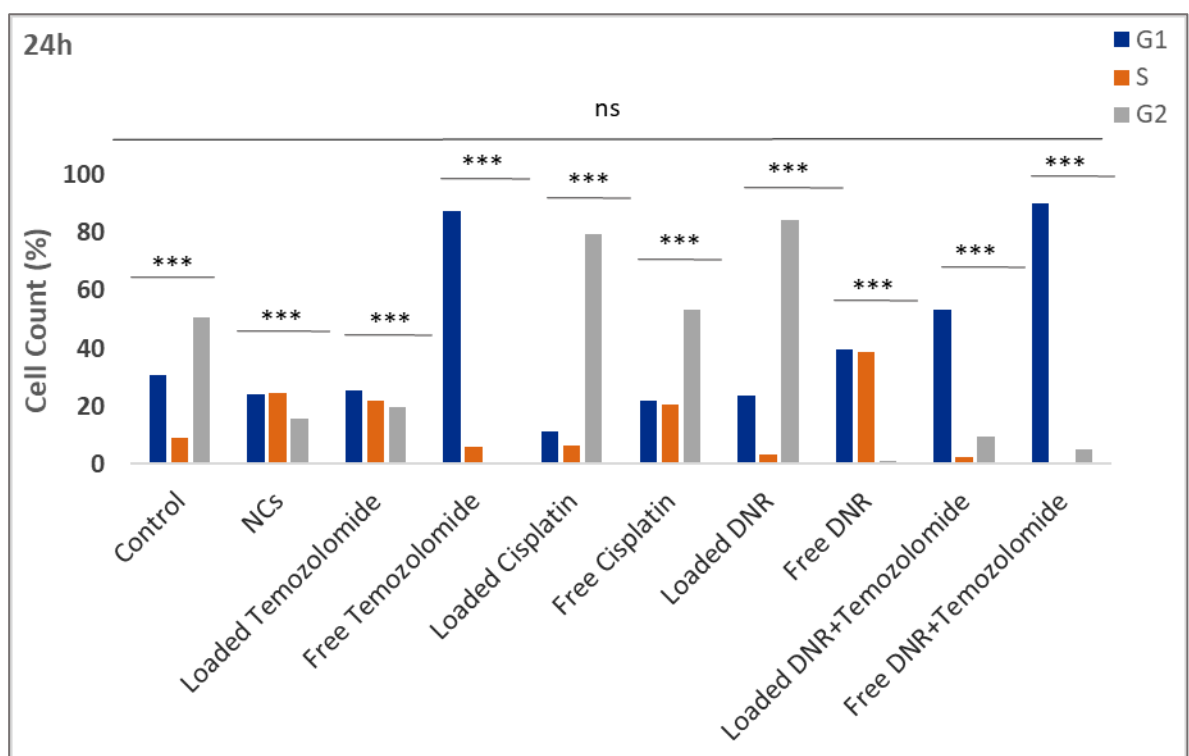


Figure 44. Percentages of the different phases of the cell cycle (G1, S, G2) of TE671 cells treated by free NCs, loaded and free temozolomide, cisplatin, DNR, and DNR/temozolomide combination for 24h. *** $P \leq 0.001$, ns $P > 0.05$ and it was a comparison between all treatments; P-values were calculated for duplicates with two-way ANOVA.

Results of the cell cycle analysis by flow cytometry of TE671 after 72h treatment with NCs, loaded and free temozolomide, cisplatin, DNR, and DNR/temozolomide combination showed variations in the levels of cell cycle phases G1, S and G2 (Figure 45).

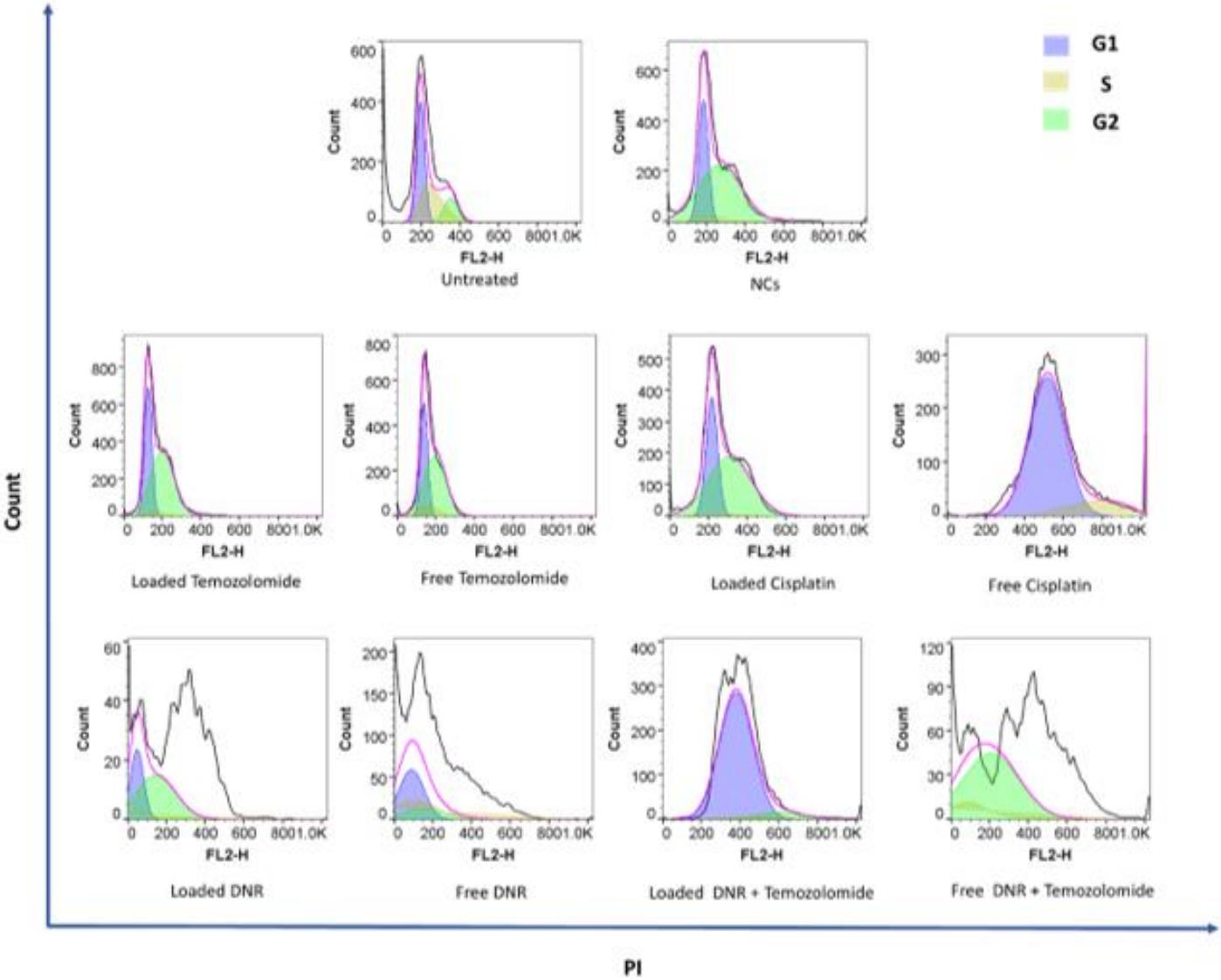


Figure 45. Cell cycle analysis of TE671 cells treated by free NCs, loaded and free temozolomide, cisplatin, DNR, and DNR/temozolomide combination for 72h. Propidium iodide (PI) stain distinguishes between the G1, S, and G2 phases based on DNA content.

Percentages of the G1, S and G2 phases of the cell cycle were variant across the applied treatments after 72h (Figure 46). Across the different treatments applied, the S phase percentages were only between 0.6% and 14%, marking a 24% decrease compared to the levels in 24h treatment. Samples treated with free cisplatin and loaded DNR/temozolomide showed the highest G1 percentages with > 80%. The highest G2 percentages of ~55% were recorded in samples treated with NCs, loaded temozolomide, free temozolomide, loaded cisplatin, and free DNR/temozolomide.

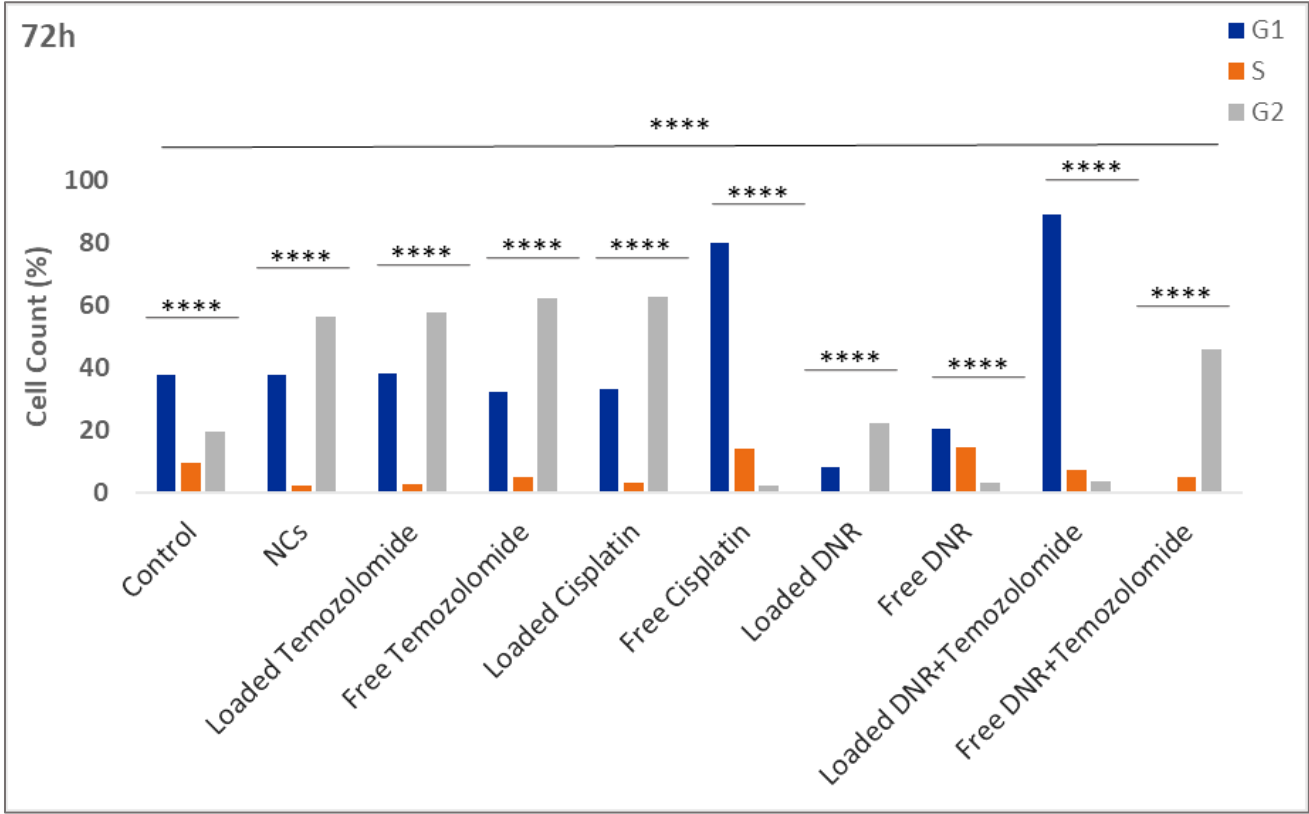


Figure 46. Percentages of the different phases of the cell cycle (G1, S, G2) of TE671 cells treated by free NCs, loaded and free temozolomide, cisplatin, DNR, and DNR/temozolomide combination for 72h. ****P ≤ 0.0001; P-values were calculated for duplicates with two-way ANOVA.

Results of the cell cycle analysis by flow cytometry of HEK293 after 24h treatment with NCs, loaded and free temozolomide, cisplatin, DNR, and DNR/temozolomide combination showed variations in the levels of cell cycle phases G1, S and G2 (Figure 47).

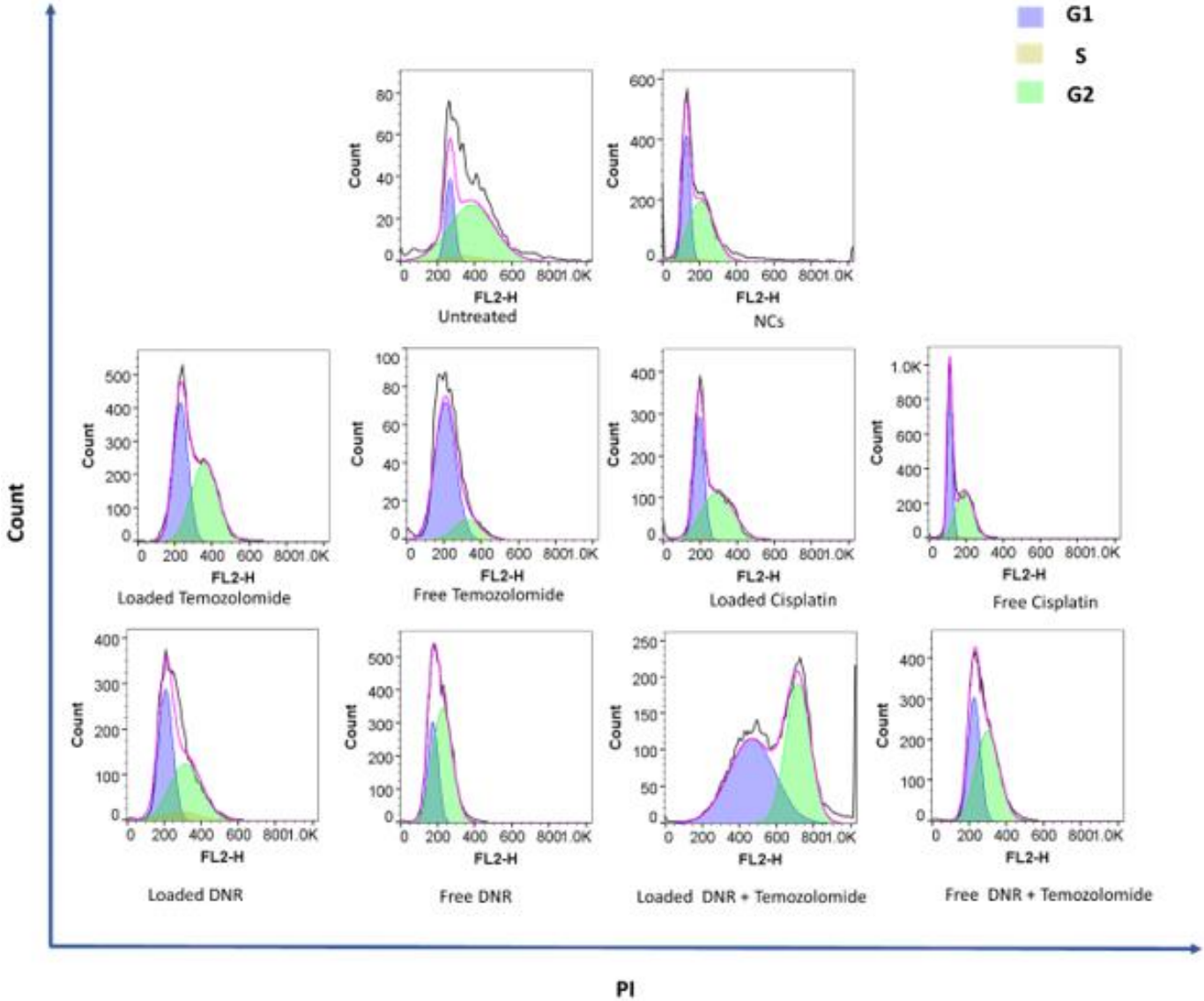


Figure 47. Cell cycle analysis of HEK293 cells treated by free NCs, loaded and free temozolomide, cisplatin, DNR, and DNR/temozolomide combination for 24h. Propidium iodide (PI) stain distinguishes between the G1, S, and G2 phases based on DNA content.

Percentages of the G1, S and G2 phases of the cell cycle were variant across the applied treatments on HEK293 cells after 24h (Figure 48). Across the different treatments applied, the S phase percentages were between 1% and 6%. Samples treated with free temozolomide, loaded DNR/temozolomide and free DNR/temozolomide showed higher G levels of > 80% than the G2 phase. The rest of the treatments applied showed relatively close percentages between the G1 and the G2 phases.

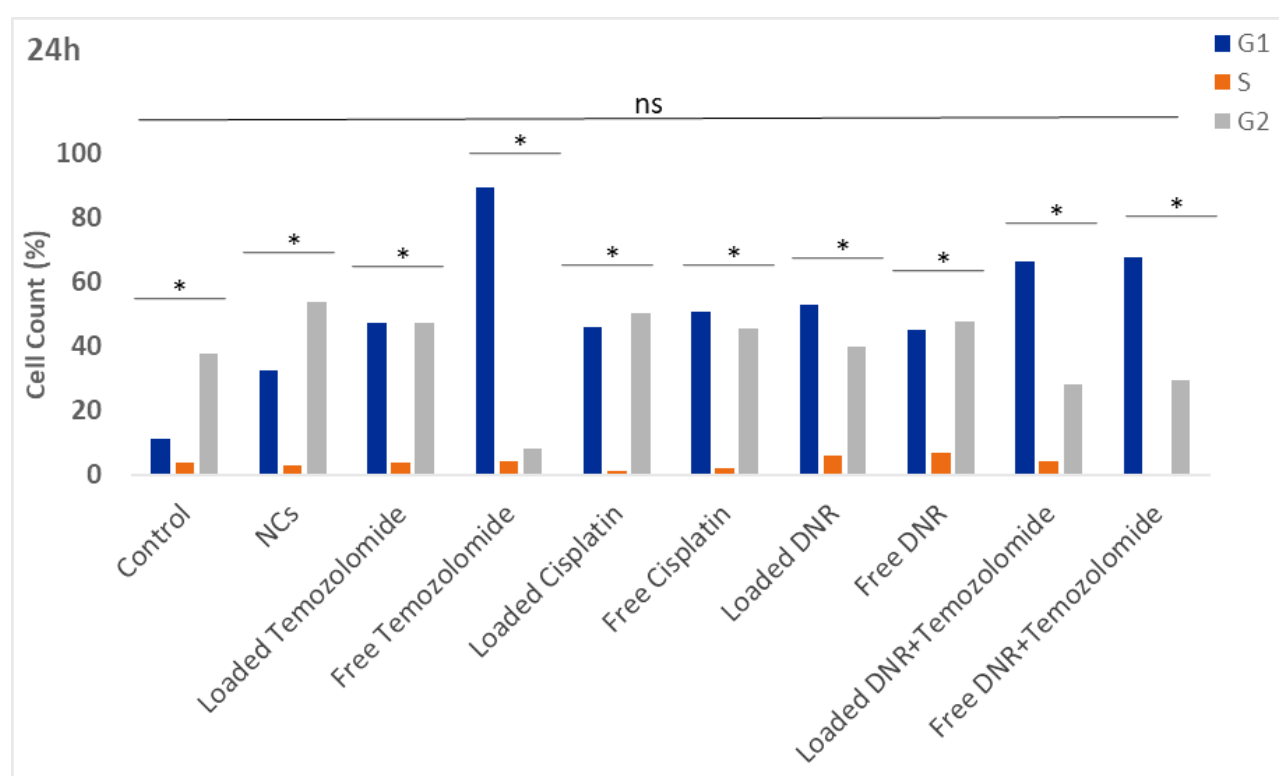


Figure 48. Percentages of the different phases of the cell cycle (G1, S, G2) of HEK293 cells treated by free NCs, loaded and free temozolomide, cisplatin, DNR, and DNR/temozolomide combination for 24h. * $P \leq 0.05$, ns $P > 0.05$ and it was a comparison between all treatments; P-values were calculated for duplicates with two-way ANOVA.

Cell cycle analysis results by flow cytometry of HEK293 after 72h treatment with NCs, loaded and free temozolomide, cisplatin, DNR, and DNR/temozolomide combination showed variations in the levels of cell cycle phases G1, S and G2 (Figure 49).

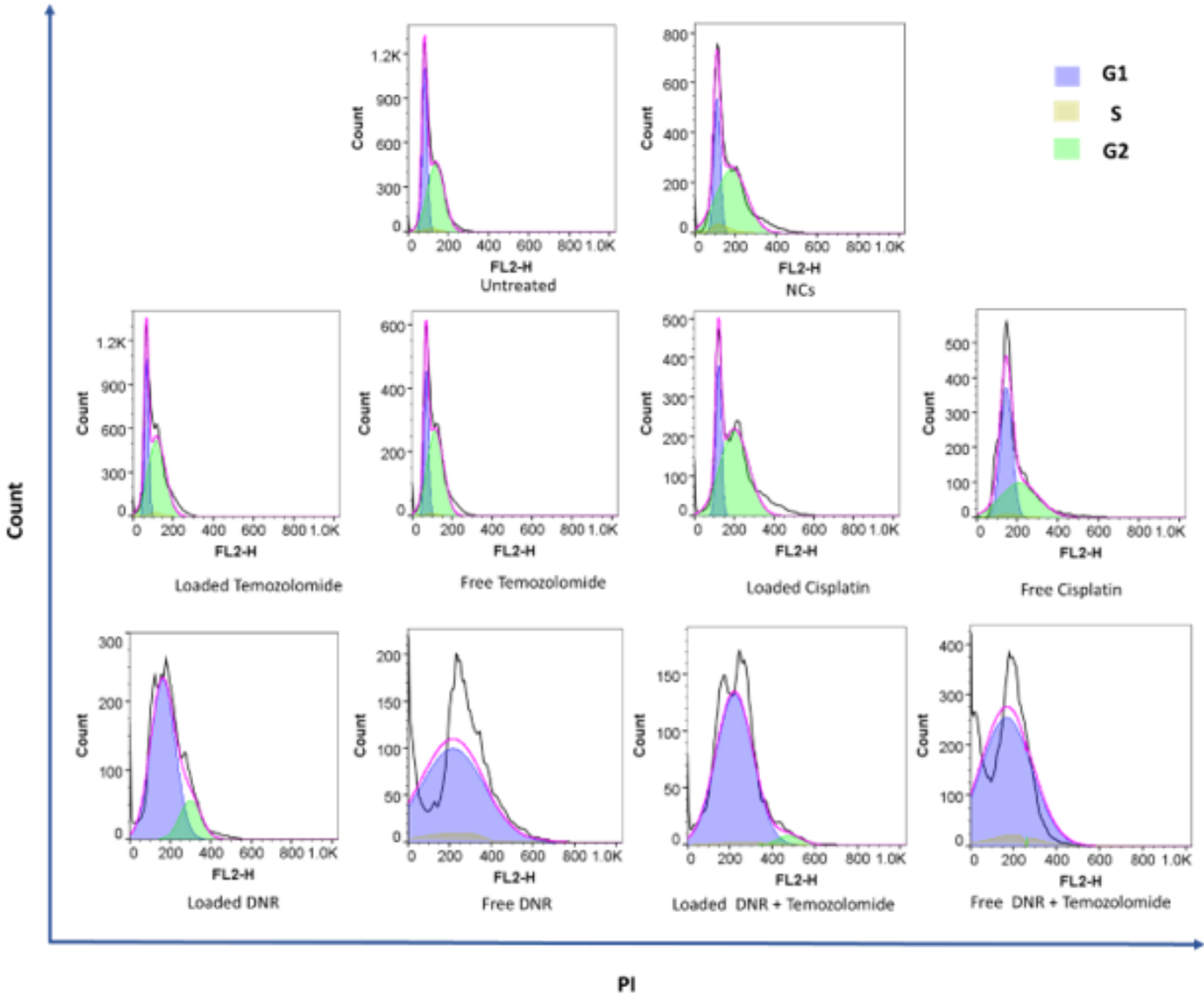


Figure 49. Cell cycle analysis of HEK293 cells treated by free NCs, loaded and free temozolomide, cisplatin, DNR, and DNR/temozolomide combination for 72h. Propidium iodide (PI) stain distinguishes between the G1, S, and G2 phases based on DNA content.

Percentages of the G1, S and G2 phases of the cell cycle were variant across the applied treatments after 72h (Figure 50). Across the different treatments applied, the S phase percentages were only up to 5%. Higher G1 phase percentages of > 50% were recorded in samples treated with loaded and free DNR and DNR/temozolomide. On the contrary, higher G2 phase levels of > 50% were recorded in the control sample and samples treated with NCs, loaded and free temozolomide and cisplatin.

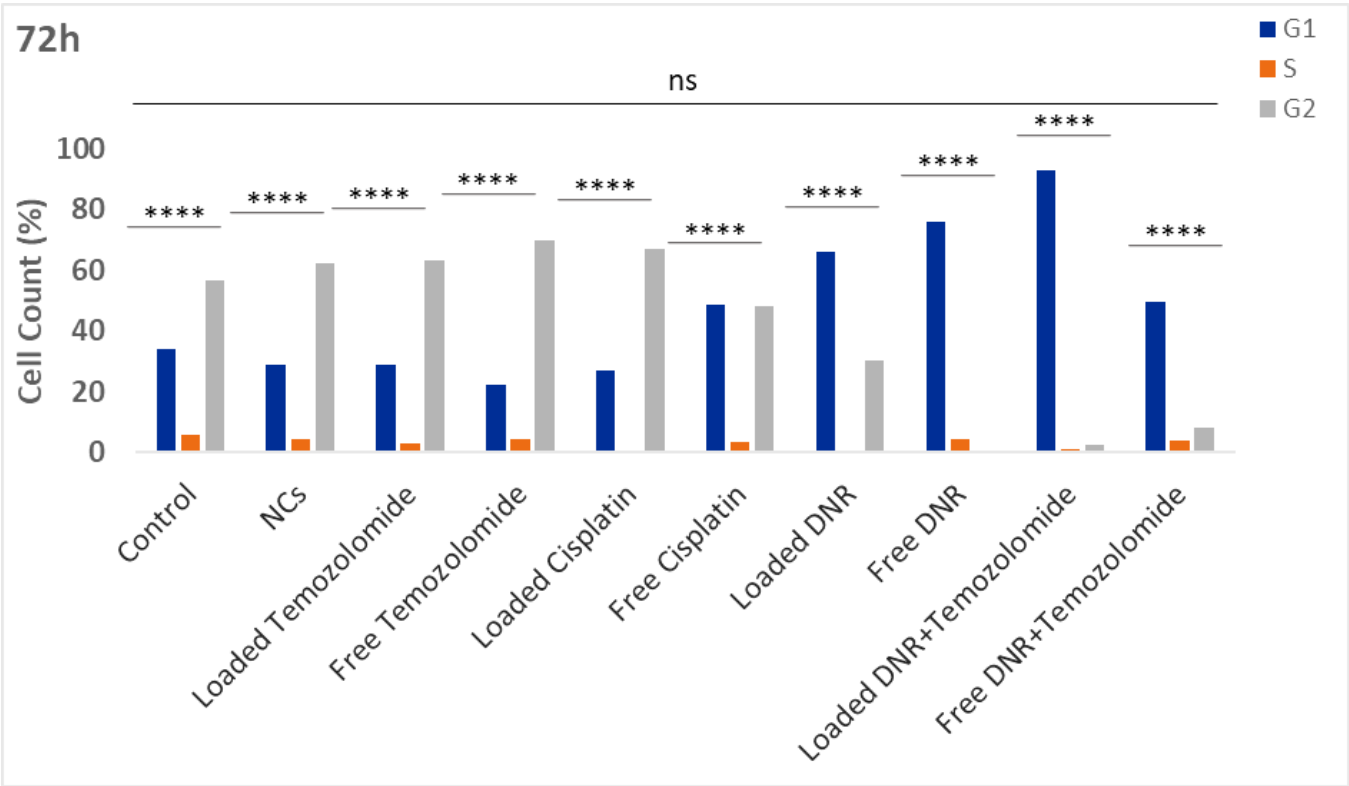


Figure 50. Percentages of the different phases of the cell cycle (G1, S, G2) of HEK293 cells treated by free NCs, loaded and free temozolomide, cisplatin, DNR, and DNR/temozolomide combination for 72h. ****P ≤ 0.0001, ns P > 0.05 and it was a comparison between all treatments; P-values were calculated for duplicates with two-way ANOVA.

3.4. Discussion

The MTT assay is a ubiquitous assay used for cell toxicity studies. This colorimetric assay evaluates the cellular viability and metabolic/mitochondrial activity through the reduction of the water-soluble yellow MTT dye to insoluble purple formazan crystals by the nicotinamide adenine dinucleotide phosphate (NADPH)-dependent cellular oxidoreductase enzymes (Ghasemi, Turnbull, Sebastian, & Kempson, 2021). The MTT dye is positively charged and lipophilic, which are two characteristics that facilitate its penetration through the cellular membrane and mitochondrial inner membrane, where its reduction takes place. The *in vitro* cytotoxicity evaluation of the free NCs in both HEK293 and TE671 cell lines for both 24 and 72h retained high percentages of viable cells that were able to reduce the MTT dye to insoluble formazan crystals. This signified an unaffected cellular and metabolic activity in the presence of free NCs. This data further added to several similar conclusions regarding polymeric nanoparticles that showed no significant cytotoxicity levels up to 72h of incubation with cancer and healthy cells (d'Amora et al., 2020; Maurya et al., 2019; Toniolo et al., 2018). In contrast, both cell lines in the presence of the free drug and drug loaded NCs: cisplatin, DNR, and temozolomide, separately, in addition to the temozolomide/DNR combination, showed increasing cytotoxicity for 24h and 72h as a result of the decreased and affected metabolic activity of the cells by the treatments. The low viability percentages were due to the cells' inability to reduce the MTT dye to formazan crystals. This could be attributed to the drug types used for the cells' treatment in their free or loaded version, separately or combined. Cisplatin is metal based drug, DNR is an anthracycline, while temozolomide is an alkylating agent. These drugs act on damaging the DNA by interfering with normal transcription through binding and intercalation into the nucleic acid, which induces cell death and, subsequently, low cell viability. This data was in line with reported claims regarding the cytotoxicity induced by the

release of the chemotherapy drug from the nanoparticles in a similar pattern to the free drug (Palanikumar et al., 2020; Toniolo et al., 2018). For instance, doxorubicin loaded polymeric particles exhibited good efficiency in killing lung cancer cells similar to free doxorubicin, yet with improved specificity (Fortuni et al., 2019)

Our drug loaded polymeric nanocontainers induced cytotoxicity in a relatively similar pattern to the free version of the drug. Yet, throughout the time points and concentrations used, the drug loaded NCs induced overall lower cytotoxicity than the free drug. This supported the sustained release feature of the polymeric NCs discussed in Chapter 2, which was a concept supported by several other studies including (Fortuni et al., 2019; Palanikumar et al., 2020). These data confirmed the non-cytotoxicity trait of free NCs considering that the induced low cytotoxicity levels were insignificant. On the contrary, the loaded NCs served as drug carriers released the encapsulated drugs in a sustained manner and induced a pattern of cytotoxicity relatively similar to the free drugs. The combination of temozolomide and DNR in loaded and free form induced slightly higher levels of cytotoxicity than their levels when introduced separately in both cell lines for 24h and/or 72h. This trend could be attributed to the dual effect of the drugs in intercalating the DNA and interfering with its transcription as well as cell division. Similar attempts to deliver two or more chemotherapeutic agents have been reported in breast cancer (Fisusi & Akala, 2019), including the delivery of co-encapsulated doxorubicin and mitomycin-C in hybrid-polymeric nanoparticles (Zhang et al., 2016). The nanosystems demonstrated efficiency in breast cancer cells including the resistant type (Zhang et al., 2016). Free temozolomide and PARP inhibitor combination for Ewing sarcoma treatment were reported to exhibit promising efficiency (Smith et al., 2015). Similar combinations approaches reported in the literature were mostly regarding cancer types with high incidence rates, including breast cancer, brain cancer, and colon cancer for instance (Al

Bostami, Abuwatfa, & Hussein, 2022; Fisusi & Akala, 2019; Zhang et al., 2016; Xiao et al., 2015). Due to the scarcity of rhabdomyosarcoma cases, focus on its treatment by novel approaches including targeted chemotherapy delivery by polymeric nanoparticles, is notably inadequate. Therefore, our work was among the few recently reported studies that attempted to develop a polymeric nanosystem for the delivery of several first line chemotherapy drugs in rhabdomyosarcoma (Moshe Halamish, Zlotver, & Sosnik, 2022; Zhang et al., 2017).

Throughout the MTT experiments, levels of cytotoxicity induced by the loaded NCs in the rhabdomyosarcoma cancer cell line were slightly higher in comparison with the healthy cell line. This difference could be attributed to the fact that the nanoparticles were synthesised with sensitivity to acidic pH and elevated temperature, which are also among the characteristics of the tumour's microenvironment. The latter observation regarding the dual responsiveness of nanocontainers in acidic and high temperature environments was in line with the discussed release profile of NCs in Chapter 2. Findings of similar stimuli responsive nanocontainers were lined with our findings and were validated both *in vitro* and *in vivo* (Palanikumar et al., 2020; Rahman, Khan, Kanwal, Awan, & Raza, 2021).

The fluorescence microscopy analysis showed a good cellular uptake of the rhodamine loaded NCs in both HEK293 and rhabdomyosarcoma TE671 cell lines, equivalent to the cellular uptake of the free rhodamine. Yet, the cells' morphology was affected, and that could be attributed to cytotoxicity induced by the rhodamine as well as the PFA fixation solution.

The cellular uptake of 50 μ M rhodamine loaded NCs in both HEK293 and rhabdomyosarcoma TE671 cell lines was good and gradual and had the same cellular uptake pattern as the free rhodamine at the same concentration. The gradual uptake shown by the slight difference in rhodamine intensities indicated the sustained release property of the nanoparticles. Good cellular uptake was seen in live cells stained by the fluorogenic mitochondrial dye for live cells

MitoView. These results were in accordance with similar DNR loaded polymeric nanoparticles that showed a good cellular uptake pattern similar to free DNR in MCF-7 breast cancer cells (Toniolo et al., 2018). Also, rhodamine and folic acid labelled pH-responsive nanoparticles showed successful cellular uptake in HeLa cells similarly to free rhodamine (Blackburn et al., 2019).

In our data, the localisation of the loaded NCs in the cells could not be precisely defined in this experiment. Other similar studies regarding the cellular uptake of polymeric nanocontainers used additional techniques to determine the precise localization of the NCs, including confocal microscopy and confocal laser scanning microscopy. These techniques allowed clearer and more detailed captured images, hence the ability to track and determine the uptake pattern of the polymeric NCs loaded with a fluorescent agent (e.g., rhodamine-B, doxorubicin) by the cells to inner compartments (e.g. nucleus, mitochondria) (Boltnarova et al., 2021; Palanikumar et al., 2020).

On the other hand, flow cytometry was used for the quantification of cellular uptake by the measurement of the fluorescence intensity of the fluorophore, rhodamine-B, doxorubicin labelled/loaded NCs in cancer cells. Data showed higher cellular uptake of the doxorubicin loaded polymeric NCs in breast cancer cells (Palanikumar et al., 2020).

Western blot analysis of the phospho-Histone H2A.X (Ser139) revealed variation in levels of expression, which were attributed to the DNA damage induced by the loaded and free temozolomide, cisplatin, DNR, and DNR/temozolomide combination. The first analysis conducted after 24h in accordance with the first time point of MTT analysis showed low DNA damage levels in all treatments applied. Since no significant expression of the H2A.X was recorded, this data was put under further processing and calculations.

Given that 72h was the second time point set in the MTT analysis, and the sustained release profile of nanocontainers continued for up to 72h, cells were treated for 72h in order to increase the treatment interaction time. Other studies that analysed the γ H2A.X levels by western blot had different treatment periods (4h, 6h, 24h, 48h, and 72h), which were dependent on their experiment settings (Al-Aamri et al., 2019; Duwa et al., 2020; Kawashima et al., 2020).

The H2A.X protein is one of the octamers (eight histones) forming the nucleosome, which is a fundamental DNA packing and condensation unit in eukaryotes i.e. chromatin. Simultaneous damage in two complementary strands of the DNA double helix with close location is a phenomenon known as DNA double-strand breaks (DSBs) (Podhorecka, Skladanowski, & Bozko, 2010).

In response to the DNA breaks, the phosphorylation of histone H2A.X at S139 residues (also known as γ H2A.X) serves as an early signal or precursor for DNA repair pathways (Jeffery et al., 2021).

DSBs can be induced by several physical, chemical, and biological factors, including chemotherapy drugs. Lower phosphorylated H2A.X protein levels were recorded in all treatments applied on the TE671 cells compared to the untreated cells, except for loaded temozolomide treatment that showed slightly higher phosphorylated H2A.X. This decrease in γ H2A.X levels was also noted in HEK293 cell line treated with the same loaded and free temozolomide, cisplatin, DNR, and temozolomide/DNR. The expected pattern was an increase in γ H2A.X levels in all treatments applied in the loaded or free version. Yet, the decrease noted in the γ H2A.X compared to the untreated cells could be attributed to the degradation of H2A.X content in the chromatin. This degradation could be linked to the effectiveness of the different

treatments applied to the cells. The untreated and NCs treated cells showed relatively similar levels of phosphorylated H2A.X, which could be attributed to the high rate of DNA damage and DNA-repair signal in cancer cells induced by the high rate of proliferation. The only increase in H2A.X levels was noted in the loaded temozolomide, which could be attributed to either treatment effectiveness or to the elevated levels of DNA repair hence the resistance of the cells to the loaded temozolomide in contrast to its free version. The literature claimed two postulations regarding the levels of γ H2A.X; the increased levels of γ H2A.X either signified treatment effectiveness or resistance. For instance, Kawashima et al. (2020) showed that colorectal cancer cells from biopsy samples of patients who underwent preoperative chemoradiotherapy and had lower γ H2A.X levels were more sensitive to radiotherapy and vice versa. They concluded that γ H2A.X levels could serve as a predictive indicator of radiosensitivity (Kawashima et al., 2020).

Similar polymeric NCs conjugated with cetuximab and loaded with temozolomide were delivered in glioma, melanoma, and colorectal cancer cell lines. Contrary to our results, western blot analysis revealed higher γ H2A.X levels after treatment compared to the untreated cells and plain NCs treated cells (Duwa et al., 2020).

The oxidative stress generates reactive oxygen species (ROS) and increases the degradation of H2A.X in the nucleoplasm resulting in reduced content of γ H2AX in chromatin. Triple negative breast cancer cells showed significant γ H2A.X degradation after several cycles of chemotherapy and chemosensitivity in patients was improved due to this decrease in γ H2A.X levels induced by oxidative stress (Gruosso et al., 2016). This claim was in agreement with our findings and supported the correlation between the decrease in H2A.X levels and the effectiveness of the chemotherapy drugs delivered in NCs-loaded form or freely. First line chemotherapy drugs, including temozolomide, cisplatin, and DNR, induce ROS and oxidative

stress resulting in the alteration of intracellular redox homeostasis (Yang et al., 2018). The decrease of γ H2A.X levels noted in our results was relatively similar in both free drug and drug loaded nanocontainer, which indicated the nanocontainers' ability to function as drugs shuttle with a sustained release. Levels of mRNA H2A.X expression levels were reported to decrease in response to effective chemotherapy in breast cancer, while high levels were related to poor survival (Katsuta et al., 2022).

Given that γ H2A.X protein gets dephosphorylated after DNA damage to complete the repair process and restore the chromatin integrity, the cellular levels of the detectable γ H2A.X foci decrease after dephosphorylation and return to standard levels within 24h (Valente et al., 2022). This could suggest that during the 72h treatment, damaged DNA was already repaired and dephosphorylation of the γ H2A.X took place, resulting in decreased levels of γ H2A.X in our result. This also suggested opting for treatment duration lower than 72h and 24h in the future to assess the changes in γ H2A.X levels (An et al., 2010). For instance, western blot results of HeLa cells exposed to radiation showed decreased levels of γ H2A.X after 4 to 10h post radiation exposure (An et al., 2010). In another example, western blot results of rhabdomyosarcoma cell line without knocked SNAI2-a major regulator of radiation-induced apoptosis- showed a decrease in levels of γ H2A.X starting from 8h post radiation exposure (Wang et al., 2021).

Overall, the γ H2AX is defined as a global sensitive marker of DSBs. However, the expression of H2A.X in different cell lines and tissue types is highly heterogeneous. This variability renders the interpretation of γ H2AX levels and their subtle changes considerably difficult (Ji et al., 2017).

Therefore, conducting additional analysis of the total γ H2A.X expression levels by RT-qPCR, immunohistochemistry, ELISA, and γ H2AX assay by flow cytometry was suggested for more

accurate detection of the subtle differences in H2A.X levels (Ji et al., 2017), which was beyond the scope of our data. Although the H2A.X Ser139 is considered a DSB marker, the H2A.X represents only 2–25% of the cellular H2A pool in mammalian cells. Therefore, other H2A.X variants and other DNA damage markers could be investigated (Dobersch et al., 2021).

Apoptosis analysis by flow cytometry in TE671 and HEK293 cell lines showed an increase in apoptotic cells after 24h treatment with loaded and free temozolomide, cisplatin, DNR, and DNR/temozolomide combination. Free NCs induced apoptosis in cells with relatively similar or slightly higher to the apoptosis in control cells after 24 and 72h in rhabdomyosarcoma. In HEK293 cells, the NCs showed higher apoptosis than the control after 24h, yet the levels were relatively similar to the untreated cells after 72h. The total apoptosis induced after 72h of treatment in both cell lines was higher than in 24h. Also, loaded and free temozolomide showed lower apoptosis levels than the other loaded and free forms of DNR, cisplatin and DNR/temozolomide combination in both cell lines and both time points. The induced apoptosis by the different chemotherapy drugs in their loaded and free form was attributed to the mode of action of the temozolomide, cisplatin and DNR had a common point in their mode of action when tackling cancer cells. These drugs acted by damaging the DNA through methylating DNA guanine bases (temozolomide), crosslinking DNA base pairs (cisplatin), and uncoiling the DNA double helix (DNR) (American Cancer Society, 2019; Pokhriyal, Hariprasad, Kumar, & Hariprasad, 2019).

Annexin V is a dye that binds to the phosphatidylserine (PS), a component of the cell membrane that becomes exposed to the outer side of the cell upon apoptosis. The 7-amino-actinomycin (7-AAD) is membrane impermeable dye that binds to/intercalates the DNA when the cells lose their membranal integrity upon late apoptosis and cell death (Gobin, Menefee,

Lattimore, Doty, & Fredenburg, 2022; Maciel et al., 2014; Wong, Kim, Robinson, Huang, & Conboy, 2021).

Therefore, the increase in total apoptosis in treated cells compared to NCs treated and untreated cells was attributed to the damage caused by the treatments applied (loaded and free) and detected by the annexin V and 7AAD dyes. This pattern came in accordance with the higher cytotoxicity levels induced by the loaded and free treatments in the MTT assay. Additionally, the intracellular and sustained release profile concept of the loaded nanocontainers for up to 72h and high cell viability of the free NCs in cytotoxicity assay were supported. This data built on recently reported results about the ability of doxorubicin loaded PEG-PPS-GSNO polymeric nanoparticles in inducing high apoptosis levels in multiple drug-resistant HepG2/ADR cell line, unlike the free nanoparticles that showed considerably low and insignificant apoptosis levels (Wu et al., 2020).

Another recent study reported the use of poly (lactic-co-glycolic acid) polymeric nanoparticles for co-encapsulation and delivery of doxorubicin and epoxomicin into MCF-7 breast cancer cell line. Results reported very low apoptosis levels when cells were exposed to plain polymeric nanoparticles, then loaded doxorubicin and epoxomicin in nanoparticles induced relatively similar apoptosis levels compared to free doxorubicin and epoxomicin (Kucuksayan et al., 2021). In contrary to the lower levels of total apoptosis in our plain polymeric nanocontainers compared to the loaded versions, plain metallic Fe-Ni ANPs nanoparticles showed about 80% apoptosis in human lung bronchial epithelial cells (Vatan, 2022).

Cell cycle analysis by flow cytometry and propidium iodide (PI) staining showed cell cycles arrest at different phases induced by the different treatments. PI binds to the DNA in proportion to its content. By definition, temozolomide and cisplatin used in our work were

not cell cycle specific unlike DNR i.e., neither of the drugs act and arrest the cell cycle at a specific phase. Yet, DNR, was reported to be G2 specific (Mills, Kolb, & Sampson, 2018; National Cancer Institute, 2023; Sun, Liu, Ma, & Hu, 2021). Therefore, there was no specific expected phase for the cell cycle arrest, except for DNR treatments, where the cell cycle arrest was anticipated at the G2. Gap1 (G1), synthesis (S), and Gap2 (G2), and mitotic (M) are cell cycle phases during which a series of events take place regarding the DNA synthesis with best integrity (Sun, Liu, Ma, & Hu, 2021). G1/S and G2/M are considered checkpoints (Alimbetov, Askarova, Umbayev, Davis, & Kipling, 2018). During the G1 phase, cells increase in size and prepare for division with a series of events, including the transcription of cyclins and similar regulation genes. At the S phase, DNA synthesis and replication take place. At the G2 phase, the cells undergo a series of checks to ensure DNA integrity and start making protein and organelles related to the mitosis division (Alimbetov, Askarova, Umbayev, Davis, & Kipling, 2018; Sun, Liu, Ma, & Hu, 2021). During the M phase, the cells divide into two identical diploid cells by splitting their DNA into two copies. After the M phase, cells can enter into a new G1 phase for further divisions or remain dormant in the G0 phase (Tan, Duncan, & Slawson, 2017).

Loaded and free forms of the drugs in both TE671 and HEK293 cell lines induced relatively cell cycle arrest at the same phase with reduced levels of the S phase. Loaded and free form of temozolomide induced cell cycle arrest at the G1 phase after 24h and at the G2 after 72h for both cell lines. Loaded and free cisplatin induced cell cycle arrest in both cell lines at the G2 and G1 in both cell lines for 24h and 72h, respectively. Yet, free cisplatin arrested the cell cycle after 24h at the G2 phase in the TE671 cell line. Loaded and free DNR arrested the cell cycle at G1 in TE671 and HEK293 after 24h and 72h at G1, excluding two occasions where the cell cycle arrest was induced at G2. This was in TE671 cells after 72h treatment with loaded DNR, and HEK293 cells after 24h treatment with free DNR. The loaded and free temozolomide/DNR

combination in both cell lines and both time points was induced at the G1 phase with the exception of the G2 cell cycle arrest that was recorded in the free form in TE671 at 72h. The S phase was overall very low in comparison to the untreated cells across the treatments. Therefore, both loaded and free forms of the different first line chemotherapy drugs used showed effectiveness in arresting the cell cycle relatively at the same phase. This data was in accordance with the apoptosis results in which all drugs in both loaded and free forms induced higher apoptosis compared to the untreated and NCs treated cells in both cells and for both time points. Kudarha and colleagues (2021) claimed that temozolomide arrests the cell cycle at the G2/M phase in its form, yet its loaded form in hyaluronic acid conjugated albumin nanoparticles showed no significant change in the G2/M phase. They attributed this to the sustained release profile of the polymeric nanoparticles that might need a longer treatment period to induce higher G2/M cell cycle arrest in glioblastoma cells (Kudarha & Sawant, 2021). This was partially in agreement with our data, since free and loaded temozolomide in both cell lines showed cell cycle arrest at the G1 and G2 for 24h and 72h, respectively.

Also, in our data the expected cell cycle arrest by the DNR in G2 was noted only on two occasions, as aforementioned. Similar variations in DNR results were reported by Sen et al., (2021) when polymeric micelles loaded with DNR showed cell cycle arrest at the G2 or M phase in cervical cancer cell line contrary to the free DNR that showed a cell cycle arrest at the G1 in the same cell line (Sen et al., 2021).

Comparable drug loaded polymeric nanocontainers showed the same effectiveness in inducing the cell cycle arrest but not necessarily at the same phase as our nanocontainers. For instance, self-assembled cholesterol–asplatin-incorporated nanoparticles (SCANs) (asplatin is platin based drug similar to cisplatin) showed significant cell cycle arrest in the S and G2 phase

similarly with the free cisplatin for 48h and 72h in human liver hepatocellular carcinoma (Cheng et al., 2015). This was partially in accordance with our results given that our loaded cisplatin showed similar G2 phase arrest both time points and cells. Yet, the free cisplatin induced cell cycle arrest in G1 and G2. Co-loaded paclitaxel and etoposide polymeric nanoparticles showed significant cell cycle arrest in G2/M phase in human osteosarcoma (Cheng et al., 2015). Paclitaxel, anti-microtubule agent was known for arresting the cell cycle at the G2/M; therefore, the levels of the G2/M were used as a reference to assess the effectiveness of the free and loaded paclitaxel and etoposide combination in arresting the cell cycle and inducing apoptosis. Results of the co-delivery of paclitaxel and etoposide by the polymeric nanoparticles induced higher G2/M phase arrest percentages compared to the free paclitaxel and etoposide. Although these data were in accordance with our results in regard to the effectiveness of the nanoparticles in delivering the drug, certain limitations were noted. For instance, a “reference action” of the free drug in arresting the cell cycle and inducing apoptosis at a specific and known phase was lacking in our data, except for DNR. Literature reported anti-microtubule agents, including paclitaxel, docetaxel, and vincristine as G2/M phase-specific, antimetabolites including 6-mercaptopurine, 5-fluorouracil, cytarabine and methotrexate among others as G1/S specific and anti-tumour antibiotics including daunorubicin and doxorubicin as G2/M (Mills, Kolb, & Sampson, 2018).

To overcome the limitation of the lack of cell cycle arrest specificity, cell could undergo synchronization to a specific phase in order to ensure reliable comparisons and draw an accurate conclusion. A similar suggestion was followed by Huang and colleagues (2016), where human ovarian adenocarcinoma cells were synchronized at the same starting phase and cell cycle analysis and drug effect were assessed. Enzymatically triggered nanoparticles loaded with cisplatin and free cisplatin showed cell cycle arrest at the S phase and G0/G1,

respectively. Although results did not report additional differences between the effect of the loaded and free forms of cisplatin in synchronized and non-synchronised cells, this allowed for further results validation (Huang et al., 2016).

3.5. Conclusions

In conclusion, polymeric nanoparticles loaded with temozolomide, cisplatin, and DNR were assessed -separately or in combination- for effective treatment of rhabdomyosarcoma by testing their cytotoxicity, cellular uptake, levels of phosphorylated H2A.X and DNA damage, apoptosis, and cell cycle effects. Overall, all data were collectively evaluated and showed induced cytotoxicity by the drug loaded NCs by the MTT assay, good cellular uptake by the fluorescence microscopy, effective induction of DNA damage by the western blot, induction of apoptosis and cell cycle arrest by the Annexin/7AAD and PI in flow cytometry analysis. These results revealed promising drug efficacy improvement, hence, treatment enhancement. Yet, further in vivo assessment would better confirm the targeting ability of these polymeric nanocontainers in rhabdomyosarcoma and the resulting reduction of systemic and long-term side effects. Also, these polymeric nanocontainers could be considered as a very good and preliminary base for the unlocking of their additional and exceptional properties with further modifications with targeting agents and assessment of further efficacy. There is a lack in recent studies regarding the application of polymeric nanoparticles in the treatment of paediatric rhabdomyosarcoma. As aforementioned, most recent studies focused on other types of cancer cell lines and loaded mainly gold standard drugs, including daunorubicin and doxorubicin. For this, our work was considered among the few recent studies that assessed the treatment of paediatric rhabdomyosarcoma with three different loaded drugs in polymeric nanocontainers.

CHAPTER 4

4. GLIOBLASTOMA

4.1. Introduction

Glioblastoma is the most aggressive and common type of primary brain malignancy. It accounts for about 48% of all malignant central nervous system (CNS) cases (Grochans et al., 2022). Based on the latest classification of the world health organisation (WHO), glioblastoma is a CNS WHO grade 4 and is referred to as “glioblastoma, IDH-wildtype CNS WHO grade 4” as the IDH-mutant gliomas are now considered astrocytoma (Kim, Park, & Lee, 2021; Louis et al., 2021). Cell of origin of glioblastoma has been an area of extensive research over the years in order to decrypt the cellular origination of this complicated and aggressive brain tumour (Azzarelli, Simons, & Philpott, 2018; Evans et al., 1992; Mandal, Brem, & Suckling, 2023; Stoyanov & Dzhenkov, 2018). According to the latest studies regarding the origin of glioblastoma, the subventricular zone (SVZ) region in the brain where neurogenesis takes place was reported to be the anatomic origin of glioblastoma (Figure 1) (Lee et al., 2018; Mandal, Brem, & Suckling, 2023). As the largest niche for neural stem cells, the SVZ is anatomically located in the walls of the lateral ventricles of the brain (Beiriger et al., 2022; Lim & Alvarez-Buylla, 2016).

Furthermore, SVZ includes stem-like cells including neural stem cells (NSCs), astrocytes precursor cells (APCs), oligodendrocyte precursor cells (OPCs), and neural progenitor cells (NPC) (Mandal, Brem, & Suckling, 2023). Glioblastoma can originate in these progenitor/precursor cells that were found to give rise to further differentiated glial and neural cells, including astrocytes, oligodendrocytes and neurons. The mature astrocytes are also a source of glioblastoma origination (Mandal, Brem, & Suckling, 2023).

Resistance of glioblastoma to several treatments is associated with its cellular heterogeneity. It is reported that there is currently an agreement on the hypothesis of the ability of glioblastoma cells to reside in any of four cell states including astrocyte-like, neural progenitor cell-like, oligodendrocyte precursor cell like, and mesenchymal (Mandal, Brem, & Suckling, 2023).

The NSC in the SVZ were found to comprise somatic dysregulation and cancer driver mutations of the glioblastoma (Lee et al., 2018). Those include telomerase reverse transcriptase (*TERT*) promoter, epidermal growth factor receptor (*EGFR*), tumour protein P53 (*TP53*) and phosphatase and tensin homolog deleted on chromosome 10 (*PTEN*) (Lee et al., 2018). These are involved in a set of deregulated signalling pathways, including Ras, phosphatidylinositide 3-kinase (PI3K), receptor tyrosine kinase (RTK), p53, and retinoblastoma (Rb) signalling pathways (Kim, Park, & Lee, 2021). Figure 51 below shows the SVZ with the cells of origin of glioblastoma and associated genetic mutations.

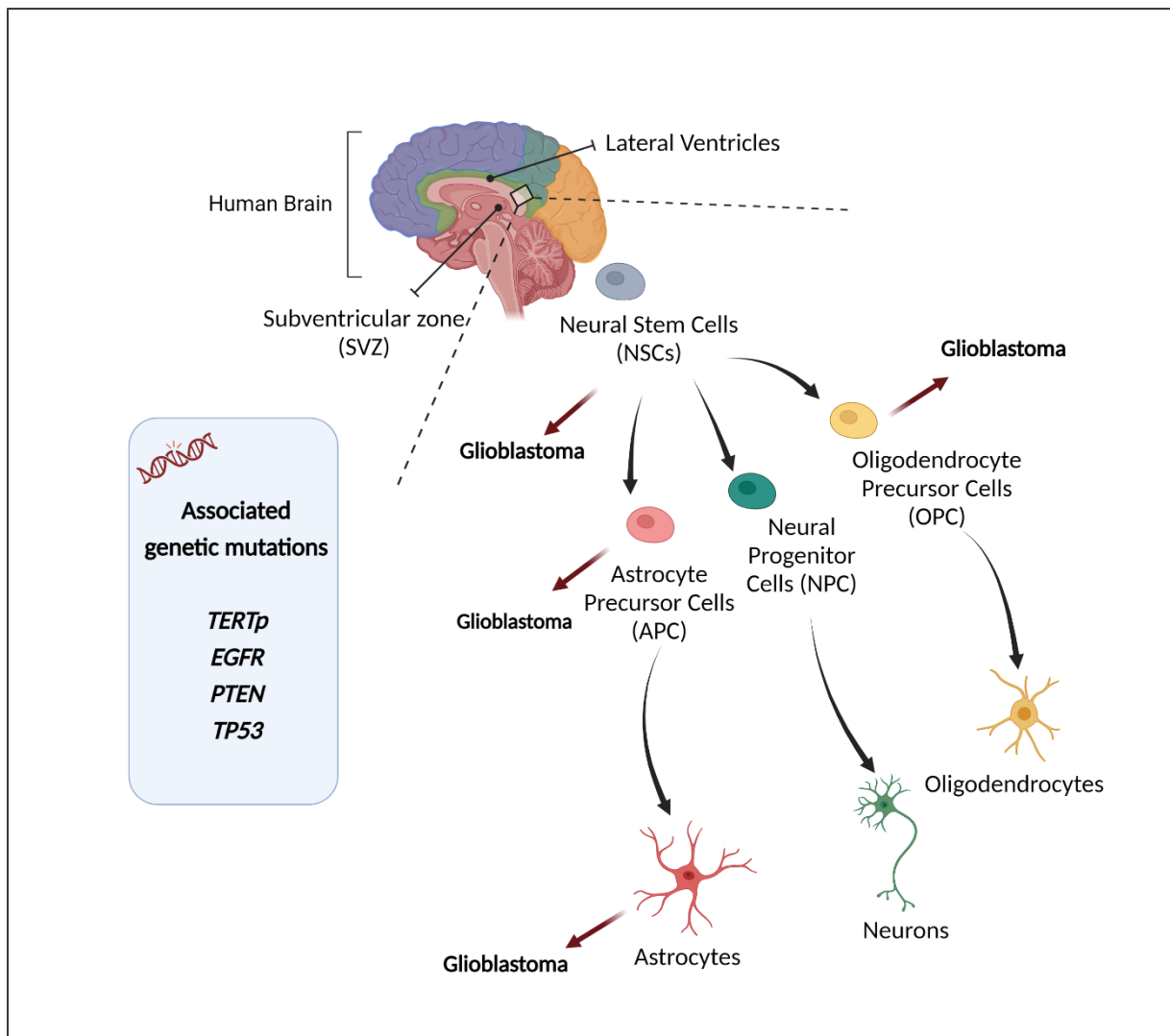


Figure 51. Illustration of the glioblastoma cell of origin. The illustration shows the subventricular zone (SVZ), neural stem cells (NSCs), neural progenitor cells (NPC), astrocyte and oligodendrocyte precursor cells (APC and OPC), and mature astrocytes, neurons, and oligodendrocytes. Inspired by (Azzarelli, Simons, & Philpott, 2018; Kim, Park, & Lee, 2021; Laurence, Huillard, Bielle, & Idbaih, 2023; Mandal, Brem, & Suckling, 2023). Created in BioRender.com

TERT gene and its encoded protein play a role in restoring the telomere length in continuously dividing cells such as stem cells. It plays a tumour suppressor role as it is turned off in healthy somatic cells. However, its abnormal activation in cancer cells stabilises the length of the telomerase and promotes cancer cells' abnormal proliferation and immortalization (Trybek, Kowalik, Gózdź, & Kowalska, 2020). About 82% of glioblastoma IDH-wildtype exhibit *TERT*_p mutation (Kim, Park, & Lee, 2021). It was reported that the neurogenic niche of the postnatal human brain contains a high frequency of *TERT*_p mutations suggesting that glioblastoma driver mutations were acquired by NSCs in the SVZ (Körber et al., 2019).

EGFR gene and its encoded protein regulate cell growth and cell survival by regulating several signalling pathways including PI3K/AKT and RAS/MAPK pathways. When mutated, it plays an oncogenic role and promotes tumour survival and unregulated cell proliferation (Oprita et al., 2021).

TP53 is a major tumour suppressor gene, and it encodes a protein p53 that tackles damaged cells, prevents cell transformation from normal to malignant, and reduces the proliferative activity of cancer cells. *TP53* and its encoded protein p53 regulate transcriptional genes, hence it is involved in various cellular processes, including DNA repair, cell cycle, and apoptosis. Consequently, when *TP53* is mutated, the p53 pathway that comprises a network of genes that regulate several aforementioned cellular processes, cells enter a phase of uncontrolled proliferation, hence acquiring tumorigenesis in normal cells (Lee et al., 2020; Zhang et al., 2018)

PTEN is a tumour suppressor gene that is involved in regulating phosphoinositide 3-kinase (PI3K) pathway (Benitez et al., 2017). Aberrant activation of the PI3K pathway is induced when *PTEN* is mutated or lost, resulting in a dysregulation of intracellular signalling pathways

including cell growth, proliferation and migration (Zhao et al., 2021). Metastasis has been linked to the loss of PTEN function in brain tumours including glioblastoma (Benitez et al., 2017).

Metastasis of glioblastoma to peripheral areas from the primary site is rare. In the case of metastasis, glioblastoma spreads to the lungs, regional lymph nodes, bones, liver and extracranial with 60%, 51%, 31%, 22%, and 0.5%, respectively (Grochans et al., 2022; Liu et al., 2020; Zhang et al., 2018). The most common location of glioblastoma in the brain is the frontal, temporal and parietal lobes (Miller et al., 2021). The brain is a critical and sensitive organ and part of the CNS that is crucial for all body functions, hence, any impairments in its integrity, including cancer, induces complications and dysregulation in all human body systems (Wang, Pan, & Li, 2020). As previously described in Chapter 1, the frontal lobe controls intellectual activities such as organization ability, problem solving, decision making, speech, personality, and memory, among others (Neulinger, Oram, Tinson, O’Gorman, & Shum, 2015). The temporal lobe controls cognitive functions such as hearing and language comprehension; the parietal lobe controls: the perception of several sensations, including touch and temperature, processing of sensations including analysing and recognition, in addition to coordination and body awareness (Jawabri & Sharma, 2022; Flinker et al., 2015).

4.1.1. Epidemiology

Glioblastoma accounts for 14% of all CNS neoplasms, 48% of all malignant CNS tumours, and 55% of all gliomas (Grochans et al., 2022; Lin et al., 2020). With an estimated incidence rate of 4 cases per 100,000 persons, there are about 340,000 to 650,000 global cases of brain and CNS tumours cases diagnosed yearly, with about 251,000 brain and CNS related deaths (Fan et al., 2022; Patel et al., 2019). Rather rare in a pediatric population, glioblastoma accounts

for 0.18 per 100,000 persons aged between 0 to 18 years. Yet, the latest WHO CNS5 indicates that the term “glioblastoma” is no longer used for the description of pediatric neoplasms (Louis et al., 2021).

Notably, there is an increase in incidence in men than women, with a ratio of 1.6:1 male to female (Bello-Alvarez & Camacho-Arroyo, 2021). The risk of developing glioblastoma increases with age as higher incidence rates were found in individuals > 40 years of age, with peaks recorded between 75 and 84 years (Fan et al., 2022; Grochans et al., 2022). Besides, the global 5-year survival year (age-standardized) ranges between 4% to 17% recording by that the lowest survival rate among other adult-type diffuse gliomas including oligodendroglioma with a 5-year survival rate of 32% to 69%. Yet, the median survival remains poor for up to 20 months from the diagnosis date (Gilard et al., 2021; Girardi et al., 2022).

The 5-year age standardized survival rates between 2000 and 2014 were poor and did not surpass 17% in six continents (Figure 52): Europe (3.6% to 12.4%), North America (7.8% to 10.3%), South America (3.8% to 12.6%), Oceania (6.5% to 12.2%), Africa (up to 13.9%), and Asia (11% to 16.9%). Mauritius was the only country that reported 31% 5-year survival rate between 2010 and 2014, but no data were reported for the earlier years (Girardi et al., 2022).

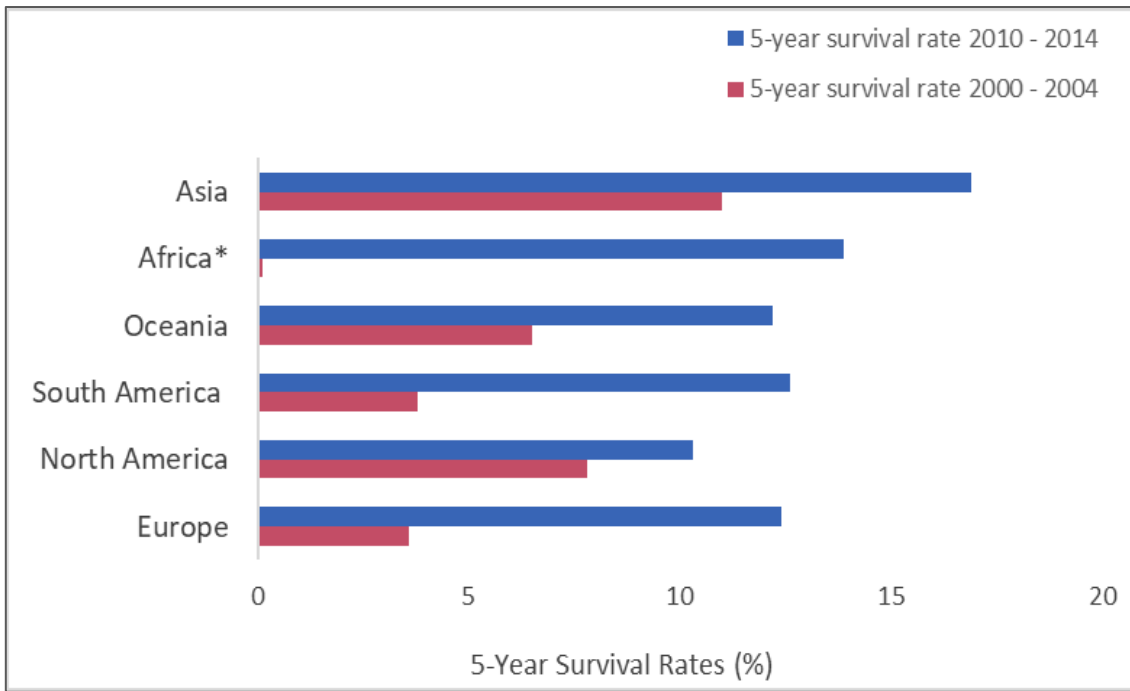


Figure 52. Five-year net survival rates between 2000-2014 and 2010-2014 in Europe, North America, South America, Oceania, Africa and Asia.*With the exception of Mauritius, data for only 2 countries were available (Girardi et al., 2022).

4.1.2. Diagnosis

After exhibiting symptoms related to glioblastoma including disrupted neurocognitive functions (e.g. learning, memory, speech, and movement), persistent headaches, and new onset seizures, diagnosis and clinical examinations start immediately (Oronsky, Reid, Oronsky, Sandhu, & Knox, 2021). Diagnosis of glioblastoma comprises several approaches including genetics and molecular screening and radio-imaging after obtaining biopsy samples (Weller et al., 2020).

IDH mutation status is the starting point to distinguish glioblastoma from other adult diffuse gliomas since both oligodendrogliomas and astrocytomas are IDH-mutant (Louis et al., 2021). After confirming the IDH status, WHO CNS5 and the European Association of Neuro-Oncology (EANO) recommend the incorporation of three genetic/molecular parameters in the diagnosis of glioblastoma and those include *TERT* mutation or *EGFR* gene or amplification or gain of chromosome 7 and loss of chromosome 10 (Weller et al., 2020). *TERT* promoter mutation is exhibited in about 82% of IDH-wildtype. It plays a role in stabilising the telomerase length of the glioblastoma cells rendering them immortalized and aggressively proliferative (Kim, Park, & Lee, 2021; Trybek, Kowalik, Gózdź, & Kowalska, 2020).

EGFR gene and its encoded protein are involved in the regulation of cell growth and survival through crucial pathways, including the RAS/MAPK pathway. *EGFR* gene amplification is harboured in about 50% of glioblastoma IDH-wildtypes cases (Brat et al., 2018; Lassman et al., 2022).

The combination of gain and loss of entire chromosomes 7 and 10, respectively, referred to as (+7/-10), is considered a signature chromosomal abnormality related to glioblastoma IDH-wildtype (Brat et al., 2018; Louis et al., 2021).

The WHO CNS5 report indicates that featuring the aforementioned genetic imbalances combined or separately is adequate to assign the highest WHO grade, hence glioblastoma IDH-wildtype WHO grade 4 (Louis et al., 2021).

Radiographic evaluation of brain tumours including glioblastoma, consists of using magnetic resonance imaging (MRI) as a standard choice for an accurate radiographic diagnosis pre and post-operative surgery (Bernstock et al., 2022; Grover et al., 2015). Conventional MRI procedure uses a strong magnetic field, radio waves, and a contrast agent (e.g., gadolinium) to generate detailed pictures of the brain. MRI imaging scans for any abnormal tumorous masses, and in glioblastoma, the tumour appears as a heterogenous mass with the presence of peritumoral edema and central necrotic core (Bernstock et al., 2022).

In addition to the conventional MRI there are two more types of advanced MRI, called diffusion MRIs and perfusion MRI that produce more detailed images with additional microstructural details. (Baliyan, Das, Sharma, & Gupta, 2016; Bernstock et al., 2022). Diffusion tensor MRI works by generating signal contrast based on the movement of water molecules by Brownian motion. Hence, tissue with denser cellular mass will be distinguishable via quantitative diffusion coefficient from tissue with less cellular density (Bernstock et al., 2022). In healthy cells, water molecules are divided between the inner and extracellular compartments in a characteristic way between different body tissues. Intracellular compartments exhibit restricted diffusion, while the extracellular compartment exhibits free diffusion. In glioblastoma cases, i.e., disrupted conditions, the diffusion is relatively more restricted as a result of the increased intracellular proportions (Baliyan, Das, Sharma, & Gupta, 2016).

Perfusion MRI known as perfusion dynamic susceptibility contrast (DSC) MRI, assess the blood flow through the brain tissue via an intravascular contrast agent. These three types of perfusion MRI dynamic susceptibility contrast (DSC) MR, dynamic contrast-enhanced (DCE) MR, and arterial spin labelling (ASL) MR. Based on the kinetics of the contrast agent, information about the cerebral blood flow and blood volumes are obtained reflecting microvasculature and angiogenesis of the brain tumours (e.g. astrocytomas and glioblastomas) (Bernstock et al., 2022; Cha et al., 2002).

Several studies have reported the potential advantage of using liquid biopsy for early detection and screening of gliomas, including glioblastoma, via the of cell-free tumour DNA in the plasma and cerebrospinal fluid (Juratli et al., 2018; Mouliere et al., 2018; Zill et al., 2018; Piccioni et al., 2019). Thus far, such techniques have not been approved yet as further evidence of their reliability in detecting and screening for glioblastoma remains to be proven (Weller et al., 2020).

4.1.3. Therapy

Treatment of brain malignancies including glioblastoma IDH-wild type 4 consists of surgery, chemotherapy, and radiotherapy. Patients generally undergo adjuvant therapy (surgery with chemotherapy and/or radiotherapy) with a synergetic effect for maximal tumour eradication.

4.1.3.1. Surgery

Performing surgery for maximal tumour resection is the treatment of choice. Fluorescence guided surgery, neuronavigation and intraoperative ultrasound (Bonosi et al., 2023). Fluorescence guided neurosurgery uses fluorescence dyes such as synthetic amino acid 5-ALA which was approved by the US Food and Drug Administration (FDA) in 2017 for intraoperative optical imaging in high grade gliomas (Hadjipanayis & Stummer, 2019). Upon metabolization

of 5-ALA, an intermediate fluorescent metabolite (protoporphyrin IX) is produced and accumulates with high concentrations in tumour cells, hence differentiating boundaries between healthy and cancer tissue (Bonosi et al., 2023). The use of 5-ALA in fluorescent guided resection surgery was linked with higher gross total resection and overall survival (Lakomkin & Hadjipanayis, 2018). Neuronavigation is a neurosurgical technique that is based on visualization of the surgical scenario in a 3D model. This technique allows for better planning of the surgery and enhanced total resection of the tumour (Bonosi et al., 2023).

Intraoperative ultrasound guided surgery is a time and cost-effective surgical technique that is used to maximise glioblastoma resection through the identification of the tumour mass via ultrasound (Bonosi et al., 2023). Contrast enhanced ultrasound technique provide potentially improved identification of tumour residues during the resection procedure. Also, this technique provides better protection of the healthy tissue surrounding the tumour, hence protection of the patient from potential neurological harm during resection and creating better surgical outcomes (Incekara et al., 2021).

4.1.3.2. Radiotherapy

As part of the multimodal therapy of glioblastoma, surgical resection is followed by radiotherapy. Starting radiotherapy post-surgery is recommended to be as soon as three to six weeks after surgical tumour resection (Zhang et al., 2019). Partial-brain radiation using conventional fraction radiotherapy is recommended over the whole brain radiotherapy despite the infiltrative characteristic of glioblastoma. 60 Gy given in 30 fractions of 2 Gy over 6 weeks is the optimal recommended dose of radiation for patients up to 70 years (Zhang et al., 2019).

On the other hand, hypofractionated radiotherapy (HFRT) is recommended for radiotherapy in patients over 70 years with poor prognosis. For this group of patients, HFRT is applied in shorter periods, less exposure times, and less fractionations (e.g. 45 to 60 Gy given in 10 to 20 fractions of >2 Gy) (Zhang et al., 2019).

Literature reported the efficacy and overall survival improvement of short course HFRT compared to long course radiation. A randomized trial reported significant better overall survival in patients over 70 years treated with short course HFRT (34 Gy in 10 fractions over 2 weeks) versus those treated with long course HFRT (60 Gy in 30 fractions over 6 weeks) (Malmström et al., 2012; Witteler, Schild, & Rades, 2021).

Additionally, Liao and colleagues (2019) reported in their review that HFRT was safer and more effective than conventional radiotherapy in treating elderly patients with glioblastoma (over 70 years). Their conclusions were based on comparing several phase II and phase III trials on the use of HFRT and conventional radiotherapy (Liao, Zhao, Yang, & Li, 2019). Conversely, it was reported that elderly patients who received short course hypofractionated radiotherapy had worse survival compared to patients who received conventionally fractionated long course radiotherapy, with median survival of 4.9 months and 8.9 months, respectively (Mak, Agarwal, Qureshi, & Truong, 2017). It was also reported that short-course (25 Gy, five daily fractions, over 1 week) or standard radiotherapy (40 Gy, 15 daily fractions, over 3 weeks) regimens had similar median overall survival time (7.9 months and 6.4 months) in patients between 70 and 90 years (Roa et al., 2015).

Since glioblastoma treatment is considered multimodal, chemotherapy is used as an adjuvant treatment with radiotherapy. Better overall survival median was reported in elderly glioblastoma patients treated with short course radiotherapy (40 Gy in 15 fractions) with

adjuvant temozolomide chemotherapy compared to a group of patients who received radiotherapy only (Perry et al., 2017).

For this, further investigations are required to standardise the use of short or long course HFRT and conventional radiotherapy in elderly glioblastoma patients (Lee et al., 2021).

The American Society of Cancer Oncology (ASCO) endorsed the guidelines of the American Society for Radiation Oncology (ASTRO) for glioblastoma radiotherapy and recommended the following (Sulman et al., 2017):

- In patients, up to 70 years of age and good performance (based on the Karnofsky performance score that assesses the patient's ability to perform ordinary tasks) after surgery or biopsy, a dose of 60 Gy in 2 Gy fractions delivered over 6 weeks is considered optimal.
- In patients older than 70 years of age, there was no evidence of better efficacy treatment of conventionally fractionated radiotherapy (60 Gy in 30 fractions over 6 weeks) over the hypofractionated radiotherapy (40 Gy in 15 fractions over 3 weeks).
- After a biopsy or resection of newly diagnosed glioblastoma in patients up to 70 years of age, partial brain fractionated radiotherapy with adjuvant and simultaneous temozolomide is recommended as the standard care.
- In elderly patients with fair to good performance, it is appropriate to use hypofractionated radiotherapy.
- The addition of temozolomide as adjuvant therapy simultaneously with HFRT is considered safe in elderly patients with good performance score. In patients with poor performance status, either hypofractionated radiotherapy only, or temozolomide only are considered suitable.

Of note, prognostic factors should be taken into consideration for radiotherapy in patients with glioblastoma, particularly in patients over 70 years and with poor performance to appoint the appropriate plan and type radiotherapy, radiation dose, and addition of adjuvant temozolomide chemotherapy (Abedi et al., 2021; Lee et al., 2021).

4.1.3.3. Chemotherapy

Chemotherapy for the treatment of patients with glioblastoma is one of the main therapeutic approaches besides surgery and radiotherapy. Chemotherapy can be delivered as adjuvant therapy pre- or post-surgery (resection and biopsy), as well as concurrently with radiotherapy depending on the diagnosis outcome and therapeutic plan set by the clinicians (Weller et al., 2020). Temozolomide is an alkylating agent and is considered the golden standard chemotherapy drug. It was FDA approved in 1999 for the treatment of anaplastic astrocytoma and, subsequently for glioblastoma. Temozolomide, after its oral administration and well absorption in the small intestine, it penetrates the blood brain barrier (BBB) with its small size of 194Da and reaches the tumour mass. Then, temozolomide undergoes hydrolysis that results in an active and potent metabolite known as active metabolite 5-(3-methyl-1-triazeno)imidazole-4-carboxamide (MTIC). This active metabolite intercalates the DNA by methylating the guanine bases. Thus, induction of DNA damage and cell apoptosis (Strobel et al., 2019; Wesolowski, Rajdev, & Mukherji, 2010).

In newly diagnosed glioblastoma cases, the standard therapeutic regimen, according to the European Association of Neuro-Oncology (EANO) guidelines, includes the temozolomide administration following maximal surgical tumour resection and radiotherapy. The administered dose of temozolomide consists of 75 mg/m² daily, simultaneously with radiotherapy. Then, an additional dose of six cycles of maintenance is administered with 150–

200 mg/m², for 5 days (Weller et al., 2020). In glioblastoma cases with methylated MGMT (a prognostic factor of glioblastoma), temozolomide is administered solely with 150–200 mg/m², 5 days out of 28 days for 12 months or until noted improvement in tumour remission (Weller et al., 2020). It was reported that long term adjuvant temozolomide administration simultaneously with radiotherapy resulted in 5 months of improvements in median progression-free survival (PFS) and a 30 % improvement in 2-year survival rate. Yet, no significant improvement was noted in the overall survival (Huang, Yu, & Liang, 2021).

A combination of lomustine (six courses of 100 mg/m² on day 1 of the cycle) and standard temozolomide dose plus radiotherapy in patients with newly diagnosed glioblastoma and methylated *MGMT* promoter was assessed in a randomised phase III trial. Results of the trial showed potential overall survival enhancement as a result of combining -two alkylating agents- lomustine and temozolomide chemotherapy concurrently with radiotherapy. Yet, these results will require further validation due to the small cohort of patients in this trial (Herrlinger et al., 2019).

The use of bevacizumab -an anti-VEGF antibody- in combination with lomustine for recurrent glioblastoma after receiving standard chemoradiotherapy was assessed in a randomized phase III trial (Wick et al., 2017). The outcome of the trial revealed no significant improvement in overall survival. Despite these findings, bevacizumab is approved for use in the USA and several other European countries including Switzerland. (Weller et al., 2020; Wick et al., 2017).

4.1.3.4. Pioneering therapy

Survival rates of glioblastoma remain a burden over the years despite advances in diagnostic techniques and therapeutic regimens. Over the past four decades, the 5-year survival rate of glioblastoma had only a 3% to 10% improvement, from 4% during the 1975 to 7% - 17% in

2015 (Miller et al., 2021). For this, several teams have been investigating approaches to enhance the overall survival rates through the improvement of the treatment's efficacy, such as nanotechnology (Taiarol, Formicola, Magro, Sesana, & Re, 2020). It consists of employing nanosystems such as nanoparticles to deliver first line chemotherapy drugs in a targeted way by exploiting genetic abnormalities/molecular markers of the malignancy and characteristics of its microenvironment (Taiarol, Formicola, Magro, Sesana, & Re, 2020). Also, these miniature systems bypass the BBB, which is one of the main obstacles in brain cancer treatments (Marei, 2022). For instance, a biodegradable wafer (Gliadel®) made of poly [bis (p-carboxyphenoxy propane) sebacic acid] polymer and loaded with an alkylating agent carmustine (BCNU) was used for targeted delivery of carmustine in newly diagnosed and recurrent glioblastoma. The Gliadel® wafers are intracranially implanted in the resection cavity then the carmustine is released in a sustained manner for up to 4 days without having to bypass the BBB (Shapira-Furman et al., 2019). Gliadel® wafers were FDA approved in 2003, and results of its intracranial implantation with concurrent temozolomide administration and radiotherapy have demonstrated a 4 to 7 months improvement in median survival rates in newly diagnosed and recurrent glioblastoma cases (Affronti et al., 2009; Ashby, Smith, & Stea, 2016). Despite promising results, these polymeric wafers remain a controversial topic among clinicians as this treatment might not contribute to significant improvement in the treatment outcome and overall survival (Qi, Xing, Shao, Yang, & Wang, 2015; Sage et al., 2017). Also, these wafers could manifest additional side effects to the chemo-radiotherapy ones including wound complications and infections that require revision surgery (Sage et al., 2017).

Paclitaxel (a plant alkaloid) loaded in transferrin receptor-T12 peptide-modified polyethylene glycol-poly(lactic acid) (PEG-PLA) micelles were delivered in glioblastoma cells. Transferring receptor, a cell surface marker that is overexpressed both in the BBB and glioblastoma cells,

therefore it is considered a potential therapeutic target. *In vivo* results showed enhanced cellular uptake of the loaded paclitaxel and significant suppression of tumour growth with administrated loaded paclitaxel compared to free paclitaxel (Sun et al., 2020).

Anti-EGFR modified conjugated polymeric nanoparticles (PPVN-A) were used for targeted photodynamic therapy in glioblastoma cells with overexpressed EGFR. These nanoparticles exhibited high ROS generation under white light. Results showed also 90% toxicity in tumour cells treated with EGFR modified PPVN nanoparticles with light exposure compared to 20% cytotoxicity in non-modified PVVN nanoparticles with the same light exposure (Liang, Li, Yuan, Wang, & Gao, 2021).

4.1.4. Prognosis

The poor prognosis of glioblastoma is defined by several factors including MGMTp status, age, the extent of tumour resection, location of the tumour, and KPS factor. Relapse of glioblastoma is estimated to occur *in situ* in 90% of cases, with no significant association has been proven between the choice of treatment regimen and these high recurrence percentages (Chen et al., 2021).

The methylation of the O⁶-methylguanine-DNA methyltransferase (MGMT) gene has been reported to be a key prognosticator of glioblastoma responsiveness to chemotherapy by alkylating agents such as temozolomide (Yu, Zhang, Wei, & Shao, 2020). The MGMT promoted is overexpressed in glioblastoma, and temozolomide works by inducing DNA damage in glioblastoma cells through methylation. Yet, this damage can be repaired by the MGMT repair mechanism and antagonizes the effect of temozolomide, hence, chemotherapy resistance (Taylor & Schiff, 2014).

As a result, the European Association of Neuro-Oncology guidelines recommend testing for MGMT status as a predictive marker for both the eligibility of patients to undergo chemotherapy and for the chemotherapy outcome (Weller et al., 2020).

Age is another factor that predicts and plays a key role in the prognosis of glioblastoma. Age is inversely proportional to good prognosis; the older the patient, the worse the prognosis is. Based on one of the major population-based registries conducted by The Central Brain Tumor Registry of the United States (CBTRUS), the 1-year survival rates of glioblastoma decreased from ~54% to 31.2% in age group ≤ 64 and > 65 years. The 5-year survival rate also decreased from 21% to 4.1% in the age group ≤ 64 and > 65 years. The 1-year and 5-year survival rate in the age group > 75 years was only 4.8% and 1.7%, respectively (Ostrom et al., 2019). Therefore, worse prognosis and unfavourable treatment outcomes in glioblastoma are associated with older age (Weller et al., 2020). Due to the fragility of patients above the age of 75 years, the application of treatment regimens including total resection surgery, chemotherapy and/or radiotherapy, is limited (Nunna et al., 2021). Such treatments were less frequently used in elderly patients and despite the fact that they can improve survival outcome, the patient's quality of life is severely affected (Nunna et al., 2021). Therefore, treatment strategies in patients with glioblastoma should be balanced between treating the neoplasm and preserving the quality of life (Nunna et al., 2021).

Two more prognostic factors are total resection of the tumour and location of the tumours, where the first factor is highly related to the latter one. Survival rates in patients with glioblastoma is related to the extent of the tumour resection. Due to the infiltrative biology of glioblastoma and other diffuse gliomas, total removal of the tumour cells is practically impossible (Cahill, 2021). A meta-analysis results of 37 studies reported that lower risk of

mortality i.e., higher survival chances, were associated with increasing extent of gross total resection of the tumour (Brown et al., 2016). Given the latter reported results and given that glioblastoma develops in critical brain areas including the frontal lobe, gross total resection of the tumour can be affected by the neoplasm's location in the brain (Chaichana et al., 2013). This is due to the surgical procedure's risk in affecting adjacent areas to the tumour and leading to "postoperative morbidity" and potential impairment in KPS (Baik, Kim, Na, & Cho, 2023).

Karnofsky performance scale or KPS factor grades the performance of patients with cancer post-therapy in the 0 to 100 range (worst to best performance) (Péus, Newcomb, & Hofer, 2013). Data analysis on 335 patients with gliomas including glioblastoma, showed a correlation between low KPS and poor prognosis. Patients with KPS <70 had up to three times higher mortality risk within the first year after treatment (Liang et al., 2020). The ASCO guidelines indicated that older age and poor performance were associated with shorter survival in glioblastoma patients, and treatment options after resection surgery -if eligible- are limited to either hypofractionated radiotherapy, temozolomide administration, or most suitable supportive care (Sulman et al., 2017).

The aim of the current study was to assess the ability of dual sensitive polymeric nanocontainers (pH and temperature) in delivering first line chemotherapy drugs sustainably and effectively in glioblastoma. Through this approach, the current study aimed at improving the efficacy of the chemotherapy drugs; hence, reducing their underlying side effects as a result of cargo targeted delivery.

4.2. Materials and Methods

4.2.1. Materials

DMEM High Glucose w/L-Glutamine w/Sodium Pyruvate culture media (Biosera, NUAILLE, France), Dulbecco's phosphate buffered saline (DPBS) (Biosera, NUAILLE, France), Fetal Bovine Serum (Biosera, NUAILLE, France), Trypsin-EDTA (Biosera, NUAILLE, France), Poly-L-Lysine (Innoprot, Derio, Pais Vasco, Spain), MTT Reagent in powder (Cayman, Michigan, USA), RIPA Lysis Buffer System (Santa Cruz Biotechnology, Inc, Texas, USA), Mini Trans-Blot System (Bio-Rad, California, USA), p-Coumaric acid (Sigma-Aldrich Darmstadt, Germany), Luminol (Sigma-Aldrich Darmstadt, Germany), BCA Protein Assay Kit (Cell Signalling, Massachusetts, USA.), Glycine for molecular biology (PanReac AppliChem, ITW Reagents Division, Chicago, USA), Tris (PanReac AppliChem, ITW Reagents Division, Chicago, USA), Tween 20 (PanReac AppliChem, ITW Reagents Division, Chicago, USA), GAPPDH antibody, rabbit anti-mouse IgG-HRP, m-igG fc BP -HRP anti-mouse antibody (Santa Cruz Biotechnology, Inc, Texas, USA), Phospho-Histone H2A.X (Ser139) Antibody (Affinity Biosciences, China), Opti-Protein marker (ladder) (Applied Bioscience Material, Richmond, Canada), Sodium dodecyl sulfate or SDS (Bio-Basic, Toronto, Canada), Amersham Protran nitrocellulose blotting membranes 0.2 μ m (Cytiva, Germany), Thick Blot Filter Paper (Bio-Rad, California, USA), Buffered formalin 10% (Atom Scientific, Manchester, UK), Anatomix RP Fixer and Anatomix RP Developer Replenisher (FUJIFILM, Tokyo, Japan), Medical X-ray Film (FUJIFILM, Tokyo, Japan), Amersham hypercssette autoradiography cassettes (Fisher scientific, Massachusetts, USA), Propidium iodide (Sigma-Aldrich Darmstadt, Germany), Annexin-V, 7AAD, and binding buffer (BD Bioscience, New Jersey, USA). Incubator thermos HEPA class 100 (Thermofisher Scientific. Massachusetts, USA), OMAX Fluorescent microscope 40X-1600X EPI (OMAX, USA). Rocking and waving shaker (OHAUS, New Jersey, USA), Becton Dickinson FACSCalibur flow cytometer (BD Bioscience, New

Jersey, USA), Elisa microplate reader (Biobase Biodustry, Shandong, China). Band intensity quantification in western blot membranes were quantified by GelQuantNet 1.6.6 (BiochemLab Solutions.com, University of California, San Francisco) software. Statistical analysis was carried out using Prism GraphPad 9 and Microsoft Excel Spreadsheet software.

4.2.2. Cell culture

Glioblastoma U87 MG (ATCC, Maryland, USA) and healthy human embryonic kidney HEK293 (ATCC, Maryland, USA) cell lines were thawed and introduced into a T 75mm² culture flask with 20ml of 10% FBS high glucose DMEM culture media. The cells were then left inside the incubator for growth and attachment at 37°C and 5% CO₂. After the cells' attachment the following day, the media was changed, and the cells were examined under the microscope in order to verify their growth and morphology. After ~85% confluency, cells were subcultured in a 1 to 10 ratio. The rest of the collected cells were either cryopreserved and kept in liquid nitrogen or seeded for further experiments in the appropriate plate accordingly.

4.2.3. MTT assay

The U87 MG and HEK293 cell lines were seeded in 96 well plates with a concentration of 6×10^3 to 8×10^3 cells/well. Cells were left in the incubator to grow one night prior to the experiment and until reaching ~75% confluency. Then, 100µl of the seven different increasing concentrations of free NCs, loaded and free DNR, cisplatin, temozolomide, and DNR/temozolomide combination, were introduced in the wells in triplicates. The control wells contained only culture medium. Plates were then introduced in the incubator and after 24h and 72h, suspensions were removed from the wells and replaced with 100µl of MTT solution and introduced back in the incubator. After 2-4h, after observing the formation of the

formazan crystals, MTT solution was removed from each well and replaced with 100µl of DMSO. After the full dissolution of crystals, the absorbance of each plate was measured using an Elisa microplate reader (Biobase Biodustry, Shandong, China) at 560nm wavelength. Cell viability percentage calculations were carried out as follows:

$$\text{Cell Viability \%} = \left(\frac{\text{Mean } OD_{560}(\text{Sample})}{\text{Mean } OD_{560}(\text{Control})} \right) \times 100$$

4.2.4. Wound healing

U87 MG and HaCat (ATCC, Maryland, USA) cell lines were seeded in separate 6 well plates in 2×10^5 to 4×10^5 cells/well. After 12h, 80% confluency was checked, the culture media was removed, and a wound was created using a 200µl sterile pipette tip. Then, each well was washed with PBS before introducing 1.5ml ($1 \mu\text{M}$) of the different suspensions of free nanocarriers, loaded nanocarriers, and free DNR. Pictures of the wound were taken by optical microscope at t_0 and at three more different time points (19h,24h,48h) in order to monitor the wound closure. After collecting all the measurements data, the wound closure percentages were calculated using the following equation:

$$\text{Wound closure \%} = \left(\frac{A_{t=0h} - A_{t=xh}}{A_{t=0h}} \right) \times 100$$

where A is the wound area at different time points, $t = 0h$ and xh .

Of note, after conducting this experiment one time and after the 18 monthly progress assessment, we were advised by the examiners to avoid carrying out this experiment again since it was indirectly leading to the same conclusions with MTT assay about the cytotoxicity of the loaded and free nanocontainers.

4.2.5. Fluorescence microscopy

In a 6 well plate, square coverslips (22mm) were placed in each well and then soaked in polylysine for 30min. After removing the polylysine and drying the wells, cells were seeded with 2×10^5 to 4×10^5 cells/well about 12h prior to the experiment. After ensuring the cells' attachment on the surface of the coverslips with an 80% confluency, the culture medium was then replaced with 500 μ l of DNR loaded NCs and free DNR in 1 μ M and 10 μ M concentrations. After each set time point, the suspensions were removed from the corresponding wells and fixed with 250 μ l 4% PFA. After 30min, the fixation solution was removed and the wells were washed twice with PBS. After that, the coverslips were gently picked using tweezers and flipped on a pre-mounted microscope slide. The microscope slides were viewed and evaluated using a fluorescent microscope 40X-1600X EPI (OMAX, USA).

4.2.6. Western blot

4.2.6.1. Protein extraction and quantification

Both U87 MG and HEK293 were seeded in 6 well plates and treated with 30 μ M of different suspensions of free NCs, loaded and free DNR, cisplatin, temozolomide, and DNR/temozolomide combination. After 72h incubation, suspensions were removed and 100 μ l of RIPA lysis buffer was introduced in each well while the plates were placed on ice. The lysis buffer was prepared according to the manufacturer's instructions and every 1ml of the lysis buffer contained 10 μ l of protease inhibitors cocktail, PMSFA, and sodium orthovanadate. About 5min later, cells were scratched, collected, and introduced in Eppendorf tubes and preserved on ice until all other cells were collected from the rest of the wells. Then, Eppendorf tubes containing lysed cells were sonicated for 10 sec and introduced back to the ice for

another 10 sec. This action was repeated about 10 times before centrifuging the cells at 4°C, 16128 RCF for 20 min. After centrifugation, the supernatant was collected, and the palette was discarded. The protein quantification was determined using the BCA protein assay kit (Cell Signalling, Massachusetts, USA) and BSA standard curve.

4.2.6.2. Samples and SDS-PAGE gels preparation

Next, the required amount of protein for loading - 30µg/40ul in these experiments- was calculated and samples were prepared with ¼ of the final sample volume as Laemmli buffer (see appendix 1 for Laemmli buffer preparation).

Running gels were prepared based on the size of the protein of interest, i.e., the smaller the protein, the higher the SDS gel concentration. The H2A.X with 15kDa molecular weight was the protein target of the western blot. Therefore, the gels prepared were 15% SDS. After the solidification of the gels, loading samples were boiled for 5min at 95°C.

4.2.6.3. Running the gels

After assembling the gels in the chamber and introducing them to the buffer tank, combs were removed, and the chamber between the two gels was filled with running buffer. Samples were then loaded in the corresponding wells with the ladder in the first well. A running buffer was added to the appropriate level and the tank was closed. The gels were run for 15 to 20 min at 80V until the sample surpassed the staking gel before increasing the voltages in the power supply to 110V. After 2h and after the protein separation reached the bottom of the gel, the power supply was turned off and the running step was stopped. The sandwiches for protein transfer from the gels to the membranes were prepared with sponges or foam pads,

membranes and filter paper, all pre-soaked in transfer buffer. The components ordered in the gel holder cassette was as follows: black side of the gel holder cassette, sponge, filter paper, gel, membrane, filter paper, sponge, white side of the cassette. The sandwiches were then closed and introduced inside the electrode assembly with its black side facing the one of the cassettes to insure the appropriate transfer of the protein from the gel to the membrane. The electrode assembly containing both sandwich cassettes was introduced in the transfer tank, then filled with cold transfer buffer and the whole tank was introduced inside an ice container, with ice surrounding the transfer tank. The transfer step was run at 400mA for 2.5 hours using a current power supply connected by power cables to the transfer tank. After the transfer was over, membranes were retrieved from the sandwiches and stained with red ponceau in order to have a primary evaluation of the protein separation and band quality. After that, the membranes were well washed with dH₂O until most of the red stain was removed before they were blocked with 5% non-fat milk for 1h. Primary antibodies of the protein of interest were prepared in 5% non-fat milk in 1:1000 final concentration. In order to avoid using large volumes of antibodies, 3ml final volume with 1:1000 antibody concentration solution was introduced in a 50ml falcon in which the membrane was introduced and left to shake on a rocking shaker overnight at 4°C. Next morning, the membranes were removed from the falcons and washed with TBS-T buffer 3 times, 10min each. Secondary antibodies were prepared with the way as the primary antibody (1:2000 to 1:10000), and membranes were left to probe on a rocking shaker (OHAUS, New Jersey, USA) for an hour, after which washing was carried out for 3 times, 10min each, with TBS-T buffer.

4.2.6.4. Developing the films and imaging the membranes

After the washing was over, membranes were incubated for 3min with ECL solutions (prepared from scratch in the lab, see appendix 2) then wrapped in a transparent film and fixed on an autoradiography cassette. In a dark room with only safe red light, x-ray film was exposed to the membranes in the cassettes for 3 to 5min. Immediately after the exposure time was over, films were dipped in developing solutions in the following order: developer solution for 5 sec, water, fixer solution for 5 secs then water again. Based on the intensity of the bands, exposure might be repeated for a shorter or longer time until bands with appropriate intensity and suitable for quantification were obtained. Membranes images were obtained by Fluorchem 8800 imager (Alpha Innotech, San Leandro, USA), where the membranes were covered with ECL immediately before imaging and the exposure time was set between 3 to 8 min.

4.2.7. Flow cytometry

Both U87 MG and HEK293 were seeded in 6 well plates or 25mm² culture flask at least 12h prior to their treatment with 30µM of different suspensions of free NCs, loaded and free DNR, cisplatin, temozolomide, and DNR/temozolomide combination. After 24h and 72h of treatment, cells were harvested by trypsin and then centrifuged at 800rpm for 3 min. For Annexin-7AAD protocol, about 1x10⁵ cells were well resuspended in 100µl of binding buffer, then stained 5µl of annexin-V and 5µl of 7AAD and left to incubate for 20min in the dark. After the incubation time was over, 400µl of binding buffer was added, and the sample was measured with Becton Dickinson FACSCalibur flow cytometer (BD Bioscience, New Jersey, USA).

For Propidium Iodide (PI) protocol, 1×10^6 cells were fixed with cold 70% ethanol. The fixation was done with a thorough vortex of the cells (pipetting cells up and down) in order to avoid clumping. After 1h, cells were washed with PBS and resuspended in 500ml PI solution and left to incubate for 40min before Fluorescence-Activated Cell Sorting (FACS) flow cytometry measurement.

4.3. Results

4.3.1. Cytotoxicity

The MTT assay results after 24h incubation with free NCs, cisplatin loaded NCs and free cisplatin (Figure 53) showed high cell viability of more than 80% and 58% throughout the increasing concentrations of the free NCs in U87 MG (Figure 53a) and HEK293 (Figure 53b) cell lines, respectively. Increasing concentrations of cisplatin loaded NCs and free cisplatin in both cell lines showed decreasing cell viability i.e., increasing cytotoxicity. The lowest cell viability percentages in both cell lines were recorded at 30 μ M with ~63% and ~59% for loaded NCs and free cisplatin, respectively.

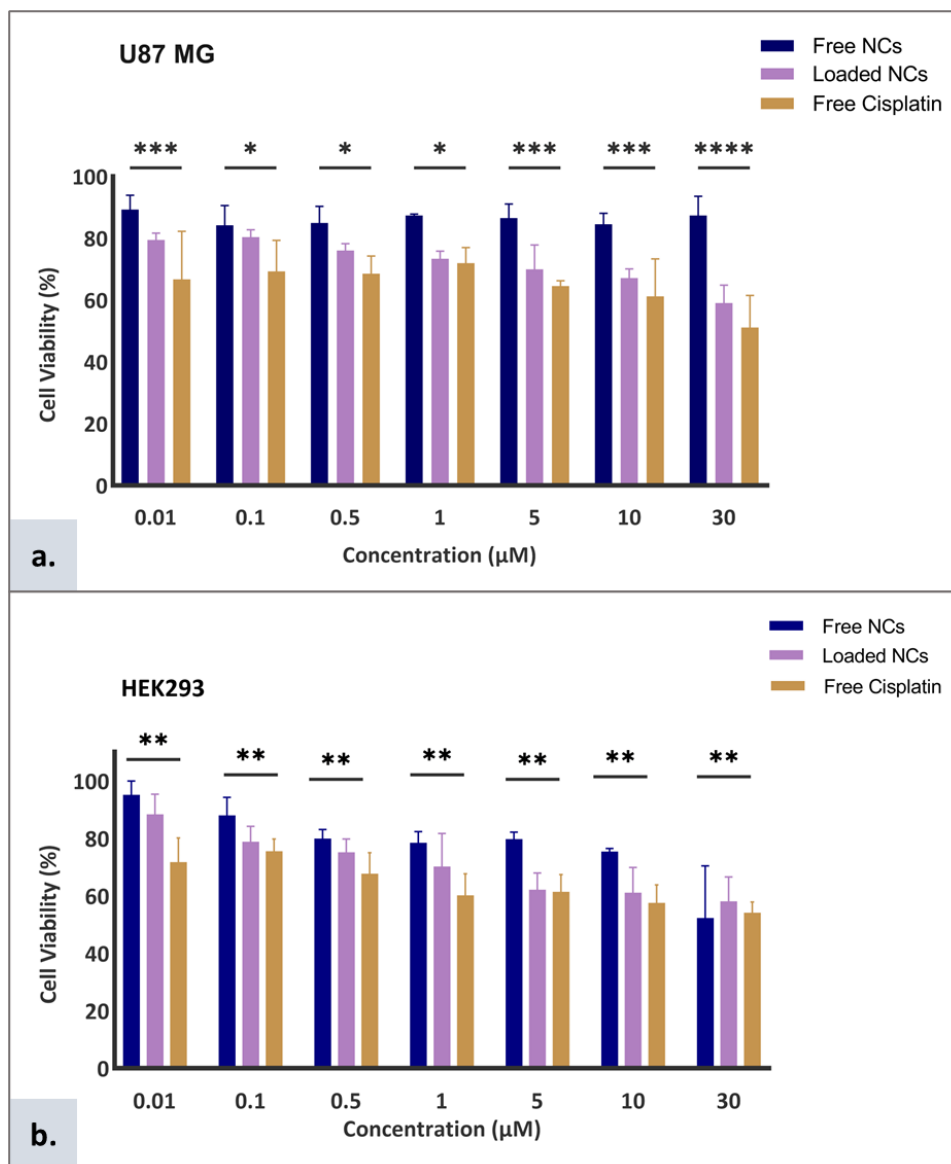


Figure 53. Evaluation of the cell viability via MTT assay. Cytotoxicity levels in **a).** U87 MG, and **b).** HEK293 cell lines after 24h treatment with free NCs, cisplatin loaded NCs, and free cisplatin. Two-way ANOVA test (U87 MG) and 2 tailed paired student t test (HEK293) (* $P \leq 0.05$, ** $P \leq 0.01$, *** $P \leq 0.001$, **** $P \leq 0.0001$); error bars are based on mean \pm SD of three independent experiments.

In the U87 MG and HEK293 cells that were treated with free NCs, DNR-loaded NCs, and free DNR (Figures 25a and 25b, respectively), cell viability percentages were all higher than 78% across the increasing concentration of free NCs. A pattern of decreasing viability percentages was recorded in both cell lines treated with increasing concentrations of loaded and free DNR, reaching 60% and 56%, respectively, at 30 μ M. Treatments with loaded and free DNR in both U87MG and HEK293 showed about an 18% decrease in cell viability at 30 μ M compared to the lowest concentration of 0.01 μ M.

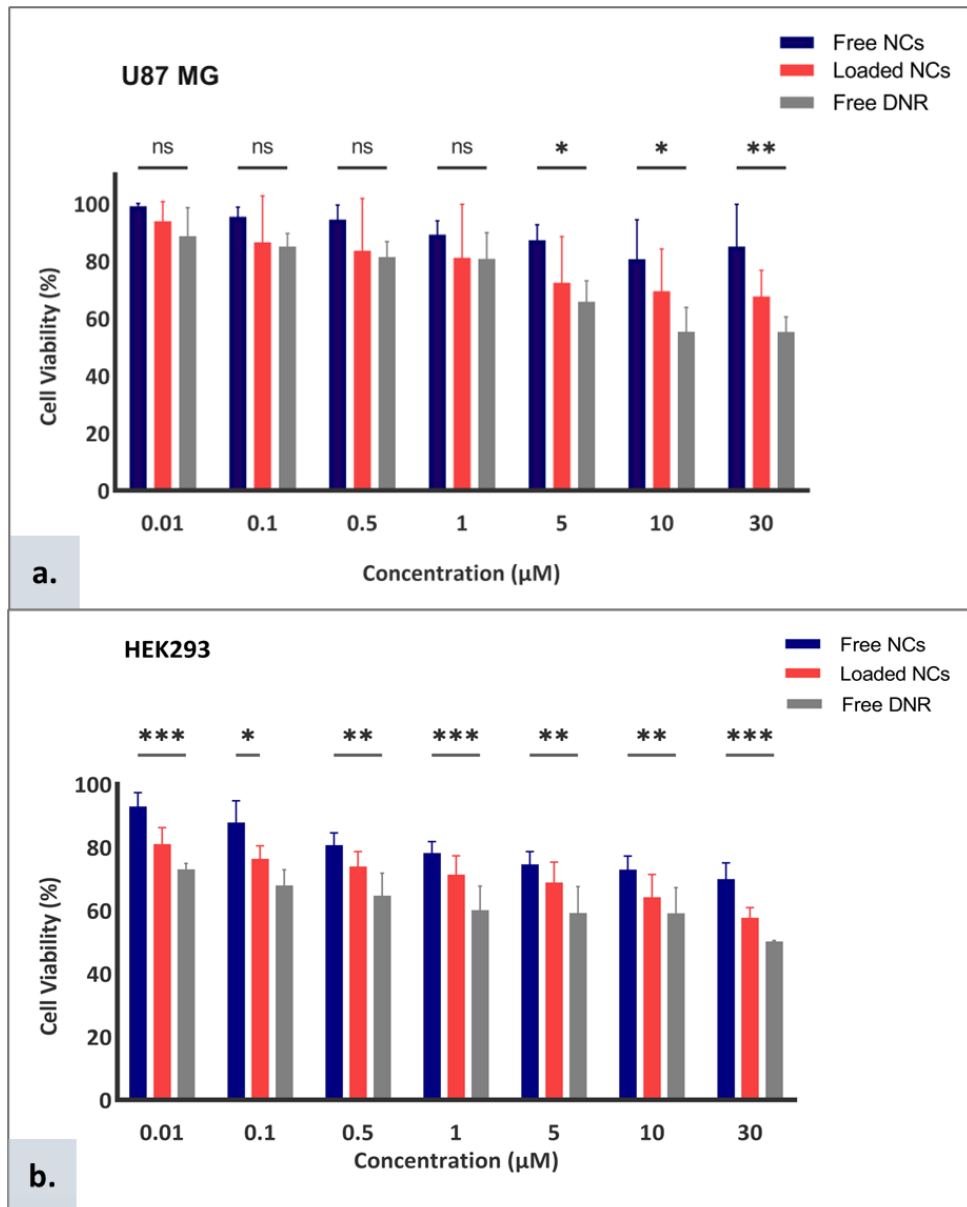


Figure 54. Evaluation of the cell viability via MTT assay. Cytotoxicity levels in **a).** U87 MG, and **b).** HEK293 cell lines after 24h treatment with free NCs, DNR loaded NCs, and free DNR. Two-way ANOVA test (ns $P > 0.05$, * $P \leq 0.05$, ** $P \leq 0.01$, *** $P \leq 0.001$); error bars are based on mean \pm SD of three independent experiments.

Similarly, with the aforementioned treatments, both U87 MG and HEK293 cells were also treated with free NCs, temozolomide-loaded NCs, and free temozolomide (Figure 55a and 55b, respectively). Results showed high percentages of cell viability (>78%) in cells treated with free NCs regardless of the increasing concentration. Yet, cellular viability percentages of temozolomide-loaded NCs and free temozolomide treated cells reached ~60% to 63% at 30 μ M which is 22% less than the cell viability recorder at lower treatment concentrations of 0.01 μ M.

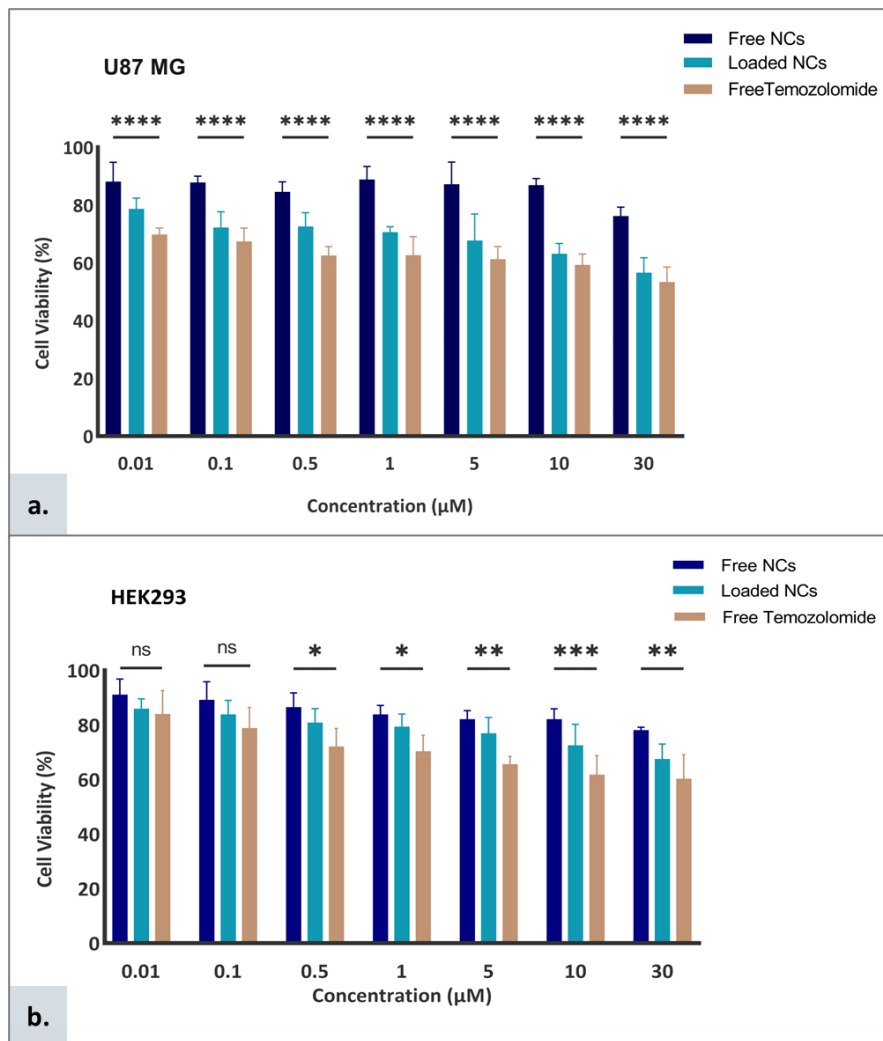


Figure 55. Evaluation of the cell viability via MTT assay. Cytotoxicity levels in **a).** U87 MG, and **b).** HEK293 cell lines after 24h treatment with free NCs, temozolomide loaded NCs, and free temozolomide. Two-way ANOVA test (ns $P > 0.05$, * $P \leq 0.05$, ** $P \leq 0.01$, *** $P \leq 0.001$, **** $P \leq 0.0001$); error bars are based on mean \pm SD of three independent experiments.

The cell viability percentages of both U87 MG (Figure 56a) and HEK293 (Figure 56b) treated with the free and loaded combination of temozolomide and DNR were ~48% and ~60%, respectively. This was ~8 lower than the cells treated with the same drugs (DNR and temozolomide) separately across the different concentrations. These viability percentages were ~20% to 50% lower than the cell viability levels recorded at lower treatment concentrations (0.01 μ M). For the NCs treated cells, results showed high percentages of cell viability of up to ~90%, regardless of the increasing concentration, similar to the aforementioned MTT experiments. Cellular viability percentages of temozolomide/DNR-loaded NCs and free temozolomide/DNR treated cells reached 58% and 43% at 30 μ M, respectively.

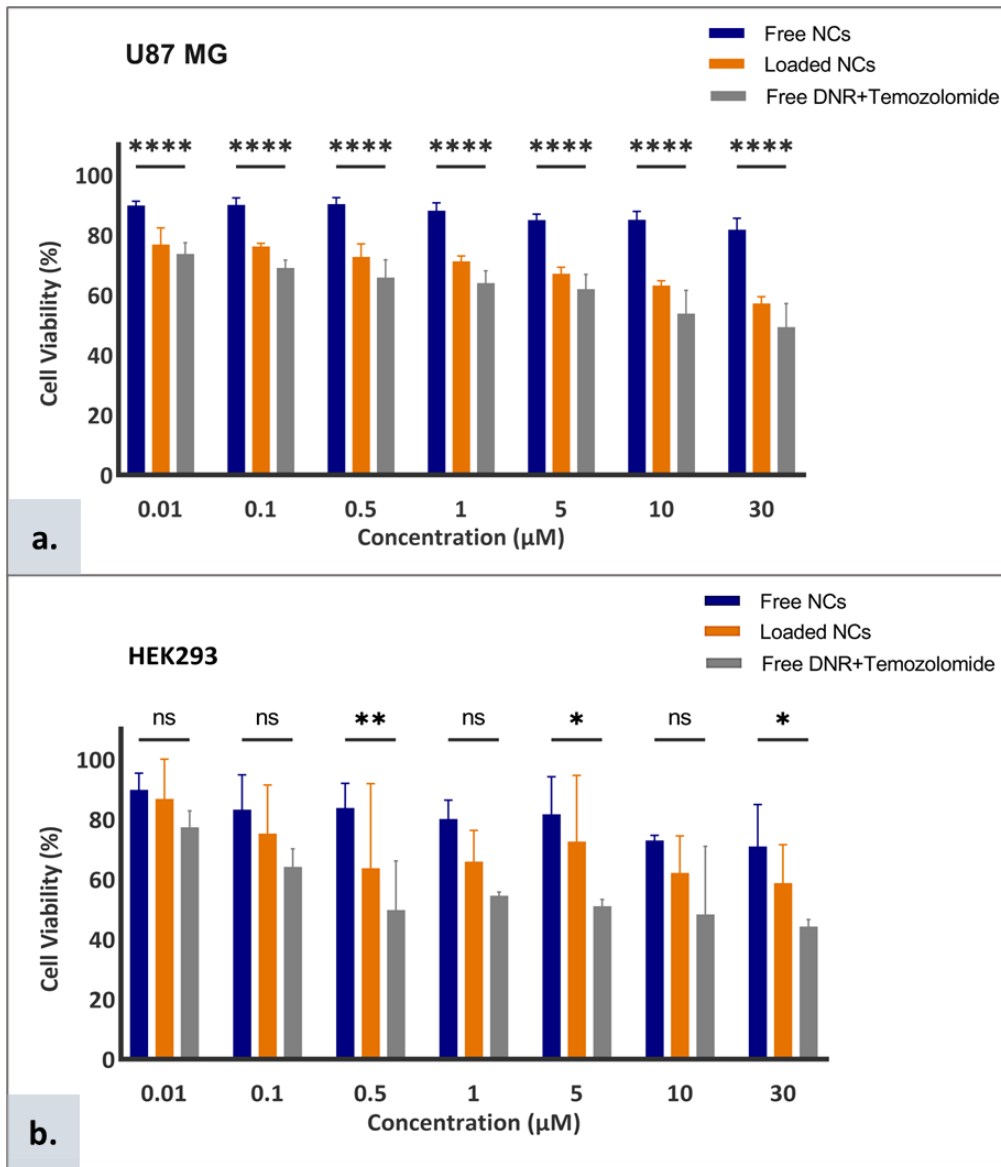


Figure 56. Evaluation of the cell viability via MTT assay. Cytotoxicity levels in **a).** U87 MG, and **b).** HEK293 cell lines after 24h treatment with free NCs, DNR/temozolomide loaded NCs, and free DNR/temozolomide. Two-way ANOVA test (ns $P > 0.05$, * $P \leq 0.05$, ** $P \leq 0.01$, **** $P \leq 0.0001$); error bars are based on mean \pm SD of three independent experiments.

The MTT assay results after 72h incubation with free NCs, cisplatin loaded NCs and free cisplatin in U87 MG (Figure 57a) and HEK293 (Figure 57b) showed high cell viability percentages of more than 78% throughout the increasing concentrations of the free NCs in both U87 MG and HEK293 cell lines. Increasing concentrations of cisplatin loaded NCs and free cisplatin in both cell lines, showed decreasing cell viability percentages. The lowest cell viability percentages of ~38% in U87 MG and ~58% in HEK293 were recorded at 30 μ M of loaded and free cisplatin. Loaded cisplatin at 30 μ M showed 10% less cell viability in U87 MG cells than the loaded cisplatin at the same concentration in HEK293 cells.

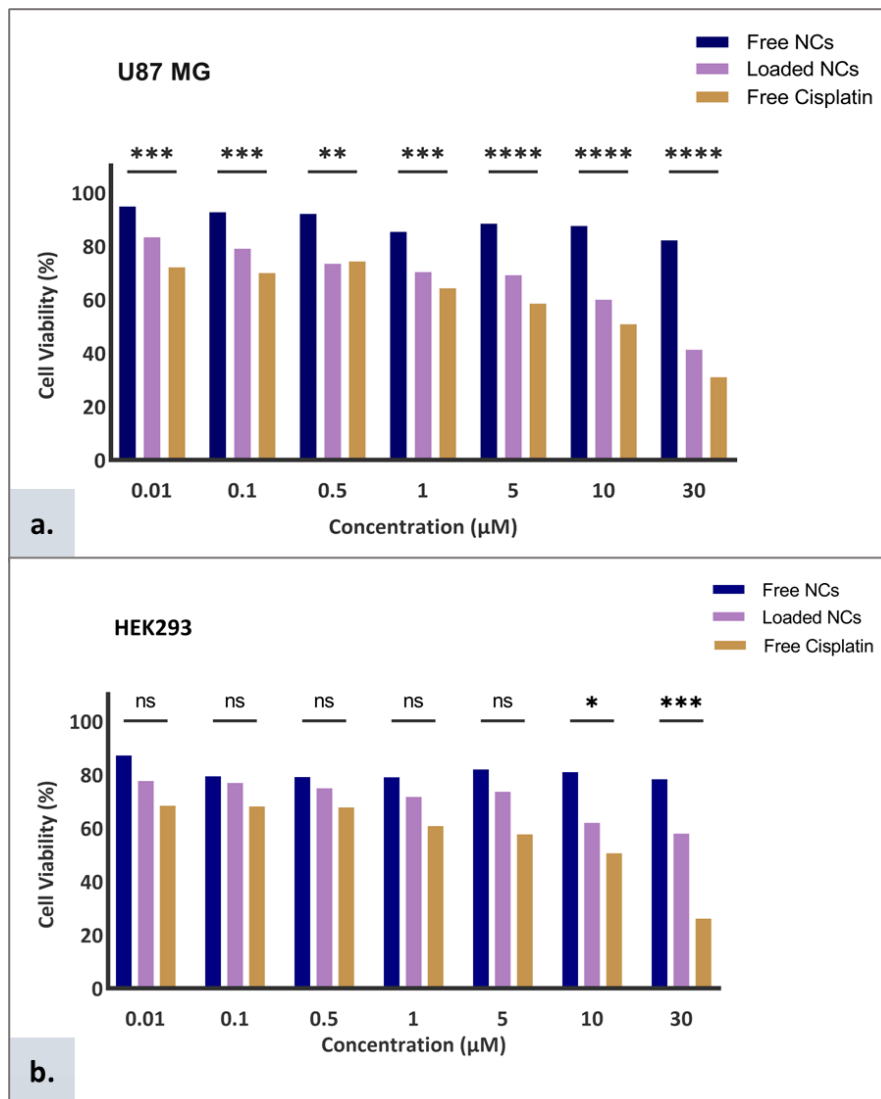


Figure 57. Evaluation of the cell viability via MTT assay. Cytotoxicity levels in **a).** U87 MG, and **b).** HEK293 cell lines after 72h treatment with free NCs, cisplatin loaded NCs, and free cisplatin. Two-way ANOVA test (ns $P > 0.05$, * $P \leq 0.05$, ** $P \leq 0.01$, **** $P \leq 0.0001$), two independent experiments.

The cell viability percentages in both U87 MG and HEK293 cell lines treated with free NCs for 72h were above 78% regardless of the concentration (Figure 58a and 58b, respectively). Conversely, treatment of both cell lines for 72h with increasing concentrations of DNR loaded NCs and free DNR showed a remarkable decrease in cell viability percentages reaching ~40% and 30%, respectively, at 30 μ M (Figure 58). Free NCs retained high viability percentages for both 24h and 72h. However, DNR-loaded NCs and free DNR showed 18% and 20% decrease, respectively, in cell viability percentages compared to the 24h treatment.

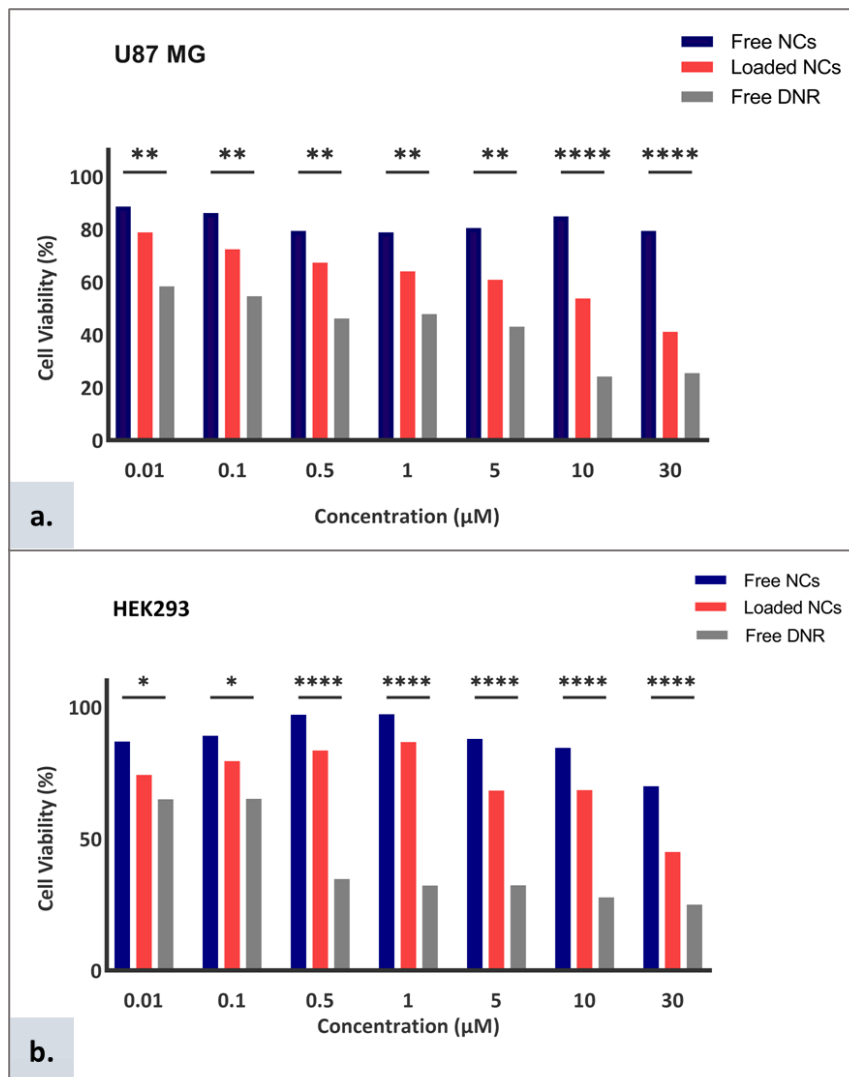


Figure 58. Evaluation of the cell viability via MTT assay. Cytotoxicity levels in **a).** U87 MG, and **b).** HEK293 cell lines after 72h treatment with free NCs, DNR loaded NCs, and free DNR. Two-way ANOVA test (* $P \leq 0.05$, ** $P \leq 0.01$, **** $P \leq 0.0001$), two independent experiments.

Treatment with loaded and free temozolomide for 72h showed a decreasing pattern of cell viability percentages (Figure 59). At 30 μ M loaded and free temozolomide, cell viability reached the lowest levels of 48% and 38%, respectively, in U87 MG (Figure 59a) and 58% and 42%, respectively, in HEK293 (Figure 59b). These levels were about 20% to 28% lower than the treatment with loaded and free temozolomide at 24h. The 72h treatment with free NCs retained the cell viability percentages between 90% and 79% throughout the increasing concentrations for both cell lines, similarly with the 24h treatment.

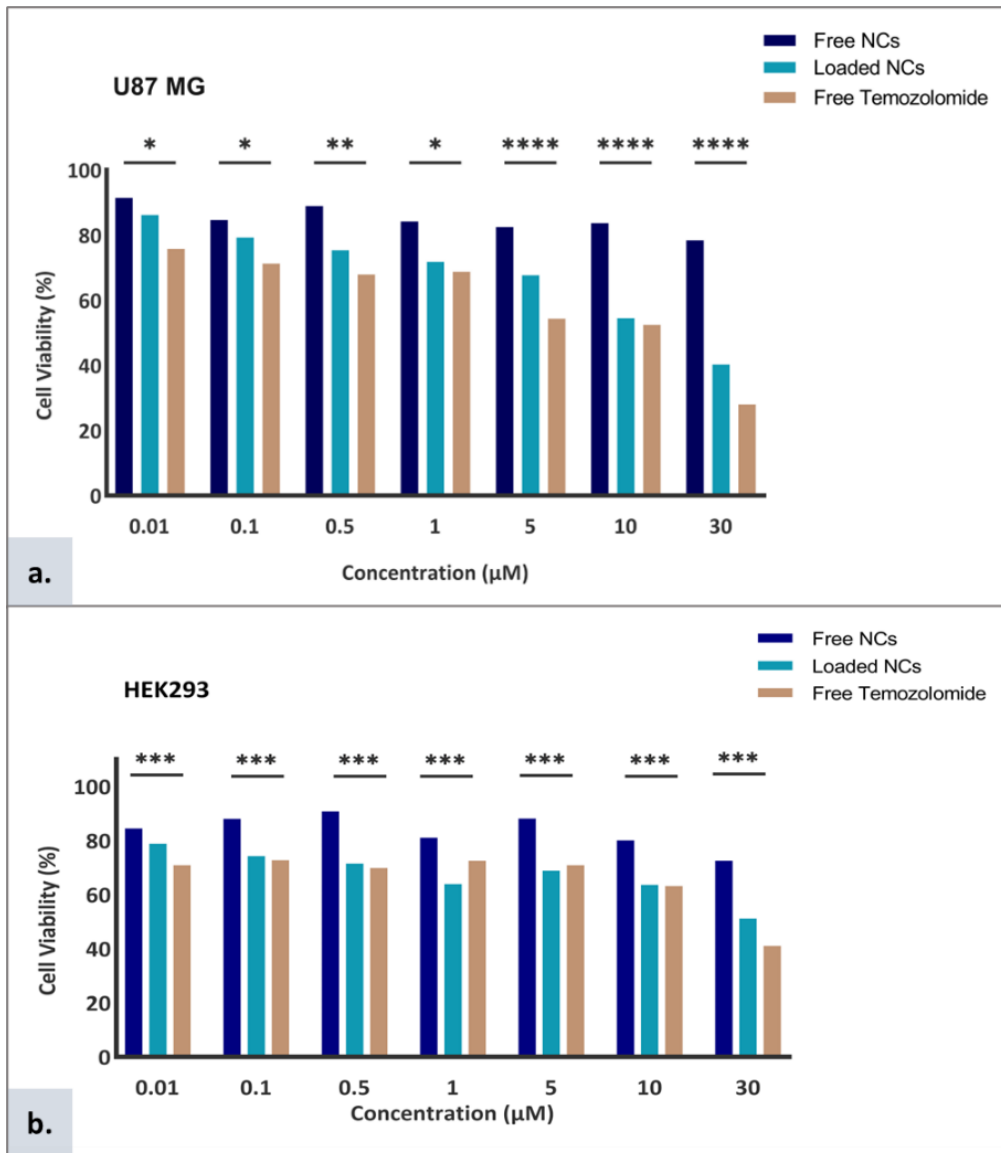


Figure 59. Evaluation of the cell viability via MTT assay. Cytotoxicity levels in **a).** U87 MG, and **b).** HEK293 cell lines after 72h treatment with free NCs, temozolomide loaded NCs, and free temozolomide. Two-way ANOVA test (* $P \leq 0.05$, ** $P \leq 0.01$, *** $P \leq 0.001$, **** $P \leq 0.0001$), two independent experiments.

The 72h treatment with a free and loaded combination of DNR and temozolomide showed decreasing cell viability percentages throughout the increasing concentrations in both U87 MG (Figure 60a) and HEK293 (Figure 60b) cell lines. At 30 μ M, the lowest cell viability levels of 50% to 30% and 28% were recorded in loaded and free DNR and temozolomide, respectively. The cell viability levels at 72h treatment with the loaded and free DNR and temozolomide combination was ~10% to 20% lower compared to the 24h with the same combination. Free NCs maintained cell viability levels above 70% throughout the increasing concentrations similar to the 24h treatment.

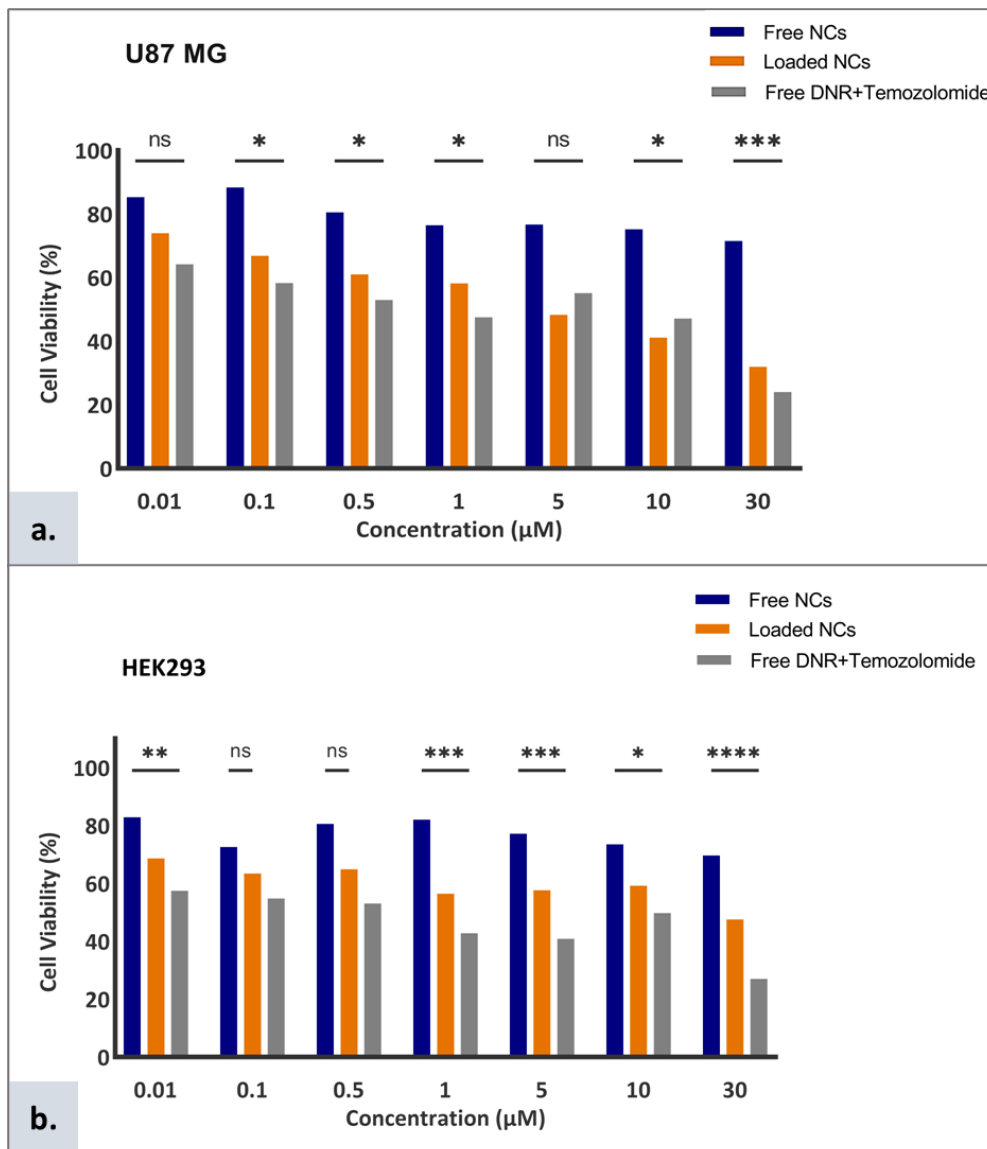
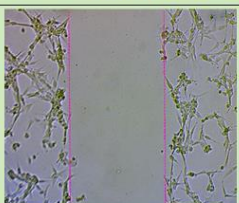
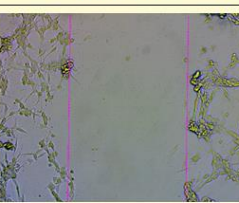
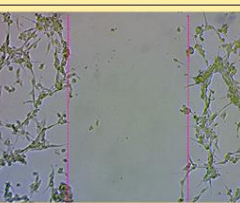
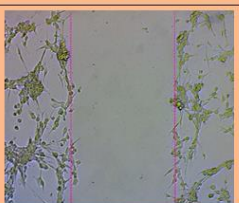
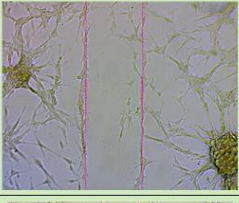
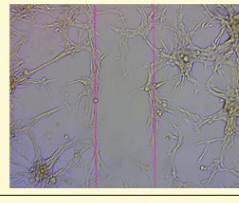
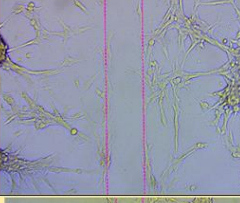
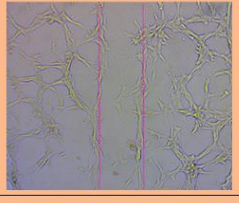
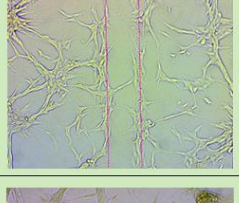
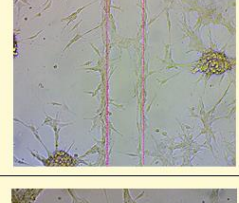
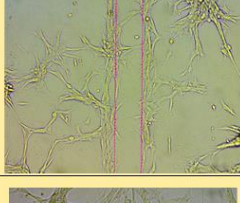
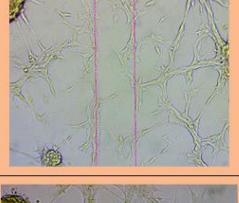
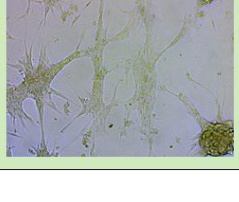
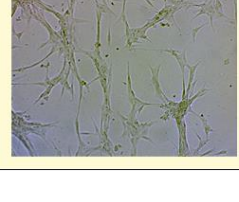
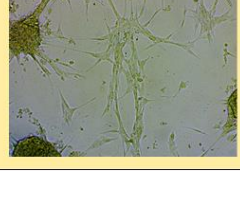
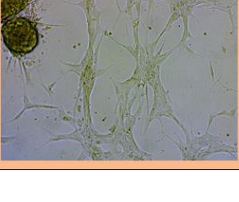


Figure 60. Evaluation of the cell viability via MTT assay. Cytotoxicity levels in **a).** U87 MG, and **b).** HEK293 cell lines after 72h treatment with free NCs, DNR/temozolomide loaded NCs, and free DNR/temozolomide. Two-way ANOVA test (ns $P > 0.05$, * $P \leq 0.05$, ** $P \leq 0.01$, *** $P \leq 0.001$, **** $P \leq 0.0001$), two independent experiments.

4.3.2. Wound healing

The wound closure monitoring by optical microscope in U87 MG cells (Table 15), showed a gradual wound closure throughout the time points until full closure after 40h in the control cells and the cells incubated with free NCs. However, the cells incubated with loaded NCs and free DNR, showed a visible slowdown in their wound closure after 24h.

Table 15. Wound closure monitoring in U87-MG cell line by optic microscope at different time points.

Time Point	Wound Area			
	Control	Loaded NCs	Free NCs	Free DNR
0h				
19h				
24h				
48h				

The calculated wound closure area (Figure 61) displayed a continuous wound closure in the cells incubated with free NCs reaching 85% healing at 48h and total healing progress of 16.8% between 19h and 48h. The same closure pattern was observed in the control cells that had a wound healing of 23% between the same time points. On the contrary, the cells incubated with loaded NCs and free DNR showed a lower rate of wound healing of 11% and 15%, respectively, between 21h and 48h.

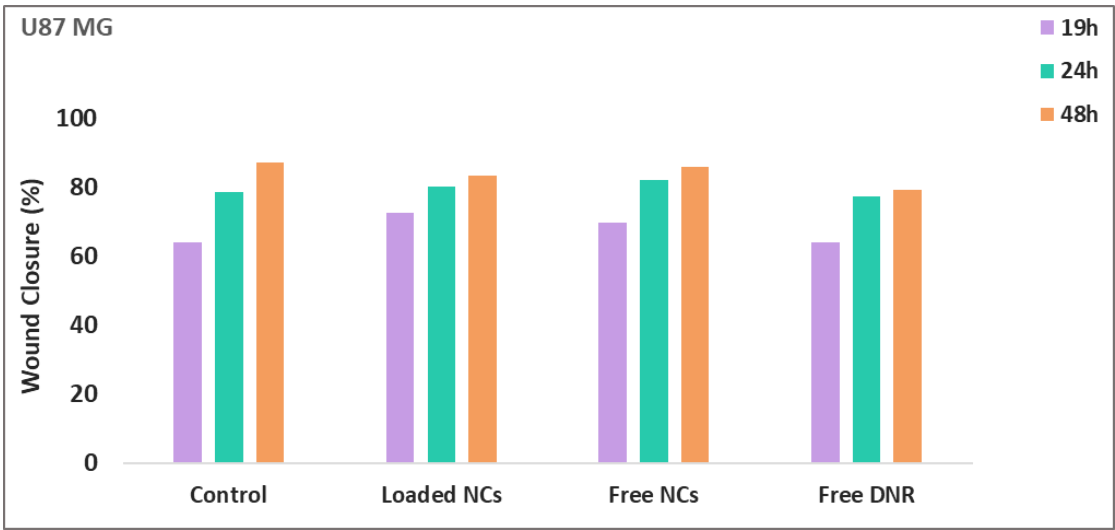
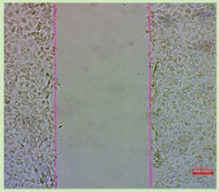
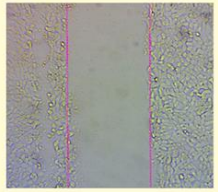
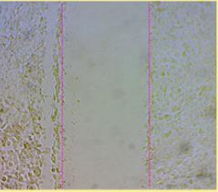
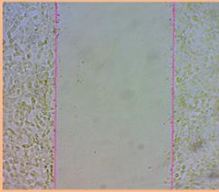
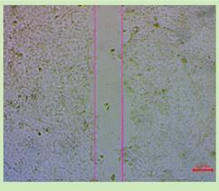
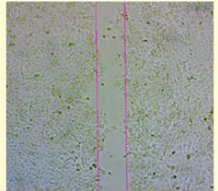
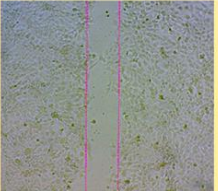
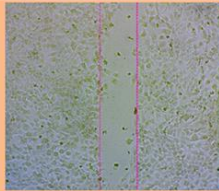
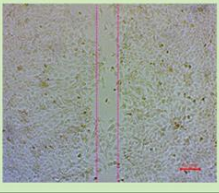
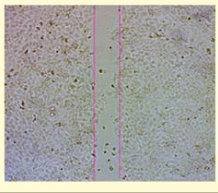
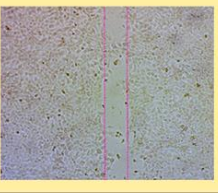
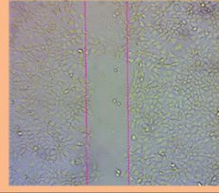
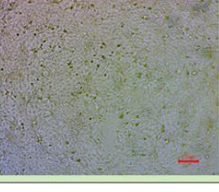


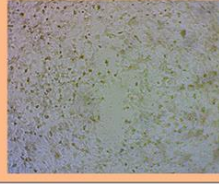


Figure 61. Wound closure percentage in U87 MG cell line at 19h, 24h, and 40h after NCs, DNR loaded DNR, and free DNR treatment.

The wound closure monitoring at different time points by optical microscope in the HaCat cell line (Table 16), showed a gradual wound closure throughout the time points until fully closed after 40h, in both control cells and the ones incubated with free NCs. However, the cells incubated with loaded NCs and free DNR showed a slowdown in wound closure after 24h.

Table 16. Wound closure monitoring in HaCat cell line by optic microscope at different time points.

Time Point	Wound Area			
	Control	Loaded NCs	Free NCs	Free DNR
0h				
21h				
24h				
40h				

The calculated wound closure area (Figure 62) showed a continuous wound closure in the cells incubated with free NCs reaching 91% healing at 40h. Hence, a 41% healing progress between 21h and 40h. Similarly, the control cells had a healing progress of 31.6% between the same time points, reaching 100% closure after 40h. On the contrary, the cells incubated with loaded NCs and free DNR showed a lower rate of wound healing of 29.7% and 8%, respectively, between 21h and 40h.

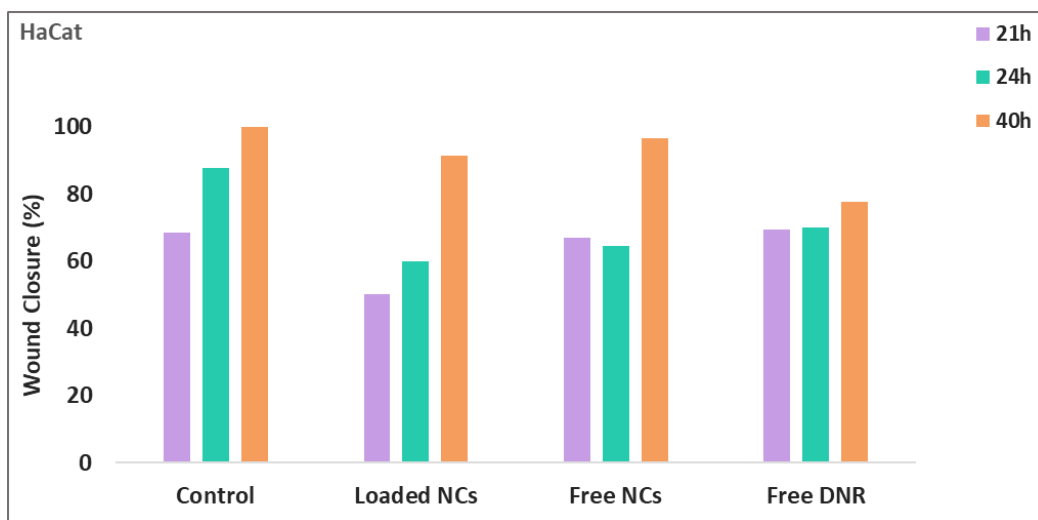


Figure 62. Wound closure percentage in HaCat cell line at 21h, 24h, and 40h after NCs, DNR loaded DNR, and free DNR treatment.

4.3.3. Cellular uptake and internalization

The cellular uptake analysis in U87 MG (Figure 63) and HaCat (Figure 64) cell lines of the DNR loaded NCs (1 μ M) by fluorescence microscopy, showed red fluorescence at different time points of incubation (2h, 6h, and 24h) (Figures 63a to 63l and 64a to 64l, respectively). The fluorescence of the loaded NCs (1 μ M) (Figures 63a to 63c; 64a to 64c) was comparably similar to the fluorescence exhibited in the cells incubated with free DNR (1 μ M) (Figures 63d to 63f; 64d to 64f) at the same time points. Similarly, when cells were incubated with higher concentration (10 μ M) of loaded NCs and DNR, results showed red fluorescence but with higher intensity (Figures 63g to 63l; 64g to 64l). Fluorescence of the loaded NCs with higher DNR concentration (10 μ M) in both cell lines (Figures 63a to 63c; 64a to 64c) was also comparably similar to the fluorescence exhibited in the cells incubated with free DNR (10 μ M) (Figures 63d to 63f; 64d to 64f) at the same time points.

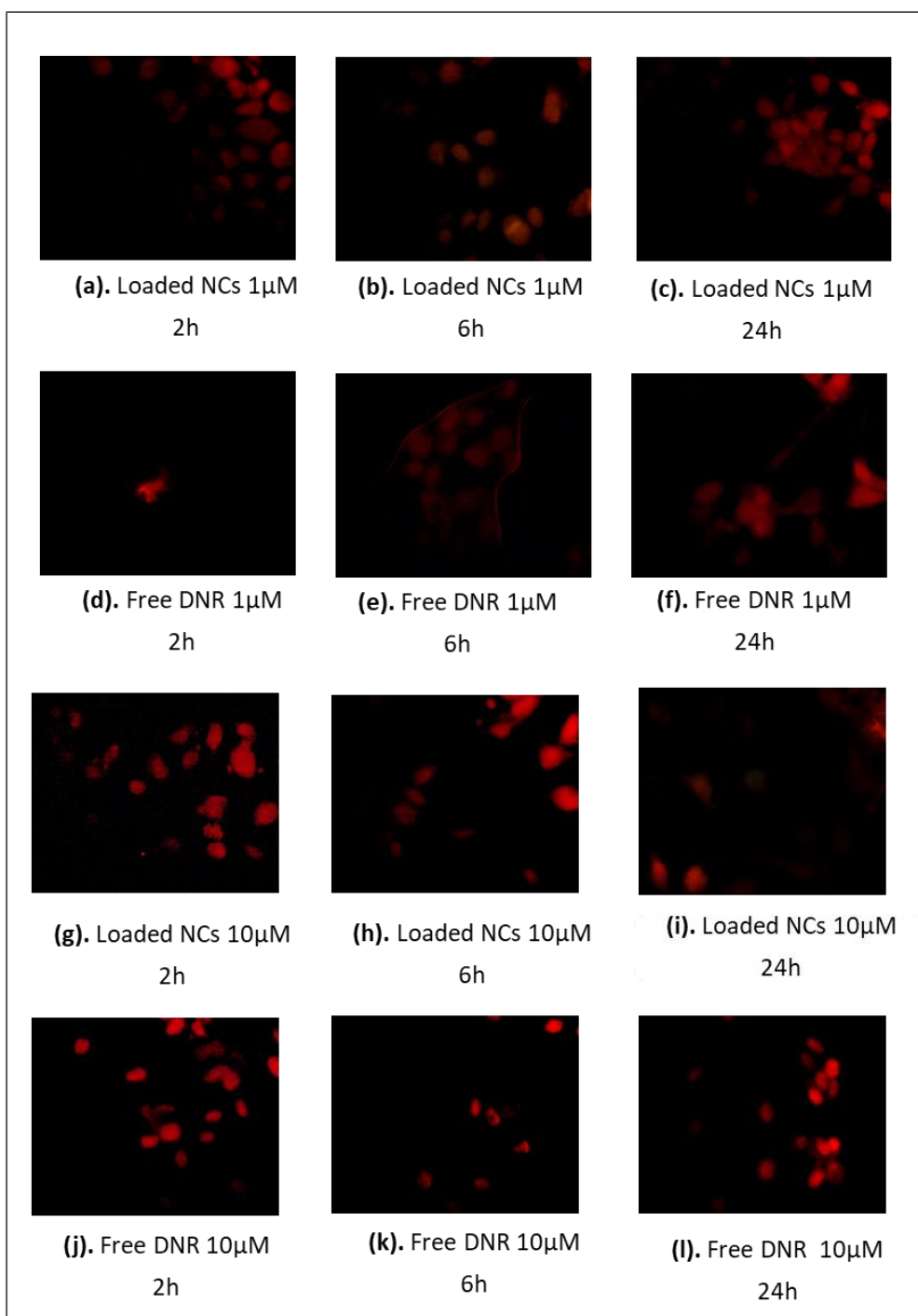


Figure 63. Fluorescence microscope images of the cellular uptake of DNR loaded NCs and free DNR in U87 MG cell line. **a-c).** Cells treated with DNR loaded NCs (1μM) for 2h, 6h, and 24h; **d-f).** Cells treated with free DNR (1μM) for 2h, 6h, and 24h; **g-i).** Cells treated with DNR loaded NCs (10μM) for 2h, 6h, and 24h; **j-l).** Cells treated with free DNR (10μM) for 2h, 6h, and 24h.

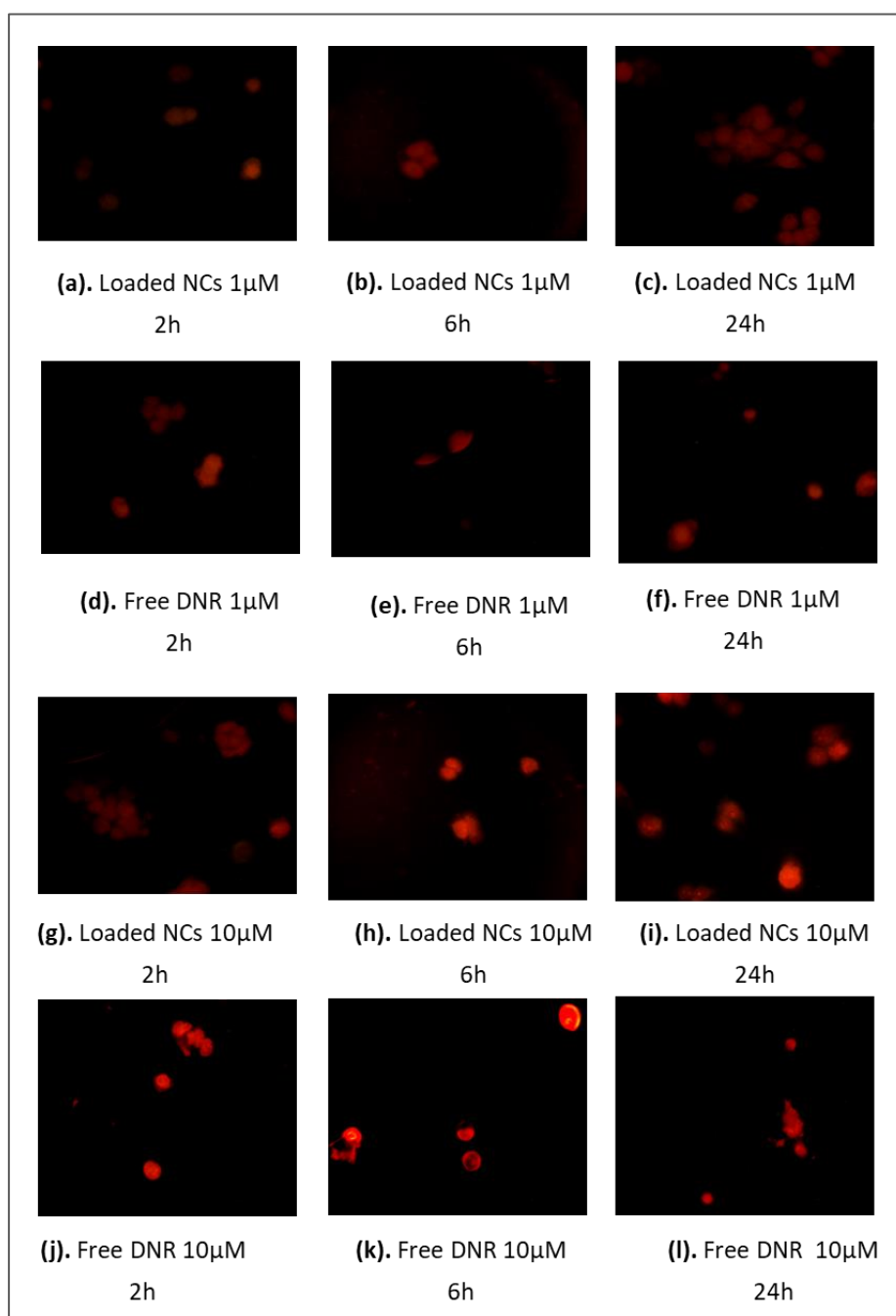


Figure 64. Fluorescence microscope images of the cellular uptake of DNR loaded NCs and free DNR in HaCat cell line. **a-c).** Cells treated with DNR loaded NCs (1 μ M) for 2h, 6h, and 24h; **d-f).** Cells treated with free DNR (1 μ M) for 2h, 6h, and 24h; **g-i).** Cells treated with DNR loaded NCs (10 μ M) for 2h, 6h, and 24h; **j-l).** Cells treated with free DNR (10 μ M) for 2h, 6h, and 24h.

4.3.4. Western blot

Assessment of DNA damage protein expression by western blot in brain cancer cell line treated with different loaded and free chemotherapy drugs (temozolomide, cisplatin, DNR, DNR/temozolomide combination) for 72h showed good quality of bands (Figure 65a and b) and variation in levels of proportional H2A.X/GAPDH intensities (Figure 65c). Results of the visualised membrane by Fluorchem 8800 imager (Figure 65b) showed protein bands at 15kDa in the U87 MG samples treated with free NCs, loaded temozolomide, free temozolomide, loaded cisplatin, and untreated cells. In samples treated with free cisplatin, loaded DNR, free DNR, loaded DNR/temozolomide, and free DNR/temozolomide, negative bands were recorded in their corresponding lanes at 15kDa. Figure 65a showed equal -housekeeping gene- GAPDH bands for all samples at 37kDa. Results of the calculated proportional intensity of phosphorylated H2A.X and GAPDH (Figure 65c) corresponded to the band intensity results in Figures 65a and b. The highest H2A.X intensity levels were recorded in the positive control with a 1.97 ratio followed by ~ 1.3 less intensity in the free NCs and loaded temozolomide treated samples. Untreated samples, samples treated with free temozolomide, and loaded cisplatin showed intensity ratios between 0.07 and 0.2. Accordingly, with the membranes' images, no H2A.X/GAPDH ration were recorded in samples treated with free cisplatin, loaded DNR, free DNR, loaded temozolomide/DNR combination, and free temozolomide/DNR combination.

Western blot results of HEK293 were reported in chapter 3, Figure 34. Briefly, results showed variation in phosphorylated H2A.X band intensities for the different samples (Figures 34a and b). Samples treated with free NCs, loaded temozolomide, free temozolomide, and loaded cisplatin showed the highest bands intensity compared to the fainter bands in samples treated with free cisplatin, loaded DNR, free DNR, loaded DNR/temozolomide, and free

DNR/temozolomide (Figure 34b). The GAPDH bands at 37kDa appeared equally intense for all analysed samples (Figure 34a). Results of the calculated proportional intensity of H2A.X and GAPDH (Figure 34c) corresponded to the band intensity results in Figures 33a and 33b. The highest H2A.X/GAPDH ratio was recorded in the untreated NCs, loaded temozolomide, free temozolomide and loaded cisplatin samples with 0.9 to ~1.5. Samples treated with free cisplatin, free DNR, loaded and free DNR/temozolomide combination showed a lower H2A.X/GAPDH ratio of 0.1 to 0.4.

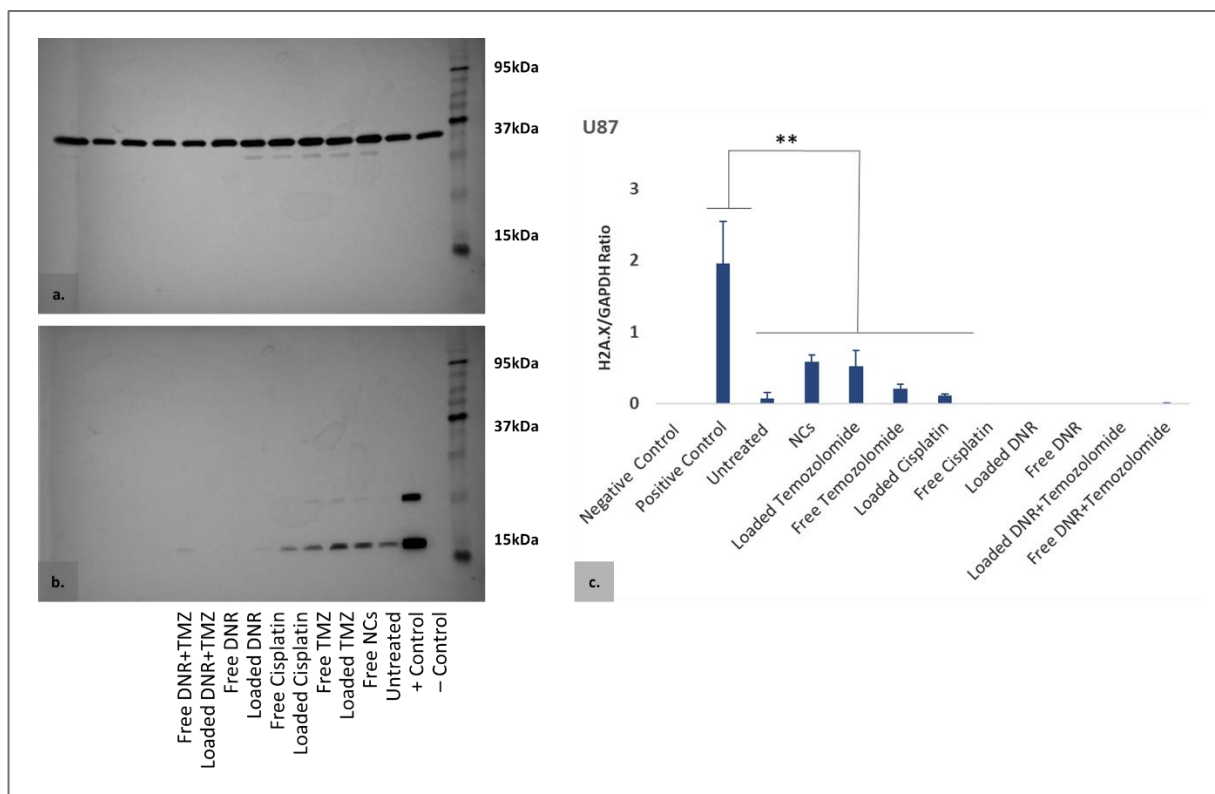


Figure 65. Western blot analysis results of DNA damage protein expression in U87 MG brain cancer cell line. a) and b). GAPDH and γ -H2A.X protein expression in U87 MG cell line; Samples of U87 MG cell line were treated with free nanocontainers, free and loaded temozolomide, cisplatin, DNR, and DNR/temozolomide combination. HaCat and HEK293 cell lines were used as negative and positive control, respectively; c). Protein bands quantification results expressed as ratio of H2A.X/GAPDH. Error bars represent \pm SD of three experiments. *** $P \leq 0.001$; P-values were calculated with two tailed paired student t test.

4.3.5. Flow cytometry

Apoptosis analysis by flow cytometry for 24h in the U87 MG cell line showed different apoptosis levels for the different treatments applied (Figure 66). The four different quadrants Q4, Q3, Q2, and Q1 in the dot plots corresponded to the viable cells, early apoptotic cells, late apoptotic cells, and necrotic cells, respectively. Lower percentages of viable cells and higher percentages of early apoptotic, late apoptotic, and necrotic cells were observed in samples treated with loaded and free temozolomide, cisplatin, DNR, and DNR/temozolomide combination compared to the untreated and NCs treated samples.

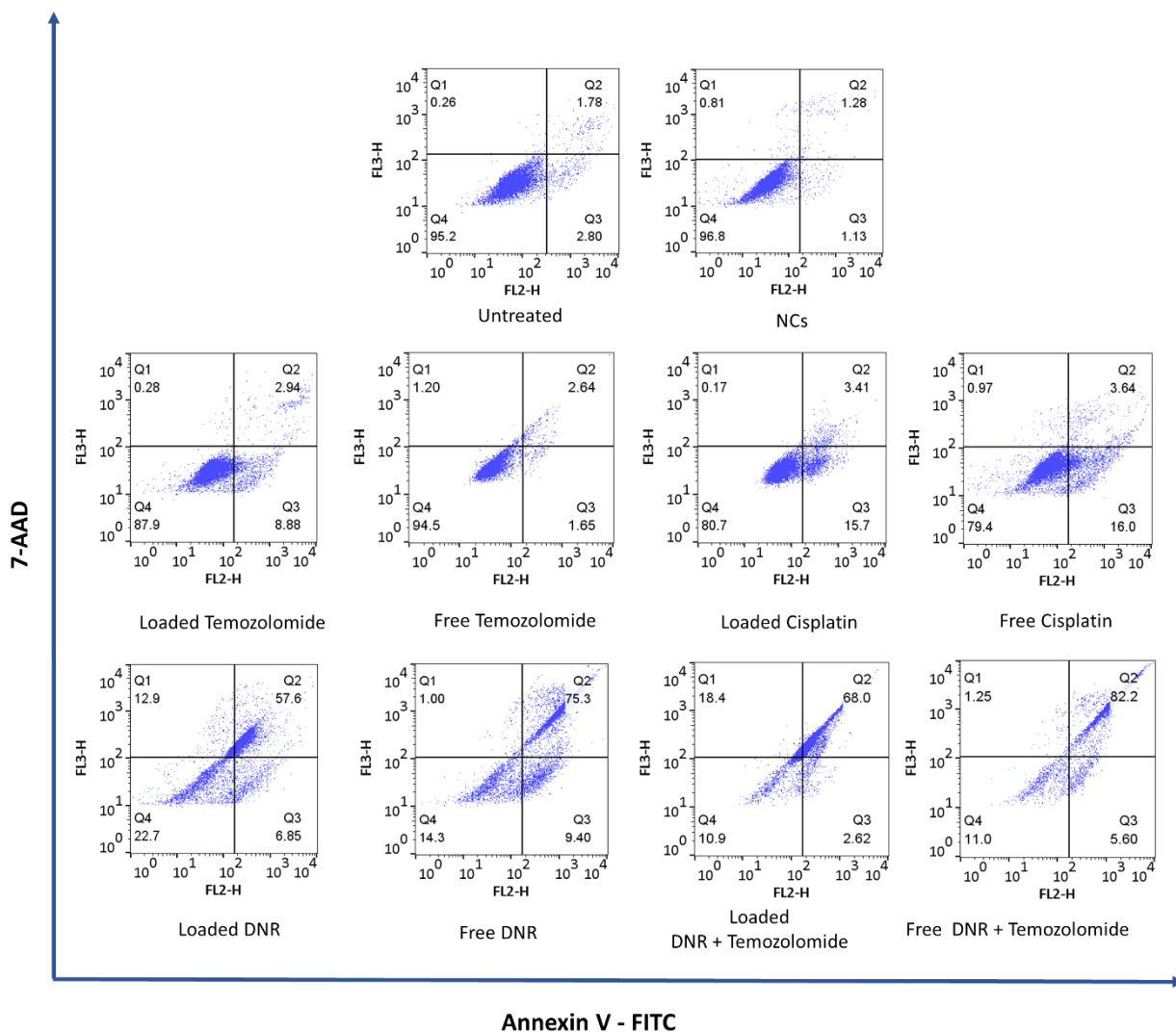


Figure 66. Apoptosis analysis by flow cytometry in U87 MG cells treated by free NCs, loaded and free temozolomide, cisplatin, DNR, and DNR/temozolomide combination for 24h. Based on Annexin V/7AAD staining, Q4 (Annexin V⁻/7AAD⁻) represents viable cells, Q3 (Annexin V⁺/7AAD⁻) represents early apoptotic cells, Q2 (Annexin V⁺/7AAD⁺) represents late apoptotic cells, Q1 (Annexin V⁻/7AAD⁺) represent necrotic/dead cells.

Calculated percentages of total apoptotic, necrotic, and viable cells for the different treatments applied in U87 MG for 24h were shown in Figure 67. Higher total apoptotic cell percentages of 20% to 79% were recorded in samples treated with loaded and free cisplatin, DNR, and DNR/temozolomide combination compared to the untreated and NCs treated samples. Samples treated with loaded and free temozolomide showed relatively close percentages in viable cells and total apoptosis as the untreated sample. The highest necrotic percentages of ~12% were recorded in samples treated with loaded DNR and loaded DNR/temozolomide. Viable cell percentages were all above 78%, excluding loaded and free DNR and DNR/temozolomide samples which showed a 58% to 70% lower cell viability than the untreated sample.

Calculated percentages of total apoptotic, necrotic, and viable cells for the different treatments applied in HEK293 for 24h were shown in chapter 3, Figure 40. All treatments applied for 24h showed 20% to 70% higher apoptotic levels than the 10% apoptosis in the untreated samples. The highest apoptosis percentage of ~85% was recorded in the samples treated with free DNR/temozolomide combination. The necrotic percentages remained under 7% in all samples. Viable cell percentages showed an inversely proportional trend with the total apoptosis percentages in all samples.

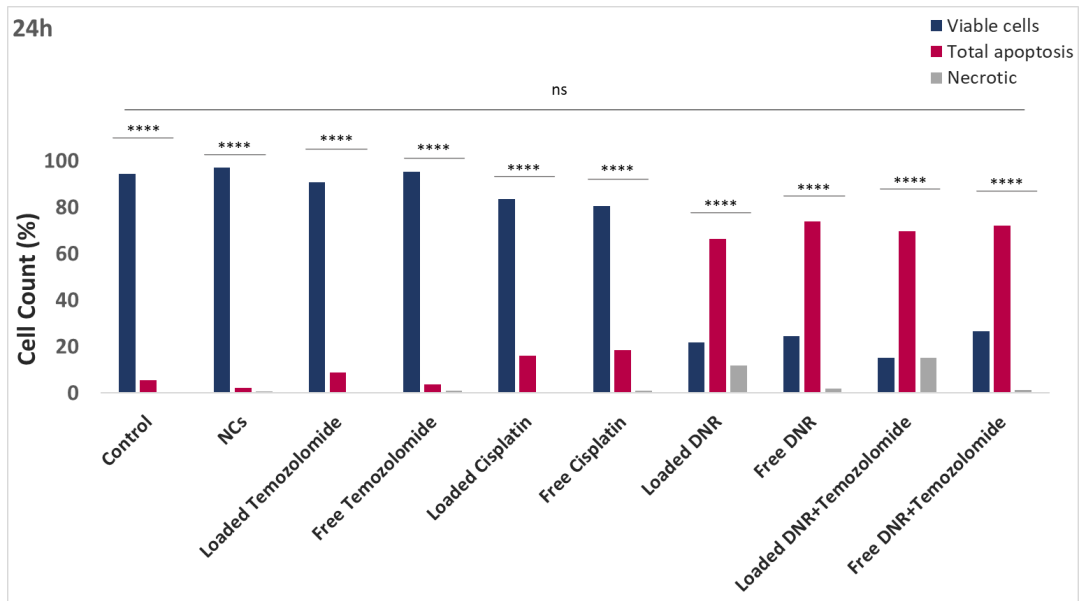


Figure 67. Calculated percentages of cell apoptosis in U87 MG cells treated by free NCs, loaded and free temozolomide, cisplatin, DNR, and DNR/temozolomide combination for 24h. Total apoptosis percentage represents the late and early apoptosis percentages together. **** $P \leq 0.0001$, ns $P > 0.05$ and it was a comparison between all treatments; p-values were calculated for duplicates with two-way ANOVA.

Apoptosis analysis of U87 MG cell line after 72h treatment (Figure 68) showed higher apoptosis levels for the different treatments applied compared to the 24h. Higher percentages of early apoptotic, late apoptotic, and necrotic cells were observed in corresponding quadrants in the samples treated with loaded and free temozolomide, cisplatin, DNR, and DNR/temozolomide combination compared to the untreated and NCs treated samples.

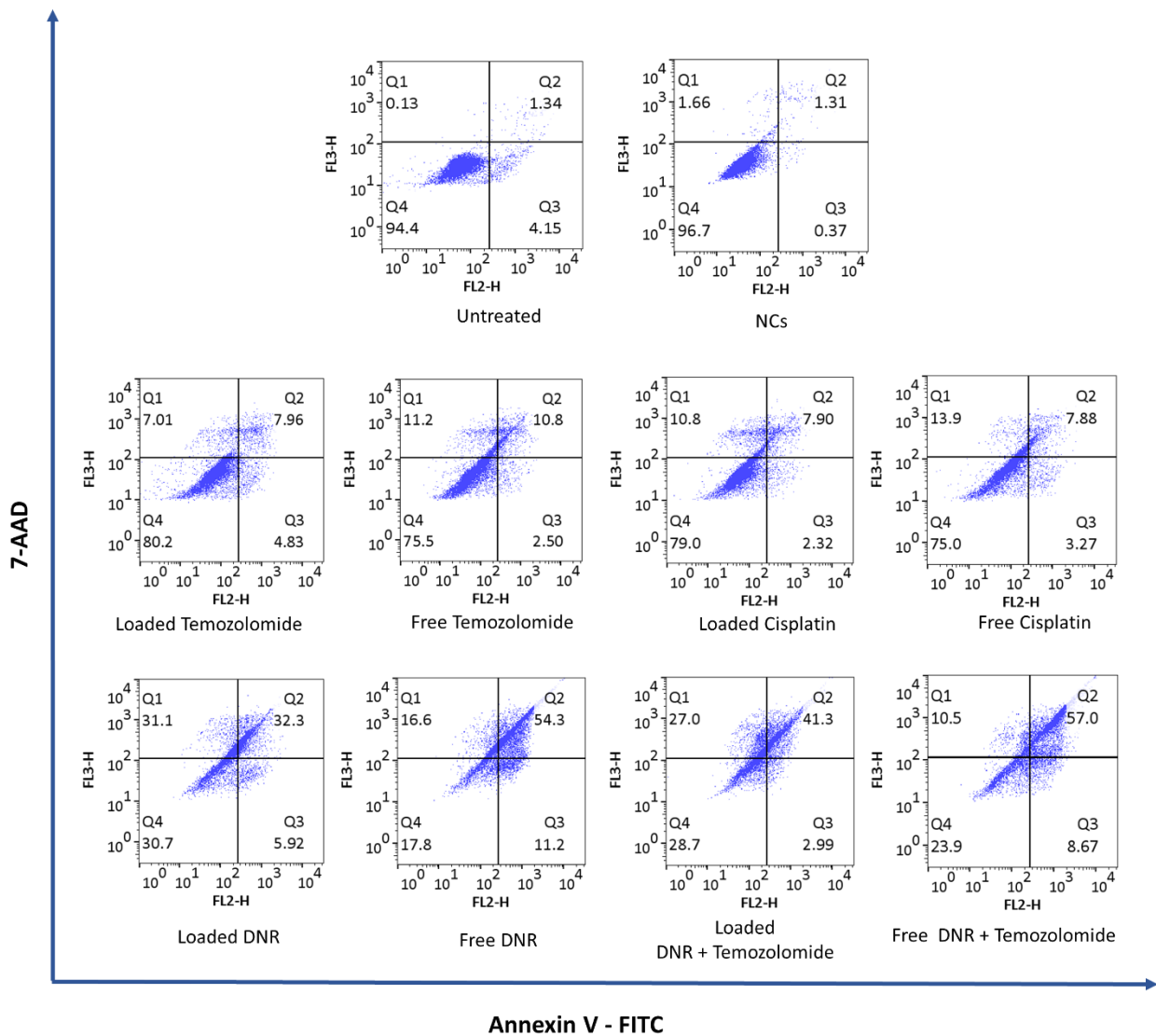


Figure 68. Apoptosis analysis by flow cytometry in U737 MG cells treated by free NCs, loaded and free temozolomide, cisplatin, DNR, and DNR/temozolomide combination for 72h. Based on Annexin V/7AAD staining, Q4 (Annexin V⁻/7AAD⁻) represents viable cells, Q3 (Annexin V⁺/7AAD⁻) represents early apoptotic cells, Q2 (Annexin V⁺/7AAD⁺) represents late apoptotic cells, Q1 (Annexin V⁻/7AAD⁺) represent necrotic/dead cells.

Calculated percentages of total apoptotic, necrotic, and viable cells for the different treatments applied to U87 MG cells are shown in Figure 69. Higher total apoptotic percentages of 38% to 50% were recorded in samples treated with loaded DNR, free DNR, loaded DNR/temozolomide, and free DNR/temozolomide. These percentages were ~10% to 30% lower than the total apoptosis percentages after 24h with the same treatments. Yet, these samples recorded a 20% increase in necrotic cell percentages compared to the 24h treatment. Samples treated with loaded and free temozolomide and cisplatin showed relatively similar total apoptotic cell percentages compared to the 24h treatment, with > 15% necrotic cells. Untreated cells and NCs treated cells showed relatively similar total apoptotic percentages of 10% to 14% and > 70% viable cells for both 24h and 72h. Necrotic cells retained the same low percentages in these samples with $\leq 5\%$.

Calculated percentages of total apoptotic, necrotic, and viable cells for the different treatments applied on the HEK293 cell line for 72h were shown in Figure 42. All treatments applied for 72h showed an average of ~30% higher apoptotic levels than apoptosis in the untreated samples. Also, the total apoptotic percentages were ~20% lower than the 24h across treatments applied. Yet, necrotic percentages were, on average, ~15% higher than the levels recorded in the 24h treatment. The highest apoptotic percentage of ~30% and ~60% were recorded in the free DNR and free DNR/temozolomide, respectively. In all samples analysed after 72h treatment, viable cells retained > 50% levels, excluding the sample treated with free DNR that showed 20% viable cells.

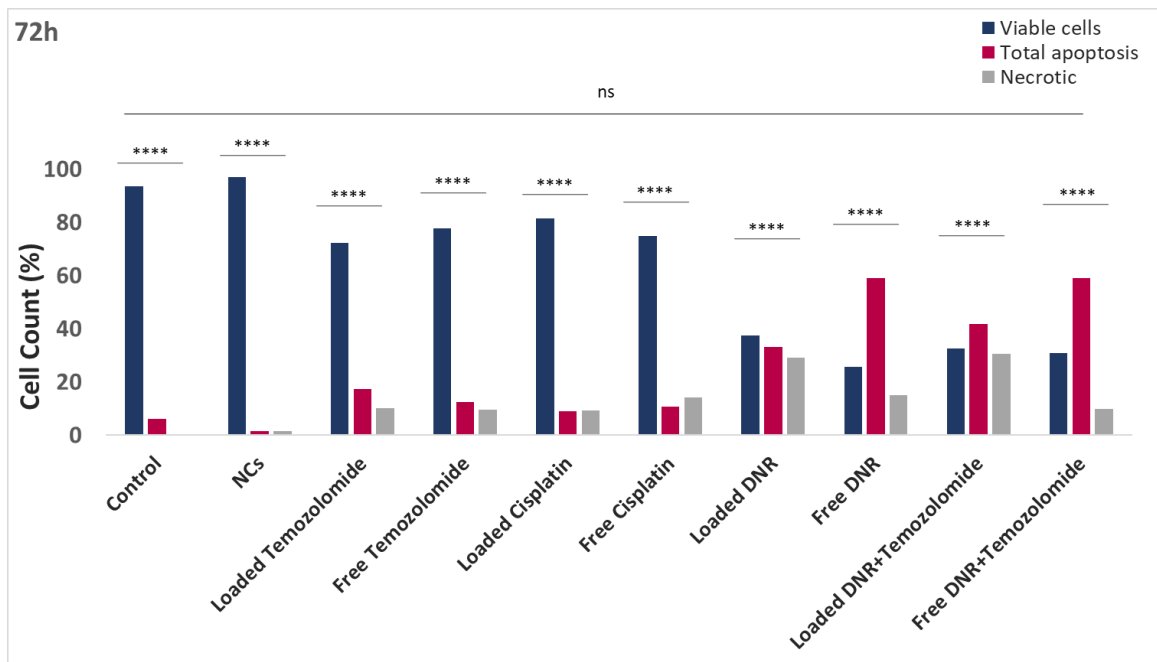


Figure 69. Calculated percentages of cell apoptosis in U87 MG cells treated by free NCs, loaded and free temozolomide, cisplatin, DNR, and DNR/temozolomide combination for 72h. Total apoptosis percentage represents the late and early apoptosis percentages together. **** $P \leq 0.0001$, ns $P > 0.05$ and it was a comparison between all treatments; P-values were calculated for duplicates with two-way ANOVA.

4.3.6. Cell cycle

Results of the cell cycle analysis by flow cytometry of U87 MG cells after 24h treatment with NCs, loaded and free temozolomide, cisplatin, DNR, and DNR/temozolomide combination showed variations in the levels of cell cycle phases G1, S and G2 (Figure 70).

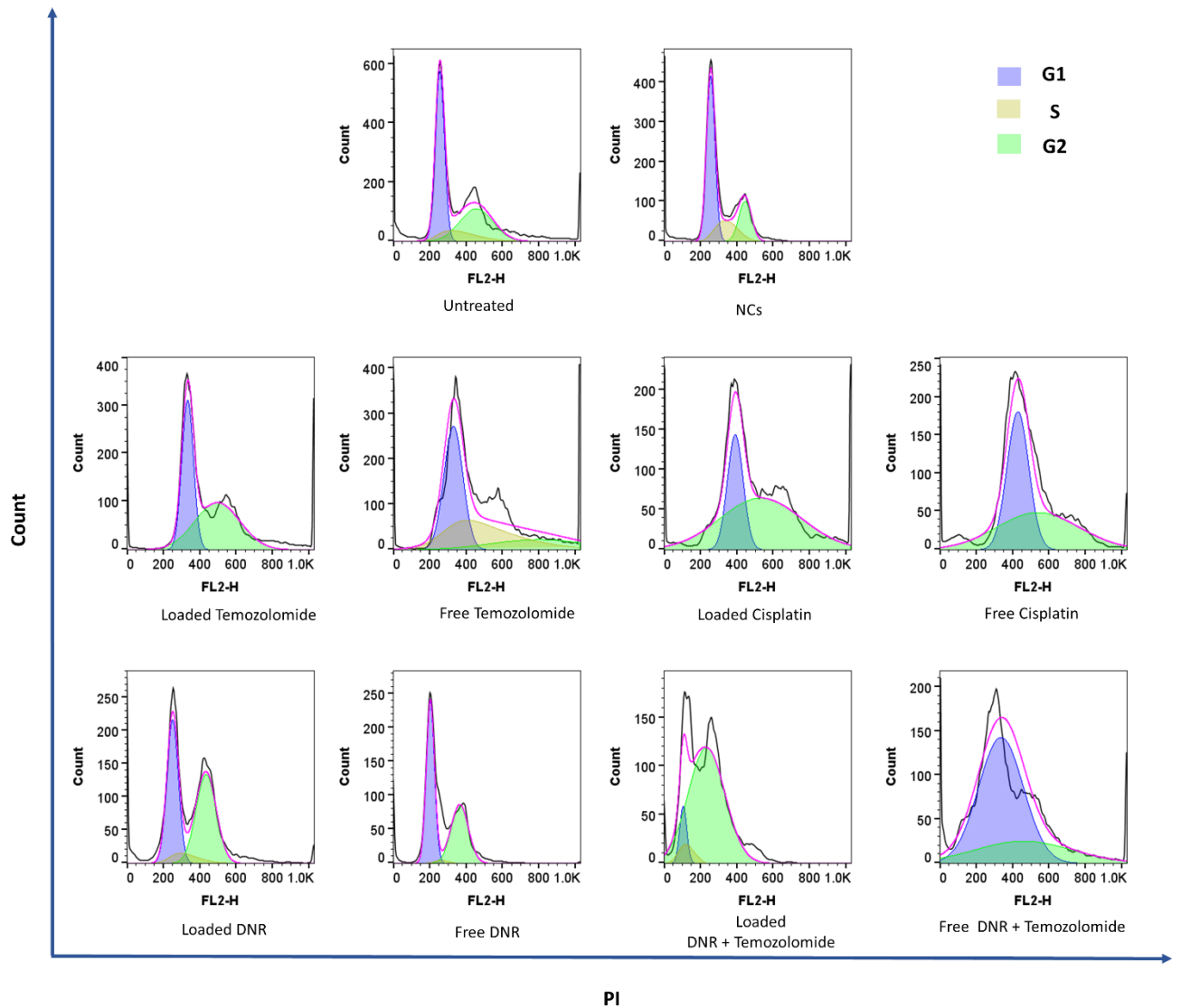


Figure 70. Cell cycle analysis of U87 MG cells treated by free NCs, loaded and free temozolomide, cisplatin, DNR, and DNR/temozolomide combination for 24h. Propidium iodide (PI) stain distinguishes between the G1, S, and G2 phases based on DNA content.

Percentages of the G1, S and G2 phases of the cell cycle were variant across the applied treatments on U87 MG for 24h (Figure 71). Untreated cells and NCs treated cells showed ~40% cells in G1 with ~20% lower percentages of cells in G2. Samples treated with loaded temozolomide, cisplatin, DNR, and DNR/temozolomide showed higher percentages of cells in G2 with 50% to 80%. However, free temozolomide, cisplatin, DNR, and DNR/temozolomide showed higher percentages of cells in G1, with 48% to 82%. Percentages of cells in the S phase were between ~10% to 2% across applied treatments in loaded and free forms.

Percentages of the G1, S and G2 phases of the cell cycle were variant across the applied treatments after 24h in HEK293 cells (Figure 48). Across the different treatments applied, the S phase percentages were between 1% and 6%. Samples treated with free temozolomide, loaded DNR/temozolomide and free DNR/temozolomide showed higher G levels of > 80% than the G2 phase. The rest of the treatments applied showed relatively close percentages between the G1 and the G2 phases.

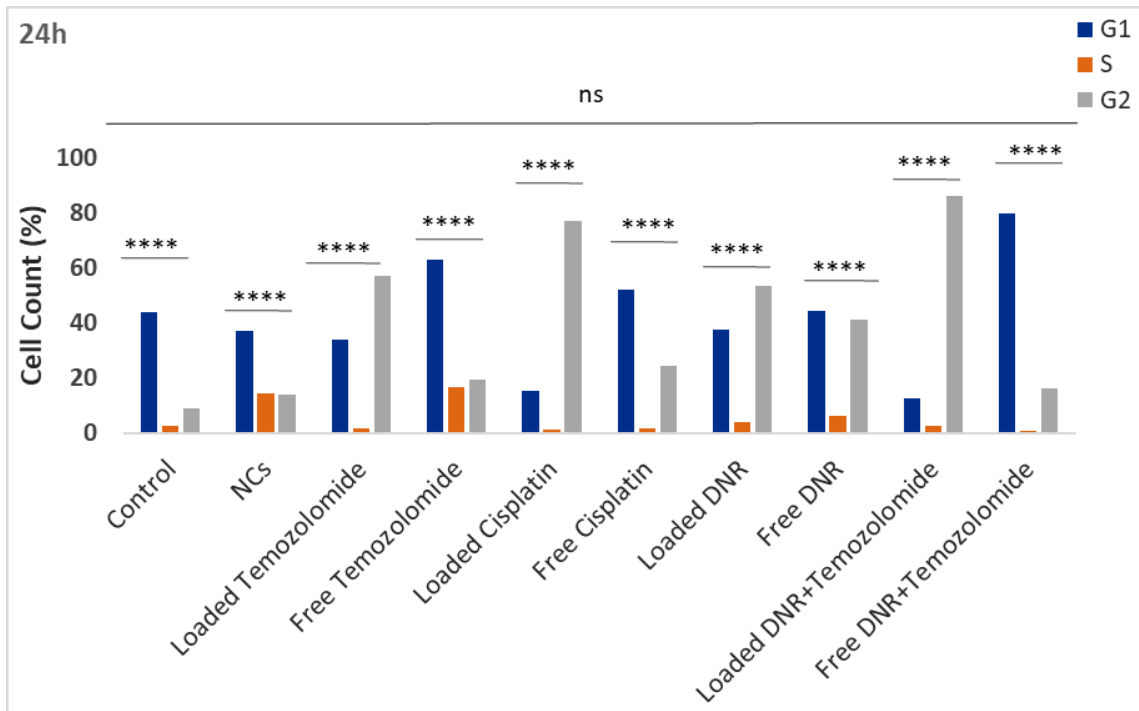


Figure 71. Percentages of the different phases of the cell cycle (G1, S, G2) of U87 MG cells treated by free NCs, loaded and free temozolomide, cisplatin, DNR, and DNR/temozolomide combination for 24h. **** $P \leq 0.001$, ns $P > 0.05$ and it was a comparison between all treatments; P-values were calculated for duplicates with two-way ANOVA.

Results of the cell cycle analysis by flow cytometry of U87 MG after 72h treatment with NCs, loaded and free temozolomide, cisplatin, DNR, and DNR/temozolomide combination showed variations in the levels of cell cycle phases G1, S and G2 (Figure 72).

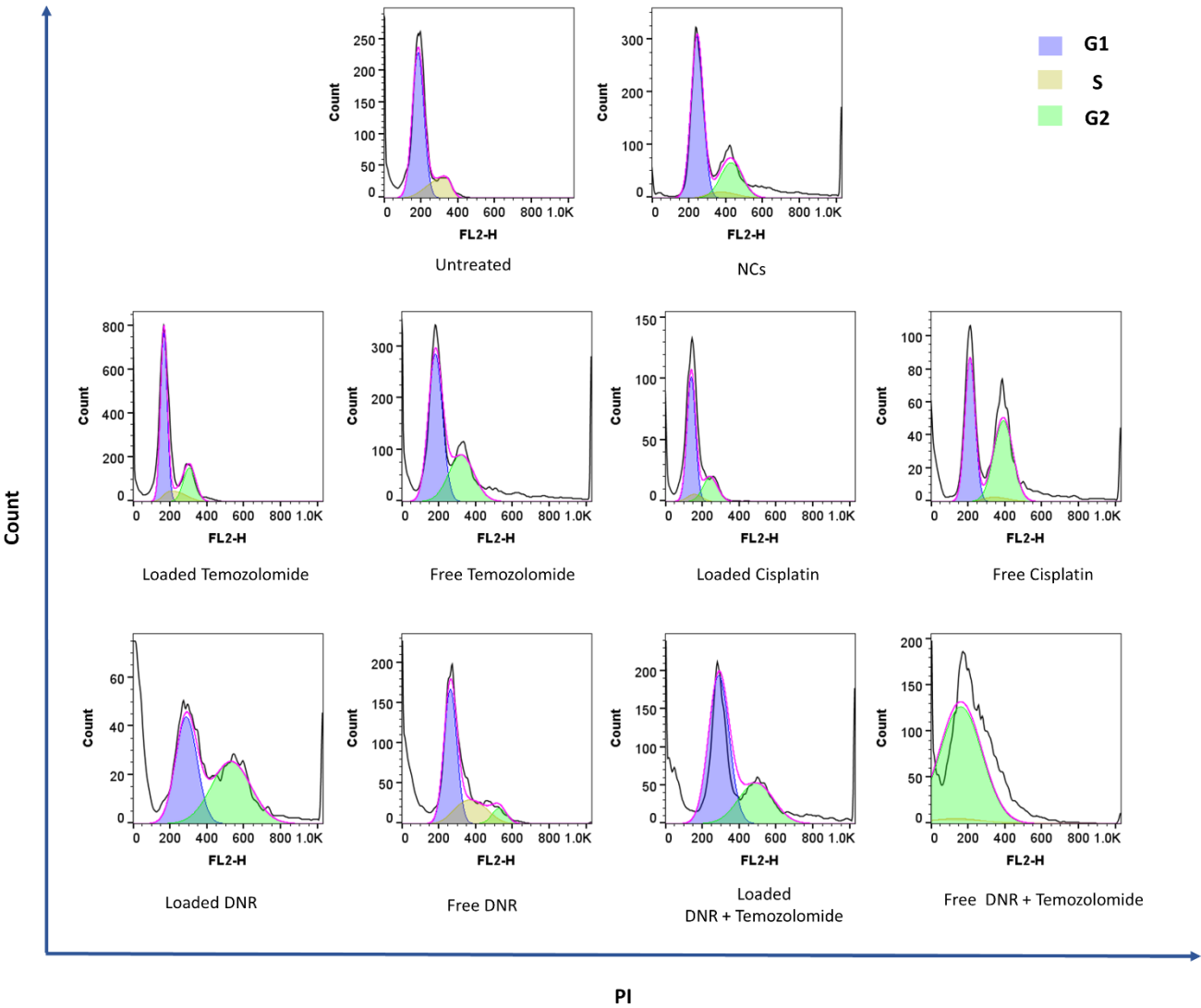


Figure 72. Cell cycle analysis of U87 MG cells treated by free NCs, loaded and free temozolomide, cisplatin, DNR, and DNR/temozolomide combination for 72h. Propidium iodide (PI) stain distinguishes between the G1, S, and G2 phases based on DNA content.

Percentages of G1, S and G2 phases of the cell cycle after 72h applied treatments on U87 MG were shown in Figure 73. Untreated and NCs treated cells showed higher G1 phase percentages with a 20% increase compared to the 24h, yet in both times, points showed higher percentages in G1. Free cisplatin treated samples showed relatively close percentages of G1 and G2 (38% and 40%, respectively), unlike the 24h treatment that showed higher G1 percentages. An opposite pattern was revealed in the free DNR treated sample, where a higher G1 percentage of 38% was recorded after 72h treatment, whereas the close G1 and G2 percentages were recorded after 24h treatment. The samples treated with free DNR/temozolomide combination showed a shift from higher G1 percentage after 24h treatment to higher G2 percentages of 40% after 72h treatment. The rest of the samples treated with the loaded and free temozolomide, loaded cisplatin, loaded DNR, and loaded DNR/temozolomide combination showed all higher G1 percentages of ~38% to ~50% after 72h compared to 24h.

In the HEK293 cell line, percentages of the G1, S and G2 phases of the cell cycle were variant across the applied treatments after 72h (Figure 50). Across the different treatments applied the S phase percentages were only up to 5%. Higher G1 phase percentages of > 50% were recorded in samples treated with loaded and free DNR and DNR/temozolomide. On the contrary, higher G2 phase levels of > 50% were recorded in the control sample and samples treated with NCs, loaded and free temozolomide and cisplatin.

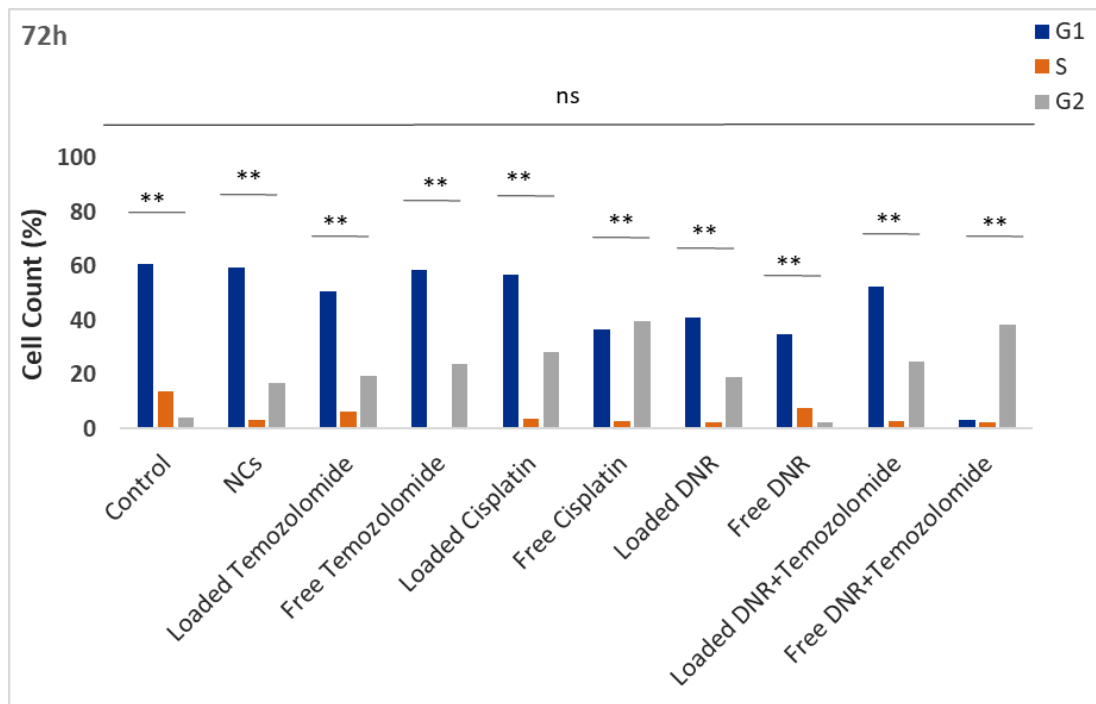


Figure 73. Percentages of the different phases of the cell cycle (G1, S, G2) of U87 MG cells treated by free NCs, loaded and free temozolomide, cisplatin, DNR, and DNR/temozolomide combination for 72h. ** $P \leq 0.01$, ns $P > 0.05$ and it was a comparison between all treatments; P-values were calculated for duplicates with two-way ANOVA.

4.4. Discussion

The *in vitro* cytotoxicity assessment showed high cell viability percentages in U87 MG and HEK293 cells treated with free NCs for 24h and 72h. This was attributed to the non-toxic trait of the polymeric formulation of the NCs, which preserved the ability of the cells to reduce the MTT dye to insoluble formazan crystals. This signified an unaffected cellular and metabolic activity of the cells in the presence of free NCs. This data further added to several similar conclusions regarding the negligible toxicity levels in cells treated with free polymeric NCs (d'Amora et al., 2020; Meteoglu & Erdemir, 2021; Maurya et al., 2019; Toniolo et al., 2018).

However, the cytotoxicity induced by the drug loaded NCs for both 24h and 72h in both U87 MG and HEK293 was attributed to the affected metabolic activity and cellular activity of the cells in the presence of the drugs; hence, their inability to reduce the MTT dye to insoluble formazan crystals. The cytotoxicity of the loaded cisplatin, DNR, and temozolomide, separately, in addition to the temozolomide/DNR combination released from the NCs was similar in pattern with the free form but not entirely identical in levels of cytotoxicity. This was attributed to the sustained release characteristic of the nanoparticles which was discussed in chapter 2. In other words, the free form of the cisplatin, DNR, temozolomide, and DNR/temozolomide combination induced slightly higher cytotoxicity compared to their loaded forms. This signified that the NCs acted as reliable drug carriers and released the drug sustainably throughout the treatment periods. This trend was reported by several other studies, including (Fortuni et al., 2019; Palanikumar et al., 2020). Also, in alignment with our results in glioblastoma, Meteoglu and colleagues (2021) reported similar low cytotoxicity levels in glioblastoma cells treated with plain polymeric nanocontainers for 24h and 48h. They also reported higher toxicity levels in cells treated with loaded and free temozolomide and

genistein separately and jointly, with higher toxicity levels recorded in co-loaded temozolomide and genistein (Meteoglu & Erdemir, 2021). Our data showed relatively similar lowest cytotoxicity levels in both U87 MG and HEK293 cells upon treatment with a loaded and free combination of DNR/temozolomide. This outcome could be attributed to the dual effect of the drugs in intercalating the DNA and interfering with its transcription as well as cell division. Similar attempts of polymeric NCs co-encapsulation and co-delivery of two or more chemotherapeutic agents, including paclitaxel/methotrexate, methotrexate/curcumin, paclitaxel/etoposide, and paclitaxel/temozolomide have been reported in glioblastoma (Madani et al., 2020; Maleki et al., 2021; Mujokoro, Madani, Esnaashari, Khosravani, & Adabi, 2019; Xu et al., 2016).

Overall, the *in vitro* cytotoxicity studies showed non-cytotoxic developed polymeric NCs when delivered plain in U87 MG and HEK293 cells. Our drug loaded polymeric nanocontainers induced significant cytotoxicity levels in both 24h and 72h of treatments in a comparatively similar patterns to the free version of the drugs. This indicated the effectiveness of our nanocontainers as drug carriers and drug delivery systems with a sustained pattern of drug release.

Faster wound closure and unaffected cell migration were recorded in U87 MG and HaCat cells treated with free NCs. On the contrary, treatment of the same cells with loaded and free DNR showed a relatively slower wound closure rate resulting from an affected migration. This data indirectly signified the non-cytotoxic and cytotoxic effects of free NCs, and loaded and free DNR, respectively. This data also supported the previously discussed MTT results. Partially similar data were reported in glioblastoma cells treated with polymeric loaded and free genistein /temozolomide NCs. Both loaded and free genistein /temozolomide showed slower

and incomplete wound closure after 48h. Yet, our data showed a slight difference in wound closure rate between free DNR and its loaded form, when the data of Meteoglu and colleagues (2021) reported a higher effect of the loaded genistein/temozolomide on the wound closure and cell migration than the free genistein/temozolomide (Meteoglu & Erdemir, 2021).

Monitored by fluorescence microscopy, DNR loaded NCs and free DNR showed good and gradual cellular uptake throughout the time points in U87 MG and HEK293 cell lines. The cellular uptake of the loaded DNR was comparatively similar to the cellular uptake of the free DNR in both 1 μ M and 10 μ M. The lower uptake of the loaded DNR reflected by the lower fluorescence intensities in both concentrations could be attributed to the sustained release trait of the NCs that was previously discussed. Similar results were reported by the use FITC-conjugated paclitaxel loaded polymeric nanoparticles delivered in glioblastoma cells. Results showed gradual and good cellular uptake with an increase green FITC fluorescence after 4h (Wang et al., 2021). Our results were also in accordance with similar DNR loaded polymeric nanoparticles, which showed good cellular uptake patterns similar to free DNR in MCF-7 breast cancer cells (Toniolo et al., 2018). Another similar outcome was reported by Duwa et al., (2020), in which fluorescence microscope images showed good cellular uptake of cetuximab loaded polymeric PLGA nanoparticles in glioblastoma, colorectal cancer and melanoma cell lines.

In our data, the localisation of the loaded NCs in the cells could not be precisely defined in this experiment. Other similar studies regarding the cellular uptake of polymeric nanocontainers used additional techniques to determine the precise localization of the NCs, including confocal microscopy and confocal laser scanning microscopy. These techniques allowed clearer and more detailed captured images, hence the ability to determine the precise uptake pattern of

the polymeric NCs loaded with a fluorescent agent (e.g. rhodamine-B, doxorubicin) by the cells to inner compartments (e.g. nucleus, mitochondria) (Boltnarova et al., 2021; Palanikumar et al., 2020). An aforementioned instance of cetuximab loaded polymeric PLGA nanoparticles delivered in glioblastoma, colorectal cancer and melanoma cell lines also loaded with fluorescent dye-free coumarin-6 (cou-6). Confocal laser scanning microscopy showed good internalization and cellular uptake with detailed pictures distinguishing the accumulation of the nanoparticles in the cytoplasm (Duwa et al., 2020).

Assessment of cellular uptake and internalization of hybrid polymeric nanocontainers loaded with methotrexate in glioblastoma cells showed extensive internalisation after 4h. Results reported accumulation of the methotrexate loaded hybrid polymeric nanoparticles in the cytoplasm based on images taken by confocal laser scanning microscopy (Bhattacharya, 2021). Another approach was reported by the same study for the determination of brain uptake potential of methotrexate *in vivo* by high-performance liquid chromatography (HPLC). The methotrexate was administrated intravenously, and its levels were measured in blood plasma and homogenised brain tissue. The HPLC results showed 2.23 times higher drug concentration in the brain than in the plasma. This approach could afford the potential assessment of the uptake and drug release profile of methotrexate loaded NCs as well as other NCs loaded chemotherapy drugs (Bhattacharya, 2021).

On the other hand, flow cytometry was used for the quantification of cellular uptake by the measurement of the fluorescence intensity of the fluorophore, rhodamine-B, and doxorubicin labelled/loaded NCs in cancer cells. Data showed higher cellular uptake of the doxorubicin loaded polymeric NCs in breast cancer cells (Palanikumar et al., 2020).

The DNA damage assessment by measurement of phospho-Histone H2A.X (Ser139) expression in western blot showed different levels of expression that were attributed to the treatment of U87 MG and HEK293 with NCs, loaded and free forms of temozolomide, cisplatin, DNR, and DNR/temozolomide combination. The H2A.X protein is defined as one of the DNA damage markers. It is one of the octamers (eight histones) forming the nucleosome, which is a fundamental DNA packing and condensation unit in eukaryotes i.e. chromatin. A phenomenon known as DNA double-strand breaks (DSBs) is induced when simultaneous damage in two complementary strands of the DNA double helix with close location takes place (Podhorecka, Skladanowski, & Bozko, 2010). In response to the DNA breaks onset, the phosphorylation of histone H2A.X at S139 residues (also known as γ H2A.X) serves as an early signal or precursor for DNA repair pathways (Jeffery et al., 2021; Valente et al., 2022). Several physical, chemical, and biological factors including radiation and chemotherapy drugs, can induce DSBs (Valente et al., 2022).

The variation of expression levels of the phosphorylated H2A.X in U87 MG was not expected. Levels of phosphorylated H2A.X were expected to increase in samples treated with different loaded and free drugs similar to the positive control. Yet, the percentages of expression showed higher levels of phosphorylated H2A.X in the loaded temozolomide and NCs treated samples, whereas lower levels were recorded in the samples treated with free temozolomide, loaded cisplatin, free cisplatin, loaded DNR, free DNR, loaded DNR/temozolomide, and free DNR/temozolomide. Also, in HEK293, the levels γ H2A.X decreased in samples treated with the different loaded and free temozolomide, cisplatin, DNR, and DNR/temozolomide compared to the higher levels recorded in the untreated sample and NCs treated sample. These results were previously discussed in chapter 3. Regarding the U87 MG results, there were two postulations that could explain its γ H2A.X pattern of expression. The first postulation could be

that among all treatments applied, loaded temozolomide was the only treatment that induced DNA damage hence effectiveness of the treatment. Also, free NCs had induced DNA damage levels similar to the loaded temozolomide sample. Previously reported outcomes were partially similar to our results, where free PLGA polymeric nanoparticles induced low γ H2A.X levels in glioblastoma cells, contrary to our data (Duwa et al., 2020). However, loaded temozolomide in PLGA polymeric nanoparticles showed higher γ H2A.X levels and induced more DNA damage than the free temozolomide, which lined with our results (Duwa et al., 2020).

Another previous postulation regarding the levels of H2A.X, the increased levels of γ H2A.X either signified treatment effectiveness or resistance. For instance, Kawashima et al. (2020) showed that colorectal cancer cells from biopsy samples of patients who underwent preoperative chemoradiotherapy and had lower γ H2A.X levels were more sensitive to radiotherapy and vice versa. They concluded that γ H2A.X levels could serve as a predictive indicator of radiosensitivity (Kawashima et al., 2020). The second explanation -following the previous postulation- could be that the increase in levels of γ H2A.X in NCs and loaded temozolomide treated sample were attributed to the basic DNA damage and DNA-repair signal in cancer cells present as a result of the high rate of proliferation. But the decreased levels of γ H2A.X could be attributed to the degradation of γ H2A.X content in the chromatin induced by free temozolomide, loaded and free cisplatin, DNR, and DNR/temozolomide combination.

Temozolomide, cisplatin and DNR, among other first line chemotherapy drugs were reported to increase the reactive oxygen species (ROS) levels in cancer cells above the baseline levels (Yang et al., 2018). The oxidative stress generates ROS which is reported to be in elevated

levels in cancer cells compared to the redox homeostasis in healthy cells. The presence of ROS in high levels was reported to be a mediator factor for tumour development, whereas other claims reported a strong correlation between reduced levels of ROS and increased tumourigenesis (Huang et al., 2021; Wang et al., 2021). This opened a window for a more likely postulation that ROS levels have both pro-tumourigenic and anti-tumourigenic roles (Yang et al., 2018).

Similar outcomes to our results based on the aforementioned postulation were reported in triple negative breast cancer cells that showed significant γ H2A.X degradation after several cycles of chemotherapy (Gruosso et al., 2016). It was also suggested that chemosensitivity in patients was improved due to this decrease in γ H2A.X levels induced by oxidative stress (Gruosso et al., 2016). This claim supported the correlation in our data between the decrease in H2A.X levels and the effectiveness of the chemotherapy drugs delivered in NCs-loaded form or freely.

After the DNA repair onset, γ H2AX starts dephosphorylation as a result of DNA repair hence the absence of DNA damage foci. Phosphorylated H2A.X foci are detectable within 3 min after DNA damage induction, and their detectable levels keep on increasing until they reach a plateau within 10 to 30 min. Then, the disappearance of these detectable foci is noted after 24h after which γ H2AX levels return back to standard levels (Valente et al., 2022).

The third postulation about the decreased levels of γ H2AX could be attributed to this, which signified that the DNA was repaired after the 72h treatment period. This suggested that further western blot runs could be assessed at treatment periods lower than 24h and 72h to obtain a clearer understanding of the DNA damage induction by chemotherapy drugs *in vitro*. For instance, western blot results of HeLa cells exposed to radiation showed decreased levels

of γ H2A.X after 4 to 10h post radiation exposure (An et al., 2010). In another example, western blot findings in a rhabdomyosarcoma cell line without knocked SNAI2-a major regulator of radiation-induced apoptosis- showed a decrease in levels of γ H2A.X starting from 8h post radiation exposure (Wang et al., 2021). Further instance in a radioresistant glioblastoma cell line, assessed levels of H2A.X without anti UBA1 treatment (UBA1 is a key regulator of DNA DSBs repair) showed decreased levels of phosphorylated H2A.X after 12h of radiotherapy (Wu et al., 2023). The latter instance could suggest possible chemoresistance in our glioblastoma cell line which resulted in decreased levels of H2A.X when treated with cisplatin, DNR and DNR/temozolomide in loaded and free form. However, this speculation contradicted with the effectiveness of the free and loaded chemotherapy drugs shown in the MTT results and further in apoptosis and cell cycle results.

Overall, the γ H2AX is considered a globally sensitive marker of DSBs. However, the expression of H2A.X in different cell lines and tissue types is highly heterogeneous. This variability renders the interpretation of γ H2AX levels and their subtle changes considerably difficult (Ji et al., 2017). Therefore, conducting additional analyses of the total γ H2A.X expression levels by RT-qPCR, immunohistochemistry, ELISA, and γ H2AX assay by flow cytometry was suggested for more accurate detection of the subtle differences in H2A.X levels (Ji et al., 2017), which were beyond the scope of our data. Although the H2A.X Ser139 is considered a DSB marker, the H2A.X represents only 2–25% of the cellular H2A pool in mammalian cells. Therefore, other H2A.X variants and other DNA damage markers could be investigated (Dobersch et al., 2021).

Apoptosis analysis by flow cytometry and annexin V/7AAD staining in U87 MG cell line showed increased apoptosis when treated for 24h with loaded and free temozolomide, cisplatin, DNR, and DNR/temozolomide combination; in contrast to the low apoptosis percentages recorded

in the untreated and NCs treated samples. The 72h treatment induced lower total apoptosis, yet higher necrotic cell percentages were recorded. The untreated sample and the sample treated with NCs retained low apoptosis with no recorded necrotic cell percentages. Similar patterns of apoptosis recorded in the HEK293 cell line with the different treatments in both time points were discussed in chapter 3. The high apoptosis levels recorded in U87 MG were attributed to the effect of the free and loaded temozolomide, cisplatin, DNR, and DNR/temozolomide combination. By definition, these first line chemotherapy drugs, including temozolomide, cisplatin and DNR, act on damaging the DNA through different modes of action. Temozolomide acts by methylating the DNA guanine bases, cisplatin acts by crosslinking the DNA base pairs, and DNR acts by uncoiling the DNA double helix (American Cancer Society, 2019; Pokhriyal, Hariprasad, Kumar, & Hariprasad, 2019). Upon apoptosis, a component of the cell membrane known as phosphatidylserine (PS) becomes exposed to the outer side of the cell. Annexin V dye binds to the PS only upon its exposure to the outside of the cell after apoptosis. The 7-amino-actinomycin (7-AAD) is membrane impermeable dye that binds to/intercalates the DNA when the cells lose their membranal integrity upon late apoptosis and cell death (Gobin, Menefee, Lattimore, Doty, & Fredenburg, 2022; Maciel et al., 2014; Wong, Kim, Robinson, Huang, & Conboy, 2021).

Thus, higher apoptosis levels recorded in U87 MG cells when treated with the different loaded and free drugs were attributed to the binding of Annexin V and 7AAD dyes to the PS and DNA upon apoptosis.

This pattern of increased apoptosis in cells treated loaded and free forms of temozolomide, cisplatin, DNR, and DNR/temozolomide came in accordance with the higher cytotoxicity levels induced by the same loaded and free treatments in MTT assay for both 24h and 72h. Additionally, the intracellular and sustained release profile concept of the loaded

nanocontainers for up to 72h and high cell viability of the free NCs in cytotoxicity assay were supported. This data is built on recently reported results on the effectiveness of temozolomide loaded PLGA polymeric nanoparticles in inducing higher apoptosis levels similarly to the free temozolomide in glioblastoma cell line. Further modification of the PLGA nanoparticles with cetuximab targeting agent (anti-EGFR) showed 15% and 5% higher levels of apoptosis and necrosis than non-modified PLGA temozolomide loaded nanoparticles in U87 MG cell line (Duwa et al., 2020). Another instance with a similar outcome to our results was reported in glioblastoma cells treated by GBM-cell membrane camouflaged and pH-sensitive biomimetic nanoparticles (MNPs) coloaded with temozolomide and cisplatin. The treatment of glioblastoma cells with temozolomide and cisplatin coloaded MNPs induced 64% apoptosis which was 20% higher than treatment with temozolomide loaded MNPs and cisplatin loaded MNPs, separately (Zou et al., 2022). The DNR/temozolomide combination used in our study - in loaded and free form- also showed a similar increase of ~15% in apoptosis compared to the treatment of cells with DNR and temozolomide separately at 72h.

Cell cycle analysis by flow cytometry and propidium iodide (PI) staining in U87 MG cells showed cell cycles arrest at different phases induced by loaded and free temozolomide, cisplatin, DNR, and DNR/temozolomide combination. Cell cycle results from analysis in HEK293 were discussed in chapter 3. PI binds to the DNA in proportion to its content. By definition, temozolomide and cisplatin used in our work were alkylating agents and platin-based chemotherapy drugs, respectively, were not cell cycle specific. Yet, DNR which was an anthracycline and it was reported that it arrested the cell cycle at the G2 phase (Mills, Kolb, & Sampson, 2018; National Cancer Institute, 2023; Sun, Liu, Ma, & Hu, 2021). Therefore, there was not an anticipated cell cycle arrest phase for samples treated with loaded and free

temozolomide and cisplatin unlike DNR, which had an anticipated cell cycle arrest at the G2 phase.

The cell cycle comprises four main phases; Gap1 (G1), synthesis (S), and Gap2 (G2), and mitotic (M), during which a series of events take place regarding the DNA synthesis with the best integrity (Sun, Liu, Ma, & Hu, 2021). G1/S and G2/M are considered checkpoints (Alimbetov, Askarova, Umbayev, Davis, & Kipling, 2018). During the G1 phase, cells increase in size and prepare for division with a series of events including the transcription of cyclins and similar control genes. At the S phase, DNA synthesis and replication take place. At the G2 phase, the cells undergo a series of checks to ensure DNA integrity and start making protein and organelles related to the mitosis division (Alimbetov, Askarova, Umbayev, Davis, & Kipling, 2018; Sun, Liu, Ma, & Hu, 2021). During the M phase, the cells divide into two identical diploid cells by splitting their DNA into two copies. After the M phase, cells can enter into a new G1 phase for further divisions or remain dormant in G0 phase (Tan, Duncan, & Slawson, 2017).

The untreated and NCs treated U87 MG cells showed higher cell percentages at the G1 for 24h and 72h. In samples treated with loaded temozolomide shifted from G2 after 24h to G1 after 72h, whereas free temozolomide samples remained at G1 for both time points. Comparatively, with our data, polymeric nanoparticles loaded with a derivative of temozolomide showed cell cycle arrest at the G1/S phase in glioma cells after 72h of treatment with a significant increase in cells arrested at the G2/M compared to the control (Wang et al., 2022). Loaded and free cisplatin showed cell cycle arrest at the G2 and G1, respectively after 24h yet, they either retained or switched to G1 phase arrest after 72h. Reported similar polymeric nanoparticles loaded with cisplatin showed cell cycle arrest in sub-G0 and G1 phases after 96h of treatment in glioblastoma. Also, plain nanoparticles showed G1 cell cycle

arrest. This outcome lined with our results in NCs, loaded and free cisplatin treated samples after 72h of treatment (Maliyakkal, Appadath Beeran, & Udupa, 2021).

Loaded DNR sample showed cell cycle arrest at the anticipated G2 phase after 24h, whereas free DNR treated sample showed relatively similar levels of cells arrested at the G1 and G2 after 24h. After 72h of treatment, both treatments with loaded and free DNR showed cell cycle arrest at the G1 contrary to the anticipated G2 phase arrest. In samples treated with loaded DNR/temozolomide cell cycle arrest was recorded at the DNR's anticipated G2 phase unlike the treatment with free DNR/temozolomide that showed cell cycle arrest at the G1 phase after 24h. Contrary to the pattern recorded after 72h, loaded DNR/temozolomide samples showed cell cycle arrest at the G1, whereas the free version showed G2 cell cycle arrest as anticipated by DNR specific phase. Amphiphilic chitosan polymeric nanoparticles loaded with DNR induced cell cycle arrest at the G2/M in glioblastoma cells. This was in accordance with the induction of cell cycle arrest at the G2 phase with our DNR and DNR/temozolomide loaded polymeric NCs samples after 24h (Sen' et al., 2021).

This cell cycle analysis data in U87 MG was in accordance with the cytotoxicity and apoptosis results in both times points where loaded and free temozolomide, cisplatin, DNR, and DNR/temozolomide combination induced more cytotoxicity and total apoptosis than the untreated and NCs treated samples. Although this data further added to the effectiveness of nanoparticles as drug carriers for targeted delivery in tumour cells, certain limitations were noted. For instance, there was a lack in in our data regarding a “reference action” of the free drug in arresting the cell cycle and inducing apoptosis at a specific and known phase, except for DNR. Literature reported anti-microtubule agents, including paclitaxel, docetaxel, and vincristine as G2/M phase-specific, antimetabolites including 6-mercaptopurine, 5-

fluorouracil, cytarabine and methotrexate among others as G1/S specific and anti-tumour antibiotics including daunorubicin and doxorubicin as G2/M (Mills, Kolb, & Sampson, 2018).

To overcome the limitation of the lack of cell cycle arrest specificity, cells could undergo synchronization to a specific phase in order to ensure reliable comparisons and draw accurate conclusions. A similar suggestion was followed by Huang and colleagues (2016), where human ovarian adenocarcinoma cells were synchronized at the same starting phase and cell cycle analysis and drug effect were assessed. Enzymatically triggered nanoparticles loaded with cisplatin and free cisplatin showed cell cycle arrest at the S phase and G0/G1, respectively. Although results did not report additional differences between the effect of the loaded and free forms of cisplatin in synchronized and non-synchronised cells, this allowed for further results validation (Huang et al., 2016).

4.5. Conclusions

In conclusion, polymeric nanoparticles loaded with temozolomide, cisplatin, and DNR were assessed -separately or in combination- for effective treatment of glioblastoma by several assessments, including testing their cytotoxicity and cellular uptake, as well as their effect on wound healing, DNA damage, apoptosis, and cell cycle. Overall, all collected data were evaluated and induced cytotoxicity by the drug loaded NCs by the MTT assay and wound healing, good cellular uptake by the fluorescence microscopy, effective induction of DNA damage by the western blot, induction of apoptosis and cell cycle arrest by flow cytometry analysis with Annexin/7AAD and PI staining were shown. These results revealed promising drug efficacy improvement, hence, treatment enhancement. Yet, further *in vivo* assessment would better confirm the targeting ability of these polymeric nanocontainers in glioblastoma and their subsequent reduction of systemic and long-term side effects of first line chemotherapy drugs. Correspondingly, these polymeric nanocontainers could be considered a very good preliminary base for drug loading and delivery which could have additional and exceptional properties with further modifications, such as targeting agents to assess and unlock further efficacy advantages. There is a plethora of studies regarding the application of nanoparticles in the treatment of glioblastoma. Yet, the survival rates remain poor, particularly in metastatic and non-operable cases. In these cases, an effective and targeted delivery system that can bypass the BBB and deliver the cargo to the tumour *in situ* is an urge. For this, our work was among the recent studies that assessed the treatment of glioblastoma with three first line chemotherapy drugs loaded in dual responsive and biocompatible polymeric nanocontainers.

CHAPTER 5

5. FINAL DISCUSSIONS

Survival rates in head and brain tumours remain poor despite adjuvant therapy with surgery, radiotherapy and chemotherapy. Treatment of these neoplasms with conventional chemotherapy ensues long term side effects as a result of the untargeted delivery of first line chemotherapy drugs. Hence, there is an escalating urge to opt for novel and targeted therapy systems that can deliver chemotherapy drugs to the tumour in a selective manner which could increase treatment efficiency and reduce side effects. In fact, several studies around the globe have been working on developing novel and precision therapies for cancer treatment, including drug delivery systems. However, the application and translation of the potential effectiveness of these developed targeted drug delivery systems in rare cancers such as rhabdomyosarcoma and glioblastoma are still clinically scarce.

For this, our work focused on the development of biocompatible smart polymeric nanocontainers that are capable of delivering currently used first line chemotherapy drugs (daunorubicin, cisplatin, and temozolomide) in rhabdomyosarcoma and glioblastoma cells *in vitro*. By this approach, we aimed to assess the efficacy of the smart polymeric nanocontainers in carrying and delivering the loaded chemotherapy drugs and treating rhabdomyosarcoma and glioblastoma.

Polymeric P(MAA-co-MBA-co-NIPAM-co-EGDMA) nanocontainers with dual pH and thermo-sensitivity were successfully synthesised with PMAA, PEGDMA and PNIPAM copolymers and crosslinked with MBA. The structural characterization of the nanocarriers by FTIR confirmed the successful coating of the core template with MAA, NIPAM, and EGDMA copolymers through the identification of their characteristic peaks at their corresponding wavenumber ranges. The final core removal of MAA by hydrolysis in water and ethanol was also confirmed

by the FTIR through a decrease in the COOH characteristic peak of MAA. DLS characterization showed good distribution with increased hydrodynamic sizes that were attributed to the deprotonation of the carboxylic groups on the surface of nanoparticles when dispersed in water. Also, DLS measurement showed nanocontainers with an overall negative charge through the negative zeta potential which was attributable to the deprotonated carboxylic groups (COO⁻) at the surface of the NCs when dispersed in water with pH higher than the pKa of the carboxylic acid.

The morphological characterization of nanocontainers with SEM confirmed the achieved coating with a dual-sensitive layer after the noticeable increase in size between core spheres and coated spheres. The hollow and spherical shape of the nanocontainers with a formed cavity after the hydrolysis and removal of the template PMAA core was also confirmed by SEM analysis. This was in accordance with the structural characterization results by FTIR and DLS.

Three first line chemotherapy drugs daunorubicin, cisplatin and temozolomide were efficiently encapsulated by our polymeric nanocontainers with varying loading capacities and encapsulation efficiencies up to 63% and 97%, respectively. The loading capacity of the NCs depended on their ability to form electrostatic and hydrogen-bonding interactions with the drug i.e., binding of the negative carboxylic group of the MAA copolymer either inside or outside of the nanocarrier with the amine group and OH groups of the drug.

The release of the DNR and cisplatin from the NCs showed a sustained drug release profile for 72h in pH 7.4, 6.8 and 4.6 at 37°C and 40°C. Drug release was higher at pH 4.6 and 40°C compared to the release at pH 6.8 and pH 7.4. This confirmed the dual sensitivity of the nanocontainers to acidic pH and high temperature.

Additionally, our polymeric nanocontainers showed high biocompatibility and insignificant haemolysis levels when incubated with red blood cells (RBCs) at different concentrations. The SEM analysis also revealed healthy concave shaped RBCs treated with different concentrations of our plain polymeric nanocontainers similar to the negative control and in contrast to the haemolysed and morphologically altered positive control. This was clear evidence of the hemocompatibility of the synthesised polymeric nanocontainers.

Treatment of the control (HEK293), rhabdomyosarcoma (TE671), and glioblastoma (U87 MG) cell lines with plain polymeric nanocontainers showed high cell viability and insignificant cytotoxicity levels through different concentrations of nanocontainers for 24h and 72h incubation. This clearly showed the non-cytotoxicity characteristic of our developed dual-sensitive nanocontainers and signified an unaffected cellular and metabolic activity in the presence of free NCs. Also, the *in vitro* assessment of cytotoxicity induced by the loaded polymeric NCs with cisplatin, temozolomide, and DNR separately or in combination showed decreasing cell viability as treatment concentrations increased. The decrease in cell viability was similar to the decreased pattern of cell viability when treated with the free drugs indicating an affected cellular and metabolic activity in the presence of the free and loaded drugs. These were evidence of the reliability of the loaded nanocontainers as drug carriers and their capability of releasing the cargo drugs efficiently *in vitro* and inducing cytotoxicity in a comparatively similar pattern to the free drug in control, rhabdomyosarcoma and glioblastoma cells. Also, throughout the time points and concentrations used, the drug loaded NCs induced overall lower cytotoxicity than the free drug in the control, rhabdomyosarcoma and glioblastoma cells, which additionally supported the sustained release feature of the polymeric NCs.

The combination of temozolomide and DNR in loaded and free forms induced slightly higher levels of cytotoxicity than their levels when introduced separately in control, rhabdomyosarcoma, and glioblastoma for 24h and 72h. This trend could be attributed to the dual effect of the drugs in intercalating the DNA and interfering with its transcription as well as cell division.

The monitoring of cellular uptake of the rhodamine and DNR loaded nanocontainers in rhabdomyosarcoma and glioblastoma cells, respectively, revealed very good cellular uptake of the nanoparticles by the two cell lines as well as in control cell lines. The gradual uptake shown by the slight difference in rhodamine and DNR intensities indicated the sustained release property of the nanoparticles.

DNA damage assessment in rhabdomyosarcoma and glioblastoma cells treated with free NCs, loaded and free temozolomide, cisplatin, DNR, and temozolomide/DNR combination revealed variation in γ H2A.X levels. The decreased levels of γ H2A.X in treated samples compared to control samples were unanticipated. The unanticipated decrease in the γ H2A.X in treated samples compared to the untreated cells could be explained with two postulations. Firstly, it could be attributed to the degradation of H2A.X content in the chromatin as a result of reactive oxygen species (ROS) generated by the effectiveness of the treatment with free and loaded drugs. Secondly, it could be attributed to the dephosphorylation of the γ H2A.X that might have been ensued as a result of DNA repair after 72h of treatment; hence undetectable phosphorylated H2A.X foci and return of the γ H2A.X to the standard levels.

On the other hand, the increase of γ H2A.X levels in the loaded temozolomide samples in both rhabdomyosarcoma and glioblastoma could be attributed to either effectiveness of the treatment. Or it could be attributed to the elevated levels of DNA repair, hence the resistance

of the cells to the treatment. Also, the increase of γ H2A.X in the control samples and NCs treated samples could be attributed to either the DNA damage induced by the NCs, or due to elevated levels of DNA repair in cancer cells since they are highly proliferative. The first explanation was less likely to be correct due to the proven non-toxic trait of the plain NCs in MTT cytotoxicity experiments.

Overall, the γ H2AX is considered a sensitive marker of DNA double-strand breaks. However, the expression of H2A.X in different cell lines and tissue types is highly heterogeneous. This variability renders the interpretation of γ H2AX levels and their subtle changes considerably difficult (Ji et al., 2017). Although the γ H2A.X is considered a DSB marker, the H2A.X represents only 2–25% of the cellular H2A pool in mammalian cells. Therefore, other H2A.X variants and other DNA damage markers could be investigated (Dobersch et al., 2021).

Apoptosis analysis by flow cytometry and annexin V/7AAD staining in rhabdomyosarcoma and glioblastoma showed increased total apoptosis and/or necrotic percentages when treated for 24h and 72h with loaded and free temozolomide, cisplatin, DNR, and DNR/temozolomide combination. This was in contrast to the low apoptosis and necrosis percentages recorded in the untreated and NCs treated samples. The higher levels of induced apoptosis and necrosis were attributed to the effect of the different chemotherapy drugs in loaded and free forms and their mode of action when tackling cancer cells. This also meant that loaded and free forms of the temozolomide, cisplatin, DNR, and DNR/temozolomide induced PS exposure to the outside of the cells and disrupted the integrity of the cell membrane. This pattern came in accordance with the higher cytotoxicity levels induced by the loaded and free treatments in the MTT assay. Additionally, the apoptosis results further supported the intracellular and

sustained release profile concept of the loaded nanocontainers for up to 72h, and the high cell viability of the free NCs in cytotoxicity results.

Cell cycle analysis by flow cytometry and propidium iodide (PI) staining in rhabdomyosarcoma and glioblastoma cells showed cell cycles arrest at different phases induced by the different treatments applied. The cell cycle arrest was induced at the G2 by DNR as anticipated only on two occasions, in TE671 cells after 72h treatment with loaded DNR, and in HEK293 cells after 24h treatment with free DNR. In glioblastoma cells, loaded DNR sample showed cell cycle arrest at the anticipated G2 phase only after 24h, whereas free DNR treated sample showed relatively similar levels of cells arrested at both the G1 and G2 after 24h. Untreated samples and NCs treated samples showed relatively the same accumulation of cells at the G1 or G2 in rhabdomyosarcoma, glioblastoma and HEK293 cells. The rest of the samples treated with loaded and free temozolomide, cisplatin, and DNR/temozolomide had cell cycle arrest either at the G1 or G2 for both 24h and 72h. This cell cycle analysis data in rhabdomyosarcoma and glioblastoma cells was in accordance with the cytotoxicity and apoptosis results in both time points where loaded and free temozolomide, cisplatin, DNR, and DNR/temozolomide combination induced more cytotoxicity and total apoptosis than the untreated and NCs treated samples. This also further added to the effectiveness of nanoparticles as drug carriers for targeted delivery in tumour cells. To overcome the limitation of the lack of cell cycle arrest specificity, cells could undergo synchronization to a specific phase in order to ensure reliable comparisons and draw accurate conclusions.

In conclusion, our developed smart and hollow polymeric nanocontainers with dual sensitivity to pH and temperature exhibited high biocompatibility and non-toxicity trait when assessed by haemolysis and MTT assay, respectively. They further exhibited high drug loading capacities

and encapsulation efficiencies of up to 63% and 97%, respectively, for three different first line chemotherapy drugs (cisplatin, DNR, and temozolomide). Our smart polymeric nanocontainers also showed a good pattern of sustained release for up to 72h. The highest release percentages were recorded at the corresponding sensitivities of their layer i.e. acidic pH and high temperature, which are also characteristics of the tumour's microenvironment. Additionally, these developed hollow polymeric nanocontainers showed good cellular uptake and efficiency in carrying and delivering the encapsulated drugs in a prolonged pattern in rhabdomyosarcoma and glioblastoma tumour cells. This ensued lower tumour cell viability percentages, DNA damage, apoptosis and cell cycle arrest for up to 72h treatment with an extended and sustained therapeutic effect. This answered the first research question we raised about the ability of the nanocontainers to carry the therapeutic drug and treat the tumour effectively. The treatment combination of loaded and free temozolomide/DNR exhibited higher toxicity and apoptosis compared to the same drug treatments separately, which answered the second research question we raised. Thus, it indicated that a combination of drugs might be more efficient in tackling tumour cells. Therefore, our work showed the excellent potential of our developed smart polymeric nanocontainers as a novel therapeutic approach for the treatment of neoplasms of the head and brain, such as rhabdomyosarcoma and glioblastoma through targeted delivery of existing chemotherapy drugs.

5.1. Future prospects

In the future, an assessment of the ability of the nanocontainers to cross the blood brain barrier (BBB) and deliver the encapsulated drug to the tumour cells will be conducted. This will be performed with hCMEC/D3 BBB cell model *in vitro* by means of coculture in a trans-well system that mimics the BBB. For the same purpose, the *in vivo* assessment will be conducted with a xenograft mice model. Another *in vivo* assessment will take place with the rhabdomyosarcoma xenograft mice model to evaluate the ability of the nanocontainers to deliver the encapsulated drug to the tumour site. Further loadings of different chemotherapy drugs will take place, as well as modifications with targeting agents and radiolabelling. With gallium or technetium, radiolabelled nanocontainers will act as a theranostic tool, and the *in vivo* assessment will then evaluate the biodistribution of the nanocontainers, identify their accumulation site, and therapeutic efficiency.

Our work added to the insight into the importance of employing targeted drug delivery systems, including polymeric nanoparticles, for the therapy of cancer, including those with complicated and critical sites such as brain, head and neck tumours. Generally, in these neoplasms, maximal tumour resection is unattainable, and survival rates remain unsatisfactory with poor prognosis despite adjuvant therapy due to the aggressiveness trait of the tumour and the presence of selective barrier such as BBB. The biocompatible, cheap, and smart polymeric nanoparticles developed in our work afforded several advantageous characteristics, including small size, dual sensitivity to pH and temperature, high drug loading capacities, controlled release, and good cellular uptake. These characteristics ensued the effective tackling of tumour cells (e.g. rhabdomyosarcoma and glioblastoma). The high drug loading capacities and sustained release traits of these nanocontainers can potentially reduce the administrated doses of chemotherapy in patients which will then reduce the cost of cancer therapy, that is estimated to be between \$8000 and \$100,000 per person including head and brain tumours (Goel, Bird, Hicks, & Abdullah, 2021; Smith, Shih, & Frank, 2021). The targeted drug delivery through stimuli responsiveness potentially reduces side effects and treatment resistance in tumour cells which will result in effective treatment, increased survival rates, and lower risks of recurrence. Patients diagnosed with rare and aggressive tumours have very limited time, and clinical trials investigating novel drugs are time-consuming before any approval is issued for clinical use. For this, it is highly important to opt for more personalized/precision medicine through targeted drug delivery systems, including polymeric nanocontainers, to adapt the treatment regimen based on the patient's cancer stage and diagnostic data. In addition to the enhancement of the efficacy of existing chemotherapy drugs and significant reduction of long-term side effects, this approach will also help lift the global economic burden of cancer care cost, which is estimated to be \$25.2 trillion between

2020 and 2050, with ~\$1404 billion in brain and CNS cancer and ~\$905 billion in head and neck cancers (Chen et al., 2023). Hopefully, our current study can confirm the effectiveness of future targeted therapies and pave the way for their application from bench side to bed and back.

REFERENCES

- Abdeyrim, A., He, S., Zhang, Y., Mamtali, G., Asla, A., Yusup, M., & Liu, J. (2020). Prognostic value of lymph node ratio in laryngeal and hypopharyngeal squamous cell carcinoma: A systematic review and meta-analysis. *Journal of Otolaryngology - Head & Neck Surgery*, 49(1). doi:10.1186/s40463-020-00421-w
- Al-Anazi, A. E., Alanazi, B. S., Alshanbari, H. M., Masuadi, E., Hamed, M. E., Dandachi, I., . . . Alosaimi, B. (2023). Increased prevalence of EBV infection in nasopharyngeal carcinoma patients: A six-year cross-sectional study. *Cancers*, 15(3), 643. doi:10.3390/cancers15030643
- Bose, P., Brockton, N. T., & Dort, J. C. (2013). Head and neck cancer: From anatomy to biology. *International Journal of Cancer*, 133(9), 2013-2023. doi:10.1002/ijc.28112
- De Bakker, T., Journe, F., Descamps, G., Saussez, S., Dragan, T., Ghanem, G., . . . Van Gestel, D. (2022). Restoring p53 function in head and neck squamous cell carcinoma to improve treatments. *Frontiers in Oncology*, 11. doi:10.3389/fonc.2021.799993
- Groeger, S., & Meyle, J. (2019). Oral mucosal epithelial cells. *Frontiers in Immunology*, 10. doi:10.3389/fimmu.2019.00208
- Johnson, D. E., Burtness, B., Leemans, C. R., Lui, V. W., Bauman, J. E., & Grandis, J. R. (2020). Head and neck squamous cell carcinoma. *Nature Reviews Disease Primers*, 6(1). doi:10.1038/s41572-020-00224-3
- König, M., Osnes, T., Bratland, Å, & Meling, T. R. (2019). Squamous cell carcinoma of the paranasal sinuses: A single center experience. *Journal of Neurological Surgery Part B: Skull Base*, 81(06), 664-672. doi:10.1055/s-0039-1694967

- Lucidi, D., Cantaffa, C., Miglio, M., Spina, F., Alicandri Ciufelli, M., Marchioni, A., & Marchioni, D. (2023). Tumors of the nose and paranasal sinuses: Promoting factors and molecular mechanisms—a systematic review. *International Journal of Molecular Sciences*, *24*(3), 2670. doi:10.3390/ijms24032670
- Moro, J. D., Maroneze, M. C., Ardenghi, T. M., Barin, L. M., & Danesi, C. C. (2018). Oral and oropharyngeal cancer: Epidemiology and survival analysis. *Einstein (São Paulo)*, *16*(2). doi:10.1590/s1679-45082018ao4248
- Oren, N., Vaysberg, A., & Ginat, D. T. (2019). Updated who nomenclature of head and neck lesions and associated imaging findings. *Insights into Imaging*, *10*(1). doi:10.1186/s13244-019-0760-4
- Perri, F., Longo, F., Caponigro, F., Sandomenico, F., Guida, A., Della Vittoria Scarpati, G., . . . Ionna, F. (2020). Management of HPV-related squamous cell carcinoma of the head and neck: Pitfalls and caveat. *Cancers*, *12*(4), 975. doi:10.3390/cancers12040975
- Sanghvi, S., Khan, M. N., Patel, N. R., Yeldandi, S., Baredes, S., & Eloy, J. A. (2013). Epidemiology of sinonasal squamous cell carcinoma: A comprehensive analysis of 4994 patients. *The Laryngoscope*, *124*(1), 76-83. doi:10.1002/lary.24264
- Shen, T., Cai, W., Li, T., Yu, D., Ren, C., & Yu, J. (2022). Impact of primary site on survival in patients with nasopharyngeal carcinoma from 2004 to 2015. *Frontiers in Surgery*, *9*. doi:10.3389/fsurg.2022.1001849

- Yan, F., Knochelmann, H. M., Morgan, P. F., Kaczmar, J. M., Neskey, D. M., Graboyes, E. M., . . . Day, T. A. (2020). The evolution of care of cancers of the head and Neck Region: State of the science in 2020. *Cancers, 12*(6), 1543. doi:10.3390/cancers12061543
- Zhang, D., Li, L., Wen, T., Wu, Y., & Ma, F. (2022). Prognostic nomogram for postoperative hypopharyngeal squamous cell carcinoma to assist decision making for Adjuvant Chemotherapy. *Journal of Clinical Medicine, 11*(19), 5801. doi:10.3390/jcm11195801
- Anderson, G., Ebadi, M., Vo, K., Novak, J., Govindarajan, A., & Amini, A. (2021). An updated review on head and neck cancer treatment with radiation therapy. *Cancers, 13*(19), 4912. doi:10.3390/cancers13194912
- Anderson, G., Ebadi, M., Vo, K., Novak, J., Govindarajan, A., & Amini, A. (2021). An updated review on head and neck cancer treatment with radiation therapy. *Cancers, 13*(19), 4912. doi:10.3390/cancers13194912
- Bray, F., Ferlay, J., Soerjomataram, I., Siegel, R. L., Torre, L. A., & Jemal, A. (2018). Global cancer statistics 2018: Globocan estimates of incidence and mortality worldwide for 36 cancers in 185 countries. *CA: A Cancer Journal for Clinicians, 68*(6), 394-424. doi:10.3322/caac.21492
- Fan, Y., Zhang, X., Gao, C., Jiang, S., Wu, H., Liu, Z., & Dou, T. (2022). Burden and trends of brain and central nervous system cancer from 1990 to 2019 at the Global, regional, and Country Levels. *Archives of Public Health, 80*(1). doi:10.1186/s13690-022-00965-5
- Hahn, E., Barot, S., O'Sullivan, B., Huang, S. H., Gupta, A., Hosni, A., . . . Shultz, D. B. (2022). Adult head and neck rhabdomyosarcoma: Management, outcomes, and the effect of

- intensity modulated radiation therapy on Locoregional control. *Advances in Radiation Oncology*, 7(6), 101055. doi:10.1016/j.adro.2022.101055
- Jo, V. Y., & Demicco, E. G. (2022). Update from the 5th edition of the World Health Organization classification of head and neck tumors: Soft tissue tumors. *Head and Neck Pathology*, 16(1), 87-100. doi:10.1007/s12105-022-01425-w
- Ju, Y., Wu, X., Wang, H., Li, B., Long, Q., Zhang, D., . . . Yang, S. (2021). Genomic landscape of head and neck squamous cell carcinoma across different anatomic sites in Chinese population. *Frontiers in Genetics*, 12. doi:10.3389/fgene.2021.680699
- McDermott, J. D., & Bowles, D. W. (2019). Epidemiology of head and neck squamous cell carcinomas: Impact on staging and prevention strategies. *Current Treatment Options in Oncology*, 20(5). doi:10.1007/s11864-019-0650-5
- Ostrom, Q. T., Price, M., Neff, C., Cioffi, G., Waite, K. A., Kruchko, C., & Barnholtz-Sloan, J. (2022). CBTRUS statistical report: Primary Brain and other central nervous system tumors diagnosed in the United States in 2015–2019. *Neuro-Oncology*, 24(Supplement_5), V1-V95. doi:10.1093/neuonc/noac202
- Rasheed, S., Rehman, K., & Akash, M. S. (2021). An insight into the risk factors of brain tumors and their therapeutic interventions. *Biomedicine & Pharmacotherapy*, 143, 112119. doi:10.1016/j.biopha.2021.112119
- Reuss, D. (2023). Updates on the who diagnosis of IDH-mutant glioma. *Journal of Neuro-Oncology*. doi:10.1007/s11060-023-04250-5

- Sabatini, M. E., & Chiocca, S. (2019). Human papillomavirus as a driver of head and neck cancers. *British Journal of Cancer*, *122*(3), 306-314. doi:10.1038/s41416-019-0602-7
- Sabatini, M. E., & Chiocca, S. (2019). Human papillomavirus as a driver of head and neck cancers. *British Journal of Cancer*, *122*(3), 306-314. doi:10.1038/s41416-019-0602-7
- Sindhu, S. K., & Bauman, J. E. (2019). Current concepts in chemotherapy for head and neck cancer. *Oral and Maxillofacial Surgery Clinics of North America*, *31*(1), 145-154. doi:10.1016/j.coms.2018.09.003
- Whitfield, B. T., & Huse, J. T. (2022). Classification of adult-type diffuse gliomas: Impact of the World Health Organization 2021 update. *Brain Pathology*, *32*(4). doi:10.1111/bpa.13062
- Abid, N., Khan, A. M., Shujait, S., Chaudhary, K., Ikram, M., Imran, M., . . . Maqbool, M. (2022). Synthesis of nanomaterials using various top-down and bottom-up approaches, influencing factors, advantages, and disadvantages: A Review. *Advances in Colloid and Interface Science*, *300*, 102597. doi:10.1016/j.cis.2021.102597
- Ahire, S. A., Bachhav, A. A., Pawar, T. B., Jagdale, B. S., Patil, A. V., & Koli, P. B. (2022). The augmentation of nanotechnology era: A concise review on fundamental concepts of nanotechnology and applications in material science and Technology. *Results in Chemistry*, *4*, 100633. doi:10.1016/j.rechem.2022.100633
- Chis, A. A., Dobra, C., Morgovan, C., Arseniu, A. M., Rus, L. L., Butuca, A., . . . Frum, A. (2020). Applications and limitations of Dendrimers in Biomedicine. *Molecules*, *25*(17), 3982. doi:10.3390/molecules25173982

- Huseien, G. F., Shah, K. W., & Sam, A. R. (2019). Sustainability of nanomaterials based self-healing concrete: An all-inclusive insight. *Journal of Building Engineering*, *23*, 155-171. doi:10.1016/j.jobe.2019.01.032
- Janaszewska, A., Lazniewska, J., Trzepiński, P., Marcinkowska, M., & Klajnert-Maculewicz, B. (2019). Cytotoxicity of Dendrimers. *Biomolecules*, *9*(8), 330. doi:10.3390/biom9080330
- Kaphle, A., Navya, P. N., Umapathi, A., & Daima, H. K. (2017). Nanomaterials for agriculture, food and environment: Applications, toxicity and regulation. *Environmental Chemistry Letters*, *16*(1), 43-58. doi:10.1007/s10311-017-0662-y
- Kolahalam, L. A., Kasi Viswanath, I., Diwakar, B. S., Govindh, B., Reddy, V., & Murthy, Y. (2019). Review on nanomaterials: Synthesis and applications. *Materials Today: Proceedings*, *18*, 2182-2190. doi:10.1016/j.matpr.2019.07.371
- Mignani, S., Shi, X., Rodrigues, J., Tomás, H., & Majoral, J. (2022). Dendrimer nanoplatfoms for Veterinary Medicine Applications: A concise overview. *Drug Discovery Today*, *27*(5), 1251-1260. doi:10.1016/j.drudis.2022.01.001
- Najafi, F., Salami-Kalajahi, M., & Roghani-Mamaqani, H. (2020). A review on synthesis and applications of Dendrimers. *Journal of the Iranian Chemical Society*, *18*(3), 503-517. doi:10.1007/s13738-020-02053-3
- National Nanotechnology Initiative. (2023). About the NNI. Retrieved March 23, 2023, from <https://www.nano.gov/about-nni>

- Patel, V., Patel, P., Patel, J. V., & Patel, P. M. (2022). Dendrimer as a versatile platform for Biomedical Application: A Review. *Journal of the Indian Chemical Society*, *99*(7), 100516. doi:10.1016/j.jics.2022.100516
- Pellerino, A., Caccese, M., Padovan, M., Cerretti, G., & Lombardi, G. (2022). Epidemiology, risk factors, and prognostic factors of gliomas. *Clinical and Translational Imaging*, *10*(5), 467-475. doi:10.1007/s40336-022-00489-6
- Roco, M. C. (2011). The long view of nanotechnology development: The National Nanotechnology Initiative at 10 Years. *Journal of Nanoparticle Research*, *13*(2), 427-445. doi:10.1007/s11051-010-0192-z
- Shukla, R. K. (2016). Nanotechnology: An applied and robust approach for forensic investigation. *Foresic Research & Criminology International Journal*, *2*(1). doi:10.15406/frcij.2016.02.00044
- Taal, W., Bromberg, J. E., & Van den Bent, M. J. (2015). Chemotherapy in glioma. *CNS Oncology*, *4*(3), 179-192. doi:10.2217/cns.15.2
- Abdel-Sayed, P., Kaeppli, A., Siriwardena, T., Darbre, T., Perron, K., Jafari, P., . . . Applegate, L. A. (2016). Anti-microbial dendrimers against multidrug-resistant *P. aeruginosa* enhance the angiogenic effect of biological burn-wound bandages. *Scientific Reports*, *6*(1). doi:10.1038/srep22020
- Amendola, V., Pilot, R., Frascioni, M., Maragò, O. M., & Iatì, M. A. (2017). Surface plasmon resonance in gold nanoparticles: A Review. *Journal of Physics: Condensed Matter*, *29*(20), 203002. doi:10.1088/1361-648x/aa60f3

- Bulbake, U., Doppalapudi, S., Kommineni, N., & Khan, W. (2017). Liposomal formulations in clinical use: An updated review. *Pharmaceutics*, *9*(4), 12. doi:10.3390/pharmaceutics9020012
- Cao, J., Wang, C., Guo, L., Xiao, Z., Liu, K., & Yan, H. (2018). Co-administration of a charge-conversional dendrimer enhances antitumor efficacy of conventional chemotherapy. *European Journal of Pharmaceutics and Biopharmaceutics*, *127*, 371-377. doi:10.1016/j.ejpb.2018.02.035
- Hammami, I., Alabdallah, N. M., Jomaa, A. A., & Kamoun, M. (2021). Gold nanoparticles: Synthesis properties and applications. *Journal of King Saud University - Science*, *33*(7), 101560. doi:10.1016/j.jksus.2021.101560
- Hu, X., Zhang, Y., Ding, T., Liu, J., & Zhao, H. (2020). Multifunctional gold nanoparticles: A novel nanomaterial for various medical applications and biological activities. *Frontiers in Bioengineering and Biotechnology*, *8*. doi:10.3389/fbioe.2020.00990
- Liu, G., Lu, M., Huang, X., Li, T., & Xu, D. (2018). Application of gold-nanoparticle colorimetric sensing to Rapid Food Safety Screening. *Sensors*, *18*(12), 4166. doi:10.3390/s18124166
- Lu, H., Chen, T., Wang, Y., He, Y., Pang, Z., & Wang, Y. (2022). Dual targeting micelles loaded with paclitaxel and lapatinib for combinational therapy of brain metastases from breast cancer. *Scientific Reports*, *12*(1). doi:10.1038/s41598-022-06677-8
- Ma, P. (2013). Paclitaxel nano-delivery systems: A comprehensive review. *Journal of Nanomedicine & Nanotechnology*, *04*(02). doi:10.4172/2157-7439.1000164

- Mignani, S., Shi, X., Rodrigues, J., Tomás, H., & Majoral, J. (2022). Dendrimer nanoplatfoms for Veterinary Medicine Applications: A concise overview. *Drug Discovery Today*, 27(5), 1251-1260. doi:10.1016/j.drudis.2022.01.001
- Nsairat, H., Khater, D., Sayed, U., Odeh, F., Al Bawab, A., & Alshaer, W. (2022). Liposomes: Structure, composition, types, and clinical applications. *Heliyon*, 8(5). doi:10.1016/j.heliyon.2022.e09394
- Patra, J. K., Das, G., Fraceto, L. F., Campos, E. V., Rodriguez-Torres, M. D., Acosta-Torres, L. S., . . . Shin, H. (2018). Nano based drug delivery systems: Recent developments and future prospects. *Journal of Nanobiotechnology*, 16(1). doi:10.1186/s12951-018-0392-8
- Sercombe, L., Veerati, T., Moheimani, F., Wu, S. Y., Sood, A. K., & Hua, S. (2015). Advances and challenges of liposome assisted drug delivery. *Frontiers in Pharmacology*, 6. doi:10.3389/fphar.2015.00286
- Si, P., Razmi, N., Nur, O., Solanki, S., Pandey, C. M., Gupta, R. K., . . . De la Zerda, A. (2021). Gold nanomaterials for optical biosensing and bioimaging. *Nanoscale Advances*, 3(10), 2679-2698. doi:10.1039/d0na00961j
- Yang, Z., Wang, D., Zhang, C., Liu, H., Hao, M., Kan, S., . . . Liu, W. (2022). The applications of gold nanoparticles in the diagnosis and treatment of gastrointestinal cancer. *Frontiers in Oncology*, 11. doi:10.3389/fonc.2021.819329
- Ali, A., Zafar, H., Zia, M., Ul Haq, I., Phull, A. R., Ali, J. S., & Hussain, A. (2016). Synthesis, characterization, applications, and challenges of iron oxide nanoparticles. *Nanotechnology, Science and Applications, Volume 9*, 49-67. doi:10.2147/nsa.s99986

- Crezee, J., Franken, N. A., & Oei, A. L. (2021). Hyperthermia-based anti-cancer treatments. *Cancers*, *13*(6), 1240. doi:10.3390/cancers13061240
- Dulińska-Litewka, J., Łazarczyk, A., Hałubiec, P., Szafrąński, O., Karnas, K., & Karewicz, A. (2019). Superparamagnetic iron oxide nanoparticles—current and prospective medical applications. *Materials*, *12*(4), 617. doi:10.3390/ma12040617
- Fan, X., Xiao, J., Wang, W., Zhang, Y., Zhang, S., & Tang, B. (2018). Novel magnetic-to-thermal conversion and thermal energy management composite phase change material. *Polymers*, *10*(6), 585. doi:10.3390/polym10060585
- Huang, Y., Hsu, J. C., Koo, H., & Cormode, D. P. (2022). Repurposing ferumoxytol: Diagnostic and therapeutic applications of an FDA-approved nanoparticle. *Theranostics*, *12*(2), 796-816. doi:10.7150/thno.67375
- Janko, C., Ratschker, T., Nguyen, K., Zschiesche, L., Tietze, R., Lyer, S., & Alexiou, C. (2019). Functionalized superparamagnetic iron oxide nanoparticles (spions) as platform for the targeted Multimodal Tumor therapy. *Frontiers in Oncology*, *9*. doi:10.3389/fonc.2019.00059
- Lu, M., Cohen, M. H., Rieves, D., & Pazdur, R. (2010). FDA report: Ferumoxytol for intravenous iron therapy in adult patients with chronic kidney disease. *American Journal of Hematology*. doi:10.1002/ajh.21656
- Mohanty, S., Chen, Z., Li, K., Morais, G. R., Klockow, J., Yerneni, K., . . . Daldrup-Link, H. E. (2017). A novel theranostic strategy for *mmp-14*-expressing glioblastomas impacts

survival. *Molecular Cancer Therapeutics*, 16(9), 1909-1921. doi:10.1158/1535-7163.mct-17-0022

Moitra, P., Alafeef, M., Dighe, K., Frieman, M. B., & Pan, D. (2020). Selective naked-eye detection of SARS-COV-2 mediated by n gene targeted antisense oligonucleotide capped plasmonic nanoparticles. *ACS Nano*, 14(6), 7617-7627. doi:10.1021/acsnano.0c03822

Palzer, J., Eckstein, L., Slabu, I., Reisen, O., Neumann, U. P., & Roeth, A. A. (2021). Iron oxide nanoparticle-based hyperthermia as a treatment option in various gastrointestinal malignancies. *Nanomaterials*, 11(11), 3013. doi:10.3390/nano11113013

Palzer, J., Mues, B., Goerg, R., Aberle, M., Rensen, S. S., Olde Damink, S. W., . . . Roeth, A. A. (2021). Magnetic fluid hyperthermia as treatment option for pancreatic cancer cells and pancreatic cancer organoids. *International Journal of Nanomedicine, Volume 16*, 2965-2981. doi:10.2147/ijn.s288379

Wang, K., Zhang, W., Zhang, X., Hu, X., Chang, S., & Zhang, H. (2020). Highly sensitive gold nanoparticles–DNA nanosensor for γ -radiation detection. *ACS Applied Materials & Interfaces*, 12(37), 42403-42409. doi:10.1021/acami.0c12234

Cheng, X. L., Liu, H. Q., Wang, Q., Huo, J. G., Wang, X. N., & Cao, P. (2015). Chemotherapy-induced peripheral neurotoxicity and complementary and alternative medicines: Progress and perspective. *Frontiers in Pharmacology*, 6. doi:10.3389/fphar.2015.00234

Mukhtar, M., Bilal, M., Rahdar, A., Barani, M., Arshad, R., Behl, T., . . . Bungau, S. (2020). Nanomaterials for diagnosis and treatment of brain cancer: Recent updates. *Chemosensors*, 8(4), 117. doi:10.3390/chemosensors8040117

- Stone, J. R., Kanneganti, R., Abbasi, M., & Akhtari, M. (2021). Monitoring for chemotherapy-related cardiotoxicity in the form of left ventricular systolic dysfunction: A review of current recommendations. *JCO Oncology Practice*, 17(5), 228-236. doi:10.1200/op.20.00924
- Viegas, C., Pereira, D. S., & Fonte, P. (2022). Insights into nanomedicine for head and neck cancer diagnosis and treatment. *Materials*, 15(6), 2086. doi:10.3390/ma15062086
- Benghanem, S., Mazeraud, A., Azabou, E., Chhor, V., Shinotsuka, C. R., Claassen, J., . . . Sharshar, T. (2020). Brainstem dysfunction in critically ill patients. *Critical Care*, 24(1). doi:10.1186/s13054-019-2718-9
- Binder, J. R. (2015). The Wernicke Area. *Neurology*, 85(24), 2170-2175. doi:10.1212/wnl.0000000000002219
- Collins, A., & Koechlin, E. (2012). Reasoning, learning, and creativity: Frontal lobe function and human decision-making. *PLoS Biology*, 10(3). doi:10.1371/journal.pbio.1001293
- Diek, D., Smidt, M. P., & Mesman, S. (2022). Molecular organization and patterning of the medulla oblongata in health and disease. *International Journal of Molecular Sciences*, 23(16), 9260. doi:10.3390/ijms23169260
- Dziedzic, T. A., Bala, A., & Marchel, A. (2021). Cortical and subcortical anatomy of the parietal lobe from the neurosurgical perspective. *Frontiers in Neurology*, 12. doi:10.3389/fneur.2021.727055

- Fasano, M., Corte, C. M., Liello, R. D., Viscardi, G., Sparano, F., Iacovino, M. L., . . . Ciardiello, F. (2022). Immunotherapy for head and neck cancer: Present and future. *Critical Reviews in Oncology/Hematology*, 174, 103679. doi:10.1016/j.critrevonc.2022.103679
- Flores, L. P. (2002). Occipital lobe morphological anatomy: Anatomical and surgical aspects. *Arquivos De Neuro-Psiquiatria*, 60(3A), 566-571. doi:10.1590/s0004-282x2002000400010
- Hernández-Morato, I., Yu, V. X., & Pitman, M. J. (2023). A review of the peripheral proprioceptive apparatus in the larynx. *Frontiers in Neuroanatomy*, 17. doi:10.3389/fnana.2023.1114817
- Jicman Stan, D., Niculet, E., Lungu, M., Onisor, C., Rebegea, L., Vesa, D., . . . Tatu, A. (2021). Nasopharyngeal carcinoma: A new synthesis of literature data (review). *Experimental and Therapeutic Medicine*, 23(2). doi:10.3892/etm.2021.11059
- Kiernan, J. A. (2012). Anatomy of the temporal lobe. *Epilepsy Research and Treatment*, 2012, 1-12. doi:10.1155/2012/176157
- Kwon, D. I., & Miles, B. A. (2018). Hypopharyngeal carcinoma: Do you know your guidelines? *Head & Neck*, 41(3), 569-576. doi:10.1002/hed.24752
- Kötitz, R., Weitschies, W., Trahms, L., & Semmler, W. (1999). Investigation of brownian and néel relaxation in magnetic fluids. *Journal of Magnetism and Magnetic Materials*, 201(1-3), 102-104. doi:10.1016/s0304-8853(99)00065-7
- Larkins, E., Blumenthal, G. M., Yuan, W., He, K., Sridhara, R., Subramaniam, S., . . . Pazdur, R. (2017). FDA approval summary: Pembrolizumab for the treatment of recurrent or

metastatic head and neck squamous cell carcinoma with disease progression on or after platinum-containing chemotherapy. *The Oncologist*, 22(7), 873-878. doi:10.1634/theoncologist.2016-0496

Li, Q., Tie, Y., Alu, A., Ma, X., & Shi, H. (2023). Targeted therapy for head and neck cancer: Signaling Pathways and Clinical Studies. *Signal Transduction and Targeted Therapy*, 8(1). doi:10.1038/s41392-022-01297-0

Tate, M. C., Lindquist, R. A., Nguyen, T., Sanai, N., Barkovich, A. J., Huang, E. J., . . . Alvarez-Buylla, A. (2014). Postnatal growth of the human Pons: A morphometric and immunohistochemical analysis. *Journal of Comparative Neurology*, 523(3), 449-462. doi:10.1002/cne.23690

Ilg, P., & Kröger, M. (2020). Dynamics of interacting magnetic nanoparticles: Effective behavior from competition between Brownian and Néel relaxation. *Physical Chemistry Chemical Physics*, 22(39), 22244-22259. doi:10.1039/d0cp04377j

Bolhassani, A., Javanzad, S., Saleh, T., Hashemi, M., Aghasadeghi, M., & Sadat, S. (2013). Polymeric nanoparticles. *Human Vaccines & Immunotherapeutics*, 10(2), 321-332. Doi: 10.4161/hv.26796

Cancer Research UK. (2019). Chemotherapy drugs | Brain and spinal cord tumours | Cancer Research UK. Retrieved 28 October 2019, from <https://www.cancerresearchuk.org/about-cancer/braintumours/treatment/chemotherapy/drugs>

- Cancer Tomorrow. (2022). Retrieved 15 July 2022, from https://gco.iarc.fr/tomorrow/en/dataviz/bars?type=0&sexes=0&mode=population&group_populations=0&multiple_populations=1
- Clemons, T., Singh, R., Sorolla, A., Chaudhari, N., Hubbard, A., & Iyer, K. (2018). Distinction Between Active and Passive Targeting of Nanoparticles Dictate Their Overall Therapeutic Efficacy. *Langmuir*, 34(50), 15343-15349. doi: 10.1021/acs.langmuir.8b02946
- Dong, X. (2018). Current Strategies for Brain Drug Delivery. *Theranostics*, 8(6), 1481-1493. doi: 10.7150/thno.21254
- Feynman, R. (1992). There's plenty of room at the bottom [data storage]. *Journal Of Microelectromechanical Systems*, 1(1), 60-66. doi: 10.1109/84.128057
- Ikonomidou, C. (2018). Chemotherapy and the pediatric brain. *Molecular And Cellular Pediatrics*, 5(1). doi: 10.1186/s40348-018-0087-0
- Jeevanandam, J., Barhoum, A., Chan, Y., Dufresne, A., & Danquah, M. (2018). Review on nanoparticles and nanostructured materials: history, sources, toxicity and regulations. *Beilstein Journal Of Nanotechnology*, 9, 1050-1074. doi: 10.3762/bjnano.9.98
- John Hopkins Medicine. (2022). Brain Anatomy and How the Brain Works. Retrieved 1 October 2022, from <https://www.hopkinsmedicine.org/health/conditions-and-diseases/anatomy-of-the-brain>
- Lochhead, J., Yang, J., Ronaldson, P., & Davis, T. (2020). Structure, Function, and Regulation of the Blood-Brain Barrier Tight Junction in Central Nervous System Disorders. *Frontiers In Physiology*, 11. doi: 10.3389/fphys.2020.00914

- Louis, D., Perry, A., Reifenberger, G., von Deimling, A., Figarella-Branger, D., & Cavenee, W. et al. (2016). The 2016 World Health Organization Classification of Tumors of the Central Nervous System: a summary. *Acta Neuropathologica*, 131(6), 803-820. doi: 10.1007/s00401-016-1545-1
- Louis, D., Perry, A., Wesseling, P., Brat, D., Cree, I., & Figarella-Branger, D. et al. (2021). The 2021 WHO Classification of Tumors of the Central Nervous System: a summary. *Neuro-Oncology*, 23(8), 1231-1251. doi: 10.1093/neuonc/noab106
- Mabray, M., Barajas, R., & Cha, S. (2015). Modern Brain Tumor Imaging. *Brain Tumor Research and Treatment*, 3(1), 8. doi: 10.14791/btrt.2015.3.1.8
- Mitchell, M., Billingsley, M., Haley, R., Wechsler, M., Peppas, N., & Langer, R. (2020). Engineering precision nanoparticles for drug delivery. *Nature Reviews Drug Discovery*, 20(2), 101-124. doi: 10.1038/s41573-020-0090-8
- Niculescu, A., & Grumezescu, A. (2022). Novel Tumor-Targeting Nanoparticles for Cancer Treatment—A Review. *International Journal of Molecular Sciences*, 23(9), 5253. doi: 10.3390/ijms23095253
- OpenStax and Lumen Learning. (2019). *General Psychology* [eBook]. Pressbooks. Retrieved from <https://pressbooks.online.ucf.edu/lumenpsychology/chapter/reading-parts-of-the-brain>
- Saucier-Sawyer, J., Deng, Y., Seo, Y., Cheng, C., Zhang, J., Quijano, E., & Saltzman, W. (2015). Systemic delivery of blood–brain barrier-targeted polymeric nanoparticles enhances delivery to brain tissue. *Journal Of Drug Targeting*, 23(7-8), 736-749. doi: 10.3109/1061186x.2015.1065833

Wang, Y., Pan, Y., & Li, H. (2020). What is brain health and why is it important?. *BMJ*, m3683.

doi: 10.1136/bmj.m3683

Zazo, H., Colino, C., & Lanao, J. (2016). Current applications of nanoparticles in infectious diseases. *Journal Of Controlled Release*, 224, 86-102. doi: 10.1016/j.jconrel.2016.01.00

Zorkina, Y., Abramova, O., Ushakova, V., Morozova, A., Zubkov, E., & Valikhov, M. et al. (2020). Nano Carrier Drug Delivery Systems for the Treatment of Neuropsychiatric Disorders: Advantages and Limitations. *Molecules*, 25(22), 5294. doi: 10.3390/molecules25225294

Braun, A. C., De Mello, C. A., Corassa, M., Abdallah, E. A., Urvanegia, A. C., Alves, V. S., . . . Chinen, L. T. (2018). EGFR expression in circulating tumor cells from high-grade metastatic soft tissue sarcomas. *Cancer Biology & Therapy*, 19(6), 454-460. doi:10.1080/15384047.2018.1433498

Byeon, H. K., Ku, M., & Yang, J. (2019). Beyond EGFR inhibition: Multilateral combat strategies to stop the progression of head and neck cancer. *Experimental & Molecular Medicine*, 51(1), 1-14. doi:10.1038/s12276-018-0202-2

Janani, B., Vijayakumar, M., Priya, K., Kim, J. H., Prabakaran, D. S., Shahid, M., . . . Ramesh, T. (2022). EGFR-based targeted therapy for colorectal cancer—promises and challenges. *Vaccines*, 10(4), 499. doi:10.3390/vaccines10040499

Wang, J., Fang, C., Tzeng, Y., Hsu, H., Lin, S., Yu, M., . . . Liu, H. E. (2018). Prognostic value of localization of epidermal growth factor receptor in lung adenocarcinoma. *Journal of Biomedical Science*, 25(1). doi:10.1186/s12929-018-0451-3

- Xu, H., Zong, H., Ma, C., Ming, X., Shang, M., Li, K., . . . Cao, L. (2017). Epidermal growth factor receptor in glioblastoma. *Oncology Letters*, *14*(1), 512-516. doi:10.3892/ol.2017.6221
- Bayda, S., Adeel, M., Tuccinardi, T., Cordani, M., & Rizzolio, F. (2019). The history of nanoscience and nanotechnology: From chemical–physical applications to nanomedicine. *Molecules*, *25*(1), 112. doi:10.3390/molecules25010112
- Binnig, G., Rohrer, H., Gerber, C., & Weibel, E. (1982). Tunneling through a controllable vacuum gap. *Applied Physics Letters*, *40*(2), 178-180. doi:10.1063/1.92999
- Gagliardi, A., Giuliano, E., Venkateswararao, E., Fresta, M., Bulotta, S., Awasthi, V., & Cosco, D. (2021). Biodegradable polymeric nanoparticles for drug delivery to solid tumors. *Frontiers in Pharmacology*, *12*. doi:10.3389/fphar.2021.601626
- Gnach, A., Lipinski, T., Bednarkiewicz, A., Rybka, J., & Capobianco, J. A. (2015). Upconverting nanoparticles: Assessing the toxicity. *Chemical Society Reviews*, *44*(6), 1561-1584. doi:10.1039/c4cs00177j
- Hulla, J., Sahu, S., & Hayes, A. (2015). Nanotechnology. *Human & Experimental Toxicology*, *34*(12), 1318-1321. doi:10.1177/0960327115603588
- Joudeh, N., & Linke, D. (2022). Nanoparticle classification, Physicochemical Properties, characterization, and applications: A comprehensive review for biologists. *Journal of Nanobiotechnology*, *20*(1). doi:10.1186/s12951-022-01477-8
- Kargozar, S., & Mozafari, M. (2018). Nanotechnology and nanomedicine: Start Small, think big. *Materials Today: Proceedings*, *5*(7), 15492-15500. doi:10.1016/j.matpr.2018.04.155

- Khan, Y., Sadia, H., Ali Shah, S. Z., Khan, M. N., Shah, A. A., Ullah, N., . . . Khan, M. I. (2022). Classification, synthetic, and characterization approaches to nanoparticles, and their applications in various fields of nanotechnology: A Review. *Catalysts*, *12*(11), 1386. doi:10.3390/catal12111386
- Liu, J., He, H., Xiao, D., Yin, S., Ji, W., Jiang, S., . . . Liu, Y. (2018). Recent advances of plasmonic nanoparticles and their applications. *Materials*, *11*(10), 1833. doi:10.3390/ma11101833
- Mulvaney, P. (2015). Nanoscience vs nanotechnology—defining the field. *ACS Nano*, *9*(3), 2215-2217. doi:10.1021/acs.nano.5b01418
- Theodosiou, M., Boukos, N., Sakellis, E., Zachariadis, M., & Efthimiadou, E. K. (2019). Gold nanoparticle decorated pH-sensitive polymeric nanocontainers as a potential theranostic agent. *Colloids and Surfaces B: Biointerfaces*, *183*, 110420. doi:10.1016/j.colsurfb.2019.110420
- Toniolo, G., Efthimiadou, E. K., Kordas, G., & Chatgililoglu, C. (2018). Development of multi-layered and multi-sensitive polymeric nanocontainers for cancer therapy: In vitro evaluation. *Scientific Reports*, *8*(1). doi:10.1038/s41598-018-32890-5
- Wilhelm, S., Tavares, A. J., Dai, Q., Ohta, S., Audet, J., Dvorak, H. F., & Chan, W. C. (2016). Analysis of nanoparticle delivery to tumours. *Nature Reviews Materials*, *1*(5). doi:10.1038/natrevmats.2016.14
- Zhang, Q., Kuang, G., He, S., Lu, H., Cheng, Y., Zhou, D., & Huang, Y. (2020). Photoactivatable prodrug-backboned polymeric nanoparticles for efficient light-controlled gene delivery

- and synergistic treatment of platinum-resistant ovarian cancer. *Nano Letters*, 20(5), 3039-3049. doi:10.1021/acs.nanolett.9b04981
- Zielińska, A., Carreiró, F., Oliveira, A. M., Neves, A., Pires, B., Venkatesh, D. N., . . . Souto, E. B. (2020). Polymeric nanoparticles: Production, characterization, toxicology and ecotoxicology. *Molecules*, 25(16), 3731. doi:10.3390/molecules25163731
- Cho, H., Gao, J., & Kwon, G. S. (2016). Peg- B -pla micelles and PLGA- B -peg- b -plga sol-gels for drug delivery. *Journal of Controlled Release*, 240, 191-201. doi:10.1016/j.jconrel.2015.12.015
- Fan, S., Hao, Y., Zhang, W., Kapasi, A., Shu, Y., Wang, J., & Chen, W. (2020). Poly(Ionic liquid)-gated CuCo₂S₄ for ph-/thermo-triggered drug release and photoacoustic imaging. *ACS Applied Materials & Interfaces*, 12(8), 9000-9007. doi:10.1021/acsami.9b21292
- Feng, H., Chu, D., Yang, F., Li, Z., Fan, B., Jin, L., & Li, J. (2020). Hypoxia-responsive polymeric micelles for enhancing cancer treatment. *Frontiers in Chemistry*, 8. doi:10.3389/fchem.2020.00742
- Feng, R., Chen, Q., Zhou, P., Wang, Y., & Yan, H. (2018). Nanoparticles based on disulfide-containing poly(β -amino ester) and zwitterionic fluorocarbon surfactant as a redox-responsive drug carrier for Brain tumor treatment. *Nanotechnology*, 29(49), 495101. doi:10.1088/1361-6528/aae122
- Knapp, J. P., Kakish, J. E., Bridle, B. W., & Speicher, D. J. (2022). Tumor temperature: Friend or foe of virus-based cancer immunotherapy. *Biomedicines*, 10(8), 2024. doi:10.3390/biomedicines10082024

- Lu, Z., Zhang, Z., & Tang, Y. (2019). Conjugated polymers-based thermal-responsive nanoparticles for controlled drug delivery, tracking, and synergistic photodynamic therapy/chemotherapy. *ACS Applied Bio Materials*, 2(10), 4485-4492. doi:10.1021/acsabm.9b00640
- Mamnoon, B., Feng, L., Froberg, J., Choi, Y., Sathish, V., & Mallik, S. (2020). Hypoxia-responsive, polymeric nanocarriers for targeted drug delivery to estrogen receptor-positive breast cancer cell spheroids. *Molecular Pharmaceutics*, 17(11), 4312-4322. doi:10.1021/acs.molpharmaceut.0c00754
- Ofridam, F., Tarhini, M., Lebaz, N., Gagnière, É, Mangin, D., & Elaissari, A. (2021). Ph -sensitive polymers: Classification and some fine potential applications. *Polymers for Advanced Technologies*, 32(4), 1455-1484. doi:10.1002/pat.5230
- Palanikumar, L., Al-Hosani, S., Kalmouni, M., Nguyen, V. P., Ali, L., Pasricha, R., . . . Magzoub, M. (2020). PH-responsive high stability polymeric nanoparticles for targeted delivery of Anticancer Therapeutics. *Communications Biology*, 3(1). doi:10.1038/s42003-020-0817-4
- Petrova, V., Annicchiarico-Petruzzelli, M., Melino, G., & Amelio, I. (2018). The hypoxic tumour microenvironment. *Oncogenesis*, 7(1). doi:10.1038/s41389-017-0011-9
- Poojari, R., Mohanty, B., Kadwad, V., Suryawanshi, D., Chaudhari, P., Khade, B., . . . Panda, D. (2022). Combinatorial cetuximab targeted polymeric nanocomplexes reduce PRC1 level and abrogate growth of metastatic hepatocellular carcinoma in vivo with efficient radionuclide uptake. *Nanomedicine: Nanotechnology, Biology and Medicine*, 41, 102529. doi:10.1016/j.nano.2022.102529

- Wicki, A., Witzigmann, D., Balasubramanian, V., & Huwyler, J. (2015). Nanomedicine in cancer therapy: Challenges, opportunities, and clinical applications. *Journal of Controlled Release*, 200, 138-157. doi:10.1016/j.jconrel.2014.12.030
- Yoo, J., Park, C., Yi, G., Lee, D., & Koo, H. (2019). Active targeting strategies using biological ligands for Nanoparticle Drug Delivery Systems. *Cancers*, 11(5), 640. doi:10.3390/cancers11050640
- Zhang, X., Han, L., Liu, M., Wang, K., Tao, L., Wan, Q., & Wei, Y. (2017). Recent progress and advances in redox-responsive polymers as controlled delivery nanoplatfoms. *Materials Chemistry Frontiers*, 1(5), 807-822. doi:10.1039/c6qm00135a
- Zhao, G., Long, L., Zhang, L., Peng, M., Cui, T., Wen, X., . . . Che, L. (2017). Smart PH-sensitive nanoassemblies with cleavable pegylation for tumor targeted drug delivery. *Scientific Reports*, 7(1). doi:10.1038/s41598-017-03111-2
- Bhattacharjee, S. (2016). DLS and Zeta potential – what they are and what they are not? *Journal of Controlled Release*, 235, 337-351. doi:10.1016/j.jconrel.2016.06.017
- Brodusch, N., Brahimi, S. V., Barbosa De Melo, E., Song, J., Yue, S., Piché, N., & Gauvin, R. (2021). Scanning electron microscopy versus transmission electron microscopy for material characterization: A comparative study on high-strength steels. *Scanning*, 2021, 1-19. doi:10.1155/2021/5511618
- Hoa, L. T., Chi, N. T., Nguyen, L. H., & Chien, D. M. (2011). Preparation and characterisation of nanoparticles containing ketoprofen and acrylic polymers prepared by emulsion solvent

- evaporation method. *Journal of Experimental Nanoscience*, 7(2), 189-197.
doi:10.1080/17458080.2010.515247
- Hyde, A. M., Zultanski, S. L., Waldman, J. H., Zhong, Y., Shevlin, M., & Peng, F. (2017). General principles and strategies for salting-out informed by the Hofmeister series. *Organic Process Research & Development*, 21(9), 1355-1370. doi:10.1021/acs.oprd.7b00197
- Jana, P., Shyam, M., Singh, S., Jayaprakash, V., & Dev, A. (2021). Biodegradable polymers in drug delivery and oral vaccination. *European Polymer Journal*, 142, 110155. doi:10.1016/j.eurpolymj.2020.110155
- Lammari, N., Louaer, O., Meniai, A. H., & Elaissari, A. (2020). Encapsulation of essential oils via nanoprecipitation process: Overview, progress, challenges and prospects. *Pharmaceutics*, 12(5), 431. doi:10.3390/pharmaceutics12050431
- Main, K. H., Provan, J. I., Haynes, P. J., Wells, G., Hartley, J. A., & Pyne, A. L. (2021). Atomic Force Microscopy—a tool for structural and translational DNA research. *APL Bioengineering*, 5(3), 031504. doi:10.1063/5.0054294
- Pineda-Reyes, A. M., Hernández Delgado, M., Zambrano-Zaragoza, M. D., Leyva-Gómez, G., Mendoza-Muñoz, N., & Quintanar-Guerrero, D. (2021). Implementation of the emulsification-diffusion method by solvent displacement for polystyrene nanoparticles prepared from recycled material. *RSC Advances*, 11(4), 2226-2234. doi:10.1039/d0ra07749f
- Singh, B., Kim, K., & Park, M. (2021). On-demand drug delivery systems using nanofibers. *Nanomaterials*, 11(12), 3411. doi:10.3390/nano11123411

Stetefeld, J., McKenna, S. A., & Patel, T. R. (2016). Dynamic light scattering: A practical guide and applications in biomedical sciences. *Biophysical Reviews*, 8(4), 409-427. doi:10.1007/s12551-016-0218-6

Thermo Fisher Scientific. (2022). Electron microscopy: Tem vs sem: Thermo Fisher Scientific - US. Retrieved January 25, 2023, from <https://www.thermofisher.com/gr/en/home/materials-science/learning-center/applications/sem-tem-difference.html>

Weng, L., & Xie, J. (2015). Smart Electrospun nanofibers for controlled drug release: Recent advances and new perspectives. *Current Pharmaceutical Design*, 21(15), 1944-1959. doi:10.2174/1381612821666150302151959

Yadav, K. S., & Sawant, K. K. (2010). Modified nanoprecipitation method for preparation of cytarabine-loaded plga nanoparticles. *AAPS PharmSciTech*, 11(3), 1456-1465. doi:10.1208/s12249-010-9519-4

Zielińska, A., Carreiró, F., Oliveira, A. M., Neves, A., Pires, B., Venkatesh, D. N., . . . Souto, E. B. (2020). Polymeric nanoparticles: Production, characterization, toxicology and ecotoxicology. *Molecules*, 25(16), 3731. doi:10.3390/molecules25163731

Taha, M., Hassan, M., Essa, S., & Tartor, Y. (2013). Use of fourier transform infrared spectroscopy (FTIR) spectroscopy for rapid and accurate identification of yeasts isolated from human and animals. *International Journal of Veterinary Science and Medicine*, 1(1), 15-20. doi:10.1016/j.ijvsm.2013.03.001

- Chen, B., Bao, W., Liu, R., Wang, Y., Wang, F., Xia, G., . . . Yin, H. (2015). PLGA-PLL-peg-tf-based targeted nanoparticles drug delivery system enhance antitumor efficacy via intrinsic apoptosis pathway. *International Journal of Nanomedicine*, 557. doi:10.2147/ijn.s75090
- Fu, W., You, C., Ma, L., Li, H., Ju, Y., Guo, X., . . . Lin, Y. (2019). Enhanced efficacy of temozolomide loaded by a tetrahedral framework DNA nanoparticle in the therapy for glioblastoma. *ACS Applied Materials & Interfaces*, 11(43), 39525-39533. doi:10.1021/acsami.9b13829
- Kosari, M., Borgna, A., & Zeng, H. C. (2020). Transformation of stöber silica spheres to hollow nanocatalysts. *ChemNanoMat*, 6(6), 889-906. doi:10.1002/cnma.202000147
- Kumar, N., Salar, R. K., Prasad, M., & Ranjan, K. (2018). Synthesis, characterization and anticancer activity of vincristine loaded folic acid-chitosan conjugated nanoparticles on NCI-H460 non-small cell lung cancer cell line. *Egyptian Journal of Basic and Applied Sciences*, 5(1), 87-99. doi:10.1016/j.ejbas.2017.11.002
- Metaxa, A., Efthimiadou, E. K., Boukos, N., & Kordas, G. (2012). Polysaccharides as a source of advanced materials: Cellulose hollow microspheres for drug delivery in cancer therapy. *Journal of Colloid and Interface Science*, 384(1), 198-206. doi:10.1016/j.jcis.2012.04.073
- Salar, R. K., & Kumar, N. (2016). Synthesis and characterization of vincristine loaded folic acid–chitosan conjugated nanoparticles. *Resource-Efficient Technologies*, 2(4), 199-214. doi:10.1016/j.reffit.2016.10.006

- She, X., Chen, L., Li, C., He, C., He, L., & Kong, L. (2015). Functionalization of hollow mesoporous silica nanoparticles for improved 5-Fu loading. *Journal of Nanomaterials*, 2015, 1-9. doi:10.1155/2015/872035
- Sims, K. R., He, B., Koo, H., & Benoit, D. S. (2020). Electrostatic interactions enable nanoparticle delivery of the Flavonoid myricetin. *ACS Omega*, 5(22), 12649-12659. doi:10.1021/acsomega.9b04101
- Sultan, M. H., Moni, S. S., Madkhali, O. A., Bakkari, M. A., Alshahrani, S., Alqahtani, S. S., . . . Alshamrani, M. (2022). Characterization of cisplatin-loaded chitosan nanoparticles and rituximab-linked surfaces as target-specific injectable nano-formulations for combating cancer. *Scientific Reports*, 12(1). doi:10.1038/s41598-021-04427-w
- Toniolo, G., Efthimiadou, E. K., Kordas, G., & Chatgililoglu, C. (2018). Development of multi-layered and multi-sensitive polymeric nanocontainers for cancer therapy: In vitro evaluation. *Scientific Reports*, 8(1). doi:10.1038/s41598-018-32890-5
- Ulbrich, K., Holá, K., Šubr, V., Bakandritsos, A., Tuček, J., & Zbořil, R. (2016). Targeted drug delivery with polymers and magnetic nanoparticles: Covalent and noncovalent approaches, release control, and clinical studies. *Chemical Reviews*, 116(9), 5338-5431. doi:10.1021/acs.chemrev.5b00589
- Xu, H., Yang, D., Cai, C., Gou, J., Zhang, Y., Wang, L., . . . Tang, X. (2015). Dual-responsive MPEG-PLGA-pglu hybrid-core nanoparticles with a high drug loading to reverse the multidrug resistance of breast cancer: An in vitro and in vivo evaluation. *Acta Biomaterialia*, 16, 156-168. doi:10.1016/j.actbio.2015.01.039

- Zahariev, N., Draganova, M., Zagorchev, P., & Pilicheva, B. (2023). Casein-based nanoparticles: A potential tool for the delivery of daunorubicin in acute lymphocytic leukemia. *Pharmaceutics*, 15(2), 471. doi:10.3390/pharmaceutics15020471
- Zhang, Y., Ang, C. Y., Li, M., Tan, S. Y., Qu, Q., Luo, Z., & Zhao, Y. (2015). Polymer-coated hollow mesoporous silica nanoparticles for triple-responsive drug delivery. *ACS Applied Materials & Interfaces*, 7(32), 18179-18187. doi:10.1021/acsami.5b05893
- Zhao, D., Yang, N., Xu, L., Du, J., Yang, Y., & Wang, D. (2021). Hollow Structures as drug carriers: Recognition, response, and release. *Nano Research*, 15(2), 739-757. doi:10.1007/s12274-021-3595-5
- Bobde, Y., Biswas, S., & Ghosh, B. (2020). Pegylated N-(2 hydroxypropyl) methacrylamide-doxorubicin conjugate as ph-responsive polymeric nanoparticles for cancer therapy. *Reactive and Functional Polymers*, 151, 104561. doi:10.1016/j.reactfunctpolym.2020.104561
- Calzoni, E., Cesaretti, A., Polchi, A., Di Michele, A., Tancini, B., & Emiliani, C. (2019). Biocompatible polymer nanoparticles for drug delivery applications in cancer and Neurodegenerative Disorder therapies. *Journal of Functional Biomaterials*, 10(1), 4. doi:10.3390/jfb10010004
- Gad, A., Kydd, J., Piel, B., & Rai, P. (2016). Targeting cancer using polymeric nanoparticle mediated combination chemotherapy. *International Journal of Nanomedicine and Nanosurgery*, 2(3). doi:10.16966/2470-3206.116

- Ghaeini-Hesaroeiye, S., Razmi Bagtash, H., Boddohi, S., Vasheghani-Farahani, E., & Jabbari, E. (2020). Thermoresponsive nanogels based on different polymeric moieties for biomedical applications. *Gels*, *6*(3), 20. doi:10.3390/gels6030020
- Qi, P., Bu, Y., Xu, J., Qin, B., Luan, S., & Song, S. (2016). PH-responsive release of paclitaxel from hydrazone-containing biodegradable micelles. *Colloid and Polymer Science*, *295*(1), 1-12. doi:10.1007/s00396-016-3968-6
- Xu, H., Yang, D., Cai, C., Gou, J., Zhang, Y., Wang, L., . . . Tang, X. (2015). Dual-responsive MPEG-PLGA-pglu hybrid-core nanoparticles with a high drug loading to reverse the multidrug resistance of breast cancer: An in vitro and in vivo evaluation. *Acta Biomaterialia*, *16*, 156-168. doi:10.1016/j.actbio.2015.01.039
- Zou, Y., Zhou, Y., Jin, Y., He, C., Deng, Y., Han, S., . . . Liu, Y. (2018). Synergistically enhanced antimetastasis effects by honokiol-loaded ph-sensitive polymer–doxorubicin conjugate micelles. *ACS Applied Materials & Interfaces*, *10*(22), 18585-18600. doi:10.1021/acsami.8b04854
- Jafari, N., Karimi, L., Mirjalili, M., & Derakhshan, S. J. (2016). Effect of silver particle size on color and antibacterial properties of silk and cotton fabrics. *Fibers and Polymers*, *17*(6), 888-895. doi:10.1007/s12221-016-6052-4
- Khan, T., Ullah, N., Khan, M. A., Mashwani, Z., & Nadhman, A. (2019). Plant-based gold nanoparticles; a comprehensive review of the decade-long research on synthesis, mechanistic aspects and diverse applications. *Advances in Colloid and Interface Science*, *272*, 102017. doi:10.1016/j.cis.2019.102017

- Palanikumar, L., Al-Hosani, S., Kalmouni, M., Nguyen, V. P., Ali, L., Pasricha, R., . . . Magzoub, M. (2020). PH-responsive high stability polymeric nanoparticles for targeted delivery of Anticancer Therapeutics. *Communications Biology*, 3(1). doi:10.1038/s42003-020-0817-4
- Nishchaya, K., Rai, V. K., & Bansode, H. (2023). Methacrylic acid as a potential monomer for molecular imprinting: A review of recent advances. *Results in Materials*, 18, 100379. doi:10.1016/j.rinma.2023.100379
- Socrates, G. (2001). *Infrared and Raman characteristic group frequencies: Tables and Charts*. Chichester, West Sussex: John Wiley & Sons.
- Farooqi, Z. H., Khan, H. U., Shah, S. M., & Siddiq, M. (2017). Stability of poly(n-isopropylacrylamide-co-acrylic acid) polymer microgels under various conditions of temperature, ph and salt concentration. *Arabian Journal of Chemistry*, 10(3), 329-335. doi:10.1016/j.arabjc.2013.07.031
- Stöber, W., Fink, A., & Bohn, E. (1968). Controlled growth of monodisperse silica spheres in the Micron Size Range. *Journal of Colloid and Interface Science*, 26(1), 62-69. doi:10.1016/0021-9797(68)90272-5
- Grau-Carbonell, A., Sadighikia, S., Welling, T. A., Van Dijk-Moes, R. J., Kotni, R., Bransen, M., . . . Van Huis, M. A. (2021). *In situ* study of the wet chemical etching of sio₂ and nanoparticle@sio₂ core-shell nanospheres. *ACS Applied Nano Materials*, 4(2), 1136-1148. doi:10.1021/acsanm.0c02771

- Crucho, C. I., & Barros, M. T. (2017). Polymeric nanoparticles: A study on the preparation variables and characterization methods. *Materials Science and Engineering: C*, *80*, 771-784. doi:10.1016/j.msec.2017.06.004
- Al Bostami, R. D., Abuwatfa, W. H., & Hussein, G. A. (2022). Recent advances in nanoparticle-based co-delivery systems for cancer therapy. *Nanomaterials*, *12*(15), 2672. doi:10.3390/nano12152672
- Al-Aamri, H. M., Ku, H., Irving, H. R., Tucci, J., Meehan-Andrews, T., & Bradley, C. (2019). Time dependent response of daunorubicin on cytotoxicity, cell cycle and DNA repair in Acute lymphoblastic leukaemia. *BMC Cancer*, *19*(1). doi:10.1186/s12885-019-5377-y
- Albini, S., Coutinho Toto, P., Dall'Agnese, A., Malecova, B., Cenciarelli, C., Felsani, A., . . . Puri, P. L. (2015). Brahma is required for cell cycle arrest and late muscle gene expression during skeletal myogenesis. *EMBO Reports*, *16*(8), 1037-1050. doi:10.15252/embr.201540159
- Albright, J. T., Topham, A. K., & Reilly, J. S. (2002). Pediatric head and neck malignancies. *Archives of Otolaryngology–Head & Neck Surgery*, *128*(6), 655. doi:10.1001/archotol.128.6.655
- Alimbetov, D., Askarova, S., Umbayev, B., Davis, T., & Kipling, D. (2018). Pharmacological targeting of cell cycle, apoptotic and cell adhesion signaling pathways implicated in chemoresistance of cancer cells. *International Journal of Molecular Sciences*, *19*(6), 1690. doi:10.3390/ijms19061690

American Cancer Society. (2019). How Chemotherapy Drugs Work. Retrieved March 5, 2023, from <https://www.cancer.org/treatment/treatments-and-side-effects/treatment-types/chemotherapy/how-chemotherapy-drugs-work.html>

American Cancer Society. (2020). Rhabdomyosarcoma stages and risk groups. Retrieved October 15, 2022, from <https://www.cancer.org/cancer/rhabdomyosarcoma/detection-diagnosis-staging/staging.html>

An, J., Huang, Y., Xu, Q., Zhou, L., Shang, Z., Huang, B., . . . Zhou, P. (2010). DNA-pkcs plays a dominant role in the regulation of H2AX phosphorylation in response to DNA damage and cell cycle progression. *BMC Molecular Biology*, *11*(1). doi:10.1186/1471-2199-11-18

Arboleda, L. P., De Mendonça, R. M., Lopez, E. E., Araújo, A. L., Palmier, N. R., De Pauli Paglioni, M., . . . Santos-Silva, A. R. (2020). Global frequency and distribution of head and neck cancer in Pediatrics, a systematic review. *Critical Reviews in Oncology/Hematology*, *148*, 102892. doi:10.1016/j.critrevonc.2020.102892

Arboleda, L. P., Hoffmann, I. L., Cardinali, I. A., Santos-Silva, A. R., & De Mendonça, R. M. (2018). Demographic and clinicopathologic distribution of head and neck malignant tumors in pediatric patients from a Brazilian population: A retrospective study. *Journal of Oral Pathology & Medicine*, *47*(7), 696-705. doi:10.1111/jop.12724

Azatyán, A., Gallo-Oller, G., Diao, Y., Selivanova, G., Johnsen, J. I., & Zaphiropoulos, P. G. (2019). RITA downregulates hedgehog-gli in medulloblastoma and rhabdomyosarcoma via JNK-dependent but p53-independent mechanism. *Cancer Letters*, *442*, 341-350. doi:10.1016/j.canlet.2018.11.005

- Bisogno, G., Fuchs, J., Dasgupta, R., Ferrari, A., Haduong, J. H., Rogers, T., . . . Venkatramani, R. (2022). Patients with completely resected nongenitourinary low-risk embryonal rhabdomyosarcoma are candidates for reduced duration low-intensity chemotherapy. *Cancer*, *128*(23), 4150-4156. doi:10.1002/cncr.34497
- Blackburn, C., Tai, H., Salerno, M., Wang, X., Hartsuiker, E., & Wang, W. (2019). Folic acid and rhodamine labelled ph responsive hyperbranched polymers: Synthesis, characterization and cell uptake studies. *European Polymer Journal*, *120*, 109259. doi:10.1016/j.eurpolymj.2019.109259
- Boltnarova, B., Kubackova, J., Skoda, J., Stefela, A., Smekalova, M., Svacinova, P., . . . Holas, O. (2021). PLGA based nanospheres as a potent macrophage-specific drug delivery system. *Nanomaterials*, *11*(3), 749. doi:10.3390/nano11030749
- Butler, E., Ludwig, K., Pacenti, H. L., Klesse, L. J., Watt, T. C., & Laetsch, T. W. (2021). Recent progress in the treatment of cancer in children. *CA: A Cancer Journal for Clinicians*, *71*(4), 315-332. doi:10.3322/caac.21665
- Casey, D., & Wolden, S. (2018). Rhabdomyosarcoma of the head and neck: A multimodal approach. *Journal of Neurological Surgery Part B: Skull Base*, *79*(01), 058-064. doi:10.1055/s-0037-1617450
- Chen, C., Dorado Garcia, H., Scheer, M., & Henssen, A. G. (2019). Current and future treatment strategies for rhabdomyosarcoma. *Frontiers in Oncology*, *9*. doi:10.3389/fonc.2019.01458

Chen, E., Ricciotti, R., Futran, N., & Oda, D. (2016). Head and neck rhabdomyosarcoma: Clinical and pathologic characterization of seven cases. *Head and Neck Pathology*, 11(3), 321-326. doi:10.1007/s12105-016-0771-0

Cheng, Q., Shi, H., Huang, H., Cao, Z., Wang, J., & Liu, Y. (2015). Oral delivery of a platinum anticancer drug using lipid assisted polymeric nanoparticles. *Chemical Communications*, 51(99), 17536-17539. doi:10.1039/c5cc07853a

Copyright © 2015 McGraw-Hill Education. (2015). The cavities within the head [Digital image]. Retrieved December 11, 2022, from <https://slideplayer.com/slide/9057423/>

D'Amora, M., Colucci, P., Usai, A., Landi, E., Deleye, L., Dente, L., . . . Tantussi, F. (2020). Heat-sensitive poly-acrylamide nanoparticle for cancer treatment. *Precision Nanomedicine*, 3(4). doi:10.33218/001c.17629

Darwish, C., Shim, T., Sparks, A. D., Chillakuru, Y., Strum, D., Benito, D. A., & Monfared, A. (2020). Pediatric head and neck rhabdomyosarcoma: An analysis of treatment and survival in the United States (1975–2016). *International Journal of Pediatric Otorhinolaryngology*, 139, 110403. doi:10.1016/j.ijporl.2020.110403

Dasgupta, R., Fuchs, J., & Rodeberg, D. (2016). Rhabdomyosarcoma. *Seminars in Pediatric Surgery*, 25(5), 276-283. doi:10.1053/j.sempedsurg.2016.09.011

De Lima, J. M., Bonan, P. R., Da Cruz Perez, D. E., Hier, M., Alaoui-Jamali, M. A., & Da Silva, S. D. (2020). Nanoparticle-based chemotherapy formulations for head and neck cancer: A systematic review and Perspectives. *Nanomaterials*, 10(10), 1938. doi:10.3390/nano10101938

- Dhyani, P., Quispe, C., Sharma, E., Bahukhandi, A., Sati, P., Attri, D. C., . . . Cho, W. C. (2022). Anticancer potential of alkaloids: A key emphasis to colchicine, vinblastine, vincristine, Vindesine, Vinorelbine and Vincamine. *Cancer Cell International*, 22(1). doi:10.1186/s12935-022-02624-9
- Dobersch, S., Rubio, K., Singh, I., Günther, S., Graumann, J., Cordero, J., . . . Barreto, G. (2021). Positioning of nucleosomes containing γ -H2AX precedes active DNA demethylation and transcription initiation. *Nature Communications*, 12(1). doi:10.1038/s41467-021-21227-y
- Dombrowski, N. D., Wolter, N. E., Robson, C. D., Kawai, K., Irace, A. L., Vargas, S. O., . . . Rahbar, R. (2020). Role of surgery in rhabdomyosarcoma of the head and neck in children. *The Laryngoscope*, 131(3). doi:10.1002/lary.28785
- Drummond, C. J., Hanna, J. A., Garcia, M. R., Devine, D. J., Heyrana, A. J., Finkelstein, D., . . . Hatley, M. E. (2018). Hedgehog pathway drives fusion-negative rhabdomyosarcoma initiated from non-myogenic endothelial progenitors. *Cancer Cell*, 33(1). doi:10.1016/j.ccell.2017.12.001
- Duwa, R., Banstola, A., Emami, F., Jeong, J., Lee, S., & Yook, S. (2020). Cetuximab conjugated temozolomide-loaded poly (lactic-co-glycolic acid) nanoparticles for targeted nanomedicine in EGFR overexpressing cancer cells. *Journal of Drug Delivery Science and Technology*, 60, 101928. doi:10.1016/j.jddst.2020.101928
- Fisusi, F. A., & Akala, E. O. (2019). Drug combinations in breast cancer therapy. *Pharmaceutical Nanotechnology*, 7(1), 3-23. doi:10.2174/2211738507666190122111224

- Fortuni, B., Inose, T., Ricci, M., Fujita, Y., Van Zundert, I., Masuhara, A., . . . Uji-i, H. (2019). Polymeric engineering of nanoparticles for highly efficient multifunctional drug delivery systems. *Scientific Reports*, *9*(1). doi:10.1038/s41598-019-39107-3
- Frankart, A. J., Breneman, J. C., & Pater, L. E. (2021). Radiation therapy in the treatment of head and neck rhabdomyosarcoma. *Cancers*, *13*(14), 3567. doi:10.3390/cancers13143567
- Gallego Melcón, S., & Sánchez de Toledo Codina, J. (2007). Molecular biology of rhabdomyosarcoma. *Clinical and Translational Oncology*, *9*(7), 415-419. doi:10.1007/s12094-007-0079-3
- Ghasemi, M., Turnbull, T., Sebastian, S., & Kempson, I. (2021). The MTT assay: Utility, Limitations, pitfalls, and interpretation in bulk and single-cell analysis. *International Journal of Molecular Sciences*, *22*(23), 12827. doi:10.3390/ijms222312827
- GOBIN, C. M., MENEFE, J. N., LATTIMORE, C. C., DOTY, A., & FREDENBURG, K. M. (2022). Cell dissociation enzymes affect annexin V/flow-cytometric apoptotic assay outcomes after MIRNA-based transient transfection. *Anticancer Research*, *42*(6), 2819-2825. doi:10.21873/anticancer.15763
- Gosepath, J., Spix, C., Talebloo, B., Blettner, M., & Mann, W. (2007). Incidence of childhood cancer of the head and neck in Germany. *Annals of Oncology*, *18*(10), 1716-1721. doi:10.1093/annonc/mdm278
- Grass, B., Wachtel, M., Behnke, S., Leuschner, I., Niggli, F. K., & Schäfer, B. W. (2009). Immunohistochemical detection of EGFR, fibrillin-2, P-cadherin and AP2 β as biomarkers

for rhabdomyosarcoma diagnostics. *Histopathology*, 54(7), 873-879.
doi:10.1111/j.1365-2559.2009.03303.x

Grusso, T., Mieulet, V., Cardon, M., Bourachot, B., Kieffer, Y., Devun, F., . . . Mechta-Grigoriou, F. (2016). Chronic oxidative stress promotes H2axprotein degradation and enhances chemosensitivity in breast cancer patients. *EMBO Molecular Medicine*, 8(5), 527-549.
doi:10.15252/emmm.201505891

Gusho, C. A., Blank, A. T., & Batus, M. (2021). Outcomes of brain metastasis in high-grade bone and soft tissue sarcoma: An analysis of clinicopathological characteristics and Survival Data. *Rare Tumors*, 13, 203636132110261. doi:10.1177/20363613211026151

Hinson, A. R., Jones, R., Crose, L. E., Belyea, B. C., Barr, F. G., & Linardic, C. M. (2013). Human rhabdomyosarcoma cell lines for rhabdomyosarcoma research: Utility and pitfalls. *Frontiers in Oncology*, 3. doi:10.3389/fonc.2013.00183

Huang, C., Sun, Y., Shen, M., Zhang, X., Gao, P., & Duan, Y. (2016). Altered cell cycle arrest by multifunctional drug-loaded enzymatically-triggered nanoparticles. *ACS Applied Materials & Interfaces*, 8(2), 1360-1370. doi:10.1021/acsami.5b10241

Jeffery, N. N., Davidson, C., Peslak, S. A., Kingsley, P. D., Nakamura, Y., Palis, J., & Bulger, M. (2021). Histone h2a.x phosphorylation and caspase-initiated chromatin condensation in late-stage erythropoiesis. *Epigenetics & Chromatin*, 14(1). doi:10.1186/s13072-021-00408-5

Ji, J., Zhang, Y., Redon, C. E., Reinhold, W. C., Chen, A. P., Fogli, L. K., . . . Bonner, W. M. (2017). Phosphorylated fraction of H2AX as a measurement for DNA damage in cancer cells and

potential applications of a novel assay. *PLOS ONE*, 12(2).
doi:10.1371/journal.pone.0171582

Katsuta E, Sawant Dessai A, Ebos JM, Yan L, Ouchi T, Takabe K. H2AX mRNA expression reflects DNA repair, cell proliferation, metastasis, and worse survival in breast cancer. *Am J Cancer Res*. 2022;12:793–804.

Kawashima, S., Kawaguchi, N., Taniguchi, K., Tashiro, K., Komura, K., Tanaka, T., . . . Uchiyama, K. (2020). γ -H2AX as a potential indicator of radiosensitivity in colorectal cancer cells. *Oncology Letters*, 20(3), 2331-2337. doi:10.3892/ol.2020.11788

Kucuksayan, E., Bozkurt, F., Yilmaz, M. T., Sircan-Kucuksayan, A., Hanikoglu, A., & Ozben, T. (2021). A new combination strategy to enhance apoptosis in cancer cells by using nanoparticles as biocompatible drug delivery carriers. *Scientific Reports*, 11(1). doi:10.1038/s41598-021-92447-x

Kudarha, R. R., & Sawant, K. K. (2021). Hyaluronic acid conjugated albumin nanoparticles for efficient receptor mediated brain targeted delivery of temozolomide. *Journal of Drug Delivery Science and Technology*, 61, 102129. doi:10.1016/j.jddst.2020.102129

Laubscher, D., Gryder, B. E., Sunkel, B. D., Andresson, T., Wachtel, M., Das, S., . . . Khan, J. (2021). BAF complexes drive proliferation and block myogenic differentiation in fusion-positive rhabdomyosarcoma. *Nature Communications*, 12(1). doi:10.1038/s41467-021-27176-w

Laubscher, D., Gryder, B. E., Sunkel, B. D., Andresson, T., Wachtel, M., Das, S., . . . Khan, J. (2021). BAF complexes drive proliferation and block myogenic differentiation in fusion-

positive rhabdomyosarcoma. *Nature Communications*, 12(1). doi:10.1038/s41467-021-27176-w

Levi, S., Zini, A., Fischman, S., & Czerninski, R. (2017). Epidemiology of oral, salivary gland and pharyngeal cancer in children and adolescents between 1970 and 2011. *Oral Oncology*, 67, 89-94. doi:10.1016/j.oraloncology.2017.02.010

Lian, X., Bond, J. S., Bharathy, N., Boudko, S. P., Pokidysheva, E., Shern, J. F., . . . Keller, C. (2021). Defining the extracellular matrix of Rhabdomyosarcoma. *Frontiers in Oncology*, 11. doi:10.3389/fonc.2021.601957

Liu, C., Li, D., Jiang, J., Hu, J., Zhang, W., Chen, Y., . . . Li, F. (2014). Analysis of molecular cytogenetic alteration in rhabdomyosarcoma by array comparative genomic hybridization. *PLoS ONE*, 9(4). doi:10.1371/journal.pone.0094924

Liu, C., Li, D., Jiang, J., Hu, J., Zhang, W., Chen, Y., . . . Li, F. (2014). Analysis of molecular cytogenetic alteration in rhabdomyosarcoma by array comparative genomic hybridization. *PLoS ONE*, 9(4). doi:10.1371/journal.pone.0094924

Lucas, J. T., & Pappo, A. S. (2019). Optimal dosing of cyclophosphamide in rhabdomyosarcoma: It's complicated. *Cancer*, 125(18), 3107-3110. doi:10.1002/cncr.32205

Lychou, S. E., Gustafsson, G. G., & Ljungman, G. E. (2015). Higher rates of metastatic disease may explain the declining trend in Swedish paediatric rhabdomyosarcoma survival rates. *Acta Paediatrica*, 105(1), 74-81. doi:10.1111/apa.13172

Maciel, E., Neves, B. M., Santinha, D., Reis, A., Domingues, P., Teresa Cruz, M., . . . Domingues, M. R. (2014). Detection of phosphatidylserine with a modified Polar Head Group in

human keratinocytes exposed to the radical generator aaph. *Archives of Biochemistry and Biophysics*, 548, 38-45. doi:10.1016/j.abb.2014.02.002

Makimoto, A. (2022). Optimizing rhabdomyosarcoma treatment in adolescents and young adults. *Cancers*, 14(9), 2270. doi:10.3390/cancers14092270

Martin-Giacalone, B. A., Weinstein, P. A., Plon, S. E., & Lupo, P. J. (2021). Pediatric rhabdomyosarcoma: Epidemiology and genetic susceptibility. *Journal of Clinical Medicine*, 10(9), 2028. doi:10.3390/jcm10092028

Martin-Giacalone, B. A., Weinstein, P. A., Plon, S. E., & Lupo, P. J. (2021). Pediatric rhabdomyosarcoma: Epidemiology and genetic susceptibility. *Journal of Clinical Medicine*, 10(9), 2028. doi:10.3390/jcm10092028

Mascarenhas, L., Lyden, E. R., Breitfeld, P. P., Walterhouse, D. O., Donaldson, S. S., Rodeberg, D. A., . . . Hawkins, D. S. (2019). Risk-based treatment for patients with first relapse or progression of Rhabdomyosarcoma: A report from the Children's Oncology Group. *Cancer*. doi:10.1002/cncr.32122

Maurya, A., Singh, A. K., Mishra, G., Kumari, K., Rai, A., Sharma, B., . . . Awasthi, R. (2019). Strategic use of nanotechnology in drug targeting and its consequences on human health: A focused review. *Interventional Medicine and Applied Science*, 11(1), 38-54. doi:10.1556/1646.11.2019.04

Meza, J. L., Anderson, J., Pappo, A. S., & Meyer, W. H. (2006). Analysis of prognostic factors in patients with nonmetastatic rhabdomyosarcoma treated on Intergroup

- Rhabdomyosarcoma Studies III and IV: The Children's Oncology Group. *Journal of Clinical Oncology*, 24(24), 3844-3851. doi:10.1200/jco.2005.05.3801
- Mills, C. C., Kolb, E., & Sampson, V. B. (2018). Development of chemotherapy with cell-cycle inhibitors for adult and pediatric cancer therapy. *Cancer Research*, 78(2), 320-325. doi:10.1158/0008-5472.can-17-2782
- Mohan, R., & Grosshans, D. (2017). Proton therapy – present and future. *Advanced Drug Delivery Reviews*, 109, 26-44. doi:10.1016/j.addr.2016.11.006
- Moreira, D. C., Macy, M. E., Cost, C. R., Greffe, B. S., & Garrington, T. P. (2019). Central Nervous System involvement of rhabdomyosarcoma: A single institution experience. *Journal of Pediatric Hematology/Oncology*, 41(2), 152-154. doi:10.1097/mp.0000000000001166
- Moreira, D. C., Macy, M. E., Cost, C. R., Greffe, B. S., & Garrington, T. P. (2019). Central Nervous System involvement of rhabdomyosarcoma: A single institution experience. *Journal of Pediatric Hematology/Oncology*, 41(2), 152-154. doi:10.1097/mp.0000000000001166
- Moshe Halamish, H., Zlotver, I., & Sosnik, A. (2022). Polymeric nanoparticles surface-complexed with boric acid actively target solid tumors overexpressing sialic acid. *Journal of Colloid and Interface Science*, 626, 916-929. doi:10.1016/j.jcis.2022.07.027
- National Cancer Institute. (2022). Childhood rhabdomyosarcoma treatment (PDQ®)—health professional version. Retrieved November 17, 2022, from https://www.cancer.gov/types/soft-tissue-sarcoma/hp/rhabdomyosarcoma-treatment-pdq#_133_toc

National Cancer Institute. (2023). Types of chemotherapy drugs. Retrieved March 6, 2023, from <https://training.seer.cancer.gov/treatment/chemotherapy/types.html>

Ngum, N. M., Aziz, M. Y., Mohammed Latif, L., Wall, R. J., Duce, I. R., & Mellor, I. R. (2022). Non-canonical endogenous expression of voltage-gated sodium channel α_1 1.7 subtype by the TE671 rhabdomyosarcoma cell line. *The Journal of Physiology*, *600*(10), 2499-2513. doi:10.1113/jp283055

Palanikumar, L., Al-Hosani, S., Kalmouni, M., Nguyen, V. P., Ali, L., Pasricha, R., . . . Magzoub, M. (2020). PH-responsive high stability polymeric nanoparticles for targeted delivery of Anticancer Therapeutics. *Communications Biology*, *3*(1). doi:10.1038/s42003-020-0817-4

Pfister, S. M., Reyes-Múgica, M., Chan, J. K., Hasle, H., Lazar, A. J., Rossi, S., . . . Alaggio, R. (2021). A summary of the inaugural WHO classification of pediatric tumors: Transitioning from the optical into the molecular era. *Cancer Discovery*, *12*(2), 331-355. doi:10.1158/2159-8290.cd-21-1094

Podhorecka, M., Skladanowski, A., & Bozko, P. (2010). H2AX phosphorylation: Its role in DNA damage response and cancer therapy. *Journal of Nucleic Acids*, *2010*, 1-9. doi:10.4061/2010/920161

Pokhriyal, R., Hariprasad, R., Kumar, L., & Hariprasad, G. (2019). Chemotherapy resistance in advanced ovarian cancer patients. *Biomarkers in Cancer*, *11*. doi:10.1177/1179299x19860815

- Radzikowska, J., Kukwa, W., Kukwa, A., Czarnecka, A. M., Kawecki, M., Lian, F., . . . Krzeski, A. (2016). Management of Pediatric Head and neck rhabdomyosarcoma: A case-series of 36 patients. *Oncology Letters*, *12*(5), 3555-3562. doi:10.3892/ol.2016.5072
- Rahman, M., Khan, J. A., Kanwal, U., Awan, U. A., & Raza, A. (2021). Methotrexate-loaded pegylated gold nanoparticles as hemocompatible and ph-responsive anticancer drug nanoconjugate. *Journal of Nanoparticle Research*, *23*(8). doi:10.1007/s11051-021-05296-0
- Rhee, D. S., Rodeberg, D. A., Baertschiger, R. M., Aldrink, J. H., Lautz, T. B., Grant, C., . . . Dasgupta, R. (2020). Update on pediatric Rhabdomyosarcoma: A report from the APSA Cancer Committee. *Journal of Pediatric Surgery*, *55*(10), 1987-1995. doi:10.1016/j.jpedsurg.2020.06.015
- Rudzinski, E. R., Anderson, J. R., Chi, Y., Gastier-Foster, J. M., Astbury, C., Barr, F. G., . . . Parham, D. M. (2017). Histology, fusion status, and outcome in metastatic rhabdomyosarcoma: A report from the Children's Oncology Group. *Pediatric Blood & Cancer*, *64*(12). doi:10.1002/pbc.26645
- Rudzinski, E. R., Anderson, J. R., Hawkins, D. S., Skapek, S. X., Parham, D. M., & Teot, L. A. (2015). The World Health Organization classification of skeletal muscle tumors in pediatric rhabdomyosarcoma: A report from the Children's Oncology Group. *Archives of Pathology & Laboratory Medicine*, *139*(10), 1281-1287. doi:10.5858/arpa.2014-0475-oa
- Sen', V. D., Balakina, A. A., Stupina, T. S., Mumyatova, V. A., Kulikov, A. V., Tikhonov, I. V., . . . Pliss, E. M. (2021). Amphiphilic Chitosan–polyaminoxyls loaded with daunorubicin:

- Synthesis, antioxidant activity, and drug delivery capacity. *International Journal of Biological Macromolecules*, 193, 965-979. doi:10.1016/j.ijbiomac.2021.10.170
- Shern, J. F., Chen, L., Chmielecki, J., Wei, J. S., Patidar, R., Rosenberg, M., . . . Khan, J. (2014). Comprehensive genomic analysis of rhabdomyosarcoma reveals a landscape of alterations affecting a common genetic axis in fusion-positive and fusion-negative tumors. *Cancer Discovery*, 4(2), 216-231. doi:10.1158/2159-8290.cd-13-0639
- Simon, J. H., Paulino, A. C., Smith, R. B., & Buatti, J. M. (2002). Prognostic factors in head and neck rhabdomyosarcoma. *Head & Neck*, 24(5), 468-473. doi:10.1002/hed.10070
- Skolnik, J., Hall, D., Barkauskas, D. A., Moorthy, G., Larson, T. R., Fox, E., . . . Reid, J. M. (2021). Toxicity and pharmacokinetics of actinomycin-D and vincristine in children and adolescents: Children's Oncology Group Study ADVL06B1. *Cancer Chemotherapy and Pharmacology*, 88(2), 359-365. doi:10.1007/s00280-021-04295-1
- Smith, M. A., Reynolds, C. P., Kang, M. H., Kolb, E. A., Gorlick, R., Carol, H., . . . Houghton, P. J. (2015). Synergistic activity of PARP inhibition by Talazoparib (BMN 673) with temozolomide in pediatric cancer models in the Pediatric Preclinical Testing Program. *Clinical Cancer Research*, 21(4), 819-832. doi:10.1158/1078-0432.ccr-14-2572
- Sun, X., Guo, W., Shen, J. K., Mankin, H. J., Hornicek, F. J., & Duan, Z. (2015). Rhabdomyosarcoma: Advances in molecular and Cellular Biology. *Sarcoma*, 2015, 1-14. doi:10.1155/2015/232010

- Sun, X., Guo, W., Shen, J. K., Mankin, H. J., Hornicek, F. J., & Duan, Z. (2015). Rhabdomyosarcoma: Advances in molecular and Cellular Biology. *Sarcoma*, 2015, 1-14. doi:10.1155/2015/232010
- Sun, Y., Liu, Y., Ma, X., & Hu, H. (2021). The influence of Cell Cycle Regulation on chemotherapy. *International Journal of Molecular Sciences*, 22(13), 6923. doi:10.3390/ijms22136923
- Sun, Y., Liu, Y., Ma, X., & Hu, H. (2021). The influence of Cell Cycle Regulation on chemotherapy. *International Journal of Molecular Sciences*, 22(13), 6923. doi:10.3390/ijms22136923
- Tan, E. P., Duncan, F. E., & Slawson, C. (2017). The sweet side of the cell cycle. *Biochemical Society Transactions*, 45(2), 313-322. doi:10.1042/bst20160145
- Terese Winslow LLC, Miami Cancer Institute. (2022). Head and Neck Cancer Regions [Digital image]. Retrieved December 11, 2022, from <https://cancer.baptisthealth.net/miami-cancer-institute/cancer-care/adult-cancers/head-and-neck-cancers/nasal-cavity-and-paranasal-sinus-cancer>
- Van Ewijk, R., Schoot, R. A., Sparber-Sauer, M., Ter Horst, S. A., Jehanno, N., Borgwardt, L., . . . Tolboom, N. (2021). European guideline for Imaging in Paediatric and adolescent rhabdomyosarcoma — joint statement by the European Paediatric Soft Tissue Sarcoma study group, the cooperative Weichteilsarkom Studiengruppe and the Oncology Task Force of the European Society of Paediatric Radiology. *Pediatric Radiology*, 51(10), 1940-1951. doi:10.1007/s00247-021-05081-0

- Vatan, Ö. (2022). Evaluation of in vitro cytotoxic, genotoxic, apoptotic, and cell cycle arrest potential of iron–nickel alloy nanoparticles. *Toxics*, 10(9), 492. doi:10.3390/toxics10090492
- Wachtel, M., Runge, T., Leuschner, I., Stegmaier, S., Koscielniak, E., Treuner, J., . . . Schäfer, B. W. (2006). Subtype and prognostic classification of rhabdomyosarcoma by Immunohistochemistry. *Journal of Clinical Oncology*, 24(5), 816-822. doi:10.1200/jco.2005.03.4934
- Wang, L., Hensch, N. R., Bondra, K., Sreenivas, P., Zhao, X. R., Chen, J., . . . Ignatius, M. S. (2021). Snai2-mediated repression of *bim* protects rhabdomyosarcoma from ionizing radiation. *Cancer Research*, 81(21), 5451-5463. doi:10.1158/0008-5472.can-20-4191
- Wang, X., Feng, J., Li, Z., Zhang, X., Chen, J., & Feng, G. (2020). Characteristics and prognosis of embryonal rhabdomyosarcoma in children and adolescents: An analysis of 464 cases from the seer database. *Pediatric Investigation*, 4(4), 242-249. doi:10.1002/ped4.12220
- Wolden, S. L., Lyden, E. R., Arndt, C. A., Hawkins, D. S., Anderson, J. R., Rodeberg, D. A., Donaldson, S. S. (2015). Local control for intermediate-risk rhabdomyosarcoma: Results from D9803 according to histology, group, site, and size: A report from the Children's Oncology Group. *International Journal of Radiation Oncology*Biography*Physics*, 93(5), 1071-1076. doi:10.1016/j.ijrobp.2015.08.040
- Wong, N., Kim, D., Robinson, Z., Huang, C., & Conboy, I. M. (2021). K-means quantization for a web-based open-source flow cytometry analysis platform. *Scientific Reports*, 11(1). doi:10.1038/s41598-021-86015-6

- Wu, W., Chen, M., Luo, T., Fan, Y., Zhang, J., Zhang, Y., . . . Xia, X. (2020). Ros and GSH-responsive S-nitrosoglutathione functionalized polymeric nanoparticles to overcome multidrug resistance in cancer. *Acta Biomaterialia*, *103*, 259-271. doi:10.1016/j.actbio.2019.12.016
- Xiao, B., Han, M. K., Viennois, E., Wang, L., Zhang, M., Si, X., & Merlin, D. (2015). Hyaluronic acid-functionalized polymeric nanoparticles for colon cancer-targeted combination chemotherapy. *Nanoscale*, *7*(42), 17745-17755. doi:10.1039/c5nr04831a
- Yang, H., Villani, R. M., Wang, H., Simpson, M. J., Roberts, M. S., Tang, M., & Liang, X. (2018). The role of cellular reactive oxygen species in cancer chemotherapy. *Journal of Experimental & Clinical Cancer Research*, *37*(1). doi:10.1186/s13046-018-0909-x
- Yohe, M. E., Heske, C. M., Stewart, E., Adamson, P. C., Ahmed, N., Antonescu, C. R., . . . Langenau, D. M. (2019). Insights into pediatric rhabdomyosarcoma research: Challenges and goals. *Pediatric Blood & Cancer*, *66*(10). doi:10.1002/pbc.27869
- Zaritski, A., Castillo-Ecija, H., Kumarasamy, M., Peled, E., Sverdlov Arzi, R., Carcaboso, Á M., & Sosnik, A. (2019). Selective accumulation of Galactomannan amphiphilic nanomaterials in pediatric solid tumor xenografts correlates with *glut1* gene expression. *ACS Applied Materials & Interfaces*, *11*(42), 38483-38496. doi:10.1021/acsami.9b12682
- Zhang, R. X., Cai, P., Zhang, T., Chen, K., Li, J., Cheng, J., . . . Wu, X. Y. (2016). Polymer–lipid hybrid nanoparticles synchronize pharmacokinetics of co-encapsulated doxorubicin–mitomycin C and enable their spatiotemporal co-delivery and local bioavailability in breast tumor. *Nanomedicine: Nanotechnology, Biology and Medicine*, *12*(5), 1279-1290. doi:10.1016/j.nano.2015.12.383

- Zhang, T., Ma, J., Li, C., Lin, K., Lou, F., Jiang, H., . . . Ruan, B. (2017). Core-shell lipid polymer nanoparticles for combined chemo and gene therapy of childhood head and neck cancers. *Oncology Reports*, *37*(3), 1653-1661. doi:10.3892/or.2017.5365
- Zhang, Y., Zhang, W., Huang, D., Wang, Y., Hu, H., Mei, Y., & Zhi, T. (2020). Prognostic factors in children with head and Neck Rhabdomyosarcoma: A 12-year retrospective study. *Brain and Behavior*, *10*(8). doi:10.1002/brb3.1697
- ZHU, J., ZHANG, J., TANG, G., HU, S., ZHOU, G., LIU, Y., WANG, Z. (2014). Computed tomography and magnetic resonance imaging observations of rhabdomyosarcoma in the head and Neck. *Oncology Letters*, *8*(1), 155-160. doi:10.3892/ol.2014.2094
- Goel, N. J., Bird, C. E., Hicks, W. H., & Abdullah, K. G. (2021). Economic implications of the modern treatment paradigm of glioblastoma: An analysis of global cost estimates and their utility for cost assessment. *Journal of Medical Economics*, *24*(1), 1018-1024. doi:10.1080/13696998.2021.1964775
- Smith, G. L., Shih, Y. T., & Frank, S. J. (2021). Financial toxicity in head and neck cancer patients treated with proton therapy. *International Journal of Particle Therapy*, *8*(1), 366-373. doi:10.14338/ijpt-20-00054.1
- Chen, S., Cao, Z., Prettner, K., Kuhn, M., Yang, J., Jiao, L., . . . Wang, C. (2023). Estimates and projections of the global economic cost of 29 cancers in 204 countries and territories from 2020 to 2050. *JAMA Oncology*. doi:10.1001/jamaoncol.2022.7826
- Abedi, A. A., Grunnet, K., Christensen, I. J., Michaelsen, S. R., Muhic, A., Møller, S., . . . Urup, T. (2021). A prognostic model for glioblastoma patients treated with standard therapy

based on a prospective cohort of consecutive non-selected patients from a single institution. *Frontiers in Oncology*, 11. doi:10.3389/fonc.2021.597587

Affronti, M. L., Heery, C. R., Herndon, J. E., Rich, J. N., Reardon, D. A., Desjardins, A., . . . Friedman, H. S. (2009). Overall survival of newly diagnosed glioblastoma patients receiving carmustine wafers followed by radiation and concurrent temozolomide plus rotational multiagent chemotherapy. *Cancer*, 115(15), 3501-3511. doi:10.1002/cncr.24398

Ashby, L. S., Smith, K. A., & Stea, B. (2016). Gliadel wafer implantation combined with standard radiotherapy and concurrent followed by adjuvant temozolomide for treatment of newly diagnosed high-grade glioma: A systematic literature review. *World Journal of Surgical Oncology*, 14(1). doi:10.1186/s12957-016-0975-5

Azzarelli, R., Simons, B. D., & Philpott, A. (2018). The developmental origin of brain tumours: A cellular and molecular framework. *Development*, 145(10). doi:10.1242/dev.162693

Baik, S. H., Kim, S. Y., Na, Y. C., & Cho, J. M. (2023). Supratotal resection of glioblastoma: Better survival outcome than gross total resection. *Journal of Personalized Medicine*, 13(3), 383. doi:10.3390/jpm13030383

Baliyan, V., Das, C. J., Sharma, R., & Gupta, A. K. (2016). Diffusion Weighted Imaging: Technique and Applications. *World Journal of Radiology*, 8(9), 785. doi:10.4329/wjr.v8.i9.785

Beiriger, J., Habib, A., Jovanovich, N., Kodavali, C. V., Edwards, L., Amankulor, N., & Zinn, P. O. (2022). The subventricular zone in glioblastoma: Genesis, maintenance, and modeling. *Frontiers in Oncology*, 12. doi:10.3389/fonc.2022.790976

- Bello-Alvarez, C., & Camacho-Arroyo, I. (2021). Impact of sex in the prevalence and progression of glioblastomas: The role of gonadal steroid hormones. *Biology of Sex Differences*, 12(1). doi:10.1186/s13293-021-00372-5
- Benitez, J. A., Ma, J., D'Antonio, M., Boyer, A., Camargo, M. F., Zanca, C., . . . Furnari, F. B. (2017). PTEN regulates glioblastoma oncogenesis through chromatin-associated complexes of DAXX and Histone H3.3. *Nature Communications*, 8(1). doi:10.1038/ncomms15223
- Bernstock, J. D., Gary, S. E., Klinger, N., Valdes, P. A., Ibn Essayed, W., Olsen, H. E., . . . Friedman, G. K. (2022). Standard clinical approaches and emerging modalities for glioblastoma imaging. *Neuro-Oncology Advances*, 4(1). doi:10.1093/noajnl/vdac080
- Bhattacharya, S. (2021). Methotrexate-loaded polymeric lipid hybrid nanoparticles (plhnps): A reliable drug delivery system for the treatment of glioblastoma. *Journal of Experimental Nanoscience*, 16(1), 344-367. doi:10.1080/17458080.2021.1983172
- Bonosi, L., Marrone, S., Benigno, U. E., Buscemi, F., Musso, S., Porzio, M., . . . Grasso, G. (2023). Maximal safe resection in glioblastoma surgery: A systematic review of advanced intraoperative image-guided techniques. *Brain Sciences*, 13(2), 216. doi:10.3390/brainsci13020216
- Brat, D. J., Aldape, K., Colman, H., Holland, E. C., Louis, D. N., Jenkins, R. B., . . . Weller, M. (2018). CIMPACT-now update 3: Recommended diagnostic criteria for “diffuse astrocytic glioma, IDH-wildtype, with molecular features of glioblastoma, who grade IV”. *Acta Neuropathologica*, 136(5), 805-810. doi:10.1007/s00401-018-1913-0

- Brown, T. J., Brennan, M. C., Li, M., Church, E. W., Brandmeir, N. J., Rakszawski, K. L., . . . Glantz, M. (2016). Association of the extent of resection with survival in glioblastoma. *JAMA Oncology*, 2(11), 1460. doi:10.1001/jamaoncol.2016.1373
- Cahill, D. P. (2021). Extent of resection of glioblastoma. *Neurosurgery Clinics of North America*, 32(1), 23-29. doi:10.1016/j.nec.2020.09.006
- Cha, S., Knopp, E. A., Johnson, G., Wetzel, S. G., Litt, A. W., & Zagzag, D. (2002). Intracranial mass lesions: Dynamic contrast-enhanced susceptibility-weighted echo-planar perfusion MR imaging. *Radiology*, 223(1), 11-29. doi:10.1148/radiol.2231010594
- Chaichana, K. L., Jusue-Torres, I., Navarro-Ramirez, R., Raza, S. M., Pascual-Gallego, M., Ibrahim, A., . . . Quinones-Hinojosa, A. (2013). Establishing percent resection and residual volume thresholds affecting survival and recurrence for patients with newly diagnosed intracranial glioblastoma. *Neuro-Oncology*, 16(1), 113-122. doi:10.1093/neuonc/not137
- Chen, W., Wang, Y., Zhao, B., Liu, P., Liu, L., Wang, Y., & Ma, W. (2021). Optimal therapies for recurrent glioblastoma: A bayesian network meta-analysis. *Frontiers in Oncology*, 11. doi:10.3389/fonc.2021.641878
- Evans, D. G., Huson, S. M., Donnai, D., Neary, W., Blair, V., Teare, D., . . . Harris, R. (1992). A genetic study of type 2 neurofibromatosis in the United Kingdom. I. Prevalence, mutation rate, fitness, and confirmation of maternal transmission effect on severity. *Journal of Medical Genetics*, 29(12), 841-846. doi:10.1136/jmg.29.12.841

- Fan, Y., Zhang, X., Gao, C., Jiang, S., Wu, H., Liu, Z., & Dou, T. (2022). Burden and trends of brain and central nervous system cancer from 1990 to 2019 at the Global, regional, and Country Levels. *Archives of Public Health, 80*(1). doi:10.1186/s13690-022-00965-5
- Flinker, A., Korzeniewska, A., Shestyk, A. Y., Franaszczuk, P. J., Dronkers, N. F., Knight, R. T., & Crone, N. E. (2015). Redefining the role of Broca's area in speech. *Proceedings of the National Academy of Sciences, 112*(9), 2871-2875. doi:10.1073/pnas.1414491112
- Gilard, V., Tebani, A., Dabaj, I., Laquerrière, A., Fontanilles, M., Derrey, S., . . . Bekri, S. (2021). Diagnosis and management of glioblastoma: A comprehensive perspective. *Journal of Personalized Medicine, 11*(4), 258. doi:10.3390/jpm11040258
- Girardi, F., Matz, M., Stiller, C., You, H., Marcos Gragera, R., Valkov, M. Y., . . . Lewis, C. (2022). Global survival trends for brain tumors, by histology: Analysis of individual records for 556,237 adults diagnosed in 59 countries during 2000–2014 (Concord-3). *Neuro-Oncology, 25*(3), 580-592. doi:10.1093/neuonc/noac217
- Grochans, S., Cybulska, A. M., Simińska, D., Korbecki, J., Kojder, K., Chlubek, D., & Baranowska-Bosiacka, I. (2022). Epidemiology of glioblastoma multiforme—literature review. *Cancers, 14*(10), 2412. doi:10.3390/cancers14102412
- Grover, V. P., Tognarelli, J. M., Crossey, M. M., Cox, I. J., Taylor-Robinson, S. D., & McPhail, M. J. (2015). Magnetic Resonance Imaging: Principles and techniques: Lessons for clinicians. *Journal of Clinical and Experimental Hepatology, 5*(3), 246-255. doi:10.1016/j.jceh.2015.08.001

- Hadjipanayis, C. G., & Stummer, W. (2019). 5-ala and FDA approval for Glioma Surgery. *Journal of Neuro-Oncology*, *141*(3), 479-486. doi:10.1007/s11060-019-03098-y
- Herrlinger, U., Tzaridis, T., Mack, F., Steinbach, J. P., Schlegel, U., Sabel, M., . . . Glas, M. (2019). Lomustine-temozolomide combination therapy versus standard temozolomide therapy in patients with newly diagnosed glioblastoma with methylated MGMT promoter (CeTeG/Noa-09): A randomised, open-label, phase 3 trial. *The Lancet*, *393*(10172), 678-688. doi:10.1016/s0140-6736(18)31791-4
- Huang, B., Yu, Z., & Liang, R. (2021). Effect of long-term adjuvant temozolomide chemotherapy on primary glioblastoma patient survival. *BMC Neurology*, *21*(1). doi:10.1186/s12883-021-02461-9
- Huang, R., Chen, H., Liang, J., Li, Y., Yang, J., Luo, C., . . . Xie, X. (2021). Dual role of reactive oxygen species and their application in cancer therapy. *Journal of Cancer*, *12*(18), 5543-5561. doi:10.7150/jca.54699
- Incekara, F., Smits, M., Dirven, L., Bos, E. M., Balvers, R. K., Haitsma, I. K., . . . Vincent, A. J. (2021). Intraoperative B-mode ultrasound guided surgery and the extent of glioblastoma resection: A randomized controlled trial. *Frontiers in Oncology*, *11*. doi:10.3389/fonc.2021.649797
- Jawabri, K. H., & Sharma, S. (2022). Physiology, cerebral cortex functions. Retrieved March 16, 2023, from <https://pubmed.ncbi.nlm.nih.gov/30860731/>
- Juratli, T. A., Stasik, S., Zolal, A., Schuster, C., Richter, S., Daubner, D., . . . Thiede, C. (2018). *Tert* promoter mutation detection in cell-free tumor-derived DNA in patients with *idh*

- wild-type glioblastomas: A pilot prospective study. *Clinical Cancer Research*, 24(21), 5282-5291. doi:10.1158/1078-0432.ccr-17-3717
- Kim, H. J., Park, J. W., & Lee, J. H. (2021). Genetic architectures and cell-of-origin in glioblastoma. *Frontiers in Oncology*, 10. doi:10.3389/fonc.2020.615400
- Körber, V., Yang, J., Barah, P., Wu, Y., Stichel, D., Gu, Z., . . . Lichter, P. (2019). Evolutionary trajectories of IDHWT glioblastomas reveal a common path of early tumorigenesis instigated years ahead of initial diagnosis. *Cancer Cell*, 35(4). doi:10.1016/j.ccell.2019.02.007
- Lakomkin, N., & Hadjipanayis, C. G. (2018). Fluorescence-guided surgery for high-grade gliomas. *Journal of Surgical Oncology*, 118(2), 356-361. doi:10.1002/jso.25154
- Lassman, A. B., Pugh, S. L., Wang, T. J., Aldape, K., Gan, H. K., Preusser, M., . . . Mehta, M. P. (2022). Depatuxizumab mafodotin in EGFR-amplified newly diagnosed glioblastoma: A phase III randomized clinical trial. *Neuro-Oncology*, 25(2), 339-350. doi:10.1093/neuonc/noac173
- Laurence, A., Huillard, E., Bielle, F., & Idhah, A. (2023). Cell of origin of brain and spinal cord tumors. *Advances in Experimental Medicine and Biology*, 85-101. doi:10.1007/978-3-031-14732-6_6
- Lee, J. H., Lee, J. E., Kahng, J. Y., Kim, S. H., Park, J. S., Yoon, S. J., . . . Lee, J. H. (2018). Human glioblastoma arises from subventricular zone cells with low-level driver mutations. *Nature*, 560(7717), 243-247. doi:10.1038/s41586-018-0389-3

- Lee, J. W., Kirkpatrick, J. P., McSherry, F., Herndon, J. E., Lipp, E. S., Desjardins, A., . . . Johnson, M. O. (2021). Adjuvant radiation in older patients with glioblastoma: A retrospective single institution analysis. *Frontiers in Oncology*, *11*. doi:10.3389/fonc.2021.631618
- Lee, Y., Seo, H. W., Baek, J., Lim, S. H., Hwang, S., & Kim, E. H. (2020). Gene expression profiling of glioblastoma cell lines depending on TP53 status after tumor-treating fields (TTFields) treatment. *Scientific Reports*, *10*(1). doi:10.1038/s41598-020-68473-6
- Liang, J., Lv, X., Lu, C., Ye, X., Chen, X., Fu, J., . . . Zhao, Y. (2020). Prognostic factors of patients with gliomas – an analysis on 335 patients with glioblastoma and other forms of gliomas. *BMC Cancer*, *20*(1). doi:10.1186/s12885-019-6511-6
- Liang, Y., Li, Z., Yuan, H., Wang, L., & Gao, L. (2021). Poly(P-phenylenevinylene) nanoparticles modified with ANTI EGFR VIII for specific glioblastoma therapy. *Scientific Reports*, *11*(1). doi:10.1038/s41598-021-83931-5
- Liao, G., Zhao, Z., Yang, H., & Li, X. (2019). Efficacy and safety of hypofractionated radiotherapy for the treatment of newly diagnosed glioblastoma multiforme: A systematic review and meta-analysis. *Frontiers in Oncology*, *9*. doi:10.3389/fonc.2019.01017
- Lim, D. A., & Alvarez-Buylla, A. (2016). The adult ventricular–subventricular zone (V-SVZ) and olfactory bulb (OB) neurogenesis. *Cold Spring Harbor Perspectives in Biology*, *8*(5). doi:10.1101/cshperspect.a018820
- Lin, Z., Yang, R., Li, K., Yi, G., Li, Z., Guo, J., . . . Huang, G. (2020). Establishment of age group classification for risk stratification in glioma patients. *BMC Neurology*, *20*(1). doi:10.1186/s12883-020-01888-w

- Liu, J., Shen, L., Tang, G., Tang, S., Kuang, W., Li, H., . . . Zhou, Q. (2020). Multiple extracranial metastases from glioblastoma multiforme: A case report and literature review. *Journal of International Medical Research*, 48(6), 030006052093045. doi:10.1177/0300060520930459
- Louis, D. N., Perry, A., Wesseling, P., Brat, D. J., Cree, I. A., Figarella-Branger, D., . . . Ellison, D. W. (2021). The 2021 WHO classification of tumors of the central nervous system: A summary. *Neuro-Oncology*, 23(8), 1231-1251. doi:10.1093/neuonc/noab106
- Madani, F., Esnaashari, S. S., Bergonzi, M. C., Webster, T. J., Younes, H. M., Khosravani, M., & Adabi, M. (2020). Paclitaxel/methotrexate co-loaded PLGA nanoparticles in glioblastoma treatment: Formulation development and in vitro antitumor activity evaluation. *Life Sciences*, 256, 117943. doi:10.1016/j.lfs.2020.117943
- Mak, K. S., Agarwal, A., Qureshi, M. M., & Truong, M. T. (2017). Hypofractionated short-course radiotherapy in elderly patients with glioblastoma multiforme: An analysis of the national cancer database. *Cancer Medicine*, 6(6), 1192-1200. doi:10.1002/cam4.1070
- Maleki, H., Hosseini Najafabadi, M. R., Webster, T. J., Hadjighassem, M. R., Sadroddiny, E., Ghanbari, H., . . . Adabi, M. (2021). Effect of paclitaxel/etoposide co-loaded polymeric nanoparticles on tumor size and survival rate in a rat model of glioblastoma. *International Journal of Pharmaceutics*, 604, 120722. doi:10.1016/j.ijpharm.2021.120722
- Maliyakkal, N., Appadath Beeran, A., & Udupa, N. (2021). Nanoparticles of cisplatin augment drug accumulations and inhibit multidrug resistance transporters in human glioblastoma cells. *Saudi Pharmaceutical Journal*, 29(8), 857-873. doi:10.1016/j.jsps.2021.07.001

Malmström, A., Grønberg, B. H., Marosi, C., Stupp, R., Frappaz, D., Schultz, H., . . . Henriksson, R. (2012). Temozolomide versus standard 6-week radiotherapy versus hypofractionated radiotherapy in patients older than 60 years with glioblastoma: The Nordic randomised, phase 3 trial. *The Lancet Oncology*, *13*(9), 916-926. doi:10.1016/s1470-2045(12)70265-6

Mandal, A. S., Brem, S., & Suckling, J. (2023). Brain Network Mapping and glioma pathophysiology. *Brain Communications*, *5*(2). doi:10.1093/braincomms/fcad040

Marei, H. E. (2022). Multimodal targeting of glioma with functionalized nanoparticles. *Cancer Cell International*, *22*(1). doi:10.1186/s12935-022-02687-8

Meteoglu, I., & Erdemir, A. (2021). Genistein and temozolomide-loaded polymeric nanoparticles: A synergistic approach for improved anti-tumor efficacy against glioblastoma. *Process Biochemistry*, *110*, 9-18. doi:10.1016/j.procbio.2021.07.015

Miller, K. D., Ostrom, Q. T., Kruchko, C., Patil, N., Tihan, T., Cioffi, G., . . . Barnholtz-Sloan, J. S. (2021). Brain and other Central Nervous System Tumor Statistics, 2021. *CA: A Cancer Journal for Clinicians*, *71*(5), 381-406. doi:10.3322/caac.21693

Mouliere, F., Mair, R., Chandrananda, D., Marass, F., Smith, C. G., Su, J., . . . Rosenfeld, N. (2018). Detection of cell-free dna fragmentation and copy number alterations in cerebrospinal fluid from glioma patients. *EMBO Molecular Medicine*, *10*(12). doi:10.15252/emmm.201809323

Mujokoro, B., Madani, F., Esnaashari, S. S., Khosravani, M., & Adabi, M. (2019). Combination and co-delivery of Methotrexate and curcumin: Preparation and in vitro cytotoxic

- investigation on glioma cells. *Journal of Pharmaceutical Innovation*, 15(4), 617-626.
doi:10.1007/s12247-019-09406-3
- Neulinger, K., Oram, J., Tinson, H., O’Gorman, J., & Shum, D. H. (2015). Prospective memory and frontal lobe function. *Aging, Neuropsychology, and Cognition*, 23(2), 171-183.
doi:10.1080/13825585.2015.1069252
- Nunna, R. S., Khalid, S. I., Patel, S., Sethi, A., Behbahani, M., Mehta, A. I., . . . Byrne, R. W. (2021). Outcomes and patterns of care in elderly patients with glioblastoma multiforme. *World Neurosurgery*, 149. doi:10.1016/j.wneu.2021.01.028
- Oprita, A., Baloi, S., Staicu, G., Alexandru, O., Tache, D. E., Danoiu, S., . . . Sevastre, A. (2021). Updated insights on EGFR signaling pathways in Glioma. *International Journal of Molecular Sciences*, 22(2), 587. doi:10.3390/ijms22020587
- Oronsky, B., Reid, T. R., Oronsky, A., Sandhu, N., & Knox, S. J. (2021). A review of newly diagnosed glioblastoma. *Frontiers in Oncology*, 10. doi:10.3389/fonc.2020.574012
- Ostrom, Q. T., Cioffi, G., Gittleman, H., Patil, N., Waite, K., Kruchko, C., & Barnholtz-Sloan, J. S. (2019). CBTRUS statistical report: Primary Brain and other central nervous system tumors diagnosed in the United States in 2012–2016. *Neuro-Oncology*, 21(Supplement_5), V1-V100. doi:10.1093/neuonc/noz150
- Patel, A. P., Fisher, J. L., Nichols, E., Abd-Allah, F., Abdela, J., Abdelalim, A., . . . Fitzmaurice, C. (2019). Global, regional, and national burden of brain and other CNS cancer, 1990–2016: A systematic analysis for the global burden of disease study 2016. *The Lancet Neurology*, 18(4), 376-393. doi:10.1016/s1474-4422(18)30468-x

- Perry, J. R., Laperriere, N., O'Callaghan, C. J., Brandes, A. A., Menten, J., Phillips, C., . . . Mason, W. P. (2017). Short-course radiation plus temozolomide in elderly patients with glioblastoma. *New England Journal of Medicine*, *376*(11), 1027-1037. doi:10.1056/nejmoa1611977
- Péus, D., Newcomb, N., & Hofer, S. (2013). Appraisal of the Karnofsky performance status and proposal of a simple algorithmic system for its evaluation. *BMC Medical Informatics and Decision Making*, *13*(1). doi:10.1186/1472-6947-13-72
- Piccioni, D. E., Achrol, A. S., Kiedrowski, L. A., Banks, K. C., Boucher, N., Barkhoudarian, G., . . . Kesari, S. (2019). Analysis of cell-free circulating tumor DNA in 419 patients with glioblastoma and other primary brain tumors. *CNS Oncology*, *8*(2). doi:10.2217/cns-2018-0015
- Qi, Z., Xing, W., Shao, C., Yang, C., & Wang, Z. (2015). The role of Gliadel Wafers in the treatment of newly diagnosed GBM: A meta-analysis. *Drug Design, Development and Therapy*, 3341. doi:10.2147/dddt.s85943
- Roa, W., Kepka, L., Kumar, N., Sinaika, V., Matiello, J., Lomidze, D., . . . Fidarova, E. (2015). International Atomic Energy Agency Randomized Phase III study of radiation therapy in elderly and/or frail patients with newly diagnosed glioblastoma multiforme. *Journal of Clinical Oncology*, *33*(35), 4145-4150. doi:10.1200/jco.2015.62.6606
- Sage, W., Guilfoyle, M., Luney, C., Young, A., Sinha, R., Sgubin, D., . . . Watts, C. (2017). Local alkylating chemotherapy applied immediately after 5-ala guided resection of glioblastoma does not provide additional benefit. *Journal of Neuro-Oncology*, *136*(2), 273-280. doi:10.1007/s11060-017-2649-8

- Sen', V. D., Balakina, A. A., Stupina, T. S., Mumyatova, V. A., Kulikov, A. V., Tikhonov, I. V., . . . Pliss, E. M. (2021). Amphiphilic Chitosan–polyaminoxyls loaded with daunorubicin: Synthesis, antioxidant activity, and drug delivery capacity. *International Journal of Biological Macromolecules*, *193*, 965-979. doi:10.1016/j.ijbiomac.2021.10.170
- Shapira-Furman, T., Serra, R., Gorelick, N., Doglioli, M., Tagliaferri, V., Cecia, A., . . . Domb, A. J. (2019). Biodegradable wafers releasing temozolomide and Carmustine for the treatment of brain cancer. *Journal of Controlled Release*, *295*, 93-101. doi:10.1016/j.jconrel.2018.12.048
- Stoyanov, G. S., & Dzhankov, D. L. (2018). On the concepts and history of glioblastoma multiforme - morphology, genetics and epigenetics. *Folia Medica*, *60*(1), 48-66. doi:10.1515/folmed-2017-0069
- Strobel, H., Baisch, T., Fitzel, R., Schilberg, K., Siegelin, M. D., Karpel-Massler, G., . . . Westhoff, M. (2019). Temozolomide and other alkylating agents in glioblastoma therapy. *Biomedicines*, *7*(3), 69. doi:10.3390/biomedicines7030069
- Sulman, E. P., Ismaila, N., Armstrong, T. S., Tsien, C., Batchelor, T. T., Cloughesy, T., . . . Chang, S. M. (2017). Radiation therapy for glioblastoma: American society of clinical oncology clinical practice guideline endorsement of the American Society for Radiation Oncology Guideline. *Journal of Clinical Oncology*, *35*(3), 361-369. doi:10.1200/jco.2016.70.7562
- Sulman, E. P., Ismaila, N., Armstrong, T. S., Tsien, C., Batchelor, T. T., Cloughesy, T., . . . Chang, S. M. (2017). Radiation therapy for glioblastoma: American society of clinical oncology clinical practice guideline endorsement of the American Society for Radiation Oncology Guideline. *Journal of Clinical Oncology*, *35*(3), 361-369. doi:10.1200/jco.2016.70.7562

- Sun, P., Xiao, Y., Di, Q., Ma, W., Ma, X., Wang, Q., & Chen, W. (2020). Transferrin receptor-targeted peg-pla polymeric micelles for chemotherapy against glioblastoma multiforme. *International Journal of Nanomedicine, Volume 15*, 6673-6687. doi:10.2147/ijn.s257459
- Taiarol, L., Formicola, B., Magro, R. D., Sesana, S., & Re, F. (2020). An update of nanoparticle-based approaches for glioblastoma multiforme immunotherapy. *Nanomedicine, 15*(19), 1861-1871. doi:10.2217/nnm-2020-0132
- Taylor, J. W., & Schiff, D. (2014). Treatment considerations for MGMT-unmethylated glioblastoma. *Current Neurology and Neuroscience Reports, 15*(1). doi:10.1007/s11910-014-0507-z
- Trybek, T., Kowalik, A., Gózdź, S., & Kowalska, A. (2020). Telomeres and telomerase in oncogenesis (review). *Oncology Letters, 20*(2), 1015-1027. doi:10.3892/ol.2020.11659
- Valente, D., Gentileschi, M. P., Guerrisi, A., Bruzzaniti, V., Morrone, A., Soddu, S., & Verdina, A. (2022). Factors to consider for the correct use of γ H2AX in the evaluation of DNA double-strand breaks damage caused by ionizing radiation. *Cancers, 14*(24), 6204. doi:10.3390/cancers14246204
- Wang, L., Liu, C., Qiao, F., Li, M., Xin, H., Chen, N., . . . Liu, J. (2021). Analysis of the cytotoxic effects, cellular uptake and cellular distribution of paclitaxel-loaded nanoparticles in glioblastoma cells *in vitro*. *Experimental and Therapeutic Medicine, 21*(4). doi:10.3892/etm.2021.9723
- Wang, S., Yu, Y., Wang, A., Duan, X., Sun, Y., Wang, L., . . . Sun, K. (2022). Temozolomide hexadecyl ester targeted plga nanoparticles for drug-resistant glioblastoma therapy via

- intranasal administration. *Frontiers in Pharmacology*, 13.
doi:10.3389/fphar.2022.965789
- Wang, Y., Pan, Y., & Li, H. (2020). What is Brain Health and why is it important? *BMJ*, M3683.
doi:10.1136/bmj.m3683
- Wang, Y., Qi, H., Liu, Y., Duan, C., Liu, X., Xia, T., . . . Liu, H. (2021). The double-edged roles of ROS in cancer prevention and therapy. *Theranostics*, 11(10), 4839-4857.
doi:10.7150/thno.56747
- Weller, M., Van den Bent, M., Preusser, M., Le Rhun, E., Tonn, J. C., Minniti, G., . . . Wick, W. (2020). EANO guidelines on the diagnosis and treatment of diffuse gliomas of adulthood. *Nature Reviews Clinical Oncology*, 18(3), 170-186. doi:10.1038/s41571-020-00447-z
- Wesolowski, J., Rajdev, P., & Mukherji, S. (2010). Temozolomide (Temodar). *American Journal of Neuroradiology*, 31(8), 1383-1384. doi:10.3174/ajnr.a2170
- Wick, W., Gorlia, T., Bendszus, M., Taphoorn, M., Sahm, F., Harting, I., . . . Van den Bent, M. J. (2017). Lomustine and bevacizumab in progressive glioblastoma. *New England Journal of Medicine*, 377(20), 1954-1963. doi:10.1056/nejmoa1707358
- Witteler, J., Schild, S. E., & Rades, D. (2021). Palliative radiotherapy of primary glioblastoma. *In Vivo*, 35(1), 483-487. doi:10.21873/invivo.12282
- Wu, C., Shen, Y., Shi, L., Zhang, J., Guo, T., Zhou, L., . . . Liu, X. (2023). UBA1 inhibition contributes radiosensitization of glioblastoma cells via blocking DNA damage repair. *Frontiers in Pharmacology*, 14. doi:10.3389/fphar.2023.1073929

- Xu, Y., Shen, M., Li, Y., Sun, Y., Teng, Y., Wang, Y., & Duan, Y. (2016). The synergic antitumor effects of paclitaxel and temozolomide co-loaded in MPEG-plga nanoparticles on Glioblastoma Cells. *Oncotarget*, 7(15), 20890-20901. doi:10.18632/oncotarget.7896
- Yang, H., Villani, R. M., Wang, H., Simpson, M. J., Roberts, M. S., Tang, M., & Liang, X. (2018). The role of cellular reactive oxygen species in cancer chemotherapy. *Journal of Experimental & Clinical Cancer Research*, 37(1). doi:10.1186/s13046-018-0909-x
- Yu, W., Zhang, L., Wei, Q., & Shao, A. (2020). O6-methylguanine-DNA methyltransferase (MGMT): Challenges and new opportunities in glioma chemotherapy. *Frontiers in Oncology*, 9. doi:10.3389/fonc.2019.01547
- Zhang, H., Wang, R., Yu, Y., Liu, J., Luo, T., & Fan, F. (2019). Glioblastoma treatment modalities besides surgery. *Journal of Cancer*, 10(20), 4793-4806. doi:10.7150/jca.32475
- Zhang, Y., Dube, C., Gibert, M., Cruickshanks, N., Wang, B., Coughlan, M., . . . Abounader, R. (2018). The P53 pathway in glioblastoma. *Cancers*, 10(9), 297. doi:10.3390/cancers10090297
- Zhao, Y., Qian, Y., Sun, Z., Shen, X., Cai, Y., Li, L., & Wang, Z. (2021). Role of PI3K in the progression and regression of atherosclerosis. *Frontiers in Pharmacology*, 12. doi:10.3389/fphar.2021.632378
- Zill, O. A., Banks, K. C., Fairclough, S. R., Mortimer, S. A., Vowles, J. V., Mokhtari, R., . . . Talasz, A. (2018). The landscape of actionable genomic alterations in cell-free circulating tumor DNA from 21,807 advanced cancer patients. *Clinical Cancer Research*, 24(15), 3528-3538. doi:10.1158/1078-0432.ccr-17-3837

Zou, Y., Wang, Y., Xu, S., Liu, Y., Yin, J., Lovejoy, D. B., . . . Shi, B. (2022). Brain co-delivery of temozolomide and cisplatin for combinatorial glioblastoma chemotherapy. *Advanced Materials*, 34(33), 2203958. doi:10.1002/adma.202203958

APPENDICES

Appendix 1 : Laemmli sample buffer (4X) preparation

The loading buffer or Laemmli buffer (4X) was prepared with Tris -Hcl pH 6.8 (250mM), 40% Glycerol, 8% SDS, 0.02% Bromophenol blue and adjusted with distilled water (dH₂O) to the final volume, according to the recipe below. Only before use, 10% b-mercaptoethanol was added. Laemmli was added as ¼ of the final sample volume.

Components	Final volume 50ml
250mM Tris -Hcl pH=6.8	12.5ml from 1M Tris pH 6.8
40% Glycerol	20ml
8% SDS	4gr
0.02% Bromophenol blue	0.01gr
H ₂ O (adjust to final volume)	12.5ml

And 10% b-mercaptoethanol (before use)

Appendix 2 : Enhanced chemiluminescence (ECL) solution preparation

Enhanced chemiluminescence (ECL) solution was prepared with ECL solutions A and B according to the recipe below. Solution A contained p-Coumaric acid in DMSO, Luminol in DMSO, Tris 1M pH 8.5, and double distilled H₂O. Solution B contained H₂O₂, Tris 1M pH 8.5, and double distilled dH₂O. Only before use Solution A and B were mixed in 1:1 ratio.

Solution A **final volume 5ml**

p-Coumaric acid 90mM in DMSO	22 µl
Luminol stock 250mM in DMSO	50 µl
Tris 1M pH8.5	0.5ml
ddH ₂ O	4.428ml

Solution B **Final volume 5ml**

H ₂ O ₂	32 µl
Tris 1M pH8.5	0.5ml
ddH ₂ O	4.5ml

LIST OF PUBLICATIONS

List of Publications

Review paper

Braoudaki, M., Ahmad, M. S., Mustafov, D., **Seriah, S.**, Siddiqui, M. N., & Siddiqui, S. S. (2022).

Chemokines and chemokine receptors in colorectal cancer; multifarious roles and clinical impact. *Seminars in Cancer Biology*, 86, 436-449.

Book Chapters

- Seriah, S, Efthimiadou E, Braoudaki, M., Nanotechnology in Medicine, Molecular Biology and Biotechnology 7th Edition, Royal Society of Chemistry.
- Mustafov D, **Seriah S**, Malik R, and Braoudaki, M., (2022). Microrna Biomarkers In Primary Brain Malignancies, Epigenetics - Regulation and New Perspectives, IntechOpen.

Extended abstracts

- Seriah, S, Braoudaki, M, Efthimiadou E. (2020). Development Of Smart Polymeric Nanoparticles As Targeted Drug Delivery System For The Treatment Of Pediatric Brain Malignancies

(Presented as a poster online at the 52nd congress of the International Society of Pediatric Oncology (SIOP), October 14-17, 2020; the extended abstract is published in the proceedings).
- Seriah, S, Braoudaki, M, Efthimiadou E. (2021). The Development of Smart Polymeric Nanocarriers as Targeted Drug Delivery Systems for The Treatment of Pediatric Brain Malignancies

(Presented as oral presentation online at Athens Conference on Advances in Chemistry, March 10-14, 2021; the extended abstract is published in the proceedings).

- Seriah, S, Efthimiadou E, Braoudaki, M. (2021). The Therapeutic Potential Of Smart Polymeric Nanocontainers In Pediatric Central Nervous System Malignancies.

(Presented as oral presentation online at the School of Life and Medical Sciences (LMS) conference, June 22nd, 2021; the extended abstract is published in the proceedings).
- Seriah, S, Efthimiadou E, Braoudaki, M. (2021). The Therapeutic Potential of Smart Polymeric Nanocontainers In Pediatric Central Nervous System Malignancies

(Presented as oral presentation online at the 53rd congress of the International Society of Pediatric Oncology (SIOP) October 21-24, 2021; the extended abstract is published in the proceedings).
- Seriah, S, Efthimiadou E, Braoudaki, M. (2022). Drug Delivery And Therapeutic Outcome Enhancement In Paediatric Rhabdomyosarcoma By The Use Of Dual-Sensitive Polymeric Nanocontainers.

(Presented as poster at the School of Life and Medical Sciences (LMS) conference, June 21st, 2022, in Hertfordshire, UK; the extended abstract is published in the proceedings).
- Seriah, S, Efthimiadou E, Braoudaki, M. (2022) Rhabdomyosarcoma Treatment By Using Polymeric Nanocontainers: Drug Delivery And Therapeutic Outcome Enhancement

(Presented as oral presentation online at Athens Conference on Advances in Chemistry, June 26 - July 1st , 2021 in Athens, Greece; the extended abstract is published in the proceedings).
- Seriah, S, Efthimiadou E, Braoudaki, M. (2022). Enhancement Of Chemotherapy Delivery And Outcome In Paediatric Rhabdomyosarcoma Using Smart Polymeric Nanocontainers

(Presented as a poster at the 54th congress of the International Society of Pediatric Oncology (SIOP) September 28th - October 1st, 2022 in Barcelona, Spain; the extended abstract is published in the proceedings).



Contents lists available at ScienceDirect

Seminars in Cancer Biology

journal homepage: www.elsevier.com/locate/semcancer

Chemokines and chemokine receptors in colorectal cancer; multifarious roles and clinical impact

Maria Braoudaki^a, Mohammed Saqif Ahmad^a, Denis Mustafov^a, Sara Seriah^a,
 Mohammad Naseem Siddiqui^b, Shoib Sarwar Siddiqui^{a,*}

^a Dept of Clinical, Pharmaceutical and Biological Sciences, School of Life and Medical Sciences, University of Hertfordshire, UK

^b Department of Biosciences, Faculty of Natural Sciences, Jamia Millia Islamia, Jamia Nagar, New Delhi 110025, India

ARTICLE INFO

Keywords:

Chemokines
 Chemokine receptors
 Colorectal cancer
 Tumour heterogeneity
 Drug resistance

ABSTRACT

Colorectal cancer (CRC) is considered the second cause of cancer death worldwide. The early diagnosis plays a key role in patient prognosis and subsequently overall survival. Similar to several types of cancer, colorectal cancer is also characterised by drug resistance and heterogeneity that contribute to its complexity -especially at advanced stages. However, despite the extensive research related to the identification of biomarkers associated to early diagnosis, accurate prognosis and the management of CRC patients, little progress has been made thus far. Therefore, the mortality rates, especially at advanced stages, remain high. A large family of chemoattractant cytokines called chemokines are known for their significant role in inflammation and immunity. Chemokines released by the different tumorous cells play a key role in increasing the complexity of the tumour's microenvironment. The current review investigates the role of chemokines and chemokine receptors in colorectal cancer and their potential as clinical molecular signatures that could be effectively used as a personalised therapeutic approach. We discussed how chemokine and chemokine receptors regulate the microenvironment and lead to heterogeneity in CRC. An important aspect of chemokines is their role in drug resistance which has been extensively discussed. This review also provides an overview of the current advances in the search for chemokines and chemokine receptors in CRC.

1. Introduction

1.1. Colorectal cancer

Colorectal cancer (CRC) is one of the most commonly diagnosed cancers and the second cause of cancer related death in men and women worldwide. It originates in the colon or in the rectum by the abnormal growth of cells that form a polyp. The polyps form and appear in the epithelial tissue that lines the colon or the rectum. The development of the cancerous polyps or colorectal carcinoma results from a series of accumulated somatic and germline genetic mutations [1]. The most commonly mutated genes in CRC are *APC*, *TP53*, *KRAS*, and *PIK3CA* with –82%, –55%, –45%, and –18% of CRC cases, respectively [2]. There are four stages of colorectal cancer (I, II, III, IV) classified according to the tumour severity with stage I being the least malignant and stage IV being the most malignant [1].

1.2. Epidemiology

CRC affects men more than women, as reported by the Global Cancer Observatory (23.4 in 100,000 men vs 16.2 in 100,000 women) [3]. In more detail, there are around one million cases diagnosed with colorectal cancer in men and 500,000 deaths every year worldwide. In women, the diagnosed and death related colorectal cancer cases account for around 865,000 and 418,000 cases, respectively [3]. Generally, colorectal cancer occurs in adults older than 50 years of age. The average age of men and women diagnosed with colorectal cancer is 68 and 72 years, respectively. However, CRC can also affect teenagers [3].

Furthermore, CRC is more common in high human development index (HDI) countries compared to lower HDI countries. Consequently, higher mortality cases have been reported in high HDI countries. Countries with high HDI generally follow a “westernized lifestyle”, which includes a diet with more red and processed meat, refined sugar and grains, fewer fibres, and less physical activity. CRC is also

* Correspondence to: School of Life and Medical Sciences, University of Hertfordshire, College Lane Campus, Hatfield AL10 9AB, UK.
 E-mail address: s.siddiqui3@herts.ac.uk (S.S. Siddiqui).

<https://doi.org/10.1016/j.semcan.2022.06.002>

Received 21 April 2022; Received in revised form 7 June 2022; Accepted 8 June 2022

Available online 11 June 2022

1044-579X/© 2022 The Authors. Published by Elsevier Ltd. This is an open access article under the CC BY license (<http://creativecommons.org/licenses/by/4.0/>).

12 Nanotechnology in Medicine

Sara Seriah^{a,b,c}, Eleni Efthimiadou^{*b,c} and Maria Braoudaki^{*a}

^aSchool of Life and Medical Sciences, University of Hertfordshire, College Lane, Hatfield, Hertfordshire AL10 9AB, UK; ^bDepartment of Chemistry, Inorganic Chemistry Laboratory, National and Kapodistrian University of Athens, 157 72 Athens, Greece; ^cNCSR 'Demokritos', Sol-Gel Laboratory, Institute of Nanoscience and Nanotechnology, 153 10 Athens, Greece

*E-mail: m.braoudaki@herts.ac.uk, efthim@chem.uoa.gr

12.1 Introduction

Nanotechnology is a multidisciplinary field that operates at the nanoscale, which is one billionth of a metre (10^{-9} m), and comprises several fields, including biology, physics, chemistry, engineering and medicine, among others.¹ In 1959, the physicist Richard Feynman first described this nanoscale concept at the annual American Physical Society Meeting, where he said, 'There's plenty of room at the bottom'.² At the nanoscale, the chemical, physical and biological properties and interactions of single molecules are altered; becoming optimal (*e.g.* greater surface area) in contrast to properties of equivalent materials at a larger scale.³ For instance, there are several types of nanoparticles with controllable and manipulable properties (size, composition, pH sensitivity, thermosensitivity, water solubility, magnetism, surface modification) that suit nanomedicine applications. Ultimately, they provide better outcomes such as fewer side effects and better therapeutic results attained through the delivery of cytotoxic drugs by nanoparticles.¹

Molecular Biology and Biotechnology, 7th Edition
Edited by Ralph Rapley
© The Royal Society of Chemistry 2021
Published by the Royal Society of Chemistry, www.rsc.org

MicroRNA Biomarkers in Primary Brain Malignancies

*Denis Mustafov, Sara Seriah, Roozba Malik
and Maria Braoudaki*

Abstract

Despite the concerted efforts within the management of brain malignancies over the past few decades, primary brain cancers remain an obscure challenge with unfavourable outcomes for the patients. Glioblastomas (GBM) and medulloblastomas afford the most prevalent brain tumours and account for markedly high mortality rates within affected patients. The unmet clinical requirements for an early diagnostic biomarker and effective treatment have shed light onto microRNAs (miRNAs). These are small, endogenous noncoding RNAs involved in a wide spectrum of biological processes, such as post-translational modification, tumorigenesis, angiogenesis, invasiveness, and apoptosis. Increased expression of miR-21 has been shown to have devastating effects upon patients with brain tumours, and it could be used as a diagnostic biomarker and an early relapse indicator. miRNAs such as miR-128a, miR-34a, miR-7 and miR-1253 have demonstrated tumour suppressive properties and could serve as putative therapeutic agents. MiRNA signatures, such as miR-21 and miR-10b could be incorporated as potential prognostic indicators for advanced and metastatic brain malignancies, whereas miR-221/222 cluster has a therapeutic potential to sensitise cancerous cells towards radiotherapy. Herein, we summarised current knowledge on how miRNAs with significant role in glioblastomas and medulloblastomas specifically can be effectively used as promising brain cancer diagnostics, prognostics, and therapeutics.

Keywords: microRNA, signalling pathways, biomarker, diagnosis, prognosis, therapy, glioblastoma (GBM), medulloblastoma

1. Introduction

1.1 Research background

Within the current field of primary brain cancer research, a complimentary class of potential biomarkers, known as microRNAs (miRNAs), are becoming increasingly favoured upon their pleiotropic advantages; from adopting potential diagnostic, prognostic, and therapeutic properties. In the contemporary study of the adult brain tumour, glioblastoma (GBM), several miRNAs are seen to act as potential biomarkers of the debilitating cancer. Through the revelation of current studies, miR-21,

DEVELOPMENT OF SMART POLYMERIC NANOPARTICLES AS TARGETED DRUG DELIVERY SYSTEM FOR THE TREATMENT OF PEDIATRIC BRAIN MALIGNANCIES



Sara Seriah^{1,2,3}, Eleni Efthimiadou^{2,3}, Maria Braoudaki¹

¹School of Life and Medical Sciences, University of Hertfordshire, UK; ²Department of Chemistry, Inorganic Chemistry Lab, National and Kapodistrian University of Athens, Greece; ³NCSR "Demokritos", Sol-Gel Laboratory, Institute of Nanoscience and Nanotechnology, Greece



INTRODUCTION

Paediatric brain tumours are solid neoplasms that appear in the central nervous system (CNS). Pilocytic astrocytoma (PA) classified as grade I and medulloblastoma (MB) classified as grade V account for >50% of all primary brain tumours and 20% of the malignant cases, respectively. Although, a plethora of molecular and genetic factors that drive their development and progression have been uncovered, little progress has been made in the field of curative therapeutics. Current chemotherapeutic agents lack in specificity and selectivity, which is frequently translated into unpleasant side effects for the child. Chemotherapy drugs encapsulation within nanoparticles (NPs) is one approach to improve drug efficacy and its therapeutic outcome. NPs are nanosized spherical shaped, and solid particles that can be classified into different groups and types based on their shape, size, and properties. They can be used as targeted drug delivery systems, imaging enhancers, and gene delivery therapeutics. Additionally, polymeric NPs with suitable surface and nano-size can cross the blood brain barrier without causing any damage to it.

AIMS AND OBJECTIVES

The aim of the present work is to test the efficiency of NP as an intracellular drug delivery system capable of improving the treatment of paediatric brain tumours. Therefore, we are planning to synthesize polymeric NPs to deliver first-line chemotherapy drugs at the tumour site to increase their efficacy and reduce their side effects.

METHODOLOGY



Figure 1. The Four synthesis steps of hollow polymeric nanoparticles a- Synthesis of silica core template, b- Coating with a layer of vinyl groups (MPS), c- Coating with the pH sensitive layer, d- Silica core removal and the obtaining hollow polymeric NPs

Throughout the synthesis steps, polymeric NPs were characterized structurally by Fourier Transform Infrared Spectroscopy and Dynamic Light Scattering, and morphologically by Scanning Electron Microscopy. The biocompatibility of the NPs was tested by haemolysis assay. Then, Daunorubicin (DNR) model drug was loaded in the NPs.

CONCLUSION AND FUTURE PROSPECTS

In conclusion, pH and thermosensitive polymeric nanoparticles were synthesised of MPS layer and P(MAA-co-MBA-co-EGDMA) polymer layer, and characterized structurally as well as morphologically. They were also proven to be biocompatible through the haemolysis assay, and showed good drug loading capacity. In the future, re-synthesis of the polymeric NPs will take place to obtain multifunctional NPs and further experiments will be performed to test their loading capacity and evaluate their efficacy in PA and MB cell cultures and mouse models, in addition to other biological evaluations.

References: Shadfa, S. (2016). Natural polymer drug delivery systems (pp. 33-83). Springer, Cham.
 Braoudaki, M., Lambrou, G., Giannikou, K., Nikitans, V., Stefanaki, K., & Birkis, D. et al. (2014). MicroRNA expression signatures predict patient progression and disease outcome in pediatric embryonal central nervous system neoplasms. *Journal of Hematology & Oncology*, 7(1). doi: 10.1186/s13045-014-0096-y
 Burkhard, C., Di Patre, P., Schuler, D., Schuler, G., Yasargil, M., & Yonekawa, Y. et al. (2003). A population-based study of the incidence and survival rates in patients with pilocytic astrocytoma. *Journal of Neurosurgery*, 98(6), 1170-1174. doi: 10.3171/jns.2003.98.6.1170
 Louis, D., Perry, A., Reifenberger, G., von Deimling, A., Figarella-Branger, D., Cavenee, W., Ohgaki, H., Wiestler, O., Kleihues, P. and Ellison, D. (2016). The 2016 World Health Organization Classification of Tumors of the Central Nervous System: a summary. *Acta Neuropathologica*, 131(6), pp.803-820.

RESULTS

Structural Evaluation by FT-IR and DLS

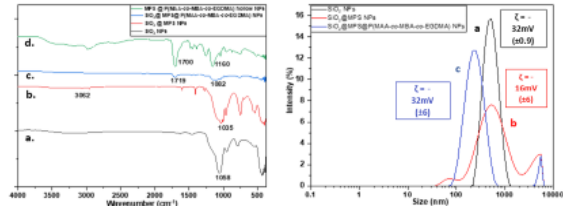


Figure 2. FTIR spectrum (left) and DLS spectrum (right) of the different synthesis steps of the polymeric nanoparticles.

Morphological Evaluation by SEM

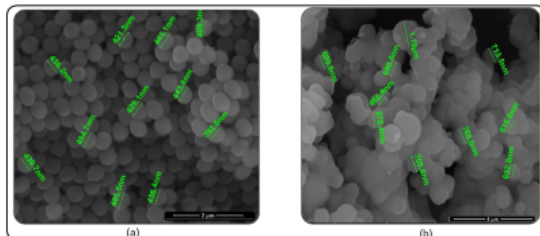


Figure 3. SEM images showing size and spherical morphology of the silica core NPs (a); and silica coated NPs with MPS and pH sensitive layer (b)

Biological Evolution: Haemolysis Assay

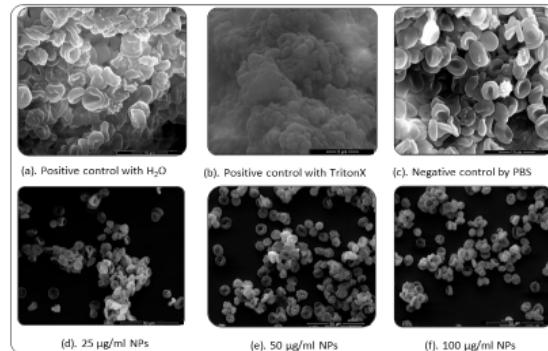


Figure 4. Haemolysis assay results analysed by SEM after 24h incubation with 3 different concentrations of NPs in addition to positive and negative controls (a). Positive control sample of RBC incubated for 24h with H₂O showing haemolysed and destroyed RBCs; (b). Positive control of RBC incubated with TritonX for 24h showing completely haemolysed and destroyed RBCs; (c). Negative control sample of RBC with no additions; (d), (e), and (f). RBC incubated with 25 µg/ml, 50 µg/ml, and 100 µg/ml NPs suspensions respectively for 24h showing healthy and unaffected RBCs

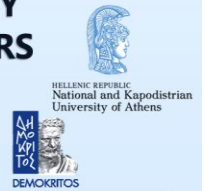
Drug Loading

After 72h of gentle shaking, DNR was loaded in the NPs with an encapsulation efficacy (EE) of 89% and loading capacity (LC) of 42%.

DRUG DELIVERY AND THERAPEUTIC OUTCOME ENHANCEMENT IN PAEDIATRIC RHABDOMYOSARCOMA BY THE USE OF DUAL-SENSITIVE POLYMERIC NANOCONTAINERS



Sara Seriah^{1,2,3}, Eleni Efthimiadou^{2,3}, Maria Braoudaki¹
¹Department of Clinical, Pharmaceutical and Biological Sciences, School of Life and Medical Sciences, University of Hertfordshire, UK;
²Department of Chemistry, Inorganic Chemistry Lab, National and Kapodistrian University of Athens, Greece; ³NCSR "Demokritos", Sol-Gel Laboratory, Institute of Nanoscience and Nanotechnology, Greece



ABSTRACT

Rhabdomyosarcoma is a rare type of paediatric CNS tumours. The overall five-year survival rate is dependent on the stage and location of the tumour along with the age of the child. Current chemotherapeutic agents affect both healthy and cancer cells resulting in poor treatment outcome and long-term side effects. Chemotherapeutic drugs encapsulation in nanocarriers is the approach through which it is aimed to enhance the efficacy and outcome of the treatment. In this project rhabdomyosarcoma cells were treated with encapsulated chemotherapy drug in synthesised polymeric nanocontainers. The cytotoxicity assay and the release profile results showed a sustained drug release in T671 cell line. Fluorescence microscopy images also showed good cellular uptake of the nanocontainers-encapsulated drug. Therefore, drug loaded nanocarriers can be used as potential enhancers for the rhabdomyosarcoma's treatment efficacy and outcome. Further experiments will be carried out with modified surface nanocarriers and different encapsulated drugs in other paediatric brain tumours cell lines.

INTRODUCTION

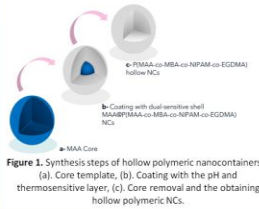
Paediatric CNS tumours are the second most common cancer and the leading cause of cancer death in children. One of the rare types of paediatric CNS tumour is the paediatric rhabdomyosarcoma with 4.5 cases reported per 1 million children (Glosli et al., 2021). Yet, this rare type is also the most common type of soft-tissue cancer in children. It originates in the head/neck area in 40% of cases. Despite the progress made in the diagnosis and treatment of moderate cases with 75% five-year survival rate, severe cases of rhabdomyosarcoma have lower survival rate (20%) and poor treatment outcome (Leiner & Le Loarer, 2019). Additionally, current chemotherapeutic agents lack in specificity and selectivity, resulting in unpleasant and long-term side effects for the child (Glosli et al., 2021). Encapsulating the chemotherapy drugs within carriers called nanocontainers (NCs) is one approach to improve both efficacy and therapeutic outcome of the drugs. Due to their nano-size and suitable modified surface, polymeric NCs can cross the blood-brain-barrier without causing any damage.

AIMS

The aim was to synthesize polymeric nanocontainers that are capable of delivering chemotherapy drugs at the tumour site to increase their efficacy and reduce their side effects.

METHODOLOGY

Synthesis of Nanocontainers



Structural characterisation by:

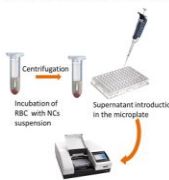
- Dynamic Light Scattering (DLS)
- Fourier Transform Infrared Spectroscopy (FT-IR)

Morphological characterisation by:

- Scanning Electron Microscopy (SEM)

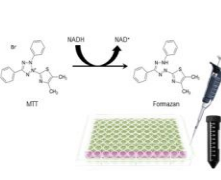
Haemolysis Assay

This assay is used for the evaluation of biocompatibility of the NCs³.



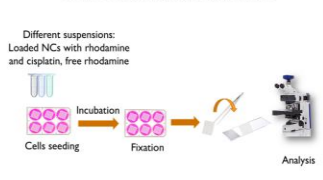
MTT Assay

This assay is used for cytotoxicity evaluation³.



Fluorescence Microscopy

This method is used for the evaluation of the cellular uptake of the NCs³.



RESULTS

Structural Characterisation by FTIR and DLS

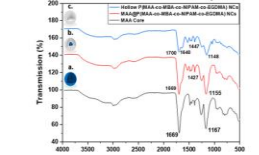


Figure 1. FTIR results showing the characteristic peaks corresponding to the vibration bonds of the different polymers used during synthesis (MAA, NIPAM, EGDMA)

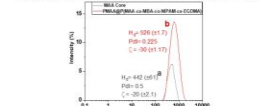


Figure 2. DLS results showing nanocontainers with a hydrodynamic diameter size of ~500nm and a negative zeta potential ranging from -20mV to -30mV.

Morphological Characterisation by SEM

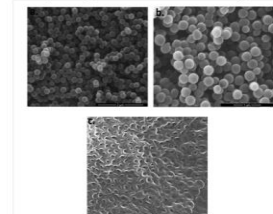


Figure 3. Images of the different nanocontainers harvested after each synthesis step. (a) and (b) represent MAA core with 270nm size and dual-sensitive core shell homogenous spheres with 350nm size, respectively. (c), (d) hollow nanocontainers appear with 350nm in size and a clear cavity (concave shape) after the core removal.

Biological Evaluation

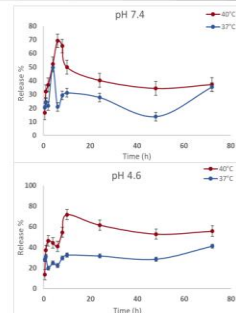


Figure 4. Release profile of cisplatin from the nanocontainers in different conditions. Release in acidic pH 7.4 at 37 and 40°C (upper top graph), release in acidic pH 4.6 at 37 and 40°C (bottom graph). Release at 40 °C was always higher than the release at 37 °C despite the pH. Yet, the highest release was achieved when the environment was acidic with 40°C. * Loading capacity of the NCs with cisplatin was 63%. Error bars are based on mean ± SD of three experiments.

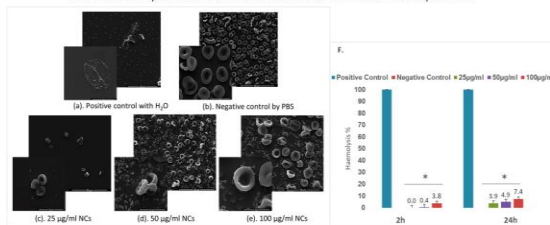


Figure 5. Haemolysis assay results analysed by SEM after 24h incubation with 3 different concentrations of NCs in addition to positive and negative controls (left). Haemolysis percentages calculated after 2h and 24h incubation with different concentrations of NCs (F). Haemolysis percentages was <8% for both time points (F). (a). Positive control sample of RBC haemolysed RBCs; (b). Negative control sample of RBC; (c), (d), and (e). RBC incubated with 25 µg/ml, 50 µg/ml, and 100 µg/ml NCs suspensions respectively for 24h showing healthy and unaffected RBCs. *Student's t test (p < 0.05); error bars are based on mean ± SD of three experiments.

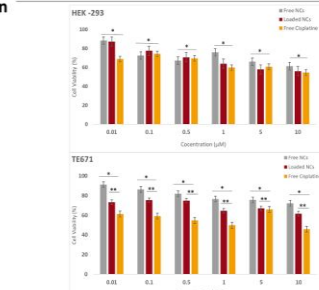


Figure 6. Evaluation of the cell viability and cytotoxicity via MTT assay in HEK-293 (top) and T671 (bottom) of cisplatin-loaded NCs, free NCs, and free cisplatin. *Student's t test (p < 0.05) ** (p < 0.01); error bars are based on mean ± SD of triplicates of three experiments.

Table 1. Cellular uptake evaluation of NCs by fluorescence microscopy. Both cell lines showed good uptake of the free and encapsulated rhodamine. However, the encapsulated rhodamine with cisplatin showed less fluorescence than the free rhodamine. This observation supports the sustained release characteristic of the NCs.

Incubation time	HEK-293 Control			T671 Rhabdomyosarcoma		
	Standard Light	Green Light	Overlay	Standard Light	Green Light	Overlay
1h	Encapsulated rhodamine	[Image]	[Image]	[Image]	[Image]	[Image]
	Free rhodamine	[Image]	[Image]	[Image]	[Image]	[Image]
5h	Encapsulated rhodamine	[Image]	[Image]	[Image]	[Image]	[Image]
	Free rhodamine	[Image]	[Image]	[Image]	[Image]	[Image]

CONCLUSIONS AND FUTURE WORK


Polymeric nanocontainers have shown good drug encapsulation, sustained release profile, and a good cellular uptake. Further optimisation of the NCs' loading capacity will take place for a sustained drug release and prolonged drug biodistribution, in addition to surface modification with targeting agents. Additional experiments will also be performed to evaluate their efficacy in other paediatric brain tumour cell cultures and mouse-models using different chemotherapeutic drugs.

References

1. Glosli, H. et al. (2021). Non-parameningeal head and neck rhabdomyosarcoma in children, adolescents, and young adults: Experience of the European paediatric soft tissue sarcoma study group (EPTSG - RMS2005 study). *European Journal of Cancer*, 151, 84-93. <https://doi.org/10.1016/j.ejca.2021.04.007>

2. Leiner, J., & Le Loarer, F. (2019). The current landscape of rhabdomyosarcomas: an update. *Virchows Archiv*, 476(1), 97-108. <https://doi.org/10.1007/s00428-019-0276-9>

3. Tzavali, C., Efthimiadou, E., Seriah, S., & Chrysiatou, C. (2019). Development of multi-layered and multi-sensitive polymeric nanocontainers for cancer therapy: in vitro evaluation. *Scientific Reports*, 9(1). <https://doi.org/10.1038/s41598-019-32890-5>




University of Hertfordshire

ENHANCEMENT OF CHEMOTHERAPY DELIVERY AND OUTCOME IN PAEDIATRIC RHABDOMYOSARCOMA USING SMART POLYMERIC NANOCONTAINERS

Sara Seriah^{1,2,3}, Eleni Efthimiadou^{2,3}, Maria Braoudaki¹

¹Department of Clinical, Pharmaceutical and Biological Sciences, School of Life and Medical Sciences, University of Hertfordshire, UK; ²Department of Chemistry, Inorganic Chemistry Lab, National and Kapodistrian University of Athens, Greece; ³NCSR "Demokritos", Sol-Gel Laboratory, Institute of Nanoscience and Nanotechnology, Greece



**HELLenic REPUBLIC
National and Kapodistrian
University of Athens**

ABSTRACT
Rhabdomyosarcoma is a rare type of paediatric CNS tumours with poor prognosis overall. Current chemotherapeutic agents lack in specificity resulting in poor treatment outcome and long-term side effects. Chemotherapeutic drugs encapsulation in nanocarriers is the approach through which it is aimed to enhance the efficacy and outcome of the treatment. In this project rhabdomyosarcoma cells were treated with drug loaded nanocontainers. The treatment of TE671 cell line with drug loaded nanocontainers showed sustained drug release and good cellular uptake of the loaded nanocontainers by cytotoxicity assay and fluorescence microscopy images, respectively. Therefore, drug loaded nanocontainers can be used as potential enhancers for the rhabdomyosarcoma's treatment efficacy and outcome. Further experiments will be carried out with modified surface nanocarriers and different encapsulated drugs in other paediatric brain tumours cell lines.

INTRODUCTION
Paediatric CNS tumours are the leading cause of cancer death in children. One of the rare types of paediatric CNS tumour is the paediatric rhabdomyosarcoma with 4.5 cases reported per 1 million children (Glosli et al., 2021). Yet, this rare type is also the most common type of soft-tissue cancer in children. It originates in the head/neck area in 40% of cases. Despite the progress made in the diagnosis and treatment of moderate cases with 75% five-year survival rate, severe cases of rhabdomyosarcoma have lower survival rate (20%) and poor treatment outcome (Leiner & Le Loarer, 2019). Additionally, current chemotherapeutic agents lack in specificity and selectivity, resulting in unpleasant and long-term side effects for the child (Glosli et al., 2021). Encapsulating the chemotherapy drugs within carriers called nanocontainers (NCs) is one approach to improve both efficacy and therapeutic outcome of the drugs. Due to their nano-size and suitable modified surface, polymeric NCs can cross the blood-brain-barrier without causing any damage.

AIMS
The aim was to synthesize polymeric nanocontainers that are capable of delivering chemotherapy drugs at the tumour site to increase their efficacy and reduce their side effects.

METHODOLOGY

Synthesis of Nanocontainers

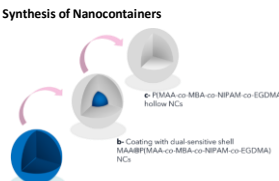


Figure 1. Synthesis steps of hollow polymeric nanocontainers³. (a). Core template, (b). Coating with the pH and thermosensitive layer, (c). Core removal and the obtaining hollow polymeric NCs.


Structural characterisation by:

- Dynamic Light Scattering (DLS)
- Fourier Transform Infrared Spectroscopy (FT-IR)

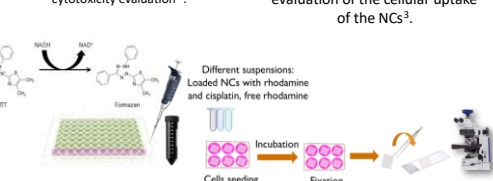
Morphological characterisation by:

- Scanning Electron Microscopy (SEM)

Haemolysis Assay
This assay is used for the evaluation of biocompatibility of the NCs³.



MTT Assay
This assay is used for cytotoxicity evaluation³.



RESULTS

Morphological Characterisation by SEM

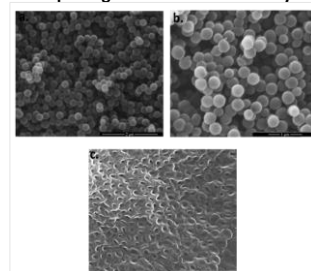


Figure 1. Images of the different nanocontainers harvested after each synthesis step. (a) and (b) represent MAA core with 270nm size and dual-sensitive core shell homogenous spheres with 350nm size, respectively. (c). Hollow nanocontainers appear with 350nm in size and a clear cavity (concave shape) after the core removal.

Release Profile

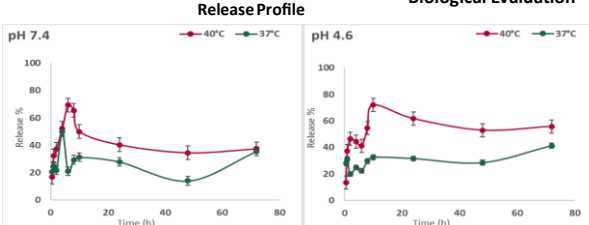


Figure 2. Release profile of cisplatin from the nanocontainers in different conditions; release in neutral pH 7.4 at 37 and 40°C (left), release in acidic pH 4.6 at 37 and 40°C (right). Release at 40°C was always higher than the release at 37°C despite the pH. Yet, the highest release was achieved when the environment was acidic with 40°C. * Loading capacity of the NCs with cisplatin was 63%. Error bars are based on mean±SD of three experiments.

Cytotoxicity

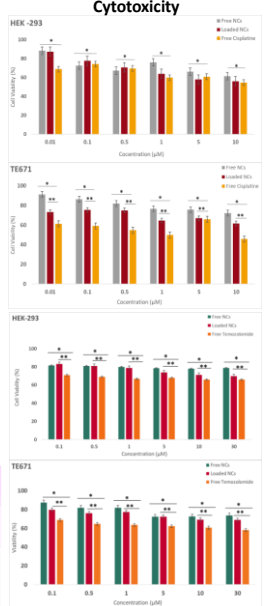


Figure 4. Evaluation of the cell viability and cytotoxicity via MTT assay in HEK293 (top graphs) and TE671 (bottom graphs) of cisplatin and temozolomide loaded NCs, free NCs, and free cisplatin and free temozolomide. *Student's t test ($p \leq 0.05$) ** ($p \leq 0.01$); error bars are based on mean±SD of triplicate experiment.

Biocompatibility

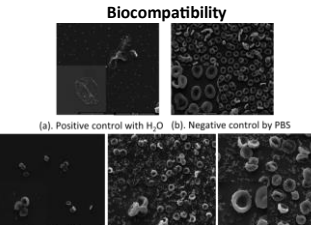


Figure 3. Haemolysis assay results analysed by SEM after 24h incubation with 3 different concentrations of NCs in addition to positive and negative controls. (a). Positive control; (b). Negative control; (c), (d), and (e). RBC incubated with 25 µg/ml, 50 µg/ml, and 100 µg/ml NCs suspensions respectively for 24h showing healthy and unaffected RBCs.

Cellular Uptake

Table 1. Cellular uptake evaluation of NCs by fluorescence microscopy
Both cell lines showed good uptake of the free and encapsulated rhodamine. However, the encapsulated rhodamine with cisplatin showed less fluorescence than the free rhodamine. This observation supports the sustained release characteristic of the NCs.

Incubation time	HEK-293 Control			TE671 Rhabdomyosarcoma		
	Standard Light	Green Light	Overlay	Standard Light	Green Light	Overlay
1h	Encapsulated rhodamine and cisplatin					
	Free rhodamine					

CONCLUSIONS AND FUTURE WORK
Polymeric nanocontainers have shown good drug encapsulation, sustained release profile, and a good cellular uptake. Further optimisation of the NCs' loading capacity will take place for a sustained drug release and prolonged drug biodistribution, in addition to surface modification with targeting agents. Additional experiments will also be performed to evaluate their efficacy in other paediatric brain tumour cell cultures and mouse-models using different chemotherapeutic drugs.

References
1. Glosli, H. et al. (2021). Nonparameningeal head and neck rhabdomyosarcoma in children, adolescents, and young adults: Experience of the European paediatric soft tissue sarcoma study group (EPSTO). *Radiology*. Study. *European Journal of Cancer* 151: 84-93. <https://doi.org/10.1016/j.ejca.2021.08.007>
2. Leiner, J., & Le Loarer, F. (2019). The current landscape of rhabdomyosarcoma: an update. *Archives of Disease in Childhood*, 94(7), 671-676. <https://doi.org/10.1136/archdischild-2019-036716>
3. Iordanis, G., Efthimiadou, E., Kostas, G., & Chalkitzioglou, C. (2018). Development of multiblock and multicomponent polymeric nanocontainers for cancer therapy: in vitro evaluation. *Sensors* 18(11), 3699. <https://doi.org/10.3390/s18113699>

**LIST OF WORKSHOPS,
SEMINARS,
TALKS, CONFERENCES,
AWARDS,
AND TRAININGS**

Research Development Sessions (RDP)

Session Title	Date	Time
How To Write A Scientific Paper (And Get It Accepted!)	3 rd June 2020	From 2pm To 4pm
Taking Care Of Your Mental Health And Wellbeing For Your PGR Journey	30 th June 2020	From 2pm To 3.30pm
Thesis Writing Bootcamp	7 th July 2020	From 2pm To 5pm
How to Be an Effective Researcher	13 th July and 15 th July 2020	From 2pm To 4pm
Time & Energy Management	16 th July 2020	From 2pm To 5pm
Unlocking Creative Potential	9 th July 2020	From 2pm to 4pm
Advanced Presentation Skills For Public Engagement	8 th July 2020	From 2pm to 5pm
Critical Reading and Writing RDP	5 th November 2020	From 1pm To 4pm
A Guide to Applying For External Research Funding For New Researchers (PGRS and ECRS)	5 th November 2020	From 11am To 12pm
Critical Thinking	4 th November 2020	From 10am To 11.30am
Thriving Resiliently	12 th November 2020	From 10am To 4pm
Maximise Your Memory	26 th November	From 1pm To 4pm

Open Transparent Knowledge	3 rd December 2020	From 1pm to 2pm
The British PhD And How to Bag One	10 th Dec 2020	From 2.30pm to 4pm
Introduction to Statistics	25 th January 2021	From 2pm to 3pm
Thesis, What Thesis?	4 th February 2021	From 1pm to 2.30pm
Registration and Doctoral Review Assessment	4 th February From	From 10am To 11am
Imposter Syndrome	17 th February 2021	From 9.30am to 12.30pm
Managing Pressure Positively	18 th February 2021	From 1.30pm to 4.30pm
Overcoming the Challenges of Research	26 th January 2022	From 1.30pm to 4.30pm

Postgraduate Research (PGR) Seminars

- **November 9th, 2020**

- “Investigations on mycoviruses found in *Dothistroma septosorum* and *Beauveria bassiana* and their effects on fungal pathogenicity” by John Oluwayemi Daudu
- “Population dynamics of *Pyrenopeziza brassicae* under Irish field conditions” by Diana - Elena Bucur
- “The role of oxidative stress in the motor neuron disorder spinal muscular atrophy” by Fathama Mutaleb

- **December 7th, 2020**

- “Understanding the impact of low temperature on seed germination in maize” by Macarena Mellado Sanchez
- “Investigating the viability of Outer Membrane Vesicle Inhibition to sensitize bacteria to phage therapy” by Dominik Brotherton.

- **January 11th, 2021 (Presenter)**

- “Investigating pathogen-plant signalling during the switch from biotrophy to necrotrophy in hemibiotrophic interactions” by Donovan William Coles.
- “Understanding interactions between fungal pathogens *Leptosphaeria maculans* (phoma stem canker) and *Pyrenopeziza brassicae* (light leaf spot) on *Brassica napus* (oilseed rape) important phytochemicals” by James Fortune.
- “Development of smart polymeric nanocontainers for the treatment of pediatric brain malignancies” by Sara Seriah

- **February 8th, 2021**

- “Identification and validation of potential inhibitors targeting enoyl-acyl carrier protein reductase (InhA) in *Mycobacterium* species: a computational approach” by Menaka Menikpurage
- “Discovery of the genetic basis of partial resistance against *Pyrenopeziza brassicae* in oilseed rape (*Brassica napus*)” by Ajisa Ali

- **March 8th, 2021**

- “The role of myocyte microvesicles in cancer metastasis” by Dona Mannaperuma
- “Prophage contribution to virulence, persistence and transmission of *Clostridioides difficile*” by Ross Kalarus.

- **April 19th, 2021 (Chair)**

- “Role of phage transduction in the spread of antibiotic resistance in *Clostridioides difficile*” by Graham McLaughlin.
- “Evaluation of healthy lifestyle interventions for overweight and obese young people aged 10 – 19 years in UK and Thailand focusing on goal setting, motivational interviewing and participant preferences” by Srila Satoh.
- “Elucidation of the autophagy networks that are disturbed in Spinal Muscular Atrophy; a pharmacological approach” by Saman Rashid.

- **November 15th, 2021**

- “Analysing and assessing the current web-based NPS scenarios; drafting an ad-hoc theoretical model to predict future drug issues in the real world” by Catalani, Valeria
- “Particle engineering approaches to control the interaction of medicinal aerosols with the humid lung” by Legh-Land, Victoria
- “Assessing ocular toxicity in vitro” by Akther-Ali, Elisa

- **February 7th, 2022**

- “Understanding host resistance to improve control of light leaf spot on winter oilseed rape in the UK” by Sapelli, Laura
- “Aryl-piperazine sulphonamides in the treatment of Levodopa-induced dyskinesia in a rat model of Parkinson’s disease” by Hassankhani, Kiana
- “Neuroprotective properties of Arylpiperazine sulphonamides in models of Parkinson's disease and Multiple Sclerosis” by Kingslake, Alice

- **May 9th. 2022 (Chair)**

- “Identifying novel theranostic interventions for aggressive childhood tumours using functional magnetic nanoparticles” by Syrios, Konstantinos.
- “Microphysiological models for the assessment of pulmonary concentration of inhaled aerosols” by Fantuzzi, Caterina.
- “Stimuli-responsive amphiphiles as advanced materials for topical drug delivery” by Rajbanshi, Abhishek.
- “Designing and delivering selective inhibitors of the calcium-binding protein S100P as anti-metastatic agents” by Tasnim, Nishat.
- “Genetic control of Lemna growth rate and protein content” by Espinosa Montiel, Javier

- **October 10th, 2022**

- “Understanding the opposing roles of the planar cell polarity proteins Celsr1 and Frizzled6 in breast cancer invasion” by Klena, Ladislav.
- “Detection of inflammatory markers in CNS neurodegeneration” by Shahin, Layal-Walid
- “Dissecting the Role of Oxidative Stress in Spinal Muscular Atrophy (SMA)” by Pacheco Torres, Paloma
- “Development and validation of a novel transport system for cell culture platforms” by Saeed, Amjad

- **January 9th, 2023 (Presenter)**

- “Pediatric Rhabdomyosarcoma Treatment Using Dual Sensitive Nanocontainers” By Sara Seriah
- “Understanding host resistance to improve control of light leaf spot on winter oilseed rape in the UK” by Sapelli, Laura

- “Neuroprotective properties of Arylpiperazine sulphonamides in models of Parkinson's disease and Multiple Sclerosis” by Kingslake, Alice
- “Development of Claim Substantiation Algorithm for Cosmetics and Personal Care Products” by Falcone, Robert

Bioscience Research Group (BRG) Seminars

- “Dynamic interaction networks and conformational plasticity of the SARS-CoV-2 protein” by Prof. Ana-Nicoleta Bondar (Freie Universität Berlin), 11th November 2020
- “Problems and possibilities of bacterial mobile genetic elements” by Prof. Peter Mullany (UCL Eastman Dental Institute), 20th January 2021
- “Tissue engineering strategies to generate functional neuronal networks” by Dr. Eric Hill (Aston University), 24th February 2021
- “A sweet approach towards the treatment of cancer and sepsis” by Dr Shoib Siddiqui (University of Hertfordshire), 28th April 2021.
- “Interplay of vascular endothelial growth factor receptors in organ-specific vessel maintenance” by Dr Sinem Karaman, (University of Helsinki & Wihuri Research Institute) 23rd February 2022
- “Combining bioinformatic and drug repurposing approaches to develop second-generation therapies for spinal muscular atrophy” by Dr Melissa Bowerman (Keele University) 23rd March 2022.

Talks

- **Live Session on Research Degrees in Biosciences**

February 8th, 2021 1pm to 3pm Session organized by Dr. Maria Dimitriadi

A 5 min talk to undergraduate students about the research topic and the journey led to pursuing a research degree.

- **Live Lectures – Careers Talks at the University of Hertfordshire - PhD Students Sessions**

Part of BRM module

March 26th, 2021 9pm to 11 am Session organized by Dr. Philip Sawle

A 20 min talk to undergraduate students about the journey to research degree, what is the presenter's research about, and what has been learnt/accomplished so far.

- **Live Lectures – Careers Talks at the University of Hertfordshire - PhD Students Sessions**

Part of BRM module

March 25th, 2022 10am to 10.30 am Session organized by Dr. Philip Sawle

A 20 min talk to undergraduate students about the journey to research degree, what is the presenter's research about, and what has been learnt/accomplished so far.

Conferences attended

- MarketsandMarkets Epigenetics 5th Annual conference, May 2020 (virtual)
- International Society of Pediatric Oncology (SIOP) 52nd congress, October 2020 – Poster presentation (virtual)
- Advances in Genetic Medicine Conference by Society for Medicines Research, December 2020 (virtual)
- Festival of Genomics & Biodata, January 2021 (virtual)
- Athens Conference on Advances in Chemistry, March 2021 – Oral Presentation (virtual)
- School Of Life And Medical Sciences (LMS) conference, June 2021 – Oral presentation (virtual)
- International Society of Pediatric Oncology (SIOP) 53rd congress, 2021 – Oral Presentation (virtual)
- UCL Cancer Domain Symposium '*Cancer Environments*' May 2022, London, UK (in person)
- School Of Life And Medical Sciences (LMS) conference, June 2022 – Poster presentation, Hertfordshire, UK (in person)
- Athens Conference on Advances in Chemistry, June 2022 Oral presentation, Athens, Greece – Oral Presentation (in person)
- International Society of Pediatric Oncology (SIOP) 54th congress, 2022 – Oral Presentation (in person).

Awards

- Nominated and shortlisted in the 2020-2021 School of Life and Medical Sciences Dean's Awards, in the category of "Department of CPBS Student engagement with research (Undergraduate or Postgraduate)", May 2021.
- The best oral presentation in the category of Bioscience, Nutrition & Dietetics research parallel session, in the LMS conference June 2021.
- The poster presentation in the category of "Mechanisms of Disease & Drug Toxicology research" in LMS conference, June 2022.
- Best Oral presentation in the Athens conference on advances in chemistry June 2022.
- Conference Grant Scheme B (Non-Genetics Society Meetings) travel grant award by Genetics Society, August 2022.

Trainings

- Bioinformatics for Biologists: An Introduction to Linux, Bash Scripting, and R
3 weeks online course by Wellcome Connecting Science, through FutureLearn – February 15th to March 7th, 2021 (completed with certificate)
- Scanning Electron Microscopy Training by Dr. Eleni Efthimiadou and Dr Elias Sakelis in National Center for Scientific Research "Demokritos"
Completed December 2021
- Cell Culture Training by Dr. Eleni Efthimiadou and Dr. Nikoleta Kostopoulou in National and Kapodistrian University of Athens
Completed March 2021